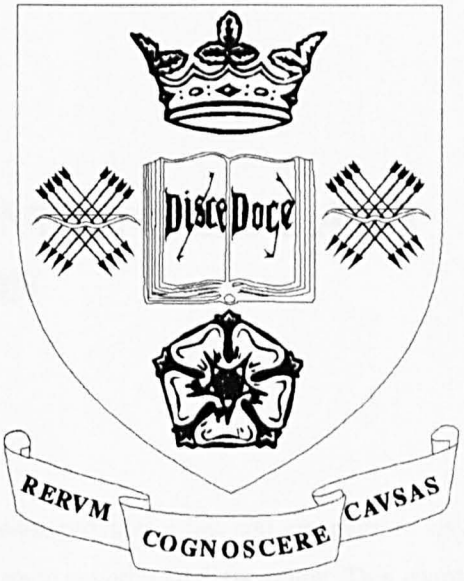

University of Sheffield
Department of Mechanical Engineering

Novel Developments of Moiré Techniques for Industrial Applications

Volume II

Manuel Eduardo Heredia Ortiz

April 2004

Thesis Submitted for the Degree of Doctor of Philosophy

CHAPTER V
MEASUREMENT OF SHAPE AND DEFORMATION

V.1 Introduction

The fringe projection technique provides a fast and inexpensive way of measuring the shape of an arbitrary object using simple experimental apparatus. This chapter describes the application of the projection moiré technique to the measurement of the shape of objects, making use of the instruments, algorithms and procedures previously described in Chapter IV. It is also possible to measure the change in shape, *i.e.* the deformation of a specimen by applying the method sequentially to measure the shape before and after the application of load and calculating the difference.

Section V.2 presents two examples of objects with complex three-dimensional shape to introduce and illustrate the shape-measurement method. The ability to quickly digitise shape information has direct application in quality control, reverse engineering, generation of computer models for finite element analysis, or archaeological, architectural and art surveys. The potential uses are truly diverse, with applications recently reported in fields such as the generation of characters for computer games and of special effects for the entertainment industry (*e.g.* Starck *et al.*, 2002), or even to assist forensic police in the identification of crime victims with facial reconstruction from skeletal remains (Kahler *et al.*, 2003), to name but a few. The terrorist attacks on the US in September 2001 have recently sparked interest as well in the use of biometrics, including the 3D scanning of faces or hands, to increase airport security.

Section V.3 describes in detail an engineering application of interest to the aerospace industry. Recent developments in digital reflection photoelasticity (*DRPE*) have made possible the measurement of the surface stress distribution in real aerospace components with complex shape. However, for these measurements to be accurate, it is necessary to consider the orientation of the surface of the component relative to the camera. A combined system based on moiré and *DRPE* has been developed capable of correcting for the effects of non-perpendicular

viewing. The section presents a description of the combined instrument and discusses the technique with a test case.

Finally, section V.4 discusses the use of the method for the measurement of deformation, using an application in the field of biomechanics to illustrate the methodology. The technique was used to provide experimental measurements of the deformation of human skin during *in vivo* mechanical tests designed to evaluate the effect of cosmetic products. The purpose of this investigation was to validate a numerical model of human skin for cosmetics testing.

V.2 Shape Measurement Examples

The basic principles of fringe projection for shape measurement were described in section II.3.2.4. A grating is projected onto the object of interest using a projector, and a camera viewing the object surface from a different direction collects an image. The shape information can be extracted using the dedicated fringe pattern analysis algorithms described in section IV.5, from the combination of the object image and a reference image of the fringes projected onto a flat plate. Finally, the phase can be related to the depth of the object surface through a set of parameters of the optical configuration, using one of the calibration expressions proposed in section IV.6. The two examples presented in this section use the simplest telecentric expressions, which is in practice appropriate in many cases. An example of the non-telecentric expressions required to obtain more precise measurements will be presented in Chapter IV

V.2.1 Buddha Statue

A small plaster statue was chosen as a case study to demonstrate the ability of the shape measurement system described in Chapter IV to deal with complex-shaped objects. The statue, with approximate dimensions 100×80×120*(mm)*, represents a sitting Buddha wearing monk clothes. The creases of the cloth in some of the areas create shadows that represent a challenge to the fringe projection technique. On the other hand, the uncoated surface of the plaster provided a matt and clear surface finish, ideal for the fringe projection technique.

The instrument was set-up to collect data as described in section IV.4. A diagram of the experimental set-up is shown in fig. 5.1(a). Distance h', measured between the reference plane and the base of the camera lens, was 1630*(mm)*. The projector was located to the right of camera, at a distance d'' of 490*(mm)*. The projector was equipped with a TV zoom lens 12.5-75*(mm)* f1:1.2. The f-stop was set between 1.2 and 2, the zoom between 50*(mm)* and 75*(mm)*, and focus at infinity. The camera used a Cosmicar Pentax TV zoom lens 8-48*(mm)* f1:1.0. Aperture was set to f5.6, zoom between 30-48*(mm)* and focus between 1.5-2. With this configuration and a 250*(lines/mm)* master grating, the pitch of the projected fringes on the reference plane was approximately 3.25*(mm)* (4 lines in 13mm). A cone with 16.7*(mm)* in

height and 35.0*(mm)* radius was used to collect a calibration image for the automatic calibration of the system, which yielded a calibration constant K=1.516*(mm/rad)* and a magnification of m_p=0.2326*(mm/pixel)*. The telecentric approximation was deemed adequate for this example.

The image shown in fig. 5.1(b) was collected with the instrument already set-up for data collection, using the projector without a grating in it as the only light source. The arrows in the figure point to areas in shadow, which are often impossible to eliminate completely in objects with complex shape, such as the one in this example. Areas in shadow will contain very poor fringe information and the technique needs to find ways to deal with this problem.

Figure 5.1(c) and (d) show respectively the object and reference images, 768×574 pixels in size. The image in fig. 5.1(b) was used as an estimate of the distribution of background illumination A in the fringe pattern, see eq. (4.1). This image was subtracted from the object in fig. 5.1(c), and the normalization algorithm described in section IV.5.3 was applied to the result to further enhance the uniformity and contrast of the object image. The result is shown in fig. 5.1(d). A mask, automatically generated by thresholding the quality map has been applied to this image to remove areas that do not contain fringe information (*i.e.* shadow areas and the dark background of the image). This eliminates areas with corrupted phase information, which otherwise may cause errors that could propagate through the image during unwrapping.

The normalised object and reference images were combined using the five-step phase-extraction algorithm to obtain the wrapped phase difference map shown in fig. 5.1(f). This map was unwrapped and calibrated to obtain the surface contour map shown in fig. 5.2(a). The graphs show surface profiles along the dotted lines in the image. A three-dimensional plot of the reconstructed surface is shown in fig. 5.2(b), side by side with an image of the statue taken from a similar perspective for comparison. The shadows in the object image cause areas where no shape information can be retrieved, but the processing algorithm is capable of avoiding these and calculates correctly the overall shape of the object. Note that the resolution of the 3D mesh has been lowered for clarity of display.

According to the conclusions of the error analysis presented in section IV.7, the accuracy of the measurement was expected to be better than 0.4*(rad)*, *i.e.* in the order of 0.6*(mm)*, for this configuration of the system. A quantitative assessment of this value would have required an alternative shape measurement technique to compare with, such as for instance a coordinate measurement machine (CMM), which was unfortunately not available for use by the author at the time of this study.

V.2.2 Fan Blade

Figure 5.3(a) shows a large fan blade from an aircraft jet engine, approximately 450*(mm)* long and 250*(mm)* wide. A 2.5*(mm)* thick photoelastic coating, which was used for stress analysis using reflection photoelasticity during vibration tests, was applied onto the root and leading edge of the fan blade.

The fringe pattern was projected onto the blade using a projector positioned to the left of the camera, to yield the object image shown in fig. 5.3(a). The pitch of the projected grating p was 6.25*(mm)* and the illumination angle θ was 30*(degrees)*. The glossy surface finish of the photoelastic material required careful illumination to prevent glare in the camera.

The system was calibrated using the automatic calibration procedure. A conservative value for the accuracy in this case was estimated at 0.7*(mm)* from the telecentric calibration constant of the system (1.7*mm/rad*), assuming the accuracy of the phase measurement was 0.4*(rad)*.

Figure 5.3(b) shows a coarse 3D mesh representation of the resulting depth map. The insert shows a detail of the 2.5*(mm)* high step formed by the edge of the photoelastic coating.

The arrow in fig. 5.3(a) points to an area with bright glare and a dark shadow, which have corrupted the phase information in the object image. As a result, the measured depth map presents a localized error in this area, as indicated by the arrow in fig. 5.3(b). The quality-guided unwrapping algorithm is designed to prevent the propagation of errors from such corrupted areas to the rest of the image.

V.3 Shape Correction In Digital Reflection Photoelasticity

Digital reflection photoelasticity (*DRPE*) is a non-destructive experimental technique that allows full-field visualization and measurement of the surface stress distribution in a real component. This technique has recently experienced important developments (Patterson, 2002a) that make it a quick and accurate method for obtaining full-field measurements, in real engineering components of arbitrary size and geometry, and under realistic static or dynamic loads. The technique is routinely used in the aerospace industry to assist in the design process of complex components, such as the landing gear assembly shown in fig. 5.4(a).

A thin birefringent coating is applied to the surface of the body that is to be analysed. Upon loading of the specimen, strains on the surface are transmitted to the coating, inducing stresses and birefringence. The coating response, in the form of a photoelastic fringe pattern, can be observed using a reflected-light polariscope, and used to infer the surface stress distribution in the specimen. Assuming ideal transmission of strains through the specimen-coating interface,

the observed isochromatic parameter α can be related to the difference of principal stresses σ_1-σ_2 in the surface of the body as follows (Dally and Riley, 1991):

$$\sigma_1 - \sigma_2 = \frac{E}{1-\nu}\frac{\lambda}{K}\frac{\alpha}{OPL} \tag{5.1}$$

where E and ν re respectively the Young's modulus and Poisson's ratio of the specimen', λ is the wavelength of the light, and K is the coating's strain coefficient. These parameters can be combined to yield a single property of the material, the fringe coefficient f *(N/mm)*

$$f = \frac{E}{1-\nu}\frac{\lambda}{K} \tag{5.2}$$

and eq.(5.1) can be rewritten

$$\sigma_1 - \sigma_2 = \frac{Nf}{OPL} \tag{5.3}$$

In order to derive correctly the stresses from the photoelastic data, it is necessary to obtain an accurate estimate of the optical path length (OPL), *i.e.* the distance travelled by the light through the birefringent material. For any given point, the OPL depends on the thickness t of the birefringent coating, and on the orientation of the surface φ relative to the observation axis, as illustrated by fig. 5.4(b).

$$OPL = \frac{2t}{\cos\varphi} \tag{5.4}$$

The preparation and bonding of a good quality photoelastic coating with relatively uniform thickness t is possible, although it is a time-consuming and skilled job, which requires an experienced technician. However, in complex-shaped engineering components the surface orientation φ changes for each point in the field of view of the camera, and the need arises for an experimental full-field technique to complement *DRPE*.

In addition to the oblique viewing effect described above, which accounts for the increased path length, there is also an oblique incidence effect on the fringe pattern when the light path is not normal to the surface (Zandman and Wood, 1956). It must be taken into account that the light is affected by the principal stress difference in the plane normal to the light path. This effect, which can be beneficial in stress separation applications (see *e.g.* Pacey, 2000), otherwise introduces further errors in the interpretation of the fringe order.

Lesniak and Zickel proposed in 1998 a technique for automatic coating thickness measurement using special tinted coatings. However, this technique cannot be used to correct for oblique incidence effects.

The aim of this project was to develop a technique easily integrated with existing methods of *DRPE* to measure the surface orientation and correct the oblique viewing and incidence effects. Among the range of shape measurement techniques, fringe projection was considered particularly appropriate due to its simplicity and robustness, and the fact that it is a non-contacting method, and the apparatus is easy to incorporate into the *DRPE* equipment.

The following two sections respectively describe the apparatus and experimental procedure for data collection, where they differ from those presented in Chapter IV. Section V.3.4 shows some experimental results to evaluate the accuracy of technique. Section V.3.5 presents an industrial application as a case study to illustrate the technique.

V.3.1 Experimental Apparatus

A combined instrument for *DRPE* and fringe projection was designed and built for this research, based on the instrument described in Chapter IV. All the elements were assembled on a tripod as shown in fig. 5.5. The instrument uses a common observation leg (CCD Camera Panasonic WV BP100) to collect both the photoelastic and fringe images. This arrangement allows the collection of photoelastic data and fringe data in the same reference system, eliminating the need for perspective corrections prior to combining the data from the two techniques. A basic reflected-light polariscope (Measurements Group Mod. 031), including polarizer, analyser, two quarter-wave plates and a standard light source was incorporated to the instrument to enable the collection of the photoelastic data. The polariscope was attached using a second accessory bar and the same quick-release standard elements (Manfrotto). Figure 5.5(a) shows the simplest version of the combined instrument, which was developed for static tests, and used the fringe projector described in Chapter IV in the projection leg of the apparatus.

A second version of the instrument was developed for the vibration tests and is shown in fig. 5.5(b). The standard light source used with the reflection polariscope was replaced by a stroboscope. Also, the standard fringe projector was substituted by a custom fitting designed to use the stroboscope, clipped to an adaptor at the back of the part, as a light source. A collecting lens focused the light from the stroboscope onto a master grating, and a large format photographic lens (Mamiya) was used to project the image of the grating onto the object.

The images collected with the instrument were downloaded into a PC computer with three software packages developed in-house for the acquisition (CatchSIX), automated photoelasticity (VISION) and fringe analysis (JOSHUA). Images 256×256 pixels in size were used for compatibility with the existing photoelastic software VISION.

V.3.2 Experimental Procedure

Figure 5.6(a) shows a demonstration sample, built by bending a piece of 1.5*(mm)* thick aluminium sheet into a relatively arbitrary shape. A 30*(mm)* diameter hole was drilled on the sample to create a stress concentration. The approximate dimensions of the specimen were 80*(mm)* height, 160*(mm)* width, and 50*(mm)* depth. A sheet of birefringent material was prepared and bonded to the surface of the specimen to perform reflection photoelasticity. An elementary loading system was devised, which allowed the application of a bending load to the sample by tightening the nut and bolt located at the back.

The set-up of the combined instrument for static tests follows the same steps described in section IV.4.2. In this example the distance from the object to the camera was h=1459*(mm)*, and the projector was located to the left of the camera at a distance d=560*(mm)*. The pitch of the fringes projected onto the reference plane were p=3.232*(mm)*.

Good quality data for digital reflection photoelasticity is normally much more difficult to obtain than the fringe data, and therefore was typically collected in first place. The methodology described in Patterson (2002a) was followed. This technique is based in the temporal phase-stepping technique by Patterson and Wang (1991) and requires six phase-stepped images obtained by incremental rotations of the optical elements of the polariscope. A typical set of photoelastic data $i_1,...,i_6$ is shown in fig. 5.6(b). This data was collected using the camera in the combined instrument with the polariscope in position. The light source from the polariscope was used to illuminate the object, and fringe projector remained switched off. Processing of photoelastic data was performed in the software package VISION, which implements the algorithms described in Wang and Patterson (1995), to yield the isochromatic fringe order map shown in fig. 5.7(d).

The collection of fringe data was typically conducted at the end of the test. Fringe projection using the apparatus and methodology described in this thesis proved robust, and therefore it was easier to obtain good quality data in adverse conditions. The polariscope was removed with care not to disturb the rest of the apparatus because it was not necessary for the collection of fringe images, and filtered some of the light reducing the contrast of the fringe patterns.

Figure 5.6(c) shows the three images needed for shape measurement: object, reference, and calibration. The object image was collected in the first place, with the fringe projector switched on. To obtain the reference image, a flat card clamped to an articulated arm was positioned in front of the specimen, and aligned perpendicular to the camera axis as described in section IV.6.2. Finally, a calibration cone 6.0*(mm)* in height and 25.0*(mm)* in diameter was attached to the reference card and a third image was collected to calibrate the system using the automatic calibration method. The size of the cone was selected to match that of the features of interest in

the specimen. The automatic calibration of the system using the reference and calibration images shown in fig. 5.6(c) yielded K= -1.3398(*mm/rad*) and m_p= 0.5050(*mm/pixel*).

V.3.3 Shape Correction Processing Algorithms

The shape measurement technique provides a full-field description of the test surface shape in the form $z=f(x, y)$, with z aligned with the viewing axis. Figure 5.7(a) shows a 3D mesh representation of the measured shape for the demonstration specimen, obtained by processing the object and reference images in fig. 5.6(c) and applying the calibration to the resulting phase map as described in previous sections.

The obliquity coefficient $\cos\varphi$ can be derived from the measured surface depth map, $z=f(x, y)$, by differentiating the depth map point-by-point to obtain the partial derivatives $\partial z/\partial x$ and $\partial z/\partial y$, and applying the following expression:

$$\cos\varphi = \sqrt{1+\left(\frac{\partial z}{\partial x}\right)^2+\left(\frac{\partial z}{\partial y}\right)^2} \tag{5.5}$$

The partial derivatives were calculated in the discrete domain using the following expressions, where m_p is the camera magnification, in *(mm/pixel)*.

$$\frac{\partial z}{\partial x}(i,j) = \frac{z(i,j+1)-z(i,j)}{m_p}$$
$$\frac{\partial z}{\partial y}(i,j) = -\frac{z(i+1,j)-z(i,j)}{m_p} \tag{5.6}$$

Differentiation in the discrete domain is very sensitive to the presence of noise in the original data. To overcome this difficulty, a median filter was applied to the depth map before calculating the derivatives, and again to the calculated obliquity map. The median filter was found particularly suitable because it reduces spike noise with minimal distortion of the shape, for instance near the sudden jumps due to unwrapping errors. Figure 5.7(b) shows the map of $\cos\varphi$ calculated using eq. (5.5) in this example.

The surface orientation can be taken into account in the calculation of the principal stress difference by using a corrected value of the isochromatic fringe order α' in the standard *DRPE* expressions (which assume that $OPL=2t$):

$$\alpha' = \alpha\cos\varphi \tag{5.7}$$

The map of corrected isochromatic fringe order α', shown in fig. 5.7(e) was calculated by application of eq. (5.7) pixel by pixel to the maps of surface orientation $\cos\varphi$ and raw fringe order α, respectively shown in figures 5.7(b) and (d).

The plot in fig. 5.7(c) illustrates the correction process showing a profile along the horizontal middle line of the maps of surface orientation (dotted line), raw fringe order (solid line) and corrected fringe order (dashed line).

V.3.4 Experimental Evaluation Of The Technique

A set of tests was conducted using a Brazilian disk to study the effects of oblique viewing and incidence in a component with two-dimensional stress field. The oblique viewing effect is independent of the relative orientation of the direction of the principal stresses with respect to the orientation of the surface. In contrast, the oblique incidence effect does depend on the orientation, and therefore it was preferred to test the correction in a component with an interesting biaxial stress field. It was decided to use the Brazilian disk (*i.e.* a thin disk under diametral compression), because this classical problem has a known analytical solution, which simplified the evaluation of the experimental results. The Brazilian disk was rotated about its two principal axes to introduce oblique viewing and incidence.

The stress-freezing process was used to lock deformations in the model. The molecules of many polymeric materials are connected in a network of strong primary bonds, and some weaker, shorter secondary bonds. At room temperature, both sets of bonds act to resist deformation, but as the temperature is increased, the secondary bonds start to degrade and break down. The specimen undergoes large deformations of elastic character, because the primary bonds carry the entire load. If the temperature is lowered gradually and the load is maintained, the secondary bonds re-form in the deformed position, locking the primary bonds in their elongated position. When the load is removed, a significant elastic deformation of the primary bonds remains permanently locked in the specimen at a molecular scale by the reformed secondary bonds. Practical details of the implementation of this method, initiated by Oppel (1936), can be found *e.g.* in Kobayashi (1987).

Although it was not strictly necessary to employ this technique in this case, it allowed a simplification of the experimental apparatus by disposing of the loading frame. This facilitated the manipulation (rotation etc) of the specimen during data collection and guaranteed the repeatability of the tests.

V.3.4.1 Preparation Of The Samples

The analytical solution to the state of stress of a thin disk of diameter D compressed by diametrically opposed forces of value F can be found in standard texts (Den Hartog, 1952). Without going into detail, the solution can be found by applying superposition of two Boussinesq solutions and a uniform field of hydrostatic tension.

A Cartesian coordinate system is chosen with the origin at the centre of the disk, and the y-axis along the diameter where the load is applied. The components of stress at the centre of the disk are

$$\sigma_x = \frac{2F}{\pi Dt}$$
$$\sigma_y = -\frac{6F}{\pi Dt}$$
$$\tau_{xy} = 0 \qquad (5.8)$$

Due to the symmetry of the problem, the directions of the principal stresses at the centre of the disk coincide with the directions of the axes, hence $\sigma_1=\sigma_x$ and $\sigma_2=\sigma_y$. Substituting in eq. (5.3) and rearranging yields an expression of the load F that produces a fringe order N at the centre point of the disk:

$$\sigma_1 - \sigma_2 = \frac{8F}{\pi Dt} = \frac{Nf}{2t}$$

$$F = \frac{f\pi D}{16} N \qquad (5.9)$$

A disk of diameter $D=50(mm)$ was cut from a sheet of photoelastic material MY750 (Kenny, 1965) of thickness $t=6(mm)$. A diametral compressive load F was applied using the fixture shown in fig. 5.8(a). The magnitude of the load necessary to achieve a fringe order of approximately 2 at the centre was roughly estimated using a value of the material's fringe constant $f=400(N/mm)$, based on the experimental data shown in Table V-1 (Patterson, 2002b).

Critical temperature	T_{crit} (℃)	*140*	*144.1*	*146.2*	*147*	*148.9*
Photoelastic fringe constant	*f (N/mm fringe)*	*0.397*	*0.460*			
Young's modulus above T_{crit}	*E (N/mm)*	*35*	*40*			

Table V-1: Properties of MY-750

The material's fringe constant f and also the critical temperature T_{crit} depend on the degree of polymerisation, which is variable with the batch due to slight changes in chemical composition and curing conditions. Although these values are normally calculated from experimental tests in samples prepared from the same batch of material, this was not deemed necessary for this study.

Substitution of the above values in eq. (5.9) yielded $F=7.85(N)$, which corresponds to a mass $m=P/g=800(g)$. The mass of the lower part of the loading fixture, without extra weight, was $930(g)$. With this load, the fringe order expected in the centre of the disk was 2.35.

The model and the loading fixture were placed in an oven with programmed temperature control for the stress freezing process (Oven manufactured by Laboratory Thermal Equipment Ltd., Greenfield, Oldham, equipped with a P1000 programmer manufactured by FGH Controls Ltd.). Figure 5.8(b) shows the curve of temperature versus time used. The model was heated rapidly to reach the critical temperature estimated from the experimental data in Table V-1 (Patterson, 2002b) as T_{crit} =145*(℃)*. This is where the secondary bonds break. Only about ±5% control of the critical temperature was necessary because the process of degradation of the bonds occurs gradually. The loaded model was left to soak for an hour to ensure a uniform temperature throughout the model. The model was cooled back to room temperature very slowly in order to minimize temperature gradients. Finally, the load was removed and the model taken out of the oven. After the stress freezing process, the front face of the disk was polished and the reverse side was sprayed with silver paint to allow stress analysis using reflection photoelasticity.

The fringe order measured at the centre of the disk in the finished specimen was 1.75. The discrepancy with the expected value is probably because the actual value of f for the batch was around 300*(N/mm fringe)*.

V.3.4.2 Description Of The Test

In the first test, the disk was tilted at 10*(degrees)* increments about the vertical axis, from -40 to +40*(degrees)*. For each case, a full set of six photoelastic images was collected, together with one fringe object image to determine the orientation of the disk. The reference and calibration images were also acquired at the end of the test to complete the data set.

Figure 5.8(c) shows examples of the experimental data. The fringe object image and one of the six phase-stepped photoelastic images are shown for the Brazilian disk at 0, 20 and 40*(degrees)* rotation about the y-axis. It can be seen that the photoelastic and fringe images, acquired using the combined instrument, share the same reference frame.

A similar set of data was collected in a second test, in which the disk was tilted between -40 and +40 at 10*(degrees)* increments, this time about the horizontal axis.

Manual readings of the fringe order at the centre of the disk were also collected for the different inclinations, in order to validate the measurements obtained with *DRPE*. The camera was removed to collect these measurements using the polariscope in the instrument and a null-balance compensator (Cloud, 1998).

V.3.4.3 Experimental Results

The correction of oblique observation and incidence effects could in principle be conducted for the general case, assuming the full state of stress (given either by σ_x, σ_y and τ_{xy}, or by σ_1, σ_2 and

the isoclinic angle) is known for each point in the field of view. Since *DRPE* yields the difference of principal stresses and the isoclinic angle, some stress separation technique would be required to complete the information needed for the correction.

Several stress separation techniques have been described in the literature, both experimental (*e.g.* the combined photo-thermo-elasticity method by Greene and Patterson, 2002) and numerical (*e.g.* the finite boundary elements method by Becker *et al.* 2002). Probably some iterative method would be necessary. However stress separation is not trivial, and was considered outside the scope of this work.

Only a simple case will be considered here, when the surface is tilted an angle θ about the axis of one of the principal stresses at a point. The diagram in fig. 5.9(a) illustrates an element where the surface normal is tilted about the axis of σ_1. From equilibrium of the triangular element shown in the figure, it is possible to relate the *effective principal stress* σ_2' to the real principal stress σ_2 in the plane of the coating

$$\sigma_2' t = \sigma_2 (t\cos\varphi)\cos\varphi$$
$$\sigma_2' = \sigma_2 \cos^2\varphi \tag{5.11}$$

This expression can be substituted into eq. (5.3) and reorganized to yield the effective fringe order number as a function of the principal stresses and the surface orientation

$$N_\varphi = (\sigma_1 - \sigma_2 \cos^2\varphi)\frac{2t}{f\cos\varphi} \tag{5.12}$$

Normalizing the effective fringe order number with the value for normal incidence yields an expression to evaluate the combined effect of oblique incidence and oblique viewing.

$$N_\varphi / N_0 = \frac{3+\cos^2\varphi}{4\cos\varphi} \tag{5.13}$$

If the element is tilted about the axis of σ_2, the following expression is obtained

$$N_\varphi = (\sigma_1 - \sigma_2 \cos^2\varphi)\frac{2t}{f\cos\varphi} \tag{5.14}$$

And normalizing yields

$$N_\varphi / N_0 = \frac{1+3\cos^2\varphi}{4\cos\varphi} \tag{5.15}$$

The experimental measurements obtained in the tests were compared with analytical expressions of the correction for oblique viewing only, and the correction for oblique viewing and incidence.

In the first test, the fringe order was measured at the centre of the disk for different values of tilt about the vertical axis of the disk. Three sets of experimental results were obtained: two sets of manual measurements using the null compensator and one set processing the photoelastic images collected with the instrument. These measurements were normalized with the zero tilt fringe order to yield the plots of *normalized effective* fringe order versus tilt angle shown on the left of fig. 5.9(b). Recall that in the first test the vertical axis coincides with the axis of the first principal stress σ_1 at the centre of the disk, and therefore the expression in eq. (5.13) yields the analytical expression of the *normalized effective* fringe order for this case (solid line in the figure). A similar exercise is possible considering the correction of oblique viewing only. Substituting eq. (5.4) in eq. (5.3) and rearranging yields $N_\varphi/N_0=1/\cos\varphi$ (dotted line in the figure).

The graph on the right of fig. 5.9(b) shows the results in the second series, where the disk was rotated about the horizontal axis, *i.e.* the axis of the second principal stress σ_2 at the centre of the disk. Thus the solid line in the right graph corresponds to eq. (5.15).

The analysis of the results in fig 5.9(b) allows several conclusions to be drawn.

- First, the correction of oblique viewing and incidence shows good correlation with the experimental results. However, there appears to be a systematic discrepancy between the measurements and the analytical expression, which can be attributed to two main sources besides random experimental errors: (i) a change in φ due to the refractive index of the birefringent material, and (ii) errors due to the stress gradient normal to the rotation axis.
- Second, the discrepancy between measured effective and *real* fringe order remains below 10% for tilt angles up to 40*(degrees)*. This would be the potential gain of correcting for oblique viewing and incidence effects. In view of these relatively small errors, the effort required to apply the correction in the general case, which as discussed above would involve separating the stresses and iterating, would only be justified in a reduced number of cases.
- Third, one could neglect the effect of oblique incidence and correct only for oblique viewing, thus avoiding the need for stress separation. This approach is however not recommended, because in reality these two effects counterbalance each other, and correcting only one produces larger errors in the fringe order than applying no correction.

V.3.5 Case Study: Vibration Test Of A Small Compressor Blade

Vibration tests of turbine blades are routinely performed in industry using reflection photoelasticity alone, and the stresses determined by means of automated photoelastic analysis, assuming that the optical path length is constant. The testing procedure using the combined technique on vibrating turbine blades is described and some qualitative results are presented to demonstrate the feasibility of the method in a real application.

The example shown is for a small compressor blade from a jet engine, courtesy of SNECMA Moteurs. The experimental set-up is shown in fig. 5.10(a). The distance from the object to the camera was approximately 1190*(mm)*, and the projector was approximately 450*(mm)* to the left of the camera. The pitch of the projected fringes on the reference plane was 1.7*(mm)*. The specimen can be seen on a vibration bench during the test, with a close-up shown in the insert.

The blade in this example measured approximately 40×50*(mm)* and was so stiff that the deflections in vibration were negligible, which allowed the shape data shown in fig. 5.10(b) (top-left) to be collected on the unloaded specimen using the standard fringe projector. Some of the more slender blades (*e.g.* the fan blade in fig. 5.3) experienced deflections up to centimetres, and therefore required stroboscopic illumination for the shape measurement, using the apparatus in fig. 5.5(b). The system was calibrated by means of the automatic routine with a cone of radius R=12.5*(mm)*, and height H=6.3*(mm)*, to yield K=-0.7079*(mm/rad)* and m_p=0.1908*(mm/pixel)*.

Figure 5.10(b) summarizes the data processing. Three fringe images, shown on the top-left of the image, were required to compute the surface shape and eventually a map of surface orientation $\cos\varphi$ (bottom left). Six photoelastic images, shown in the top-right, were acquired during a vibration test of the blade. These data were used to generate the isochromatic fringe order map shown in the bottom right, which was calculated assuming the *OPL* constant. Finally this map was combined with the shape information to calculate a map of corrected fringe order, shown in the centre. This map takes into account the effect of oblique viewing, but the oblique incidence correction has not been applied.

V.4 Deformation Measurement

In addition to the shape measurement applications described in the previous sections, the fringe projection technique can also be used for the measurement of out-of-plane deformation. The procedure is very simple, and essentially consists of applying the technique sequentially to measure the shape of (i) the object at rest, *i.e.* before the application of the load, (ii) the deformed object, *i.e.* with the loads applied, and then (iii) subtracting the resulting depth maps to calculate the change in shape.

The fringe projection system developed in this research has been used in deformation measurement applications by a number of final year project students at the University of Sheffield, with various degrees of support and involvement from the author. The students used for these applications the software developed by the author, which implements the algorithms for data processing described in this thesis. The fact that the algorithms performed successfully in all cases demonstrates the robustness of the methodology.

Mitchem (2000), Hughes (2001) and later Matthews (2002) implemented and tested a variation of the system for the monitoring aircraft wing bending tests. This application was characterised by the large scale of the object (a 1/10 scaled model of a commercial aircraft wing, several metres in length). The students developed and built a modified version of the experimental set-up described in this thesis, which was mounted on the ceiling of a laboratory in the facilities of the University. This fixed apparatus contrasts with the portable instrument used elsewhere in this research. The system provided maps of vertical displacement of the wing during bending tests continuously and almost in real time (with a delay of a few seconds), which allowed early detection of the onset of buckling and provided feedback to control the test.

In a separate application, Krueger (2002) used a modified version of the portable system with a high-speed camera to study the bounce of tennis balls, exploiting the potential of the system to deal with transient events.

The non-contacting, non-invasive nature of the fringe projection technique provides it as well with a significant potential for applications in medicine and biological sciences, of which a few of the numerous examples in the literature were cited in section II.5. The author has used the portable fringe projection system for deformation measurement in two applications related to biological materials. In both cases, the technique was used to provide experimental data to validate numerical models. The first case was a feasibility study on the use of fringe projection to provide shape and deformation data in pulse replicator tests of bioprosthetic heart valve replacements. Although the conclusions of the study were very positive, and indeed there is published literature on the topic (*e.g.* Gao *et al.*, 2001), the industrial sponsor decided not to continue this line of research.

In the second application, fringe projection was used to measure the deformation of human skin during *in vivo* tests, which involved indenting and sliding of a ball over the skin. The aim was to provide experimental validation to aid in the development of a numerical model of human skin for cosmetics testing. The remainder of this section is devoted to describing in some detail this application, which in the opinion of the author presents two interesting aspects. Firstly, it was necessary to develop a novel methodology to perform measurements of displacement obliquely to the viewing direction. The procedure will be described in section V.4.5. Secondly, and perhaps more importantly, this application illustrates the ability of the fringe projection technique to deal with transient events, which is one of its main advantages with respect to some of the alternatives.

V.4.1 Background: In Vivo *Measurement Of Deformation In Human Skin*

This work arose from the collaboration between the University of Sheffield and Unilever Research, within the project 'Feasibility study for the development of a skin model for

cosmetics testing'. The objectives of the project were (i) to characterise the main elements required to produce advanced models of product interaction with human skin tissue, and (ii) to build a demonstration model capable of simulating the behaviour of human skin in standard experimental tests. Two types of tests commonly used for the evaluation of cosmetic products were considered in this project with the aim of developing suitable numerical simulations: (i) ball indentation (vertical displacement) simulations, and (ii) ball sliding simulations. The role of University of Sheffield was to carry out experimental measurements of deformation during the indentation and sliding tests to validate the numerical simulations.

V.4.1.1 Mechanical Behaviour Of Soft Tissue

The mechanical response of soft tissue is very complex. The actual tensile behaviour of human skin undergoes three phases: (i) linear, isotropic behaviour during the first loading phase when the collagen fibres are relaxed, followed by (ii) anisotropic behaviour within the second stage, when collagen fibres tend to line up in the load direction and bear loads, and (iii) stiffening in phase three when the straighten collagens resist the load. Beyond this phase the ultimate strength is reached and fibres begin to break, which accounts for the hyperelastic behaviour (*i.e.* non-linear stiffening) of skin. In addition, there are also viscoelastic effects (*i.e.* relaxation and creep) associated to shear interaction of collagen with the connective tissue.

The most common material models used in the literature are (i) hyperelastic models *e.g.* Mooney-Rivlin or Odgen hyperelastic material models, (Wu *et al.*, 2002, Holzaphel, 2001), (ii) viscoelastic material models (Bosboom *et al.*, 2001), and (iii) combined hyperelastic and viscoelastic models (Bosboom *et al.*, 2001, Wu *et al.*, 2002).

V.4.1.2 Experimental Tests

The mechanical properties of soft tissue depend strongly on physical and chemical factors (temperature, pH), age of the patient, on the topography and on the strain rate. Experimental determination is difficult and data typically shows significant scatter.

There is some literature on the measurement of mechanical properties of soft tissue, mainly *in vivo* evaluation on animals (rats), or *in vitro* on a wide variety of tissues (*e.g.* Wu *et al.*, 2002, Holzaphel, 2001). There is also some literature on the evaluation of properties of the interface between skin and cosmetic products, and it is possible to obtain properties such as friction coefficients from the literature (Holzaphel, 2001), based on *in vivo* tests on human skin. Finally, the interaction between the skin and droplets of cosmetic products is described in Benohanian (2001).

V.4.2 Description Of The Numerical Model

A simplified finite element model of the forearm was created by Unilever Research. Several layers were defined in the model to represent (i) two layers of skin, namely epidermis and dermis, (ii) muscle, and (iii) fat. The material property data for each type of tissue were obtained from the literature and fitted to the material models implemented in the finite element code. The bone was also included in the model as a rigid body supported in all directions.

The indenter was defined as a rigid sphere, with diameters of 6.33*(mm)*, 16*(mm)* for the indentation tests and 16*(mm)* for sliding tests. Two loading stages were defined: (i) Indentation (*i.e.* vertical displacement of the indenter) corresponding to a force of 5-10*(N)*, and (ii) Application of the displacement in the sliding direction (at least 4 times the diameter of the sphere).

The contact between indenter and skin was modelled as Coulomb friction. The values of the friction coefficient were initially taken from the literature (*e.g.* Asserin *et al.*, 2000) and later adjusted to fit the observed results.

Initial investigations were carried out in 2D, using simple models such as cross- or axial-sections as shown diagrammatically in fig. 5.11(a). This allowed carrying out a parametric study to investigate the effect of morphological parameters such as fat thickness or distribution of skin tissues (stratum, epidermis, dermis), and also of material properties, in the mechanical behaviour of human skin.

Figure 5.11(b) show the vertical displacements for an indentation force of 5*(N)* considering two different sets of material properties in a 2D FE model representing the cross-section of the forearm during an indentation test. The 3D studies were then performed using the material and geometry (layer thickness) settings corresponding to the best results obtained in the 2D studies. Figure 5.11(c) shows a view of the 3D model. Note the refinement of the mesh in the vicinity of the ball indentation and sliding areas.

The example results obtained with the FE model and shown in fig. 5.11, were made available by Unilever Research to the author in order to illustrate this section. Unfortunately, the model itself was not disclosed and it was therefore not possible to evaluate the agreement between numerical and experimental results.

V.4.3 Methodology

The fringe projection technique was used to study the behaviour of human skin during indentation and sliding tests. Figure 5.12 shows a view of the experimental set-up installed at Unilever Research. The apparatus involves an actuator, which can be loaded vertically by applying weight to it. A set of weights of 10, 20, 50, 100, 200, and 500*(g)* was used for the

indentation tests. The arm of the subject rests on a specially designed test bench. The head of the actuator is an interchangeable indenter, allowing different shapes, sizes and materials to be tested.

Indentation tests involve loading the actuator and measuring the deformation of the skin in the vicinity of the contact point. Slide tests involve applying a constant speed displacement of the loaded actuator over the surface of the forearm. Force transducers are used to measure the reaction forces on the actuator in the horizontal direction during the sliding test, and hence calculate the friction coefficient of the skin, and the effect on it of the application of cosmetic products.

The portable shape measurement system described in Chapter IV was set-up on its tripod to view the forearm from above and slightly to one side. The system calibration was performed using a flat plate and a calibration cone of dimensions H=6.3*(mm)* and R=12.5*(mm)* by means of the automatic procedure detailed in section IV.6.4. The procedure to perform differential measurements of relative displacements between non-flat initial and final shapes, using fringe projection, was described in detail in section II.3.2.4.

V.4.4 Qualitative Results

V.4.4.1 Indentation Tests

The observations from several indentation tests performed on the left forearm's inner face of a number of subjects provided valuable information for the development of a numerical model.

Figure 5.13(a) shows the fringe pattern projected onto the forearm of a patient. The forearm rests horizontally on the test bench and is seen from above and slightly to one side. This was considered as the unloaded configuration of the specimen. Figure 5.13(b) shows an image of the loaded configuration, taken during one of the indentation tests. In it, a 5*(mm)* diameter indenter was pressed against the clean skin of the subject with an applied force of 500*(g)*.

Both images were combined with a common reference image of the fringe pattern projected onto a flat plate parallel to the image plane, and later digitally processed respectively to yield two contour maps of the shape in the undeformed and the deformed state. The map in fig. 5.13(c) was calculated as the difference between the loaded and the unloaded contour maps, and therefore it represents the relative displacement between the reference and object images in the direction of observation. This sequential approach to the measurement of deformation was introduced in section II.3.2.4.

Note that although the most interesting measurement for the indentation tests was the displacement in the vertical direction, the loading apparatus obstructed the view from above,

and therefore it was necessary to look obliquely at the specimen. Section V.4.5 describes a technique to obtain deformation measurements non-parallel the viewing direction.

The map in fig. 5.13(c) however allows making a few interesting observations. Note the symmetry of the displacement field. This type of axisymmetric deformation was typically found in the lower part of the forearm (*i.e.* ¼ of the forearm length, starting from the wrist). In contrast, the tests indicated that the skin in the upper part (*i.e.* about ¼ of the forearm length, starting from the elbow), tends to stretch mostly from the indent back left to the elbow. The maximum deflection in this example occurred near the tip of the indenter and was about 8mm.

The amount of side bulging was found to depend on the position of muscle. Skinnier individuals almost did not present sidewise bulge, when compared with softer ones. It was also found that tendons affect the distortion, so that whenever the indenter pushed on a tendon, in-plane movement was reduced, and a larger force was required. In general, the age of the patient was also found to affect skin flexibility, with older skin tending to stretch more than younger skin.

In fig. 5.13(c), the masked region in the displacement map corresponds to the indenter and its shadow in the object image. This region does not contain fringe information and therefore was masked for clarity.

V.4.4.2 Sliding With Indentation

In the sliding with indentation experiments the spherical indenter was first indented and then slid along the inner part of the left forearm of the subject. The indentation point varied between 10-150*(mm)*, measured from the elbow.

Figure 5.14(a) shows an image of the unloaded configuration, and fig. 5.14(b) an image of the loaded configuration. In this case, a lens-shaped indenter was used. This indenter is a solid of revolution formed by rotating an ellipse about its minor axis. A vertical force of 100*(g)* was applied and the indenter was displaced at a constant speed of 8*(mm/s)* in the direction from the elbow to the wrist, which in the image corresponds to left to right. This set of data was collected on clean skin. The set-up allows measuring the coefficient of friction independently, and in this case the value measured was 1.1.

The two images were processed to obtain the displacement map shown in fig.7.4(c) corresponds to the region highlighted in fig. 5.14(b). Note the strong asymmetry, caused by the friction between the indenter and the skin, which modifies the map of out-of-plane displacement with respect to the one shown in fig. 5.13(c). Note that the skin in front of the indenter (to the right), is compressed in plane and folds towards the camera forming a bulge (positive displacement). On the other hand, the skin left behind the indenter (to the left), is stretched, and hence the out-of-plane displacement is negative.

The results observed in fig. 5.14(c) are representative of the observations typically noted in the series of tests. The skin in front of the indenter tends to compress and fold, exhibiting a main bulge with several wrinkles. It appeared that only the upper part of the skin was bulging, leaving underlying tissue sheared and tendons undeformed. In contrast, the skin behind the indenter was stretched. This area presented an elliptical shape which typically extended up to the elbow.

V.4.5 Quantitative Results

In the application under study, deformation has a component in the direction of the applied load (*i.e.* vertical direction) and also a component in the plane normal to the loading direction. However, according to the theory underlying the fringe projection technique, which was summarised in section II.3.2.4, this method is only sensitive to the component of displacement parallel to the viewing direction, and therefore cannot be used for in-plane deformation or displacement measurement. Since the interest was focused on the vertical displacement, the most obvious set-up configuration would have considered the camera directly above the specimen and looking down the z-axis. This was made difficult by the loading apparatus, which obstructed the top view of the specimen. A possible solution would have been to install some arrangement involving a mirror tilted 45*(degrees)* to fold the light path.

An alternative approach, based on the development of a special procedure for data processing was followed in this research. Figure 5.15 shows a schematic of the algorithm. Deformation measurement requires the collection of three images, namely the unloaded state of the specimen (left), the loaded state (right), and a common flat reference perpendicular to the light path. Note that the viewing direction appears rotated an angle α with respect to the desired measurement direction (*i.e.* the vertical direction in this case).

(i) Process the image of the unloaded specimen with the reference image to obtain a depth map of the undeformed shape of the specimen. Note that the measurement is obtained in axes $x'z'$

(ii) Apply a transformation to the coordinate axes from $x'z'$ to xz, *i.e.* rotate the measured surface an angle $-\alpha$ about the y-axis.

(iii) Repeat steps (i) and (ii) with the image of the loaded component. Particular attention must be paid to rotate the depth maps resulting from the unloaded and loaded situations about the same axis. This may not be trivial due to the indeterminacy caused by the *piston* term. One possibility to overcome this difficulty is to choose as rotation centre a point with known zero displacement (*e.g.* in our example a point far from the indentation area). Alternatively it is possible to use the combined shape and location system described in the previous chapter to eliminate the piston term from both depth maps before the rotation.

(iv) Subtract the two rotated depth maps to obtain a map of the relative displacement in the measurement direction.

Figure 5.16 shows a set of results of an indentation test on human skin, where the load was gradually increased from 10 to 500*(g)*. The figures show a three-dimensional representation of the forearm deformed under load. The area was *ca.* 30×50*(mm)*. The colour-scale represents the relative displacement in the vertical direction with respect to the unloaded geometry of the forearm of the patient.

The displacement maps were obtained processing fringe patterns similar to the ones shown in fig. 5.13 (a) and (b). The first step was the calibration of the system, which required the collection of a reference image of a flat reference plate aligned perpendicular to the viewing direction and a calibration image of a small cone 12.5*(mm)* in radius and 6.3*(mm)* in height. The automatic calibration yielded K=-1.042*(mm/rad)* and m_p=0.075*(mm/pixel)*. A quick estimation of the accuracy of the depth measurements can be obtained from the telecentric calibration constant of the system K. According to the discussion in section IV.7, the accuracy of the phase measurement can be expected to be better than 0.2*(rad)*, which corresponds to an accuracy of the depth measurements in the range of 0.2*(mm)*. This considers (i) the relatively small slopes, (ii) the absence of non-telecentric effects, and (iii) the fact that the images were normalized.

The second step was the measurement of the inclination between the measurement direction and the viewing direction. In this case this was achieved by aligning the flat plate perpendicular to the measuring direction and collecting a third image, which was processed together with the reference. The inclination angles were then obtained from the slopes of the best-fitting plane to the resulting depth map, yielding α_x =-0.0393*(rad)* and α_y= 0.6207*(rad)* in this example.

The following step was to process all the object fringe patterns with the reference. This involved normalizing and generating masks for all the files involved, and then using the batch processing facility in the Joshua software to calculate the depth maps corresponding to the object unloaded, and under increasing values of the load from 10 to 500*(g)* as shown in the figure. These depth maps were piston corrected by setting the lower left corner of the image pixel (560,30) to 0, and rotated the angles α_x and α_y previously calculated. Finally the deformation maps were calculated in each case by subtracting the depth map of the unloaded object from those of the loaded situations to yield the results shown in fig. 5.16.

Observation of the results in the figure shows that the displacement maps are approximately axisymmetric, and the maximum vertical displacement occurred as expected near the tip of the indenter, with values increasing with the applied load in the range from *ca.* -0.4*(mm)* up to -10.6*(mm)*.

V.5 Conclusion

The instruments, algorithms and procedures which constitute the fringe projection technique, and which were described in the previous chapter, have been put to work in three different applications related to the measurement of the shape of objects.

Two examples of shape measurement in arbitrary objects have been presented in the first part of this chapter, to demonstrate how the fringe projection technique can deal with challenging conditions such as complex three-dimensional shapes and unfavourable surface finish. The first example was a small plaster statue of a sitting Buddha, which presented pronounced creases and shadowed areas breaking the fringe pattern. The second example was a fan blade with a glossy photoelastic coating bonded to the surface. The combination of (i) the automatic generation of masks by means of thresholding of the quality map and (ii) the normalization of the input images, allowed obtaining reliable experimental measurements in both cases with accuracies estimated in the sub-millimetre range (0.6-0.7mm).

The second part of the chapter was devoted to an application in which the technique was used to provide full-field automatic measurement of the surface orientation of three-dimensional objects. This information was used to complement digital reflection photoelasticity in the analysis of complex components. A combined instrument was developed to evaluate component shape within the same reference system as the photoelastic data, and estimate of the optical path length through the birefringent coating in order to correct the effects of oblique incidence and viewing.

An auxiliary system based in fringe projection was developed to be integrated with existing methods for automated photoelastic analysis. The apparatus and experimental procedure for data collection have been described, and a case study has been presented in which the combined use of reflection photoelasticity and fringe projection has been successfully demonstrated for the study of vibration tests on turbine blades.

While the oblique viewing effect is easy to correct, the correction of the oblique incidence effect requires a priori knowledge of stress distribution in the specimen. An evaluation of the two effects was carried out in a set of tests using stress-frozen Brazilian disks. Correcting only for the oblique viewing effect is relatively easy, but produced larger errors than applying no correction at all. In contrast, the correction of both effects produced results in good agreement with the manual measurements of the fringe order, but it would require a significant effort in the general case, because it would be necessary to separate the principal stress components. Since the potential gain in terms of accuracy is only about 10%, this effort would only be justified in a reduced number of cases.

The final part of this chapter presented an application of the fringe projection system to the measurement of out-of-plane displacements. This application was related to *in-vivo* tests on human skin in the context of cosmetic products testing. The aim was to obtain experimental measurements of the deformation of human skin to assist in the development and validation of numerical models of its mechanical behaviour.

The fringe projection technique was uniquely suited for this application due to its non-contact and non-invasive nature, together with its ability to deal with transient events. The method provided valuable qualitative information in the form of full-field maps of the displacement in the viewing direction. In addition, a novel procedure has been presented for the quantitative measurement of displacements non-parallel to the viewing direction. This method allowed the collection of experimental maps of out-of-plane displacement in the z-direction, with a resolution over 13*(pixels/mm)* over an observation area of *ca.* 15*(cm^2)*, and with an estimated accuracy of *ca.* 0.2*(mm)*.

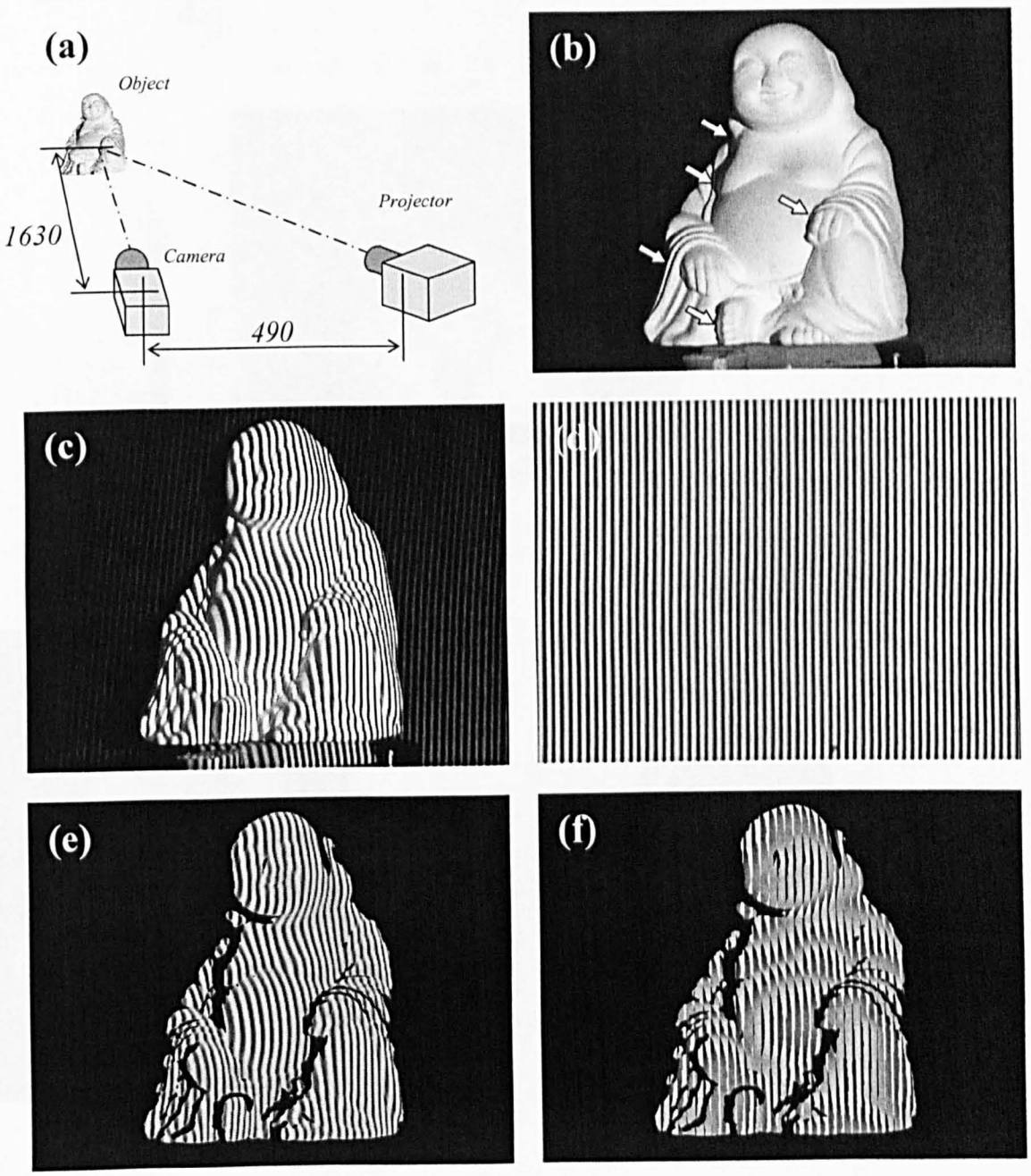

Figure 5.1: Shape measurement of a complex object. A plaster statue is used in this example. (a) Experimental setup (b) Image of the object without a grating on the projector (c) Object image with the projected fringes (d) Reference image (e) Normalized object image. A mask was automatically generated by thresholding the quality map. (f) Wrapped phase map obtained by combining (d) and (e) with the spatial phase extraction algorithm.

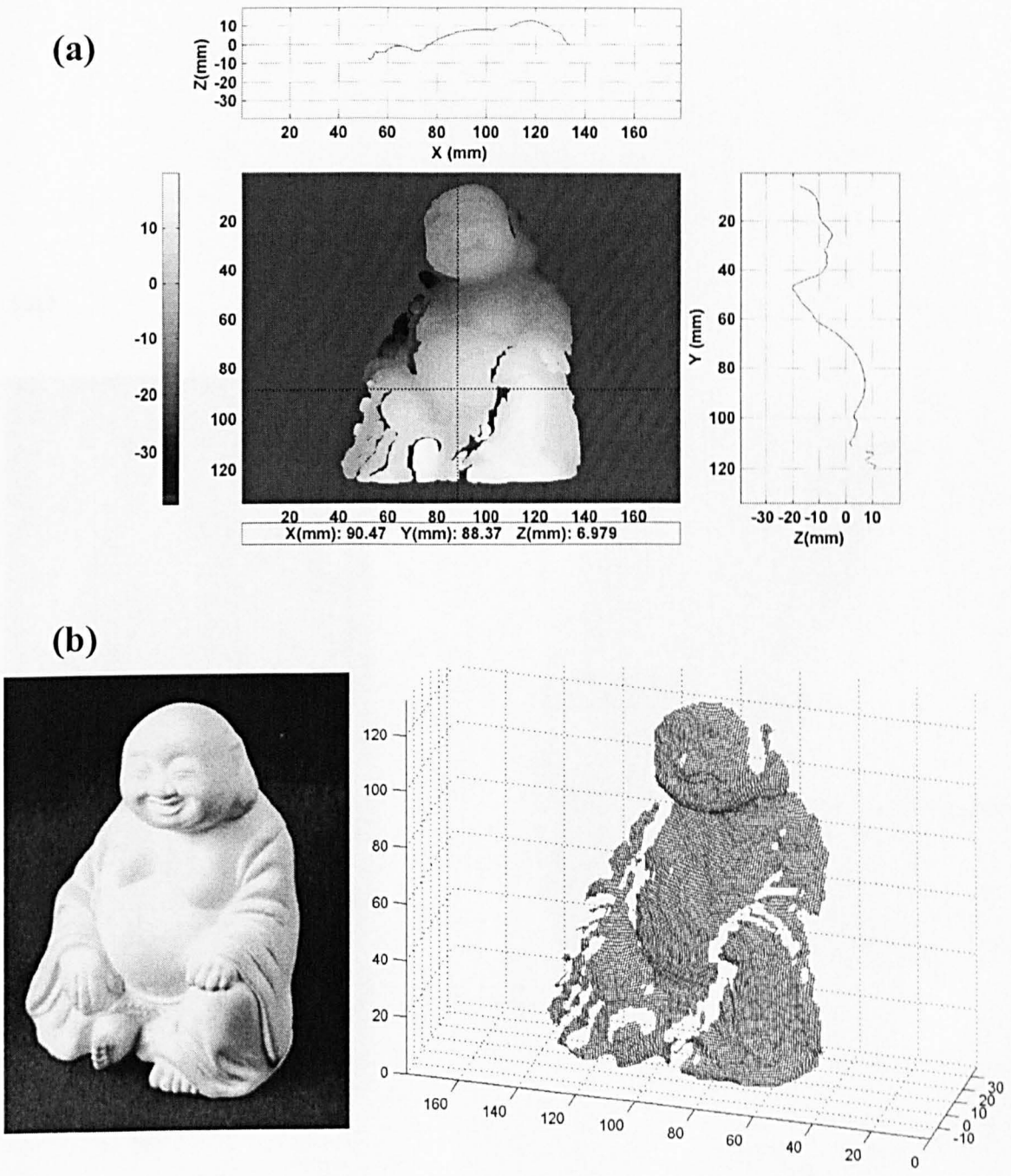

Figure 5.2: Results of the shape measurement (a) Surface contour map obtained after unwrapping and calibrating the phase map shown in fig. 5.1(f). (b) A three-dimensional plot of the reconstructed surface and an image of the object taken from a similar perspective are shown side by side for comparison. Note that the resolution of the 3D mesh has been lowered for clarity of display.

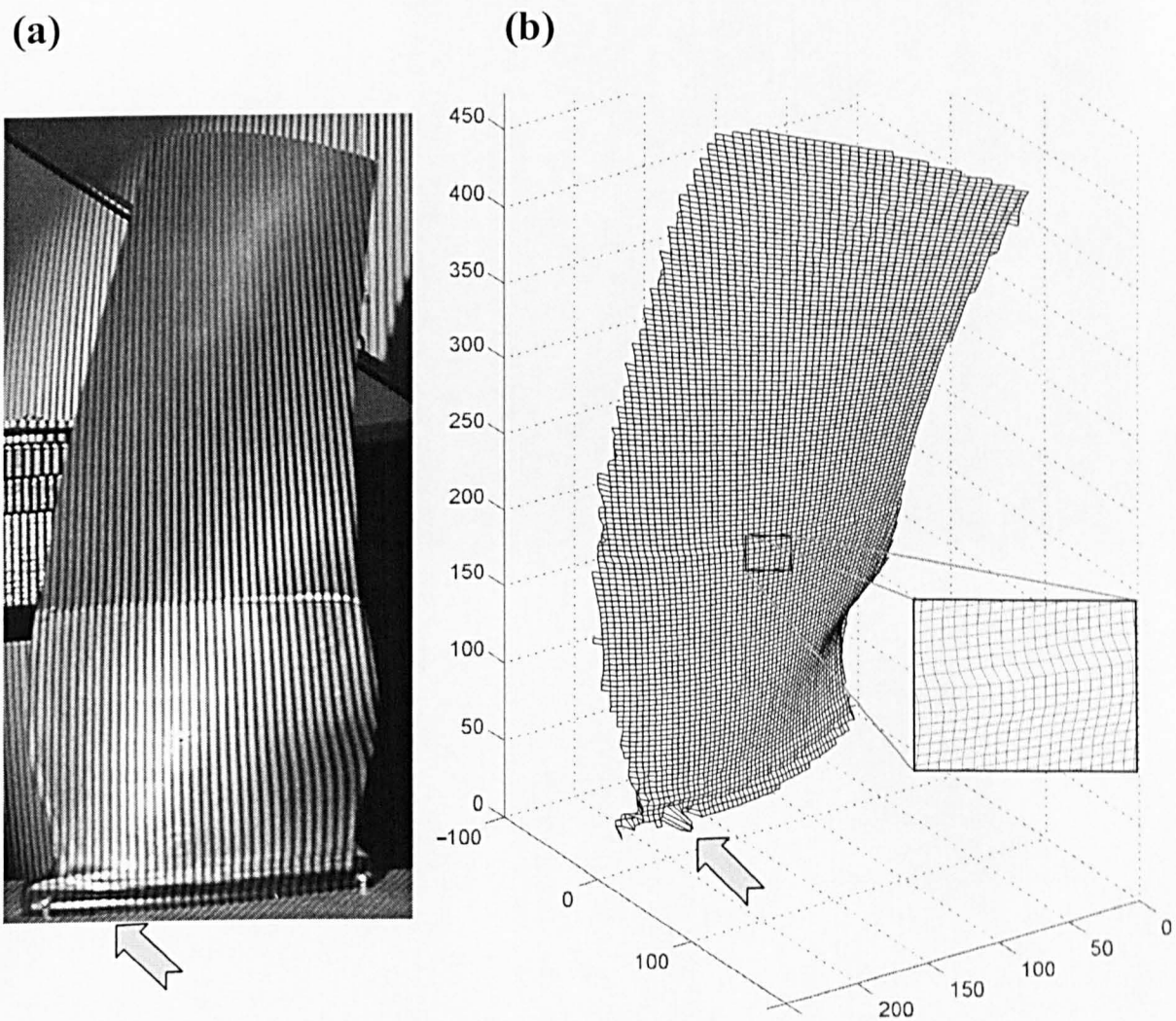

Figure 5.3: Shape determination of a fan blade using fringe projection. Blade courtesy of Rolls Royce. (a) Object image showing the fringe pattern on the blade. The projector is situated to the left of the camera. (b) Coarse 3D mesh of the measured shape. The detail shows the edge of the coating at full resolution. The arrows point to an area of corrupted phase in the image, and the resulting error in the measured shape.

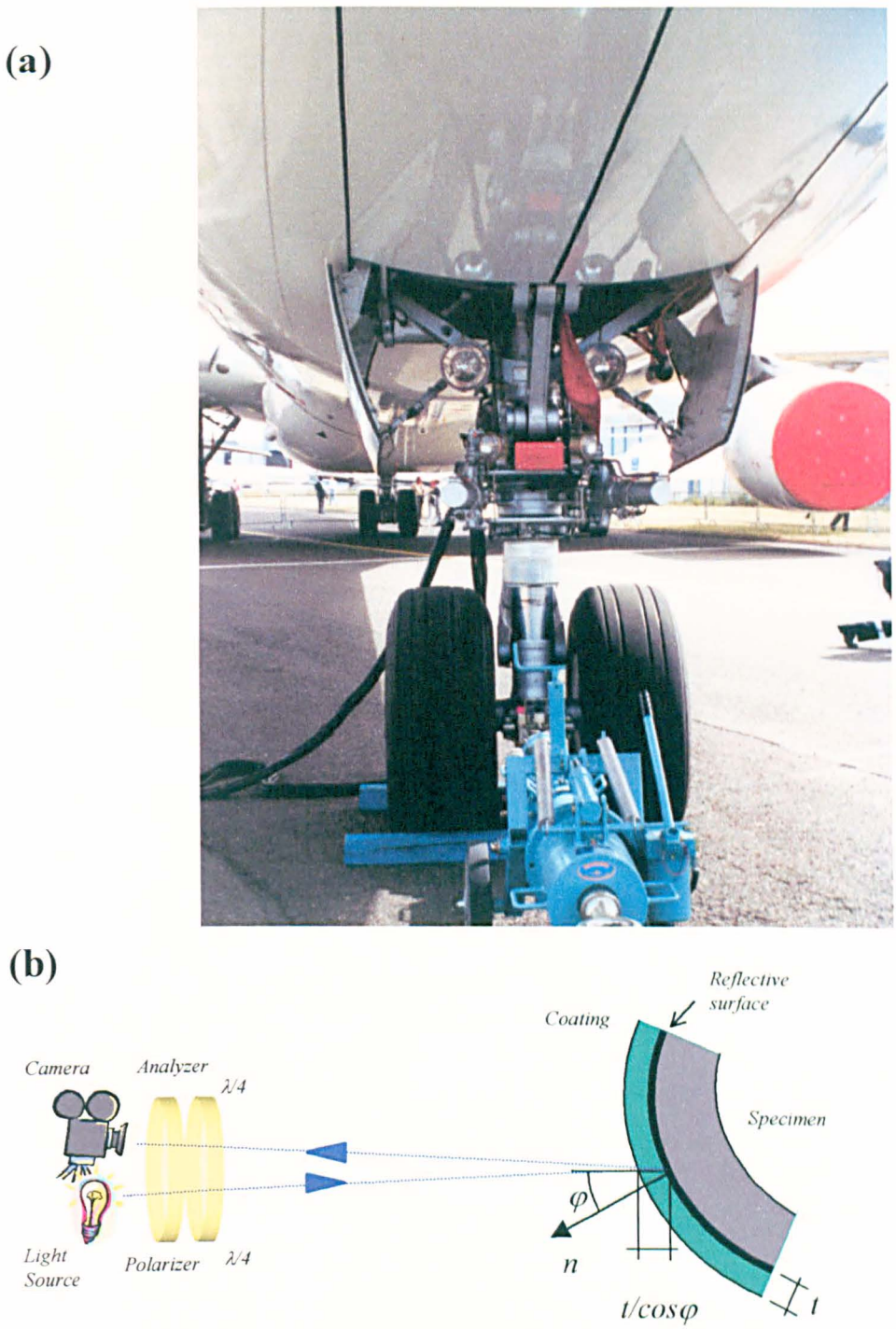

Figure 5.4: Applying photoelasticity to complex components. (a) Landing gear of Airbus A340 commercial aircraft. (b) Complex three-dimensional geometry in a component leads to non-perpendicular viewing of the reflection photoelastic coating, which must be taken into account for the correct interpretation of the isochromatic fringes.

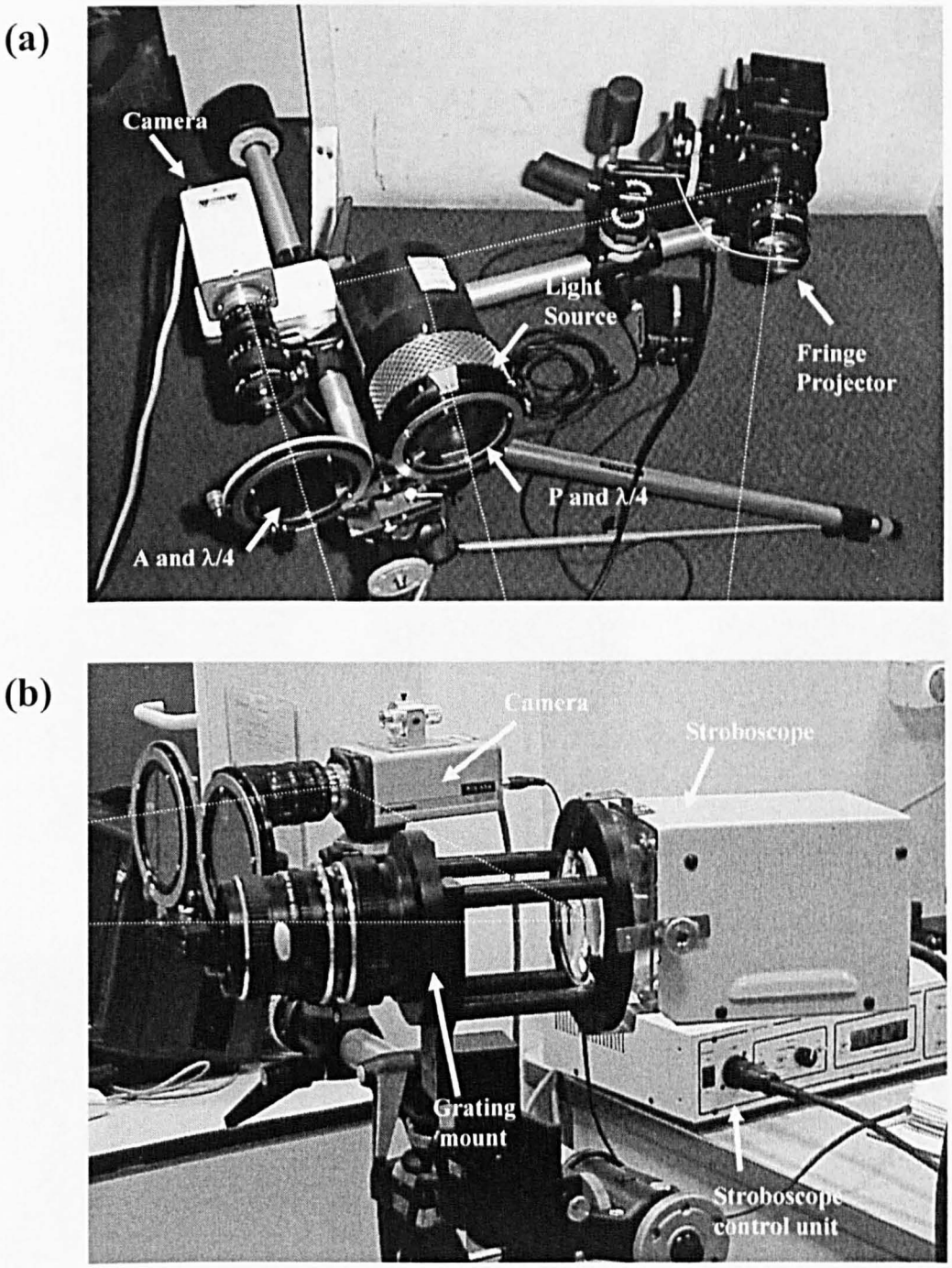

Figure 5.5: Combined fringe projection – reflection photoelasticity instrument (a) Instrument for static applications (b) Configuration for vibration analysis, which includes stroboscopic illumination.

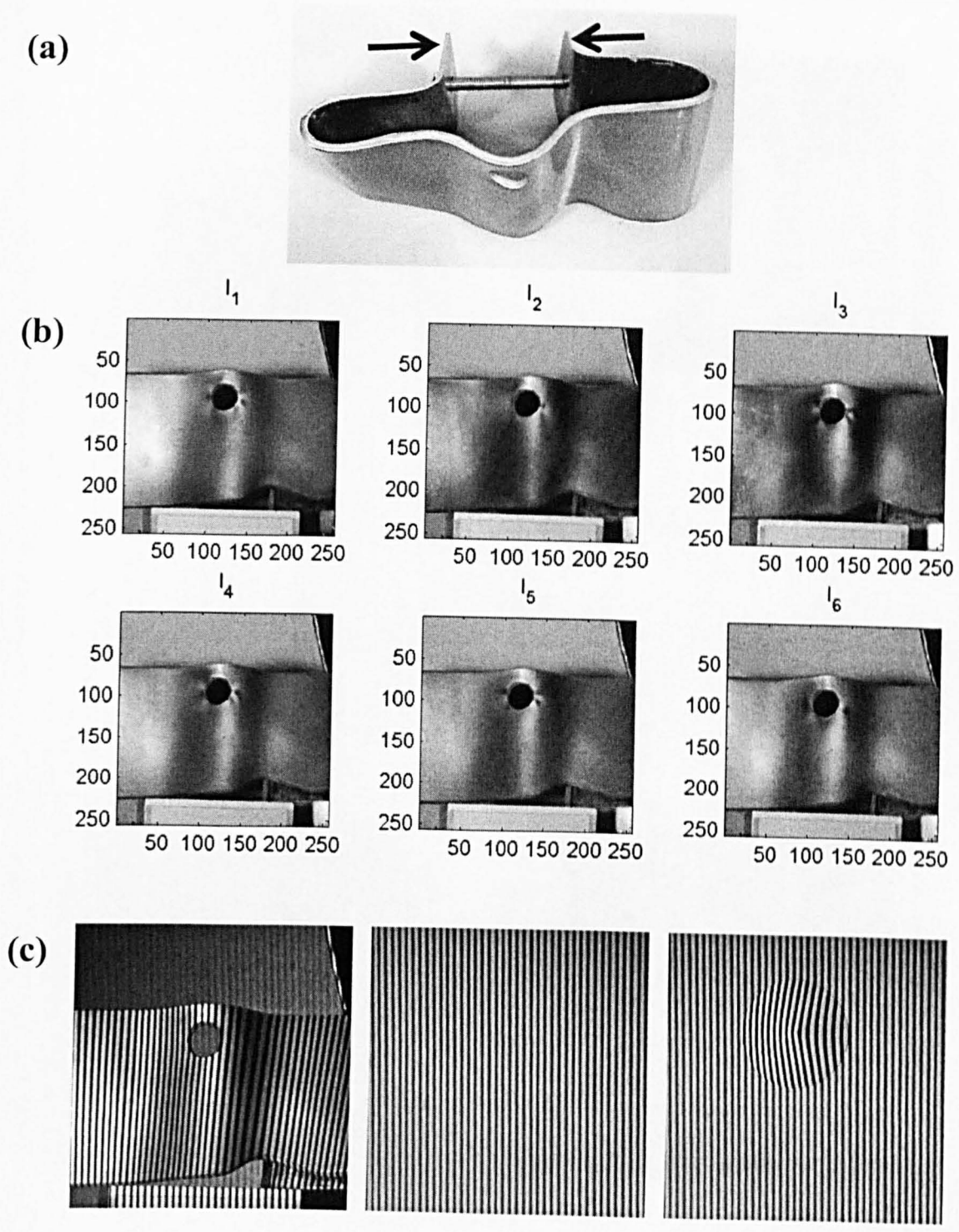

Figure 5.6: Combined fringe projection and reflection photoelasticity (a) Demonstration specimen. A bolt with a nut comprise the elementary system used to apply a bending load to the sample. (b) Photoelastic data: six phase-stepped images (c) Fringe projection data: object, reference and calibration images. All the images in (b) and (c) are 256 by 256 pixels in size and were collected with the same reference frame.

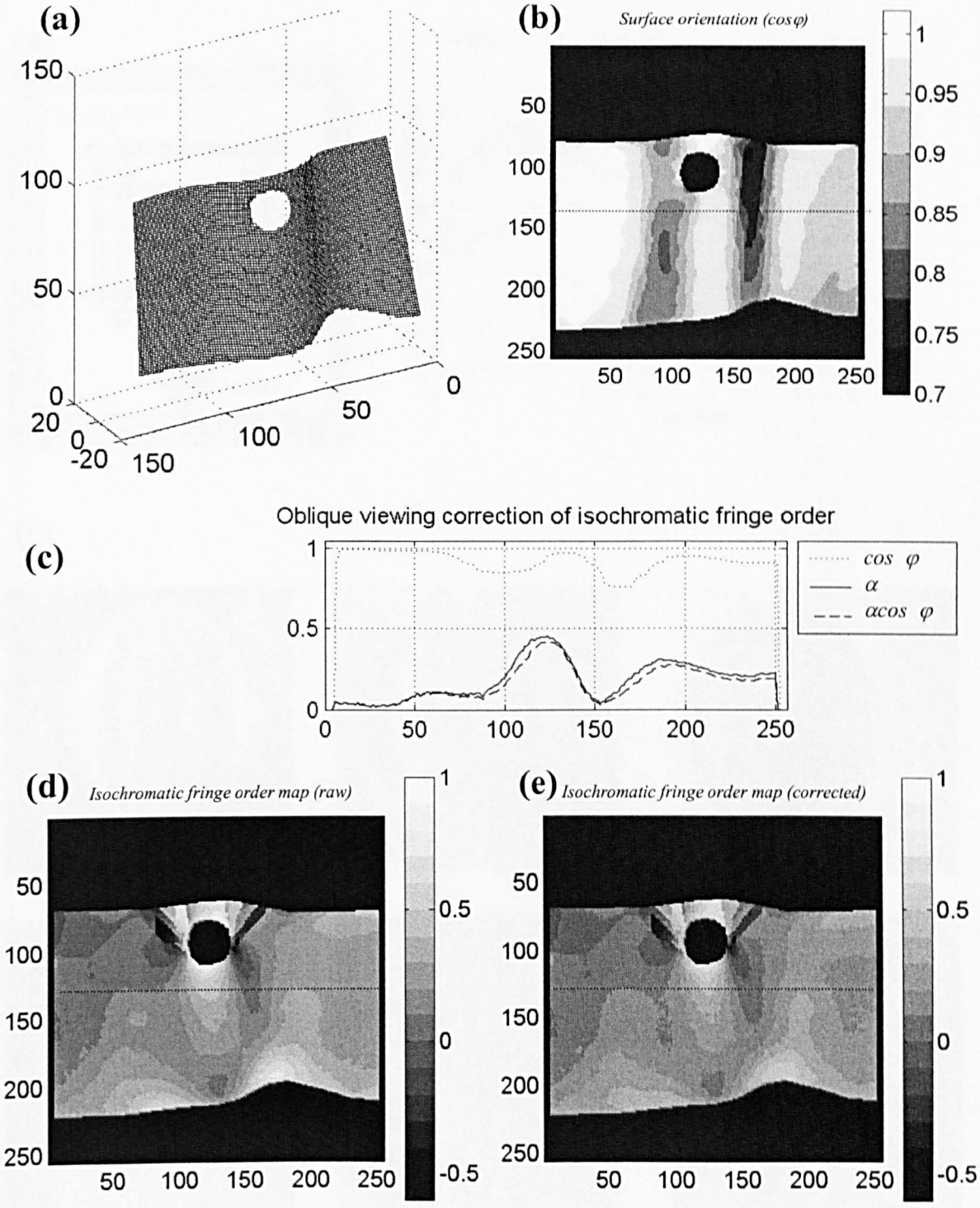

Figure 5.7: Correction of oblique viewing effects in the isochromatic fringe order. (a) 3D mesh representation of the surface shape measured using fringe projection. (b) Map of surface orientation ($\cos\varphi$), calculated differentiating the shape data in (a). (c) Plot of profiles along the horizontal line highlighted in the images for the surface orientation $\cos\varphi$ along with the isochromatic fringe order α before and after correction. The full maps are shown respectively in (d) and (e).

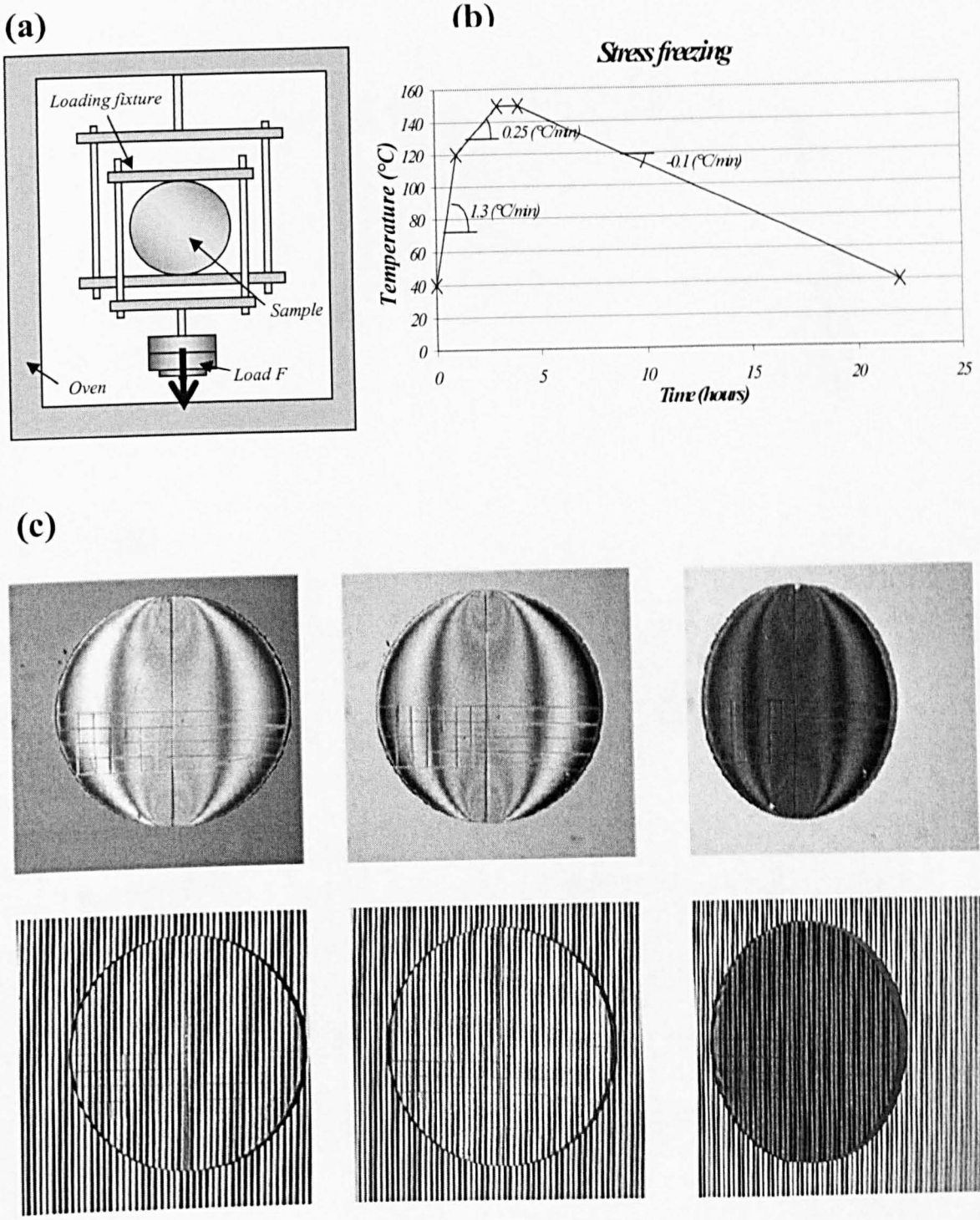

Figure 5.8: Tests on a stress-frozen Brazilian disk. (a) Loading fixture used for the stress freezing of the sample. (b) Temperature vs. time curve. (c) Example of experimental data: photoelastic and fringe images collected with the combined instrument for 0, 20 and 40 degrees rotation about the vertical axis.

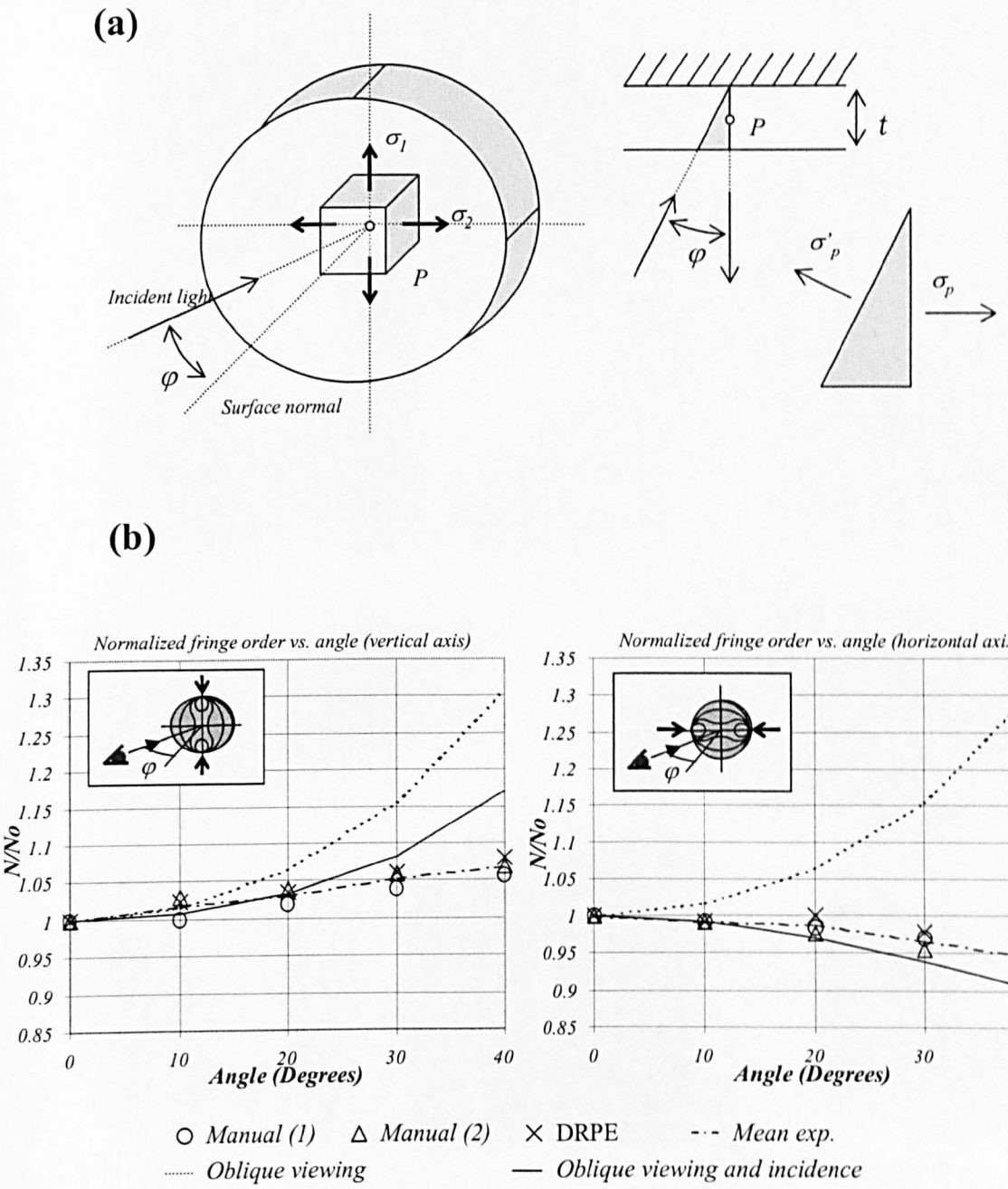

Figure 5.9: Tests on a stress-frozen Brazilian disk. (a) Oblique incidence effect (b) Experimental results. Plots of normalized fringe order measured at the centre of the disk versus the tilting angle about the vertical axis (left) and the horizontal axis (right). The graphs show three sets of experimental measurements (two sets of manual measurements with a null-balance compensator and one set of results from the processed photoelastic images), and plots of the analytical solution considering only oblique viewing and both oblique viewing and incidence effects.

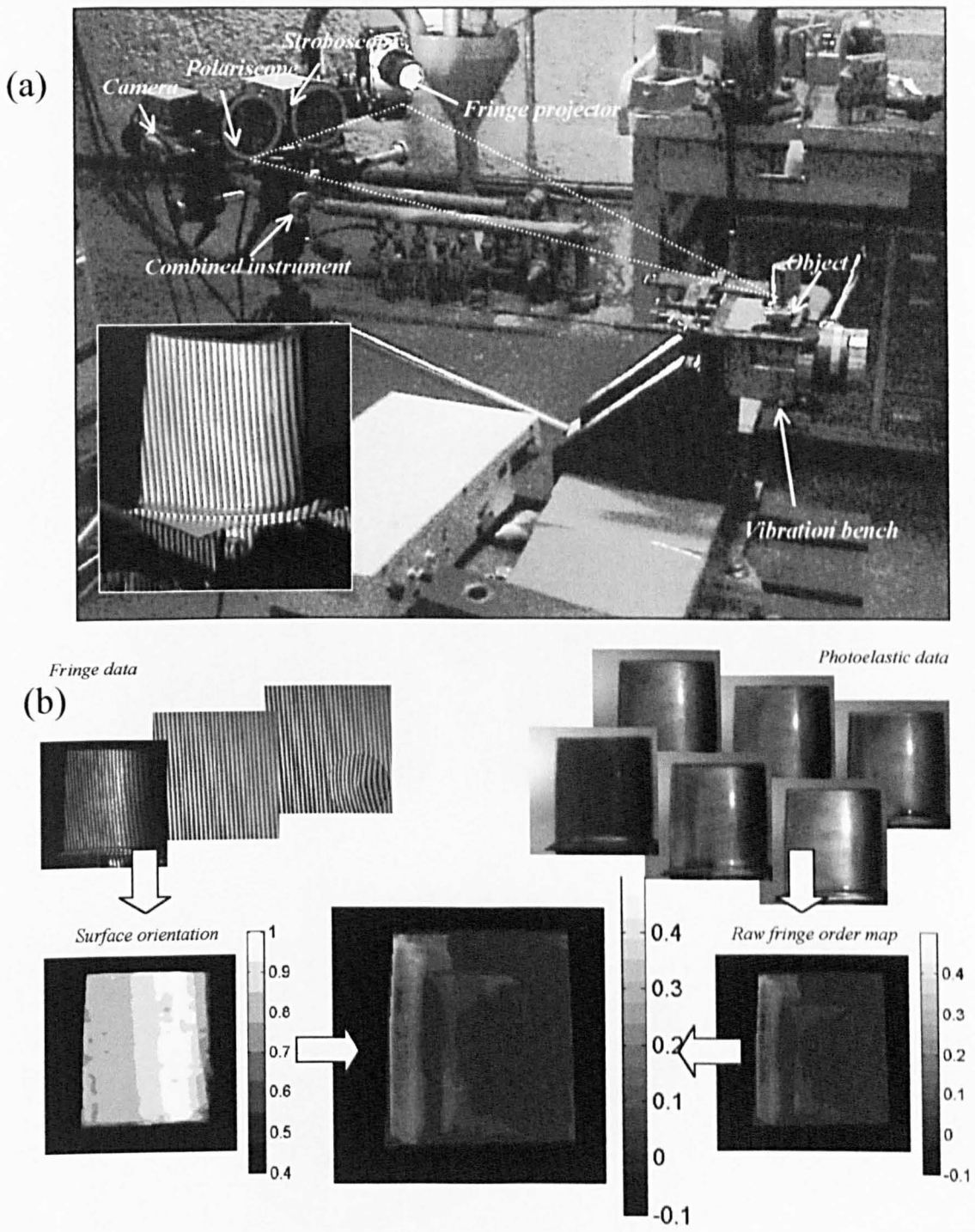

Figure 5.10: Vibration tests of turbine blades (a) Experimental set-up in a vibration chamber. Courtesy of SNECMA Moteurs (France). The insert shows a detail of the compressor blade with the projected fringe pattern. (b) The fringe data (top left) was processed to yield a map of surface orientation (bottom left). This was combined with the isochromatic fringe order map (bottom right) calculated from the photoelastic data (top right), to generate a fringe order map with correction for oblique viewing effects (centre).

(a)

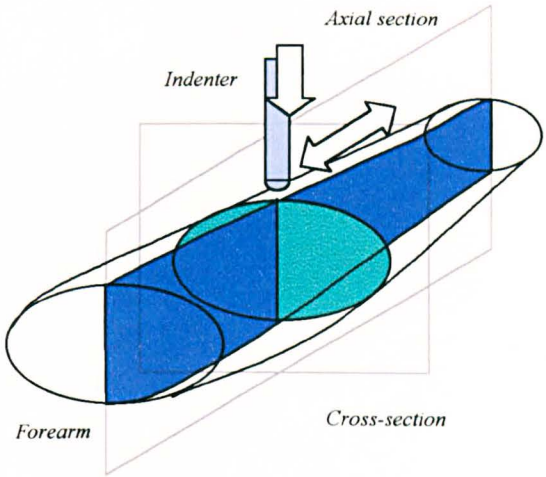

Finite element simulations (F=5N)

(b)

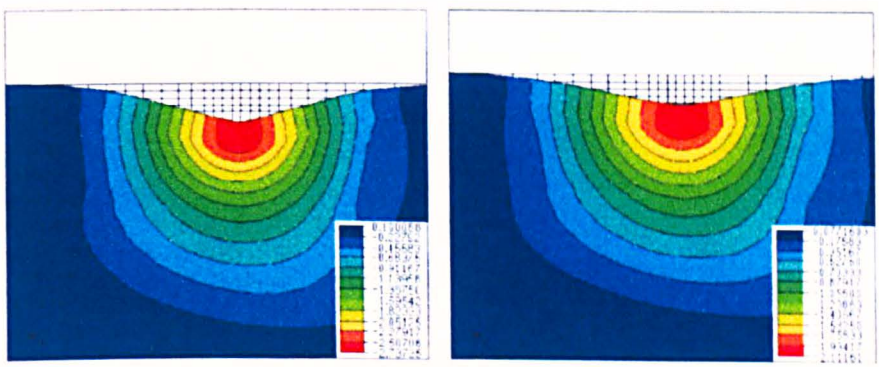

E_{skin}=25MPa E_{skin}=100MPa

3D FE model

(c)

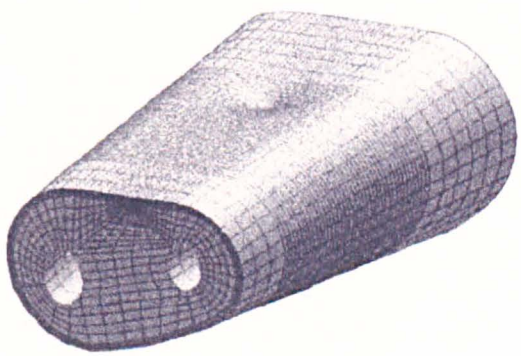

Figure 5.11: Finite element model of human forearm. (a) 2D and 3D models were used in the project. (b) Vertical displacements for indentation force F=5N for different material properties in a 2D FE model representing the cross-section. (c) Idem in a 3D model.

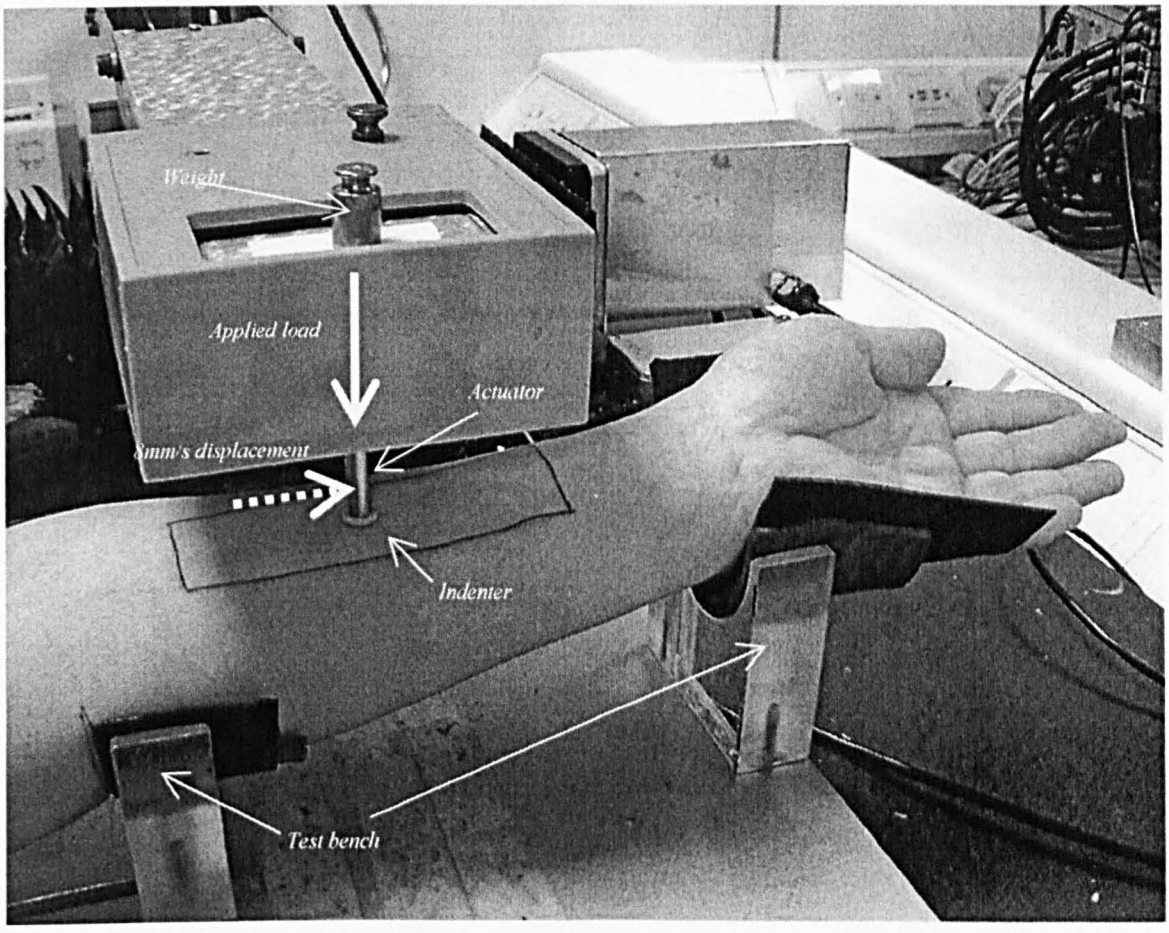

Figure 5.12: General view of the experimental set-up installed at Unilever Research to test the properties of human skin.

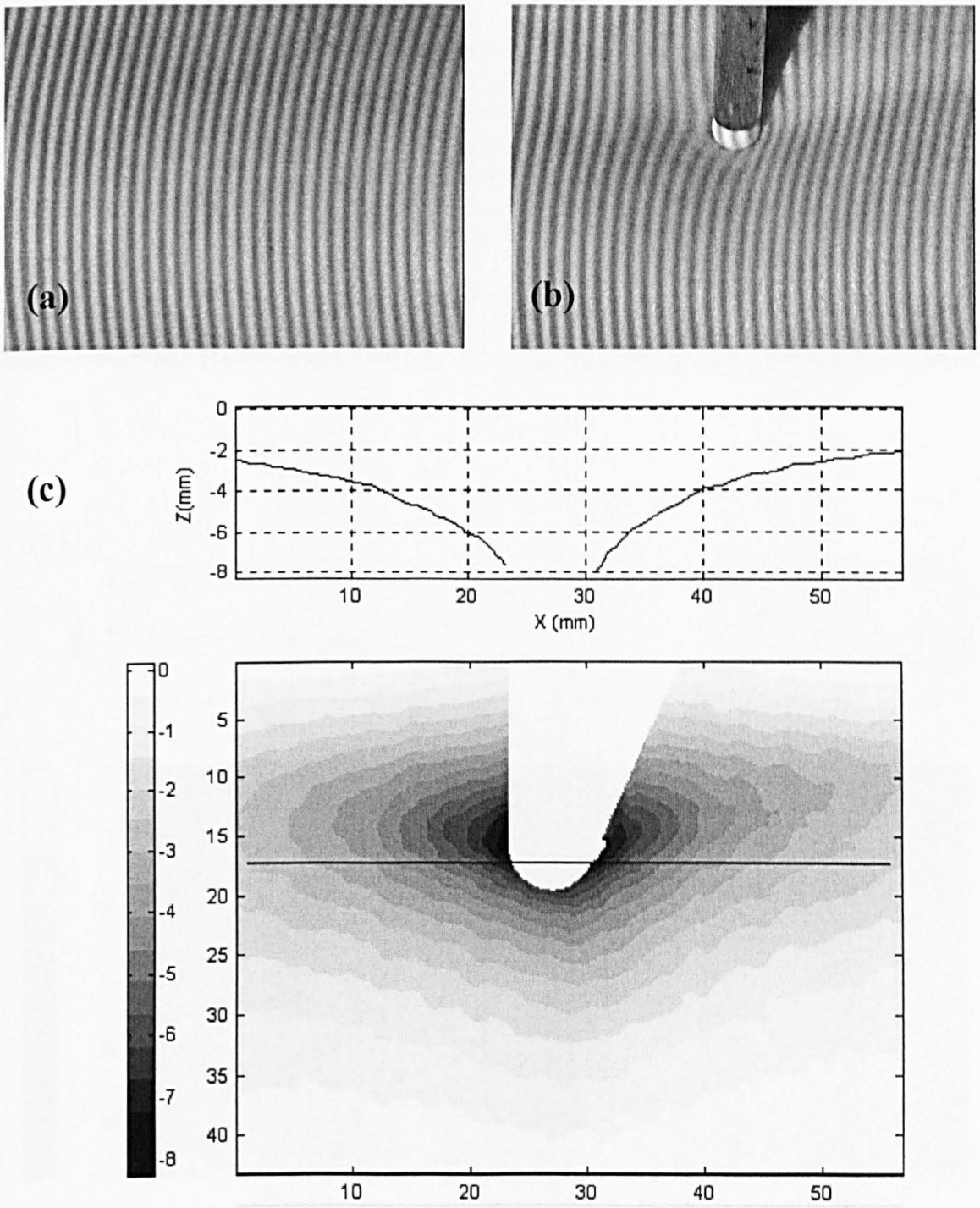

Figure 5.13: Indentation tests on human skin. (a) Reference Image and (b) object image. (c) Map of the out-of-plane displacement. The profile along the line highlighted in the map is also shown above. Units on the axes and the grey scale are millimetres. The maximum displacement occurs near the tip of the indenter as expected, with an approximate value of around 8*(mm)*.

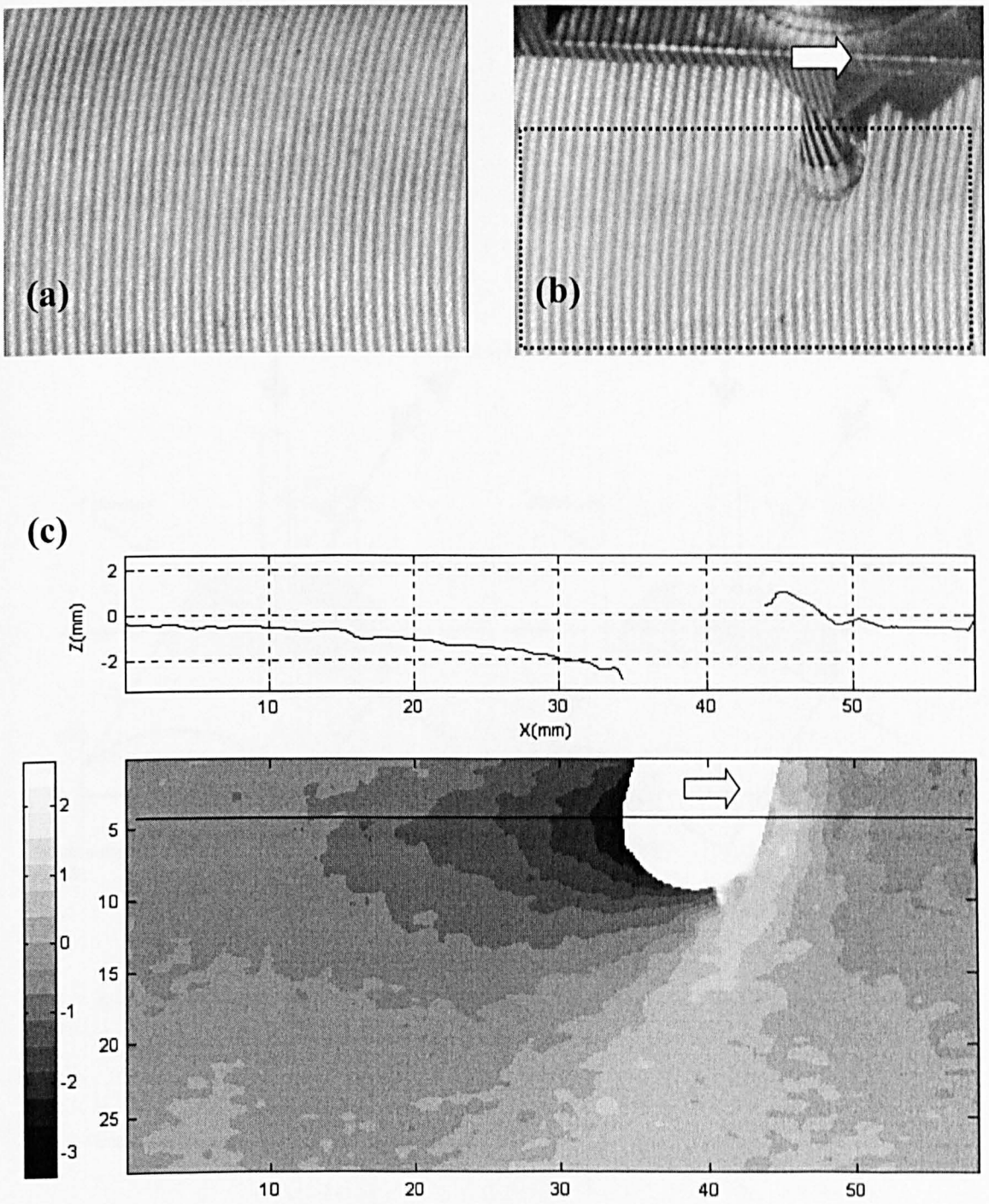

Figure 5.14: Indentation and slide tests on human skin (a) Reference image (b) Object image (c) Map of out-of-plane displacement during a slide test. The indenter is applying 0.981*(N)* of vertical force while moving from left to right at constant speed of 8*(mm/sec)*. Note the strong asymmetry of the displacement field in this case. The skin folds in front of the indenter to form a ridge (right of the indenter in the image). Units on all axes and the grey scale are millimetres.

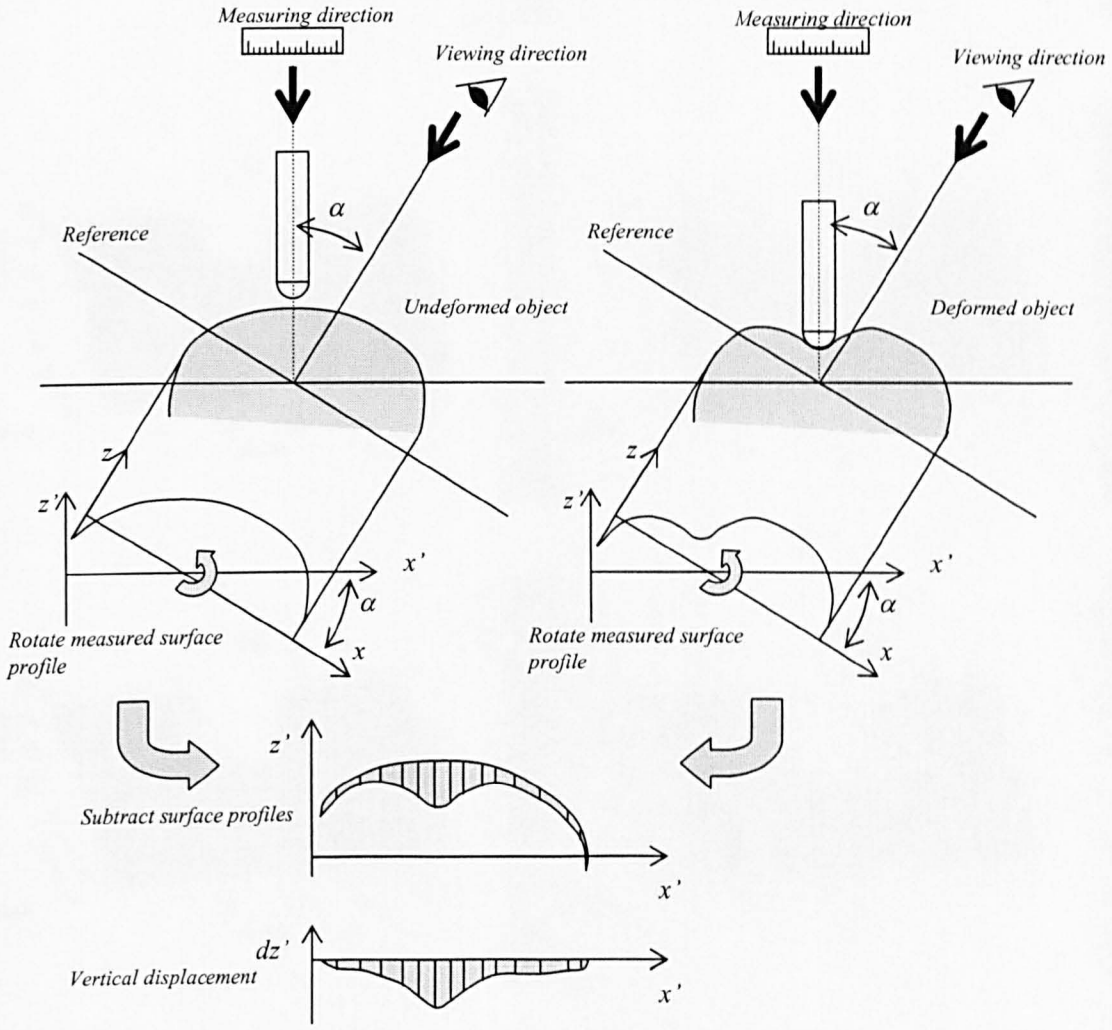

Figure 5.15: Deformation measurement with oblique viewing: data processing.

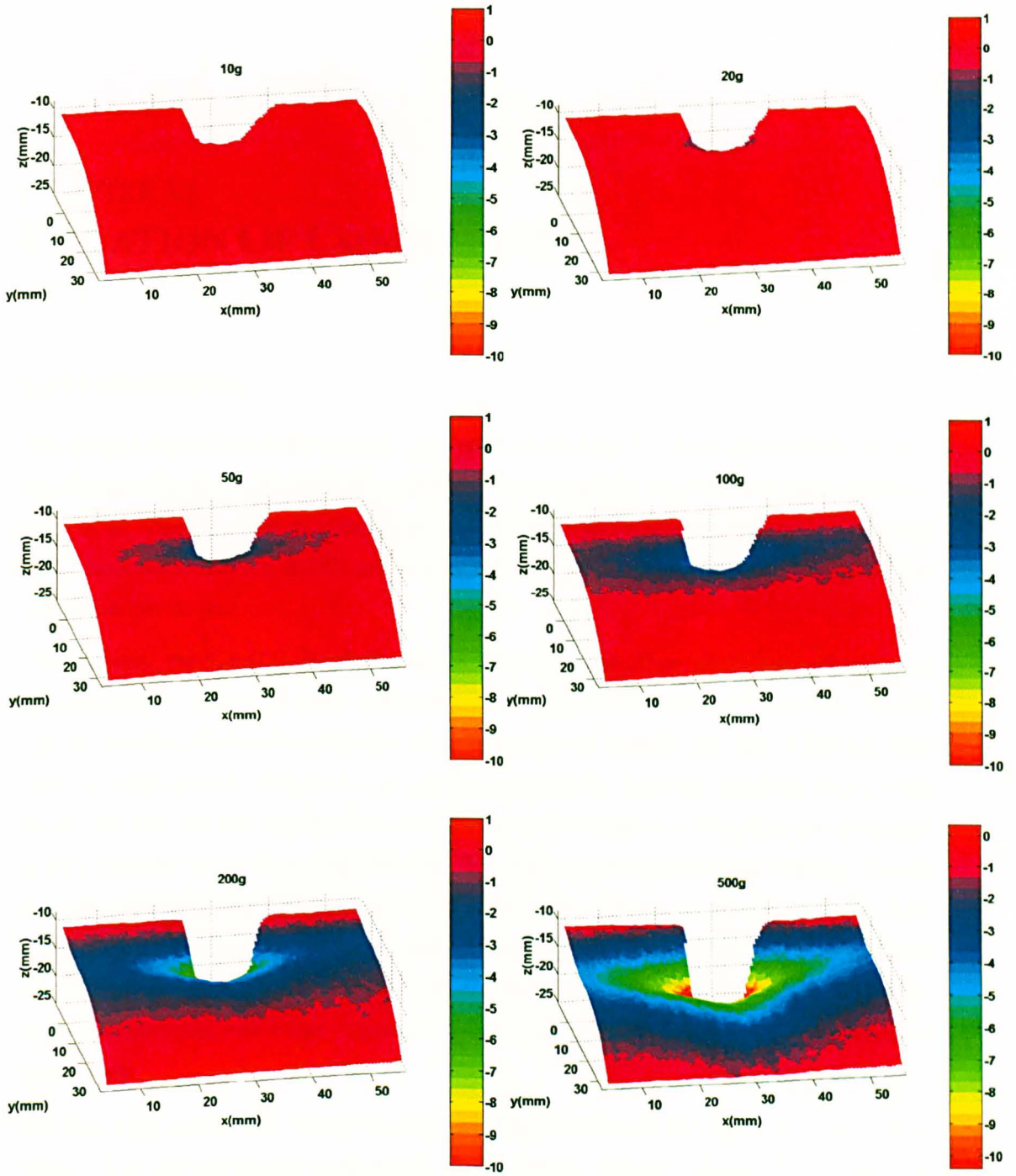

Figure 5.16: Results of the indentation tests on human skin.

CHAPTER VI
LOCATION OF COMPONENTS

VI.1 Introduction

This chapter reports the work carried out in order to develop the shape measurement system described in Chapter IV into an instrument capable of measuring the orientation and location in space of an object in addition to its shape. This capability has numerous applications assisting non-destructive evaluation (NDE) methods in the aerospace industry, some of which will be outlined in this chapter.

Unfortunately, the values in the depth map obtained with the fringe projection technique are undetermined by a constant value, sometimes referred to as the *piston* term. This term, related with the problem of identifying the zero order fringe (see *e.g.* Durelli and Parks, 1970 and other classical texts), can be interpreted as an unknown rigid body displacement of the object along the camera axis. An auxiliary location system based on the light spot technique was integrated in the instrument to overcome this limitation. The light spot technique, taken from the field of machine vision, essentially uses triangulation with a laser beam to provide fast and non-contacting measurements of distance. This technique was used to obtain the absolute location of at least one point on the surface of the object, and later this information was combined with the shape data obtained with fringe projection system to calculate the value of the undetermined *piston* term.

The following section will briefly describe the context in which this study was undertaken. Section VI.3 summarises the requirements of the location system. Section VI.4 presents the principles of the light spot technique, and the changes that were introduced into the experimental apparatus and methodology of use described in Chapter IV in order to develop the combined technique for the measurement of shape and location. The method is illustrated using a full-size aircraft component as an example in section VI.5. The section describes the measurement of shape and location, and the integration of the experimental data with the CAD model of the part. Section VI.6 discusses the application of the method to three case studies related to NDE in the aerospace industry, corresponding to three different stages of the aircraft

life cycle. The technique was demonstrated on location in an x-ray testing facility in the R&D laboratory, in a complex-geometry ultrasound inspection system in a production environment, and finally on the actual aircraft in the hangar during maintenance. Section VI.7 presents a discussion of the technique, a summary of the results, and conclusions.

VI.2 Background On NDE

NDE techniques are used extensively in the aerospace industry throughout the life cycle of an aircraft. These methods constitute an important tool for the evaluation of prototypes in the design phase, for the detection of manufacturing defects in production, and for the monitoring of flaws produced during service. Ultrasonic waves, eddy currents, x-ray, or infrared thermography, among others are examples of some of these NDE methods.

The Brite/Euram Project BE 97 – 4057 INDUCE (Advanced Integral NDE Concepts for Unified Life Cycle) congregated fifteen international partners including universities, research institutes, and major aerospace companies in Europe with an interest in the topic. A central theme of the INDUCE project was to concentrate on how NDE data could be best used throughout the complete life cycle of the aircraft.

The computer-aided design (CAD) model is widely considered an ideal vehicle to share NDE data between the many different disciplines involved in the design, manufacture and in-service support stages. During the course of the first year of work, it became apparent that the ability to register the NDE data acquired during an inspection with the CAD model of the component would substantially facilitate the integration of NDE in the life cycle.

The difficulty lies in that most NDE techniques typically provide some form of two-dimensional scan of the part, and the determination of a correspondence point-by-point between these scans, and the three-dimensional CAD model requires information about the shape of the specimen and its orientation and location with respect to the inspection device.

As a result, there was a need for a system capable of providing information about the shape of a test part, and its position and orientation with respect to the inspection device. Such a system would enable the registration of the NDE data with the CAD model, as shown diagrammatically in fig. 6.1, constituting an important advance towards the development of new technologies for (i) the integration of NDE data obtained with different methods, (ii) the transfer of information relative to NDE inspections between different disciplines, and (iii) the automation of the inspection process.

This research was carried out as part of Sub-Task 4.2.1 on '3D Moiré For External Defects Inspection Applicability', after a modification of the original scope of the task, which initially

concentrated on the application discussed in Chapter III. The partners directly involved in this study were BAE Systems and the University of Sheffield.

VI.3 Requirements

Three applications were considered in this research for the development and testing of the location system.

- Case 1 was related to the inspection of internal welds in a critical aircraft part using x-rays. In this application, the measurement system was required to locate the part inside the x-ray chamber in order to (i) assist in the remote operation of the inspection device from outside the x-ray chamber, and (ii) to enable the registration of the two-dimensional x-ray scan with the three-dimensional CAD model of the part.
- Case 2 concentrated on the ultrasound testing of complex components, which is routinely applied for quality control in the aerospace industry. During the inspection, the ultrasound probe must follow closely the surface of the part, and maintain its alignment with the normal to the surface. The set-up of the existing system requires an operator to laboriously generate the trajectory of the inspection system by manually guiding the probe over the surface of the specimen during the first run. At the production stage there is a need for highly automated inspection methods, suited to large-scale production. In this case, the measurement system was required to provide data about the shape and location of the component to assist in the automatic generation of trajectories, allowing shorter set-up times, and therefore faster and more cost-efficient inspections.
- Case 3 considered a demonstration of the system on the actual airplane under routine maintenance conditions in the hangar, in order to evaluate its performance for potential applications in-service and during assembly of the aircraft.

More details about these case studies can be found in section VI.6. The remaining of this section is a summary of an internal INDUCE report detailing the conditions of operation and the requirements of the location system (INDUCE TR-4211-UofS-02).

VI.3.1 Operating Environment

The operating environment in case 1 was particularly challenging for the shape and location measurement system. All parts of the system had to be accommodated in the limited space available inside the x-ray chamber, which was $4.3\times3.5(m)$ in size, and the object was relatively very large (*ca.* $2\times2m$) when compared with the observation distance. A short focal length camera lens, $f_c=4.5(mm)$, was required to cover a large field of view, and thus a certain amount of distortion in the input images was inevitable. As a result, the telecentric hypothesis was no

longer valid and the more complex expressions for phase to height conversion presented in section IV.6.1 had to be used in order to account for the effect of diverging optics.

In addition, the operators did not have direct access to the x-ray chamber during operation due to health and safety regulations, and consequently the system had to be designed to allow remote control.

A discussion of the difficulties created by the unfavourable ambient conditions typically found in the factory and the hangar, including limited access and inadequate illumination, was presented in Chapter III (section III.2). These unfavourable conditions applied particularly to case 3, and to a lesser degree also to case 2.

VI.3.2 Inspection Area

Inspection areas were estimated to be typically between 0.5×0.5*(m)* and 2×2*(m)*. In cases when a continuous surface map of the component was not necessary, it was considered acceptable to segment this area in a number of overlapping sub-regions that could be used to obtain the location of distinguishable features of the component.

VI.3.3 Precision

The end user set the requirements on the precision of the location system in the first two case studies considered. In the x-ray application (case 1), the system will be used to provide feedback on the position of the component, and the requirements on precision were given by the accuracy of the positioning mechanism and the tolerances in the component to be inspected. In the ultrasound application (case 2), the location data will be employed to automatically generate the trajectory of the ultrasound probe, and the requirements on precision were controlled by the tolerances of inclination and distance of the inspection device relative to the component.

According to the above criteria, the accuracy of the shape measurement was specified as ±3 *(mm)*, and the precision of the measurements of the component's location was specified in the range of ±3 *(mm)* for the position coordinates and $\pm0.5^{\circ}$ for the orientation about each axis. These requirements were not particularly strict, partly due to the relatively large size and manufacturing tolerances of the components typically used in the applications under study.

VI.3.4 Other Requirements

A common requirement for all three cases was that the location system should not interfere with the NDE testing in progress, or in case 3 with other simultaneous maintenance operations being performed on the aircraft. Preparation of the specimen should be kept to a minimum, no part of

the apparatus should be in contact or near the component, and it should not be necessary to attach sensors or targets to it.

Short set-up times and low operation costs were considered important especially in case 2 given the considerable number of components to be tested.

Flexibility was a very important attribute to the system: the instrument should be easy to use and to re-configure in order to adapt it to a wide range of applications.

Finally, the system should be able to cope with a range of surface finishes. The surface of the specimen used in case 1 was made of uncoated titanium, which provided a relatively favourable situation. However, case 2 dealt with composite fibre panels from the aircraft skin, both coated and uncoated. Similarly, the in-service inspections studied in case 3 typically involve parts presenting markings, dirt and other unfavourable conditions for the fringe projection system.

VI.4 Methodology

The fringe projection technique described in previous chapters is well suited to provide measurements of the shape and orientation of an arbitrary object using very simple experimental apparatus. In addition, it is a non-contacting technique that permits remote operation and does not interfere with most NDE methods. The technique produces a full-field map of depth of the object surface relative to a reference plane.

However, the values in the depth map are undetermined by a constant *piston* term, which can be interpreted as an unknown rigid body displacement in the direction of the camera axis. This unknown term can be safely ignored in surface contouring applications, such as those discussed in Chapter V. However, if a measurement of the absolute location is required, it is necessary to determine the location of at least one point by alternative means (Cloud, 1998).

The light spot technique (Klette *et al.*, 1998) was chosen to complement the fringe projection technique in this study. This technique is commonly used in machine vision applications to measure distances, by means of triangulation with a beam of light. The measurement is fast and simple, and no contact is necessary. Measuring the absolute location of one or more points on the surface of the object allows evaluation of the unknown *piston* term in the depth map obtained using the fringe projection technique. An auxiliary system based on this technique was designed and built into the location system. This section outlines the basic principles of the technique, and describes the methodology of use, experimental apparatus and calibration procedure developed for the particular application under study.

VI.4.1 Principles Of The Light Spot Technique

The following discussion presents a brief outline of the principles of distance measurement using the light spot technique. A simple pinhole camera model was considered, in which optical aberrations were neglected and the optical axis was assumed to intersect the CCD at its centre. Further details on this or more elaborated models can be found in standard computer vision texts (*e.g.* Faugeras, 1993, Klette *et al.*, 1998, or Trucco and Verri, 1998).

A Cartesian coordinate system *xyz* was defined with the origin located in the focal point of the camera **O** and the z-axis aligned with the optical axis, as shown diagrammatically in fig. 6.2. The image plane of the camera (*i.e.* the plane of the CCD sensor), is therefore $z=f_c$, where f_c is the effective focal distance of the camera lens. A coordinate system $\xi\psi$ was defined on the image plane with origin on the camera axis as indicated in the figure. Note that (ξ, ψ) are physical coordinates, *i.e.* have dimensions of length.

It was assumed that the laser source **S** was located on the *x*-axis at a distance *b* from the origin **O**. The direction of the laser beam **SP** was defined by the angles α in the *xz*-plane and β in a normal plane that contains **SP**. The laser beam strikes the surface of the object at point $\mathbf{P}(x_P, y_P, z_P)$, which projection onto the image plane of the camera is point $\mathbf{p}(\xi, \psi)$. The ray theorem yields:

$$\frac{x_P}{\xi} = \frac{y_P}{\psi} = \frac{z_P}{f_c} \tag{6.1}$$

Using eq. (6.1) and simple trigonometric relations, expressions can be derived to calculate the coordinates of point **P** as a function of the coordinates of its projection **p** in the image plane and the parameters defined above, *i.e.* the distance *b* between the laser source **S** and the camera focal point **O**; the effective focal length of the camera lens f_c; and the angle α between the laser beam and the *x*-axis.

$$x_P = \frac{\tan(\alpha)\cdot b\cdot \xi}{f_c + \xi\tan(\alpha)}$$

$$y_P = \frac{\tan(\alpha)\cdot b\cdot \psi}{f_c + \xi\tan(\alpha)}$$

$$z_P = \frac{\tan(\alpha)\cdot b\cdot f_c}{f_c + \xi\tan(\alpha)} \tag{6.2}$$

The light spot technique is normally used in machine vision applications for shape measurement. The laser beam is deflected by means of a set of movable mirrors to scan the surface of the object point by point and obtain the shape data. In these applications the

technique is limited by the low speed of the scanning process. In addition, shadowed areas in the surface of the object may pose a problem. In the current application however, only one measurement with the light spot technique is strictly necessary to solve for the *piston* term in the depth map calculated using fringe projection, and the above issues do not represent a serious drawback. In practice, the use of more than one light spot measurement adds robustness to the calculation of the *piston* term. It was suggested to achieve this by using two or three laser sources with fixed orientations in order to eliminate the need for a deflection system and keep the apparatus robust and simple. In this case, each laser module can be calibrated and used independently from each other.

This technique requires accurate calibration of the camera, and precise detection of the spot in the image to work properly. These requirements were addressed with the implementation of a calibration procedure for the camera, and image processing algorithms for the detection of the light spot in the image with sub-pixel accuracy.

VI.4.2 Apparatus

Figure 6.3(a) shows the prototype system for shape and location measurement, which combines the fringe projection technique and the light spot technique. The combined instrument uses the apparatus described in Chapter IV, with the addition of a second laser module (NVG Inc. M660-5), similar to the one used for alignment. The second laser module sits on the tripod next to the projector, and is used for distance measurement using the light spot technique. Additional laser modules can be added to the instrument if more than one measurement of absolute location is required in order to increase the robustness of the *piston* term determination. The lasers were connected to the control box shown in fig. 6.3(b).

The experimental set-up shown in fig. 6.3(c) was built in a laboratory at the University of Sheffield to test the location system. This test rig was a half-scaled model of an x-ray chamber in BAe Systems' facilities. The test rig was designed to simulate the operating conditions in case study 1, which will be described in more detail in section VI.6.1.

A positioning mechanism allowed the control of the orientation and location of the specimen. Two translation stages were used to modify the position along the z- and x-axis respectively. Calibrated scales with $0.5(mm)$ divisions were attached to the translation stages to provide accurate measurements of the position of the sample for the validation of the location system. It was not considered necessary to add a degree of freedom along the y-axis since for the application under study the x- and y-axes are equivalent in terms of accuracy and resolution. A rotating table was installed on the translation stage to allow adjustment of the orientation β of the specimen about the y-axis. The rotating table had a scale with $1/60^{o}$ divisions that allowed

accurate measurement of the orientation angle β. The origin and sign convention shown in the figure were chosen arbitrarily. The bracket shown in fig. 6.3(d) was used to securely attach the samples to the rotation table.

VI.4.3 Experimental Procedure

This section describes step by step the acquisition procedure of location and shape data using the combined measurement system.

(i) Switch on the distance measurement laser. A bright spot appears on the point **P** where the beam strikes the surface of the object. Collect an image of the object showing the bright spot with the camera. Figure 6.6(d) shows a typical input image of the laser spot on the surface of a component.

(ii) Determine the pixel coordinates (i_p, j_p) of the bright spot **p** in the image. A two-step image processing method was used that combines two standard techniques described by Klette *et al.* (1998): (a) scan the image searching for the pixel with the maximum intensity, and (b) calculate the weighted centroid of the intensity distribution in the vicinity, to achieve sub-pixel accuracy.

(iii) Calculate the physical coordinates (ξ_p, ψ_p) in the image plane from the pixel coordinates (i_p, j_p). In this research, optical aberrations were neglected and the optical axis was assumed to intersect the CCD plane on its centre, so that the transformation consisted of shifting the origin of the coordinate system to the centre of the image as shown in fig. 6.2, and scaling by the size of a single detector in the CCD array:

$$\begin{aligned} \xi &= k_\xi \left(j - N/2\right) \\ \psi &= -k_\psi \left(i - M/2\right) \end{aligned} \tag{6.3}$$

where M and N are respectively the number of rows and columns in the detector array. The dimensions of a single detector were calculated as the ratio between the physical dimensions of the CCD chip and the number of detectors in the x and y direction. This information can be obtained from the manufacturer of the camera. For the Panasonic camera used in the experiments, these parameters were k_ξ=6.5*(μm/pixel)*, and k_ψ=6.25*(μm/pixel)*.

(iv) Use eq. (6.2) to calculate the coordinates in space of **P** (x_p, y_p, z_p) from the image plane coordinates (ξ_p, ψ_p) and the parameters of the system configuration a, b and f. Section VI.4.4 details the calibration procedure of the system, by which these parameters can be determined.

(v) The set-up of the fringe projection apparatus, methodology for the collection of the fringe data, and the processing algorithms were described in detail in Chapter IV. That procedure yielded a map of surface shape $z'=f(x, y)$, which includes an unknown *piston* term. Figure 6.6(c) shows a typical object image.

(vi) Correct the map of surface shape by offsetting it the amount necessary to include the point measured with the light spot technique (x_p, y_p, z_p), thus eliminating the *piston* term, *i.e.*

$$z = f(x,y)+\left(z_p - f(x_p,y_p)\right) \tag{6.4}$$

VI.4.4 System Calibration

The expressions in eq. (6.2) to calculate the absolute location of point **P** (*i.e.* the point where the laser beam strikes the object surface) in terms of the coordinates of the bright spot in the image involve three parameters of the system configuration, namely the effective focal distance of the camera lens f_c, the angle α between the laser beam and the x-axis, and the position b of the laser source along the x-axis. These are parameters defined for the pinhole camera model, which must be determined indirectly in the real optical arrangement.

The angle α could not be accurately derived from the orientation of the casing of the laser source, due to misalignments between the elements. The determination of distance b between the laser source and the optical centre of the camera **O** also presented difficulties due to lack of physical references in the real optical arrangement for the measurement.

The image plane (*i.e.* the CCD sensor) is by construction situated at a distance $F=12.5(mm)$ from the edge of the lens thread for CS-mount cameras, such as the one used in this study. The optical centre **O** is situated on the viewing axis, at a distance f_c away from the image plane. This parameter, f_c is related to the focal length of the lens f_{c0} and the focusing distance (*i.e.* the distance camera-object z_P, assuming that the object is in focus) through the basic lens formula.

$$\frac{1}{f_{c0}} = \frac{1}{f_c} + \frac{1}{z_P} \tag{6.5}$$

Rearranging terms in the previous expression, f_c can be expressed as a function of f_{c0} and z_P.

$$f_c = \frac{z_P}{z_P - f_{c0}} \cdot f_{c0} \tag{6.6}$$

The difficulty is that z_P was the original unknown of the problem. The focal length of the camera lens f_{c0} corresponds to an object at infinity, and can be used as a rough estimate of f_c in many cases. In a zoom lens, the reading of the zoom setting serves the same purpose. An

improved estimate of f_c can be obtained by making an educated guess of the value of z_P and using eq. (6.6).

A calibration procedure was devised to calculate the values of the three parameters f_c, α and b from a set of images of the light spot from the distance measurement laser on a flat plate placed at known distances with respect to the camera. The remainder of this section describes the calibration method illustrated with a real example.

In order to collect the calibration set of images for the light spot technique, a flat plate was attached to the positioning mechanism and aligned perpendicular to the camera axis, *i.e.* with $\beta=3\pi/2(rad)$, using the procedure described in section IV.6.2. A set of seven light spot images was collected of the plate located at different positions along the z-axis within the range of interest. Figure 6.4(a) shows some examples.

The calibration involves four steps:

(i) Each of the images was processed as described in the previous section to determine the position of the bright spot. The data is presented in Table VI-1. The first column shows the reading z_N on the scale of the translation stage for each position of the plate. Columns two and three show the *(i, j)* coordinates of the bright spot centroid, determined by processing each of the images. Columns four and five show the physical coordinates (ξ_p, ψ_p) of the projected point **p** on the image plane, calculated with eq.(6.3).

z_N *(mm)*	*i (row)*	*j (column)*	ξ *(μm)*	ψ *(μm)*
97.0	*397.1853*	*380.7261*	*609.2*	*82.4*
130.0	*396.4823*	*392.7938*	*687.7*	*78.0*
200.0	*394.8662*	*415.9976*	*838.5*	*67.9*
270.0	*393.5588*	*435.5571*	*965.6*	*59.7*
310.0	*392.1467*	*446.0229*	*1033.6*	*50.9*
350.0	*391.0021*	*456.3118*	*1100.5*	*43.8*
390.0	*390.4049*	*465.1049*	*1157.7*	*40.0*

Table VI-1: System calibration, image plane coordinates of the light spots.

(ii) For each of the positions of the plate, independent measurements of the spatial coordinates (at least x and z) of the bright spot were conducted using an alternative technique. The z_N distances, shown in the first column of Table VI-2, correspond to the reading on the scale attached to the translation bench. The accuracy of these measurements was better than $0.5(mm)$. The second column shows measurements of the distance z_M between the plate and

the base of the camera lens mount, which were carried out using steel measuring tape, with an estimated accuracy of about $1(mm)$. The average offset z_o between the two sets of values was calculated as $900.0(mm)$. Column three of Table VI-2 shows the z-coordinates of the light spot **P**. These values refer to the origin **O** (*i.e.* the optical centre of the camera) as shown in fig. 6.3(c), and were calculated from the z_N values as follows.

$$z_M = z_N + z_o$$
$$z_p = z_N + z_o + F - f_c \tag{6.7}$$

The focal length from the camera lens, which in this example was $f_{c0}=4.5(mm)$ was considered a reasonable estimate of the focal distance f_c in order to calculate the values shown in column three of Table VI-2 with the previous expression.

The last column shows the x-coordinate of the light spot **P**, which was measured on a scale attached to the plate with an estimated accuracy of $0.5(mm)$. The bright spot **A'** where the alignment laser (parallel to the camera's optical axis z) intersects the plate was used as the reference for these measurements, as shown in the diagram in fig. 6.4(b), which illustrates as well the sign convention used, with the laser source located at $x<0$. Precise measurement of the position of the bright spots on the plate was possible by means of laser safety eyewear (Laser Line Helium-Neon goggles, Edmund Optics Ltd.), which attenuate the red wavelengths of light, filtering most of the diffused reflections and eliminating the circle of glare around the laser contact spot. Despite the low output power of the lasers, the use of safety eyewear is recommended in any case to protect the operator.

$z_N(mm)$	$z_M(mm)$	$z_p(mm)$	$x_p(mm)$
97.0	*997.0*	*1005.0*	*124.5*
130.0	*1028.0*	*1038.0*	*145.0*
200.0	*1100.0*	*1108.0*	*188.5*
270.0	*1170.0*	*1178.0*	*232.5*
310.0	*1209.0*	*1218.0*	*257.5*
350.0	*1252.0*	*1258.0*	*283.0*
390.0	*1291.0*	*1298.0*	*305.0*

Table VI-2: System calibration, 3D spatial coordinates of the light spots.

Step (ii) yielded a set of experimental measurements of the x_p and z_p coordinates of point **P** for each position of the plate. The coordinates (ξ_p, ψ_p) of the corresponding projection on the image plane **p** had been previously calculated from the calibration images in step (i) by means of the procedure described in section VI.4.3. This information could in principle be

used to solve eq. (6.2) for the three unknown model parameters, b, f_c and α provided measurements are available for a minimum of three positions of the plate. In practice, an over-deterministic system was used to improve the robustness and accuracy of the solution, which was obtained by means of a least-squares iterative method.

(iii) An estimate of the parameters was obtained to use as the initial solution in an iterative optimisation algorithm. The value of f_c estimated in step (ii) was improved by using eq. (6.6), with an assumed average focusing distance of $1200(mm)$, which yielded f_c=$4.52(mm)$ in this example. The measured values of z_p versus x_p were plotted as shown in fig. 6.4(c), and the linear best fit in the least-squares sense was calculated. The gradient and the intersection with the x-axis of this straight line were respectively used to estimate the angle α=$2.125(rad)$ between the laser beam and the camera axis, and the distance b=-$496.8(mm)$ between the laser source **S** and the camera focal point **O**, as illustrated by the diagram in fig. 6.4(b).

(iv) The values of the three unknown model parameters b, f_c and α were optimized using a least-squares algorithm to minimize the error between the experimental measurements of the light spot spatial coordinates x_p and z_p and the corresponding values resulting from eq. (6.2). The algorithm begins with the initial estimates calculated in step (iii), and iterates to minimize the error between measured and calculated values, with b and f as variables, until convergence is reached. The initial value of α=$2.125(rad)$ for the angle was considered constant in the iterative process, as this was found to increase the stability of the solution.

The iterative algorithm uses coefficients to dynamically adjust the search range for b and f_c, respectively c_b and c_f, which are plotted in fig. 6.5(a) versus the iteration number. Similarly the graphs in figs. 6.5(b), (d) and (c) show the evolution of b, f_c, and of the error function e used to measure the quality of the fit as the iterative algorithm progressed towards convergence after 14 iterations. The result of the optimisation was b=-$496.77(mm)$ and f_c=$4.91(mm)$. These values can be used in eq. (6.2) as long as the optical configuration of the system remains undisturbed. Table VI-3 shows the results of the calibration.

Columns two, three and four present respectively the direct measurements of x_p, the values calculated using eq. (6.2) with the optimised parameters, and the errors. Similarly, columns five, six and seven show the z_p measurements and the error in the z-coordinates, which is also shown in the graph of fig. 6.5(e). Note that the values in column five were re-calculated from z_N in eq. (6.7) with the optimised value of f_c. From these results, the accuracy of the measurement system in the calibrated range was estimated from the standard deviation of the data as $\pm 0.9(mm)$ for the x-coordinates, and also $\pm 0.9(mm)$ for the z-coordinates.

The value of 4.91(mm) obtained for the effective focal length is unusually large, and can only be explained because the Panasonic camera used in the experiments allows regulating the back flange distance continuously between the CS and the C standard distances, and probably it was not accurately set to the CS position at the beginning of the test.

z_N (mm)	x_p(mm)	Calculated x_p (mm)	Error (mm)	z_p (mm)	Calculated z_p(mm)	Error (mm)
97.0	124.5	124.6	+0.1	1004.2	1004.6	-0.4
130.0	145.0	145.3	+0.3	1037.7	1037.6	+0.1
200.0	188.5	189.4	+0.9	1108.8	1107.6	+1.2
270.0	232.5	231.4	-1.1	1176.9	1177.6	-0.7
310.0	257.5	256.2	-1.3	1216.8	1217.6	-0.8
350.0	283.0	282.1	-0.9	1258.8	1257.6	+1.2
390.0	305.0	305.8	+0.8	1297.0	1297.6	-0.5

Table VI-3: System calibration results.

VI.5 Results

In this section the procedure is illustrated using a full size aircraft component as an example. The sample was used in a series of experiments with the aim of evaluating the performance of the fringe projection technique in the applications under study. The collection of shape and location data is discussed. The ability to measure the absolute location of the specimen relative to the camera allows using the first order expression presented in section IV.6.1.4 to obtain more accurate shape data from the phase map. The post-processing of the data to calculate trajectories on the surface of the object is demonstrated. Finally, the procedure for integration of the shape data with the CAD model of the component is described. The comparison of the experimental shape and location measurements with the CAD model allowed the determination of the orientation and coordinates of the object, and an evaluation of the accuracy of the technique. This technique could potentially be used as well in quality control applications.

VI.5.1 Shape And Location Measurement Of A Complex Component

The measurement system was tested with an aircraft component supplied by BAE Systems. The sample, which front and back views are respectively shown in figs. 6.6(a) and (b), was a carbon fibre composite panel from the fuselage of the EF-2000 aircraft. The approximate dimensions of the panel were 950×500*(mm)*. The component was coated with primer, and presented a clear, matt finish as shown in the figure. This surface finish was favourable to achieve good contrast of the projected fringes, and is representative of parts in intermediate manufacturing stages.

The configuration of the system was chosen to replicate the unfavourable working conditions given in the case study 1, in which space constraints force a short observation distance, of the same order of magnitude as the size of the object. The camera was located *ca.* 1200*(mm)* away from the object, and the projector 346.0*(mm)* to the left. A typical set of fringe and light spot data of the specimen collected with this configuration of the system is shown in figs. 6.6(c) and (d). Note the distortion of the input images, which forced the application of the first order phase-to-height expression with perspective correction to take into account the strong effect of diverging optics. The pitch of the projected fringes on the reference plane was 8.53*(mm)* with a 200*(lines/inch)* master grating.

The fringe projection system was calibrated using the images of the reference plane and calibration cone shown respectively in fig. 6.7(a) and (b). The cone used in this case was of height 140*(mm)* with a 150*(mm)* radius. The calibration images of the cone were cropped to a 400×350*(pixels)* rectangle to remove the background near the edges, as indicated in the figure. Figure 6.7(c) shows the depth map obtained after unwrapping and calibrating the phase map of the calibration cone. The automatic calibration allowed the determination of the camera magnification factor m_p=1.50*(mm/pixel)* and the calibration constant K=-7.07*(mm/rad)* for this configuration of the system under the telecentric hypothesis. A 3D mesh representation of the surface of the calibration cone measured by the system is shown in fig. 6.7(d).

A typical input data set for the combined location and shape measurement system consists of an image of the fringes projected onto the surface of the object, such as fig. 6.6(c), and an image of the laser spot for distance measurement, such as fig 6.6(d). Whenever both images are collected using the same optical configuration as for the calibration of the system, the object image can be combined with the reference image in fig. 6.7(a) to produce a modulated phase map as demonstrated in previous chapters. Later the light spot image can be used, following the procedure detailed in section VI.4.3, to calculate the absolute distance between the object and the camera, hence removing the *piston* term from the depth map.

In addition to that, the discussion presented in section IV.7.2 showed that in order to obtain a good measurement of the surface geometry in non-telecentric conditions, it is necessary to use the first order approximation with perspective correction. The parameters needed for these expressions (introduced in section IV.6.1), can be calculated from the telecentric parameters K and m_p yielded by the automatic calibration, and the distance measurement obtained from the light spot image, by following the procedure described in section IV.6.4.

The differences between the depth map calculated with the telecentric expression and the depth map calculated with the first order expression and perspective correction can be appreciated by

comparison of figures 6.8 (a) and (b). Note the distortion in the map calculated with the telecentric expression.

Figure 6.9 shows an example of the combined measurement of shape and location for three different positions of the fuselage panel. Only two degrees of freedom (displacements along the z-axis and rotations β around the y-axis) were allowed to the component, and therefore its location was determined by the reading z_N of the scale attached to the z-translation table, shown in the second column of Table VI-4, and the angle β measured in the scale of the rotation table, and shown in column three.

Image	z_N *(mm)*	β *(degrees)*	*z*(mm)*	*i (row)*	*j (column)*	*z (mm)*	*z-z*(mm)*
o01.tif	*86.0*	*270° 0'*	*1191.3*	*392.3740*	*428.5123*	*1189.8*	*-1.5*
o03.tif	*86.0*	*255° 0'*	*1186.0*	*393.8600*	*414.0200*	*1188.4*	*+2.4*
o04.tif	*146.0*	*246° 31'*	*1237.7*	*394.0040*	*417.5122*	*1236.8*	*-0.9*

Table VI-4: Distance measurement results

The z-coordinate of point **A'**, where the alignment laser strikes the surface of the object, can be calculated as follows (refer to the diagram in fig. 6.3(c))

$$z = z_N + \Delta z - r' + F - f_c \tag{6.8}$$

where Δz is the offset between the reading z_N in the scale and the distance **OO'** between the camera centre and the axis of the rotation table, and r' is the distance **O'A'** between the rotation axis and the point **A'**.

The fourth column of Table VI-4 shows estimates z^* of the z-coordinate of point **A'**, which were calculated with eq. (6.8), assuming that the component is approximately flat in the vicinity of point **A'** and hence r' can be written as follows:

$$r' = \frac{r}{\cos(3\pi/2 - \beta)} \tag{6.9}$$

In this expression, r is the distance to the rotation axis as shown in fig. 6.3(c). The values of Δz and r yielded respectively Δz=1248.2*(mm)* and r=150.5*(mm)* in this example.

These estimates of z where used as a reference to evaluate the numerical results obtained with the measurement system. The object images shown in fig. 6.9(a) were combined with the reference shown in fig. 6.7(a) to obtain a map of modulated phase in each case. Light spot images similar to the one shown in fig. 6.6(d) where used in each case to determine the absolute

distance between the object and the camera. Column five and six of Table VI-4 show the pixel coordinates *(i, j)* of the laser spot detected for each example. This information was used to remove the *piston* term and to apply the first order calibration expression to the phase maps. The resulting depth maps, with the combination of location and shape data, are shown as contour maps in fig. 6.9(b). Finally, fig. 6.9(c) shows a 3D representation of the results as realistically shaded surfaces, where the origin of the coordinate axes is the optical centre of the camera. The numerical value of z at point **A'** obtained from the depth maps is shown in the image, and also presented in column seven of Table VI-4.

The last column in the table shows the error between the values of z for point **A'** obtained using the measurement system, and the estimates z^* calculated with equations (6.8) and (6.9) for each of the three examples. The agreement is excellent considering the uncertainties due to experimental error. Note that assuming that the phase can be measured with an accuracy better than 0.4*(rad)*, then the accuracy of the shape measurement can be estimated from the telecentric calibration constant K=-7.07*(mm/rad)* as better than ±2.7*(mm)*.

VI.5.2 Correlation With CAD Data

A CAD model of the part was kindly supplied by BAe Systems in the portable format IGES. This model, shown in fig. 6.10(a), was imported into a commercial CAD software package for manipulation. First the facets corresponding to the bottom surface of the panel were isolated from the rest of the model, as shown in fig. 6.10(b), and later a fine surface mesh of the surface was generated using a suitable meshing tool. The nodes of this mesh were exported as a text file, which was later imported into MATLAB in order to combine this information with the results of the experimental shape measurements performed on the actual part using the fringe projection technique. This is a simple general purpose approach, relatively platform and software independent, and appropriate for a wide range of applications.

The CAD model contains an idealized representation of the component, located at a nominal position. This representation can be used as an artificial reference to measure rigid body translations and rotations of the specimen with respect to the nominal position, and also deviations in the shape with respect to the nominal shape of the component defined in the CAD model.

The alignment procedure was simplified by selecting a reduced set of control points to describe the location and orientation of the specimen. Although three points are in theory sufficient for a rigid body, an over-deterministic system was preferred to reduce the effect of experimental error. A good set of control points should be evenly distributed over the surface of the object and be easy to identify precisely, both on the input fringe images and in the CAD model. In this

example, the centre points of the seven fixing holes labelled 6, 28, 31, 36, 41, 45, and 53, which were situated near the outer edges of the specimen, seemed a sensible choice (see fig. 6.8(b)).

However, shape data measured in the vicinity of edges or near the holes is not very reliable for the reasons detailed in section IV.7.1.3. Therefore the set of control points was extended as shown diagrammatically in fig. 6.11(b) by (i) defining vertical planes through five pairs **P-Q** of the original control points, (ii) sectioning the surface of the object with those planes, and (iii) selecting N equispaced sampling points ($\mathbf{P}_1,\ldots,\mathbf{P}_N$) along each of the resulting intersection curves, resulting in the extended set shown in fig. 6.11(a).

A drawback of this approach is that whenever the object (*i.e.* the experimental measurement of shape and location) is tilted with respect to the reference (*i.e.* the CAD model), then the relative inclination of the sectioning planes is different in each case and therefore matching intermediate points defined for the reference and the object may not coincide, see points $\mathbf{P}_k$ and $\mathbf{P}_k'$ in fig. 6.11(b). This difficulty was overcome by performing two iterations of the alignment algorithm. After a first iteration, in which the object is rotated and translated to match the reference, the intermediate points were re-sampled and fine adjustments were calculated in a second iteration.

Figure 6.11(c) shows the mesh generated from the CAD model, with the corresponding extended set of control points. A simple iterative alignment algorithm was implemented, which performs an initial guess of the translation and rotations, and then computes the value of the rigid body rotations and translations that optimise the match. Figure 6.11(d) shows a representation of the first iteration of the alignment, where the '+' symbols represent the control points of the measured data and the circles the CAD data. The first iteration involves (clockwise) the original location of the measured data, an initial guess, the computation of the translation, and the computation of the rotation. Figure 6.11(e) shows the CAD model rotated and translated after the first iteration, and the extended set of control points re-calculated for the new position. Fine adjustments performed in the second iteration are shown in fig. 6.11(f). Table VI-5 summarises the numerical results of the example alignment illustrated in fig. 6.11.

	Δx(mm)	Δy(mm)	Δz(mm)	$\Delta\phi_x$(rad$\times10^{-3}$)	$\Delta\phi_y$(rad$\times10^{-3}$)	$\Delta\phi_z$(rad$\times10^{-3}$)	Error(mm)
Iter. 1	*51.280*	*484.177*	*229.839*	*-91.8*	*34.1*	*-4608.5*	*18.9421*
Iter. 2	*0.145*	*0.014*	*-0.054*	*-0.1514*	*-0.0567*	*0.3500*	*18.6513*
Total	*53.314*	*479.896*	*228.248*	*-91.4*	*0.0369*	*-4607.4*	*18.6513*

Table VI-5: Alignment of the CAD model with experimental data

The first row of the table shows the translations and rotations calculated in the first iteration of the algorithm. The error shown in the last column is the squared root of the sum of the squared distances between matching points in the measured depth map and the CAD model. This expression of the error was used as target function for the optimization algorithm that calculates the alignment. The second row shows the result of the second iteration, where fine adjustments were calculated. Note the reduction of the error after the second iteration. The third row shows the result of combining the translations and rotations calculated in the first and second iterations. Note that the algorithm applies the rotations before the translations, and as a result the combination of the two sets of rigid body displacements cannot be calculated by direct addition of the values in each column.

VI.5.3 Applications

The information provided by the combined measurement of shape and location can be presented in many interesting ways. This section highlights some of the possibilities.

For instance, it is possible to generate sections of the measured surface, expressed as paths in three-dimensional space. This has direct application to the calculation of trajectories on the surface of the component needed for case study 2. Figure 6.12 shows four example sections of the aircraft fuselage panel. In each case, the solid line corresponds to the surface measured experimentally, and the dotted line to the CAD model, after having performed the alignment procedure described in the previous section. Note the close agreement between both lines in each case. As expected, discrepancies are larger near sudden changes in the orientation of the surface, where the fringe projection technique is more sensitive to errors. The use of the CAD model as a reference for dimensional control of this type of components will be further discussed below.

The alignment of the CAD model and the measured depth map provides the values of the rigid body translations and rotations that describe the location of the real specimen with respect to the reference location defined in the CAD model. An example set is shown in the last row of Table VI-5. This ability also has direct application to the generation of trajectories required for case study 2 (see section VI.6.2).

In addition, this information allows in turn the determination of relative rigid body translations and rotations of a component. The procedure would involve sequentially measuring and applying the alignment procedure to the desired specimen for two given locations, and later calculating the transformations necessary to go from the initial to the final position. This data could potentially be used as feedback for an automatic positioning system such as the one considered in case study 1.

As mentioned before, the alignment of the measured shape data and the CAD model can also be used to detect discrepancies between the ideal or nominal shape defined in the model and the 'real' shape of the component measured experimentally using fringe projection. This has potential applications for the dimensional control of manufactured parts.

Figure 6.13(a) shows a representation of these discrepancies in our example. The error map was calculated by (i) re-sampling the mesh of the aligned CAD model, shown in fig. 6.11(e), to obtain points matching the experimental measurements in fig. 6.11(a) and (ii) subtracting the *z*-coordinates. The extrapolation of data to generate a convex cloud of points explains the apparently large errors observed near the central hole and the bottom right corner, which are in fact outside the surface of the specimen. The fact that discrepancies are below *2(mm)* in *ca.* 90% of the map demonstrates the effectiveness of shape measurement method in a real application. Errors reach beyond *2(mm)* only in the bottom left area, and near the edges. Aside from the limitations of the technique discussed in Chapter IV, these discrepancies can be attributed as well to manufacturing tolerances, which for these composite panels are typically in the millimetre range. See for instance, the wrinkles of the carbon fibre cloth shown in the details of fig. 6.10(d), which are not present in the CAD model. Another limitation of using the CAD model as reference for dimensional control is that it may as well contain inconsistencies such as the unmatching edges shown in the detail of fig. 6.10(e).

Finally, the technique enables the integration of NDE data with the 3D geometry of the component as given by either the experimental measurement obtained from the fringe projection system or by CAD model. Figure 6.13(b) shows a 2D ultrasound scan of the fuselage panel such as the one shown in fig. 6.1, which has been mapped to the 3D geometry of the part. This ability has direct application to the case study 1, where the scans obtained from the x-ray inspection device must be integrated with the CAD model of the part in order to guide the inspection of internal welds.

VI.6 Case Studies

This section provides further information on the three case studies considered in this research. The section attempts to present the background and a proof-of-concept for each case study. Merely the main principles and some practical details of the implementation are discussed, although some actual experimental results are also presented for case study 3.

VI.6.1 X-Ray Inspection

An important attribute of the EF-2000 Eurofighter Typhoon aircraft is its inherent instability, which provides this aircraft with outstanding manoeuvrability. A complex flight control system is used to continuously fight against this natural tendency of the aircraft and return it to straight-

and-level flight, by actively controlling the canard foreplanes and flaperons. In particular, it is crucial to guarantee the integrity of the canard foreplanes, which bear very high loads during flight. BAe Systems designed a comprehensive quality control programme for this critical component that requires each manufactured unit to be inspected by x-ray to ensure the absence of internal defects in the diffusion bonded titanium structure.

The component needs to be properly aligned with respect to the x-ray system for a correct evaluation of the x-ray scan. The guidance of the system is performed remotely from outside the chamber, by means of a CAD model of the component. The process of integration between the three-dimensional CAD model and the two-dimensional x-ray scan requires information about the location and orientation of the component relative to the x-ray source in order to perform perspective corrections.

BAe Systems required an auxiliary 3D location system, capable of providing measurements of the position and orientation of the component independently from the positioning apparatus, in order to avoid precise calibration on the positioning table and to reduce set-up tasks for the component being inspected. This information will be used to guide the displacement of the x-ray source and to ensure the correct alignment of the component.

The system will be set-up inside the x-ray chamber and used during testing, which imposes strict space constraints, and dictates the need for remote operation. The prototype location system seemed appropriate for this particular application because both the fringe projection technique and the laser triangulation technique are non-contacting and allow remote control, and neither interferes with the x-ray tests. In addition, the example presented in section VI.5 demonstrated that the system can deal satisfactorily with heavily non-telecentric conditions.

A diagram of the x-ray chamber including the positioning assembly for the x-ray apparatus and the component under test is shown in fig. 6.14(a). The x-ray source and the detector screen are attached to translation stages that allow vertical and lateral (x- and y-axis) displacements of the system whilst maintaining the alignment of the x-ray axis. Longitudinal displacements (z-axis) of the detector are also possible to change the scaling of the x-ray image by modifying the distance between the source and the detector. In addition, the component is attached to a turntable capable of rotation about the y- and z-axis, and displacements along a longitudinal rail (z-axis). Figure 6.14(b) shows a 1:2 scaled test rig of the measurement system which was built in the laboratory in the University of Sheffield to test the system designed for installation in the x-ray chamber. Full-scale tests of the system were also performed on location. Figure 6.14(c) shows the system installed provisionally in the x-ray chamber BAe Systems during a demonstration. The x-ray source and detector screen can be seen mounted on mirror frames in the background. The positioning system of the specimen is under the wooden panels of the

floor. An example object image of the canard foreplane taken in the x-ray chamber during the demonstration is shown in fig. 6.14(d).

VI.6.2 Ultrasound Inspection

In the aerospace industry, ultrasound inspection of large composite panels from the aircraft skin is routinely performed for quality control during manufacture, which provides an application for the combined shape and location measurement system. Figure 6.15(a) shows a panel attached to the inspection rig. Note that this is the same component used in the previous sections to illustrate the methodology and shown in figures 6.6-13. During an ultrasound scan, the probe must remain normal to the surface of the panel and closely follow its shape. At present, an operator must laboriously teach the scan trajectory to the system by guiding it point-by-point.

The University of Sheffield and BAe Systems are presently considering the implementation of the system for this application to automatically calculate the scan trajectory of the probe for complex components in a production line at BAE Systems Warton. The system would also allow the registration of the two-dimensional ultrasound scan with the three-dimensional computer aided design (CAD) model of the part, in order to facilitate the interpretation and transfer of the NDE data, providing more useful feedback to the design and manufacturing stages.

The adverse illumination conditions in the workshop and the unfavourable surface finish of the panels result in poor quality fringe patterns, as shown in the right side of the image. The pre-processing of the images with the normalization algorithm described in section IV.5.3 can be used to enhance the quality of the fringe patterns, thus widening the range of application of the method. The algorithm applies a series of filters to the image so as to enhance the contrast of the fringe pattern, as shown in fig. 6.15(b). The plot in fig. 6.15(c) shows the intensity profiles along the line AA' before and after normalizing the image.

The scanning path to cover the whole surface of the component can be defined for the CAD model in its nominal position, and stored in the computer system that drives the ultrasound inspection device. These trajectories can incorporate the required offset (typically a few centimetres) in the direction normal to the surface of the component. The alignment procedure provides with the rigid body rotations and translations that describe the current location of the specimen with respect to the camera. The same transformations can be applied to the nominal trajectory to generate the trajectory of the ultrasound probe required for the actual location of the component.

There is an alternative approach, which is more elaborate, but allows dealing also with specimens that present significant changes in shape with respect to the nominal shape defined in

the CAD model (*e.g.* slender panels prone to large deformations). In this case, the scanning path can be defined in the CAD model in 2D. When the CAD model is aligned with the measured shape, the 2D path is projected onto the measured surface of the component, to obtain a collection of sections in three-dimensional space. The scanning path for the probe can then be obtained by applying the required offset in the direction normal to the surface, which can also be calculated from the measured shape data.

VI.6.3 Hangar

The image in fig. 6.16(a) shows the same component studied in case study 1, although in this case the foreplane canard is readily assembled on the plane. The data was collected under routine maintenance conditions in the hangar.

The overall dimensions of the foreplane were *ca.* 1100×1300*(mm)*. The tripod with the location system was installed in a platform and connected to a portable computer. The camera was located approximately 3050*(mm)* away, with the projector 420*(mm)* to the left of the camera. The image was collected with a focal distance of the camera lens of 12.5*(mm)*, and the focal length of the projector was 28*(mm)*.

The relatively poor contrast in the fringes (see the detail in fig 6.16(a)) was caused by the bright ambient light in the hangar. A second image of the object was collected with the fringe projector switched off, and subtracted from the image in fig. 6.16(a). This was found to help dealing with the sudden changes in the modulation due colour changes, and the shadows projected by the ceiling lights. The resulting image was normalised, yielding the image shown in fig. 6.16(b). The detail shows a significant improvement in the contrast of the fringes.

The time available for the collection of data was very limited. In order to reduce the amount of experimental work done in the adverse conditions of the hangar, the reference and calibration images were recorded in the laboratory using the same configuration of the optical elements. Figure 6.16(c) shows the reference. The normalized object image in 6.16(b) was combined with the reference in fig. 6.16(c) to produce the contour map shown in fig. 6.16(d). Finally, figure 6.16(e) shows a 3D mesh representation of the measured surface of the canard foreplane.

VI.7 Conclusion

A technique based on fringe projection has been introduced that allows full-field automatic measurement of the shape, location and orientation of 3D objects. An auxiliary distance measurement system based on triangulation with a laser beam resolves the indeterminate *piston* term in the shape data measured with the fringe projection technique, allowing absolute

location. Combining both techniques it is possible to obtain the shape, absolute location and orientation of an arbitrary component with accuracies better than 1% of the measured range.

The experimental apparatus and methodology of use of the system are based on those described in Chapter IV, with the addition of a second laser for location. The calibration routines of the system for distance measurement have been described. The accuracy of the system remains within the requirements (*i.e.* $\pm 2mm$, $\pm 0.5^{\circ}$). The system has been tested in several case studies throughout the life cycle of an aircraft, and has proved to be robust and reliable. The shape and location data provided by the system can be used in the registration of NDE data with the CAD model of the part, contributing to integrate NDE in the life cycle of the aircraft.

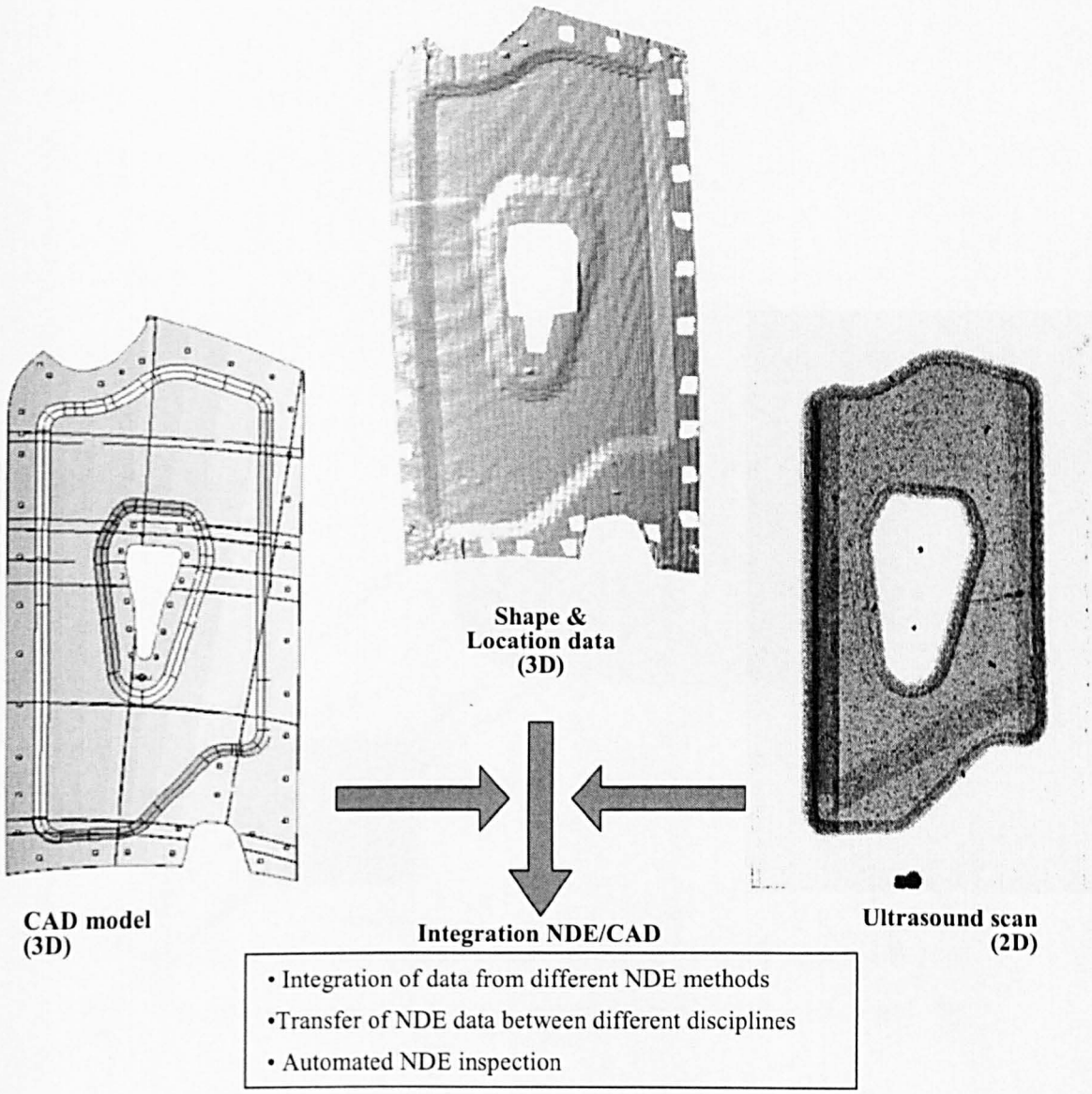

Figure 6.1: The integration of 2D maps obtained with NDE methods (e.g the ultrasound scan on the right) with the 3D CAD model of the part (left) requires information about the shape, location and orientation (top) of the test part with respect to the NDE device.

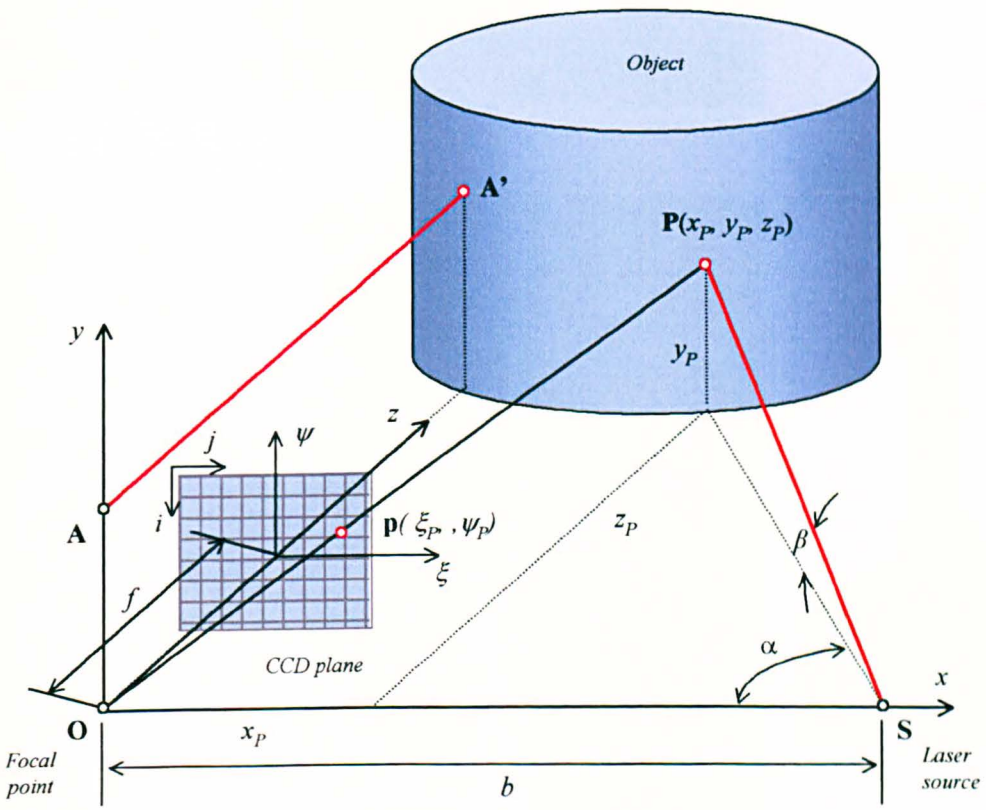

Figure 6.2: The light spot technique for distance measurement. The laser source is at **S**, and the point **P** on the object's surface is projected onto **p** in the CCD. **O** is the camera focal point.

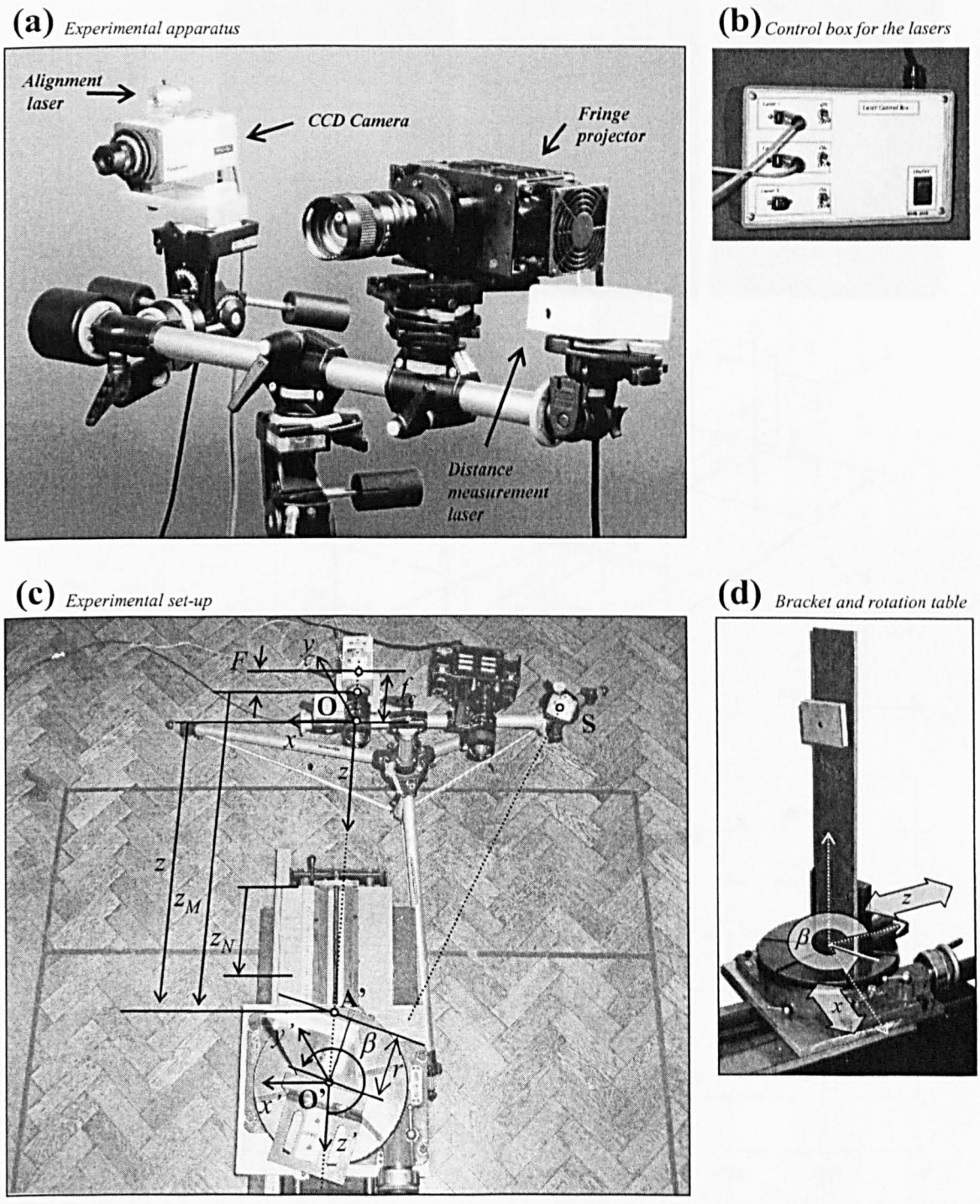

Figure 6.3: Experimental Apparatus. (a) The prototype instrument for fringe projection comprised a CCD camera, a projector and a laser source for the alignment routine. An auxiliary location system based in the laser triangulation technique was built into the system, with the addition of a second laser module for distance measurement. The second laser source sits on the tripod next to the projector. (b) Control box for the laser diodes. (c) Top view of the experimental set-up showing the instrument and the positioning apparatus. The lines on the floor represent the dimensions of the X-ray chamber of case study 1. (d) Detail of the rotation table and bracket.

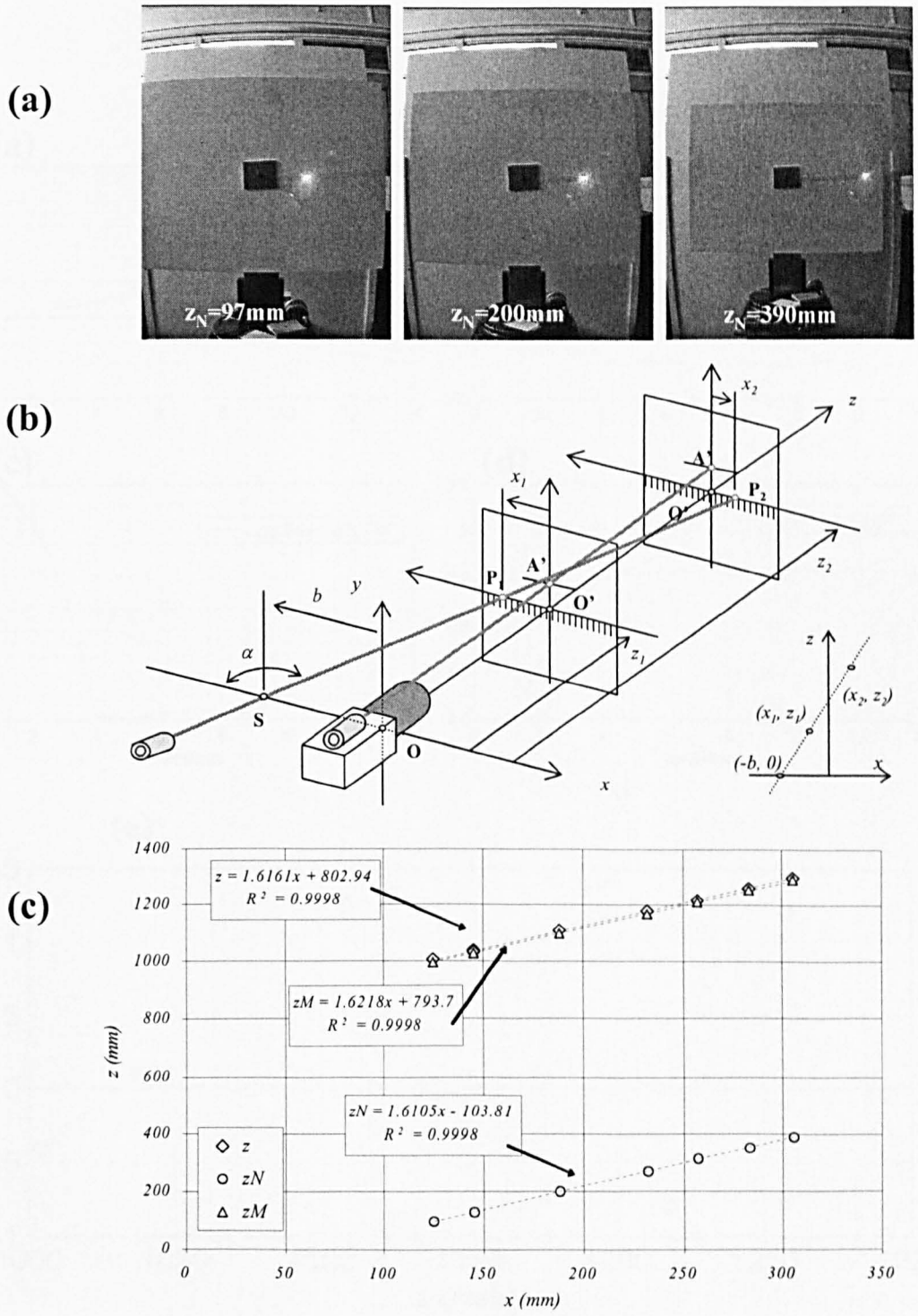

Figure 6.4: Calibration of the distance measurement system (a) Example of calibration images (b) Diagram of the calibration procedure. Two positions of the plate are represented, and the corresponding bright spots, respectively P_1 and P_2. (c) Plot of measured z_P versus x_P used to calculate the initial estimates for the configuration parameters b, α and f_c.

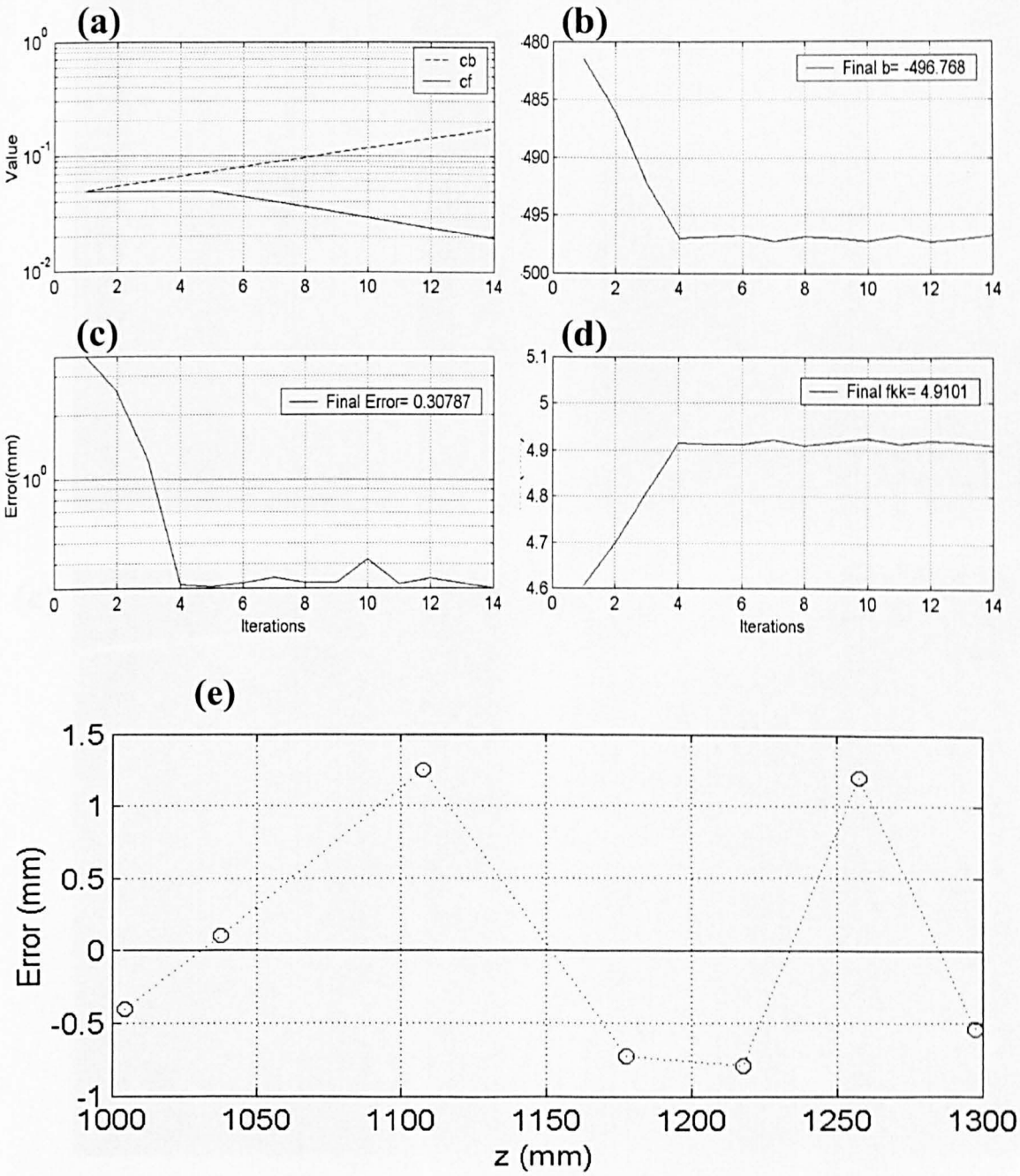

Figure 6.5: Iterative algorithm for the calculation of the calibration parameters of the distance measurement system. (a) Plot of the search coefficients c_b and c_f versus the iteration number. (b) Error function versus iteration number (c) b versus iteration number (d) f_c versus iteration number. (e) Error in z-coordinate calculated with the optimized parameters.

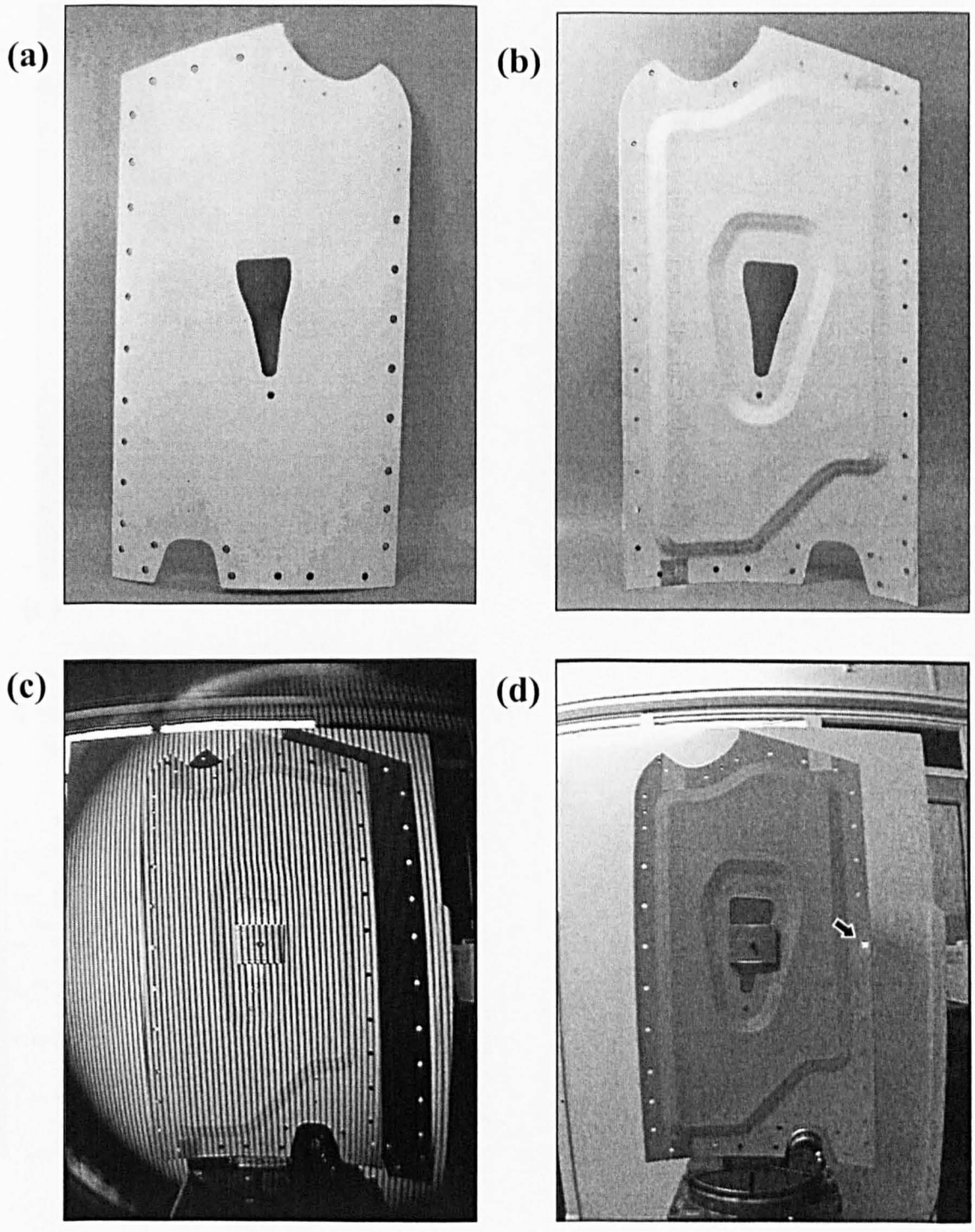

Figure 6.6: Specimen courtesy of BAe Systems. A composite panel from the EF-2000 aircraft was used to illustrate the applications of the shape and location measurement system. (a) Outer face of the panel. (b) Inner face of the panel. Typical input images: (c) object image of the fuselage panel, used for shape measurement; (d) light spot image of the same panel, used for location measurement.

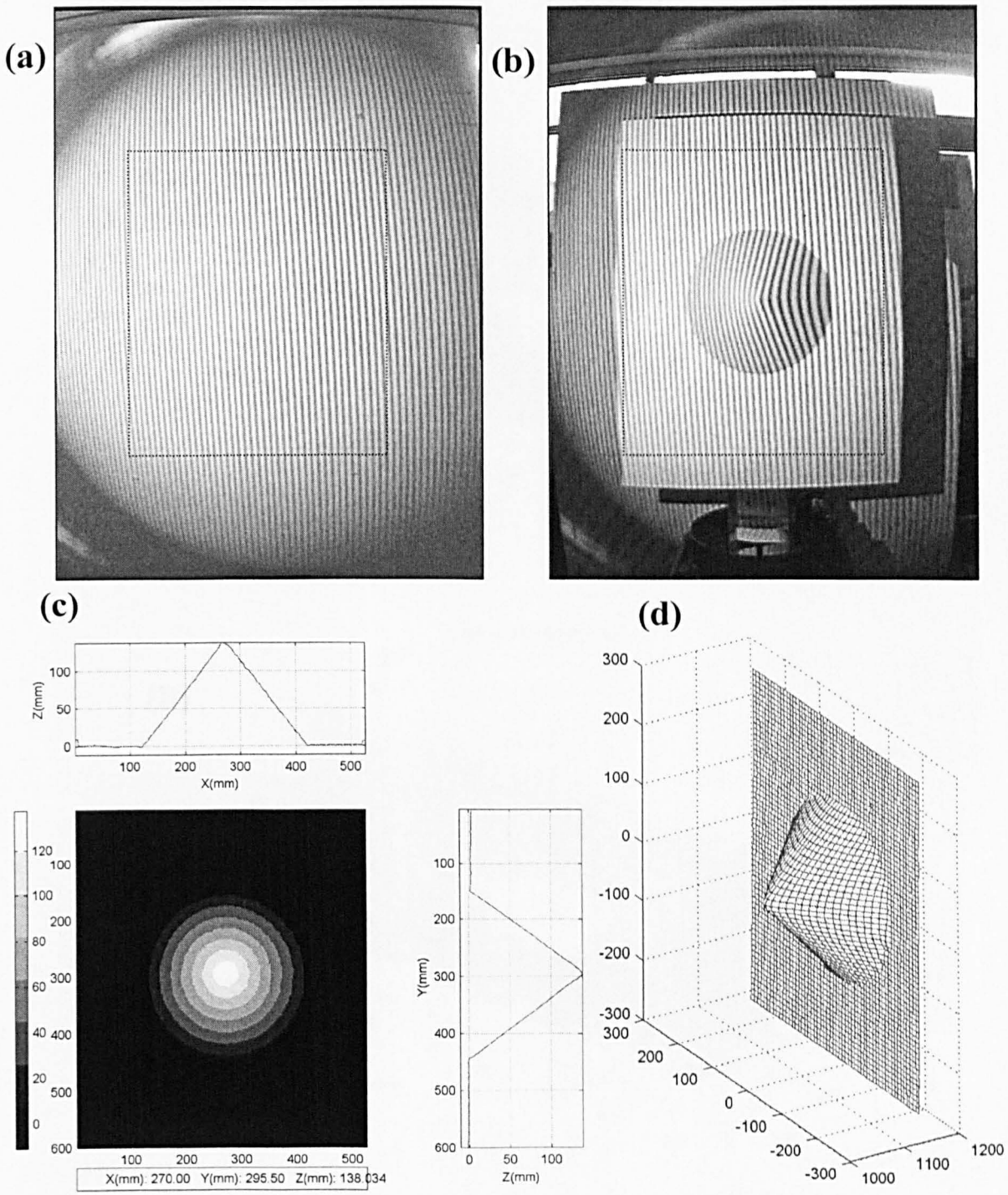

Figure 6.7: Calibration of the shape measurement system. (a) Reference image of a flat screen. (b) Image of a calibration cone of dimensions H=140mm D=150mm. The rectangular regions highlighted in the images (400×350 pixels from the centre of the images) were used as input data for the automatic calibration procedure. (c) Depth map obtained after unwrapping and calibrating the phase map. (d) 3D mesh representation of the surface of the calibration cone as measured by the system.

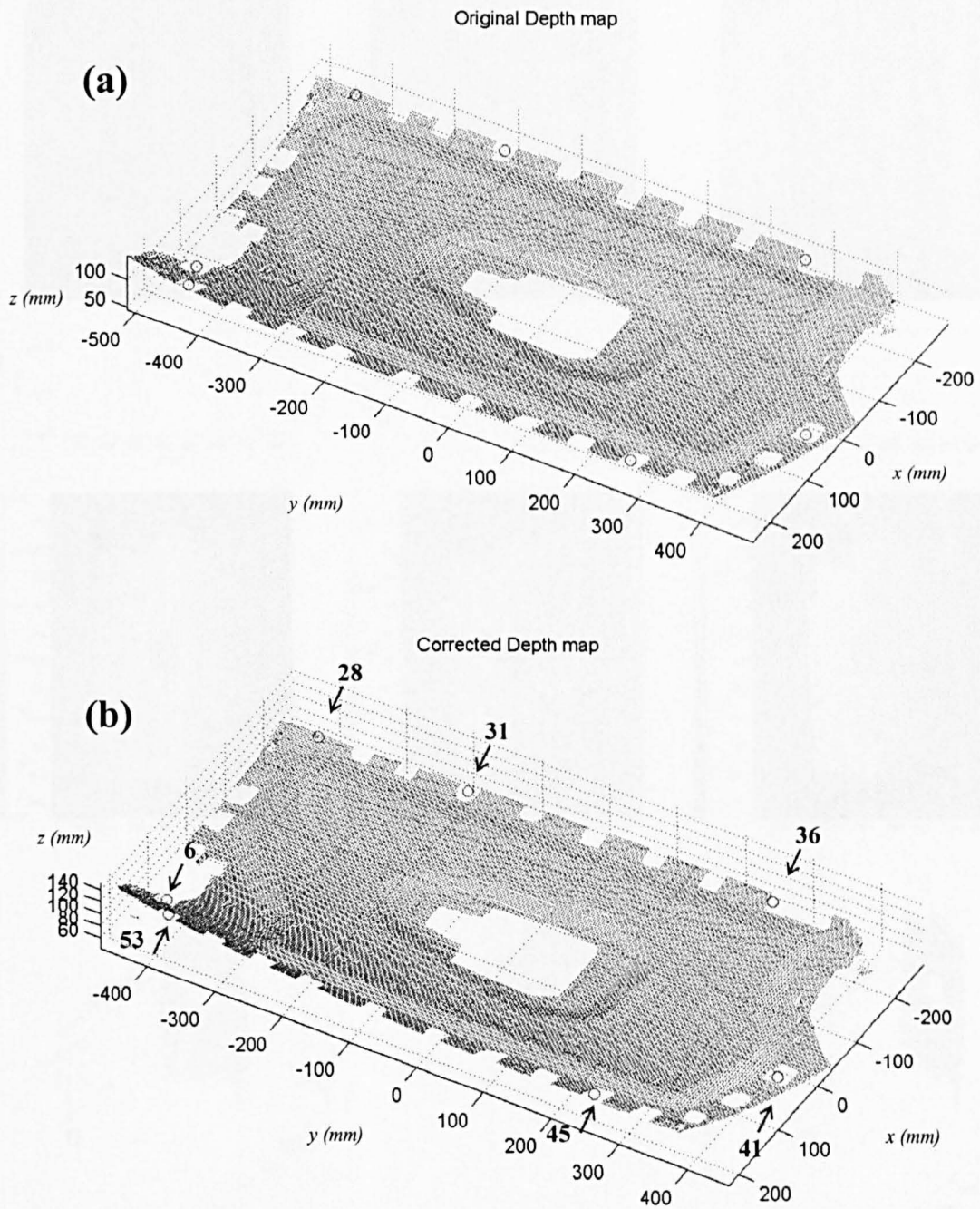

Figure 6.8: Correction of the depth map to account for the non-telecentric configuration of the system. (a) Depth map calculated with the telecentric assumption. (b) Depth map calculated with the first order $z=f(\Phi)$ expression and perspective correction. The circles in the image highlight the location of a set of seven control points used to align the measured depth map with a CAD model of the panel.

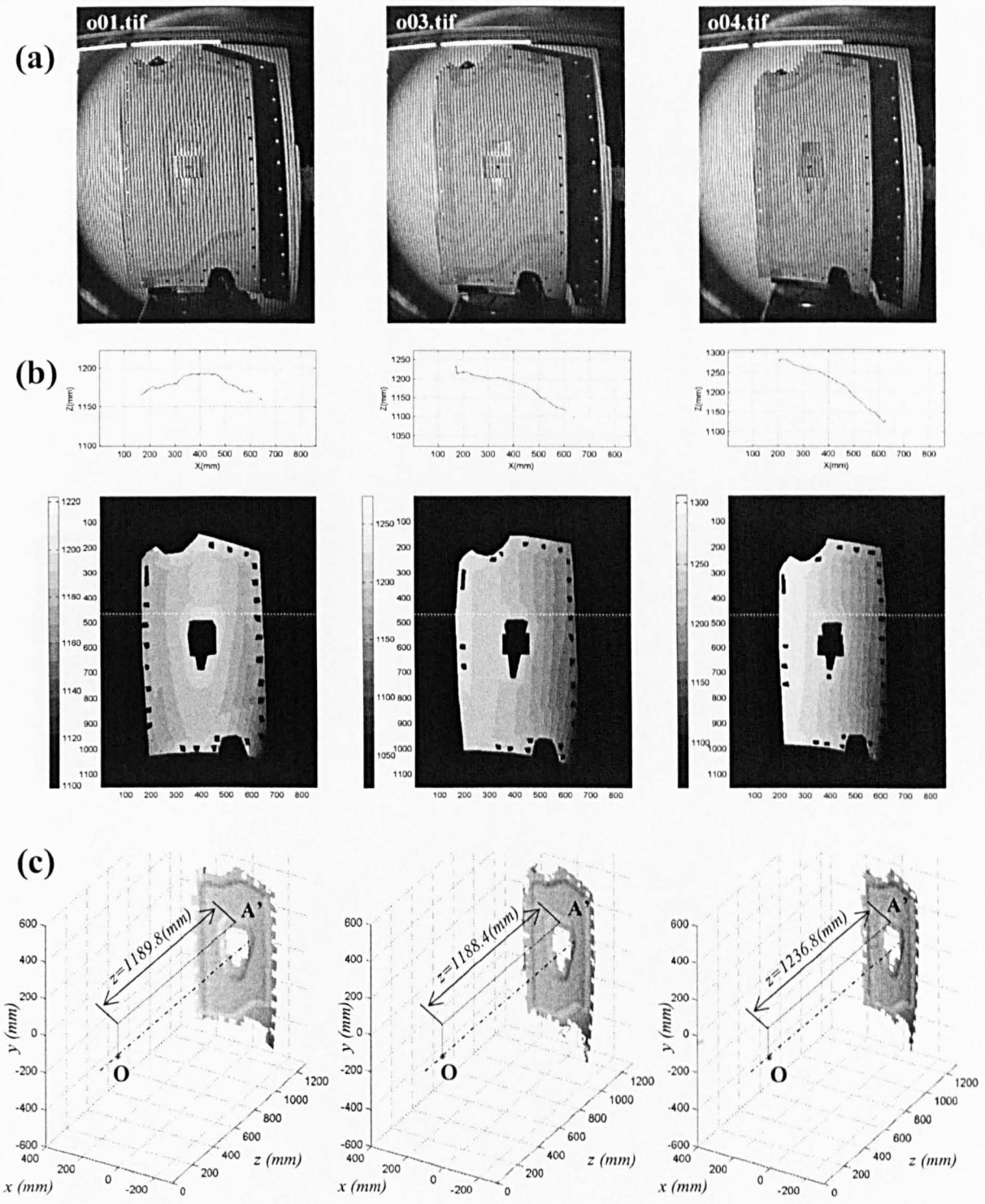

Figure 6.9: Measurement of shape and location of the aircraft fuselage panel. (a) Object images of the projected fringe patterns for three different positions of the panel. The images were combined with the reference shown in fig. 6.7(a). (b) Surface contours, obtained after unwrapping and calibrating the maps of modulated phase calculated from the images in (a). Distance measurements using light spot images such as the one in fig. 6.7(d) were used in each case to remove the *piston* term from the depth maps in (b). (c) Combined location and shape data, shown as shaded 3D surfaces. The origin of the coordinate axes is the optical centre of the camera.

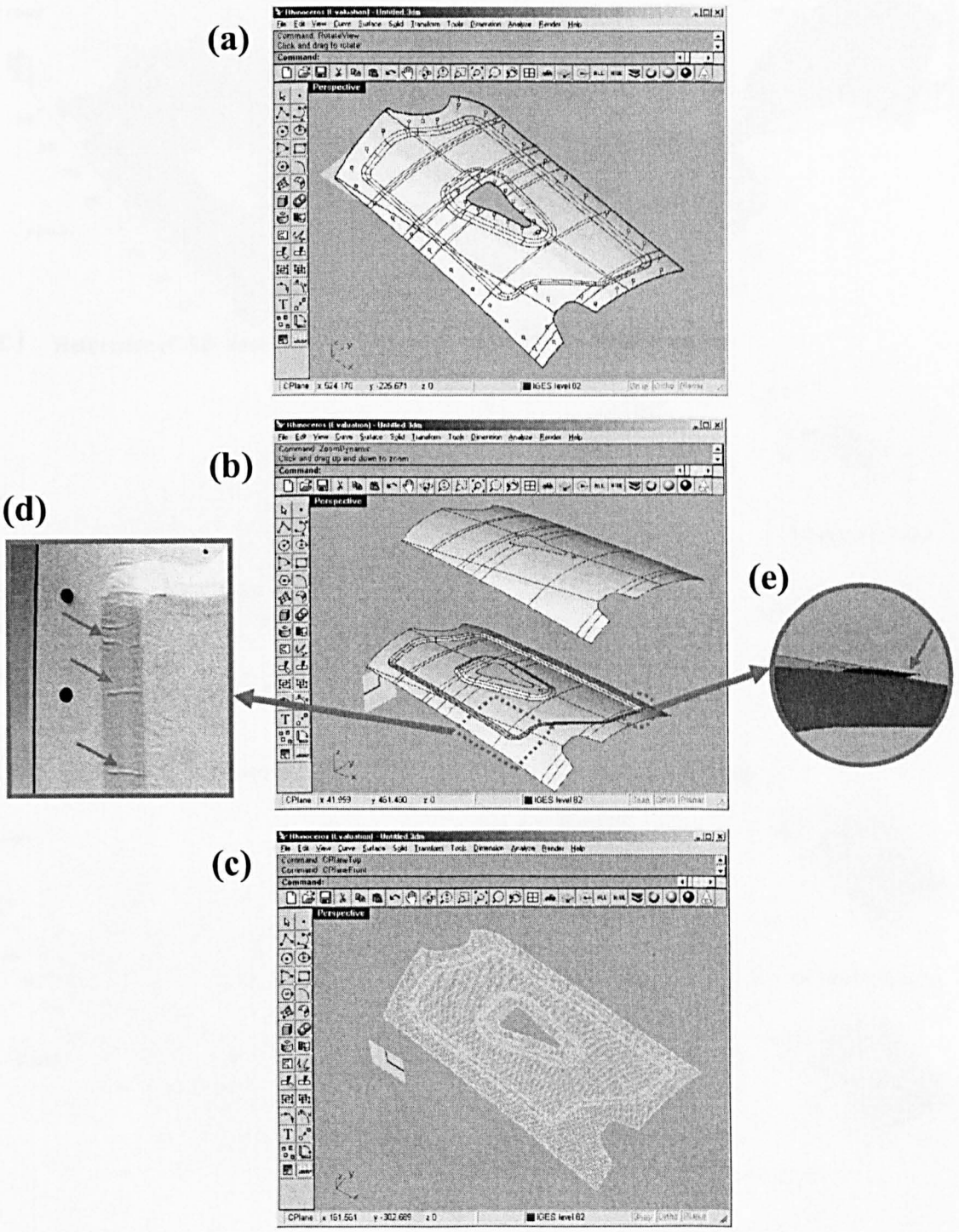

Figure 6.10: Generation of shape and location reference data from a CAD model. (a) A CAD model of the component (courtesy of BAe Systems). The model was imported in Rhinoceros for manipulation to (b) separate the bottom surface from the rest of the model, and (c) generate a fine surface mesh that can be imported into MATLAB. Note that the CAD model defines the nominal shape of the component, and tolerances for these composite panels are typically in the millimetre range. For instance, the detail (d) shows wrinkles of the carbon fibre cloth produced during manufacture, which are not present in the model. CAD models may as well contain inconsistencies such as the unmatching edge shown in the detail (e).

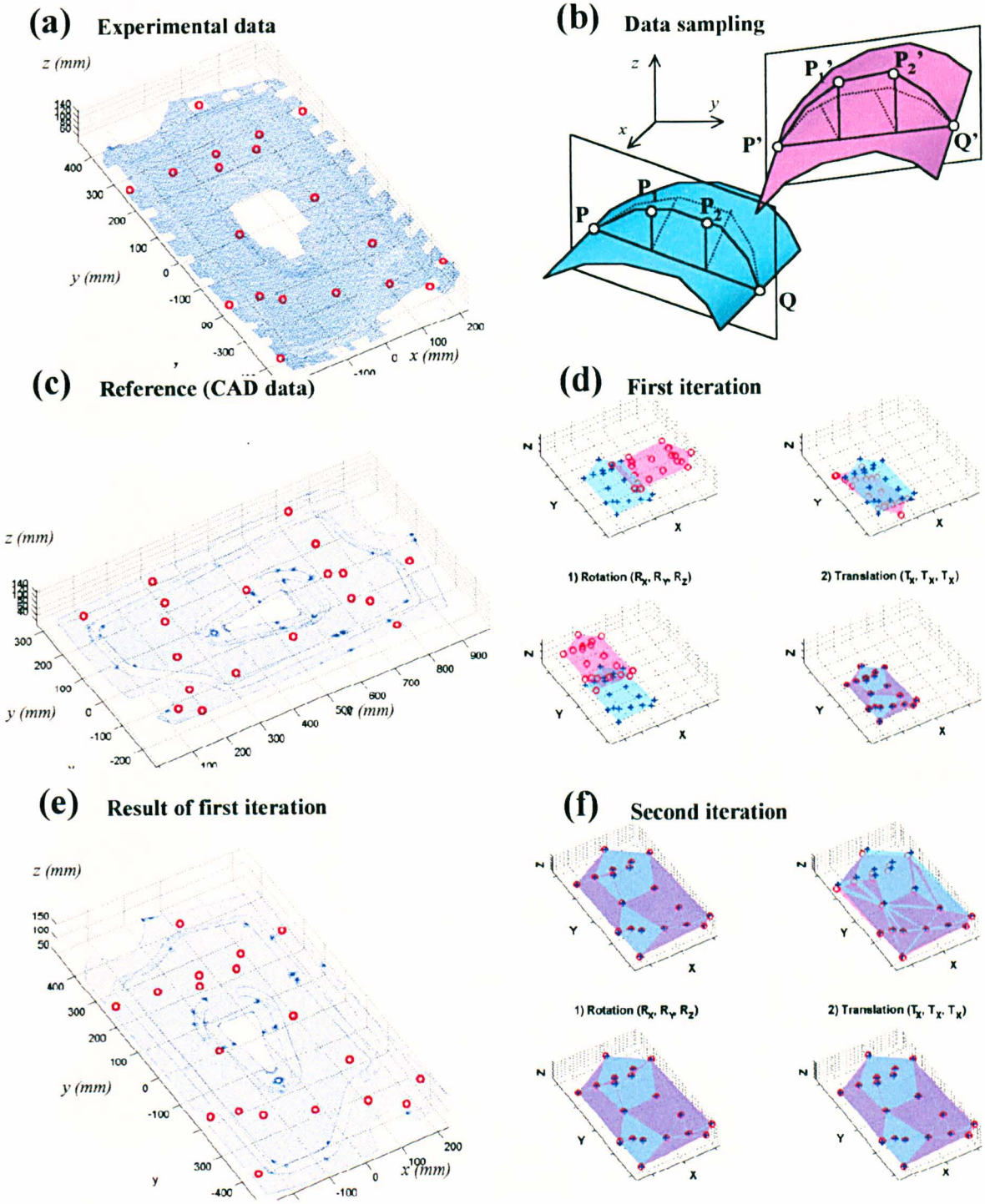

Figure 6.11: Alignment of experimental and CAD data. (a) Extended set of control points in the experimental data, obtained by (b) sectioning the surface with a vertical plane for each pair of control points P, Q and selecting N equispaced sampling points (P_1,…,P_N) along the intersection line. (c) Mesh generated from the CAD model, with the corresponding extended set of control points. (d) First iteration of the alignment algorithm, which performs an initial guess and then computes the value of the rigid body rotations and translations that optimise the match. The '+' represent the measured data and the circles the CAD data. (e) The CAD model rotated and translated after the first iteration. (f) Fine adjustments in the second iteration.

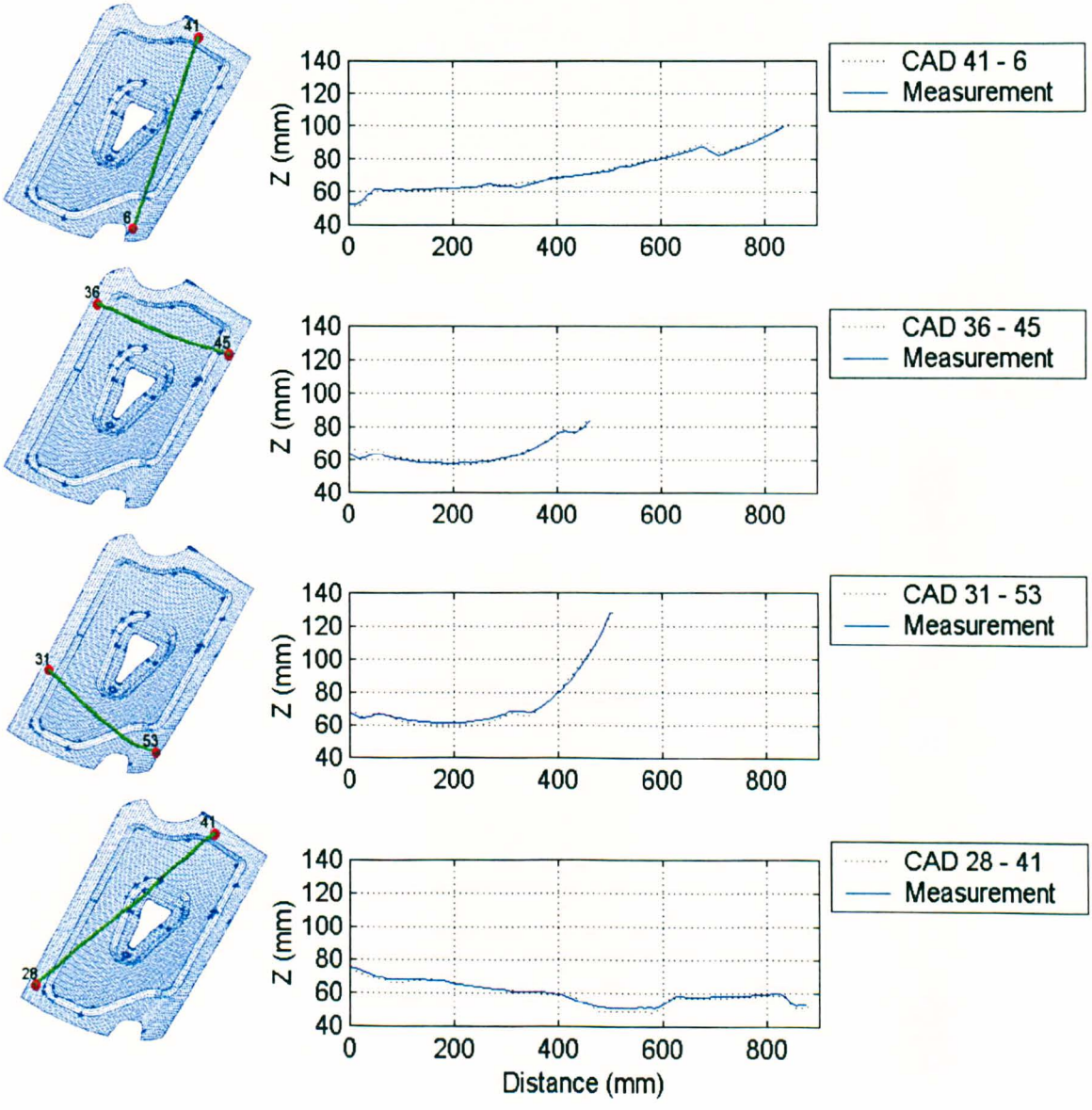

Figure 6.12: Comparison of measured shape vs. the CAD model along 4 lines on the surface of the component. The measured values are in good agreement with the nominal shape of the component defined by the CAD model. The maximum discrepancy was ±5mm, with typical values below ±2mm. These discrepancies can be attributed in part to deviations within tolerances of the real shape of the component with respect to the nominal shape defined by the model.

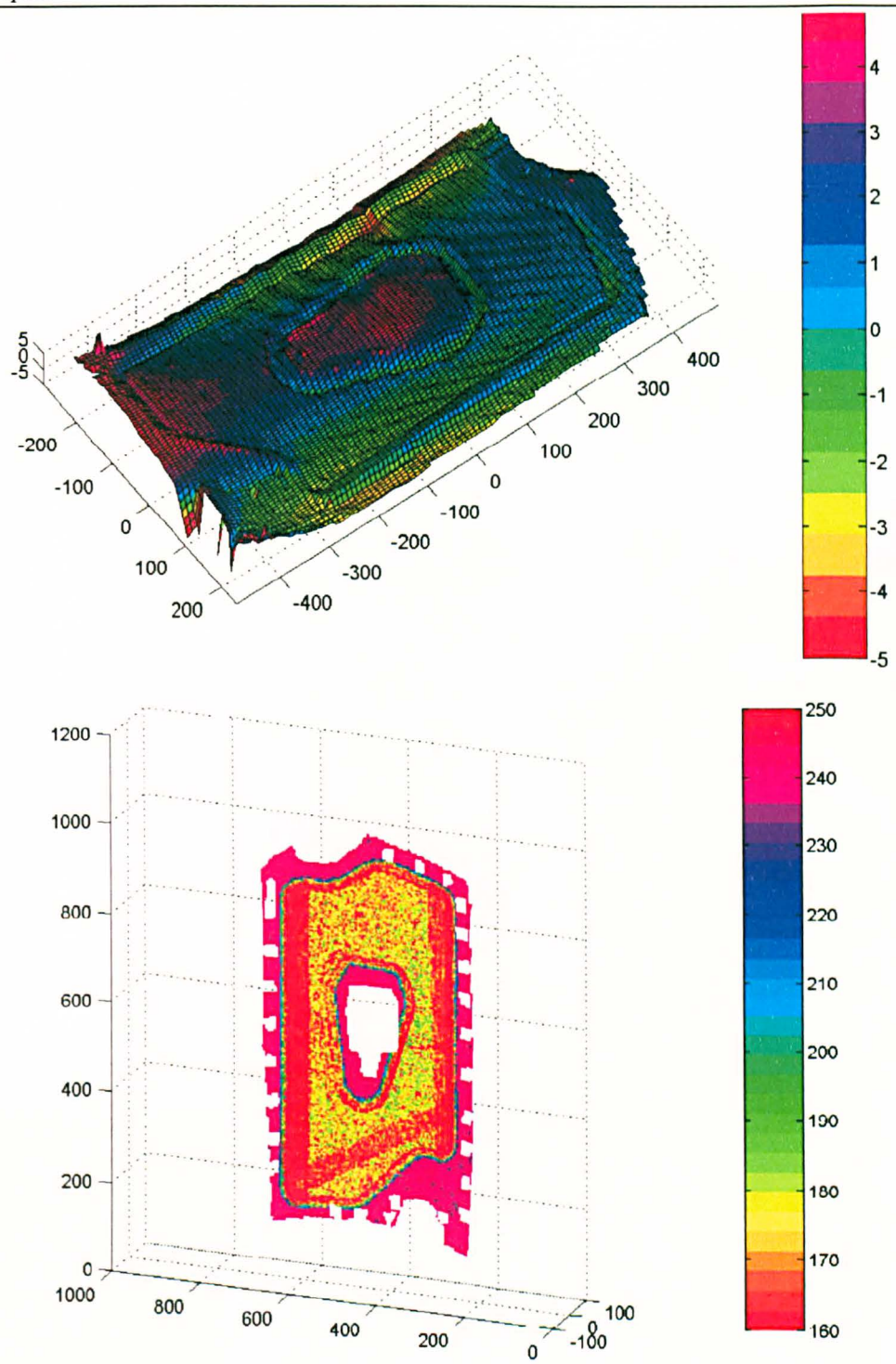

Figure 6.13: Applications (a) Difference map between the measured shape and the CAD model after the alignment. Discrepancies are below *2(mm)* in about 90% of the map. Note that large errors near the central hole and the bottom right corner are an artefact of the display routine, which extrapolates the data to generate a convex cloud of points. (b) Integration of NDT data and shape data. Units in the axes are millimetres. The colour scale represents the ultrasound signal, used for the detection of internal defects.

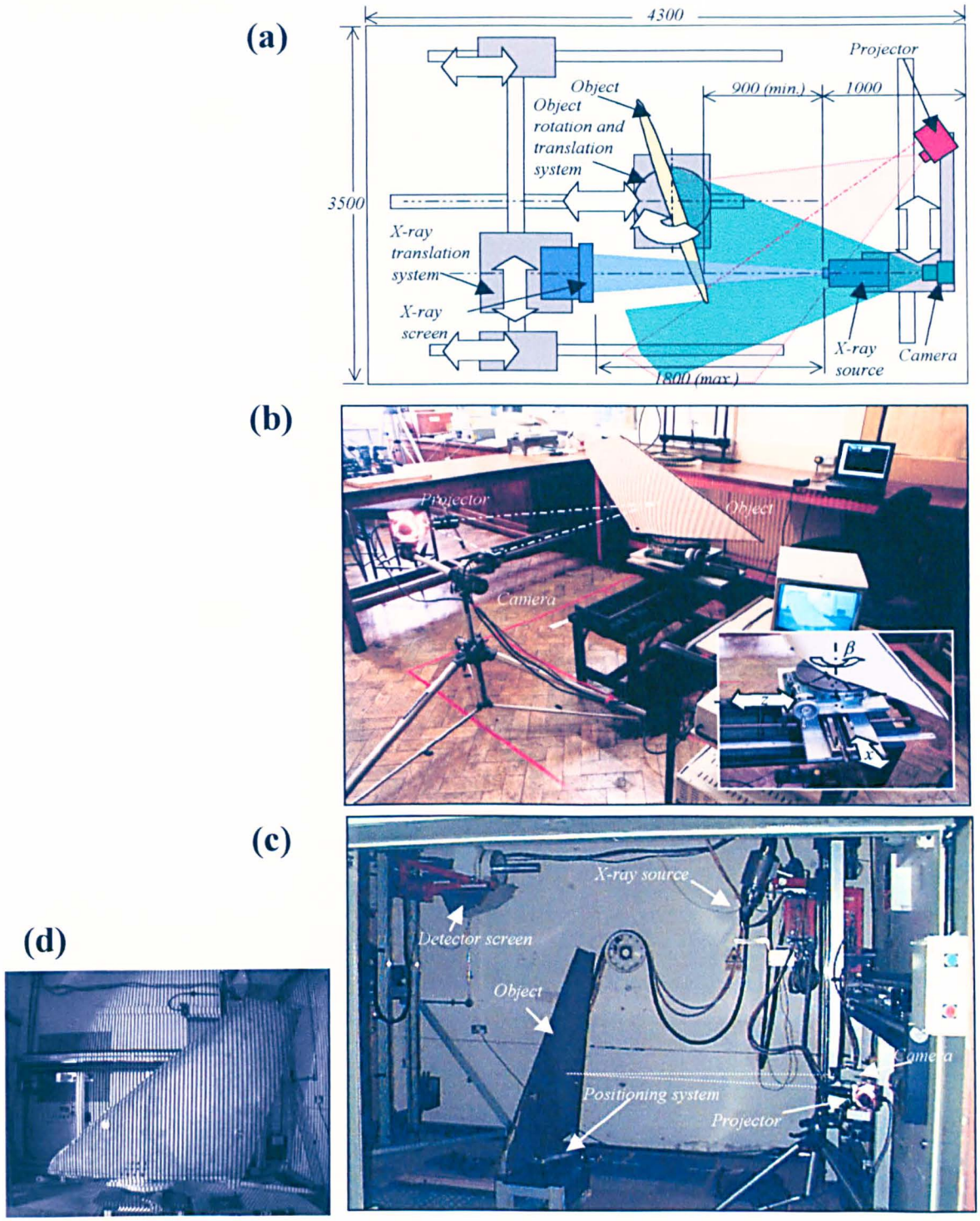

Figure 6.14: Case Study 1: (a) A plan view of the x-ray chamber with a schematic diagram of the inspection system. (b)1:2 scaled test rig of the moiré apparatus designed for installation in the X-ray chamber. This set-up was used to test the location system in the University of Sheffield. (c) Provisional installation of the system in the x-ray chamber in BAe Systems for testing. (d) Example image of the canard foreplane taken in the x-ray chamber.

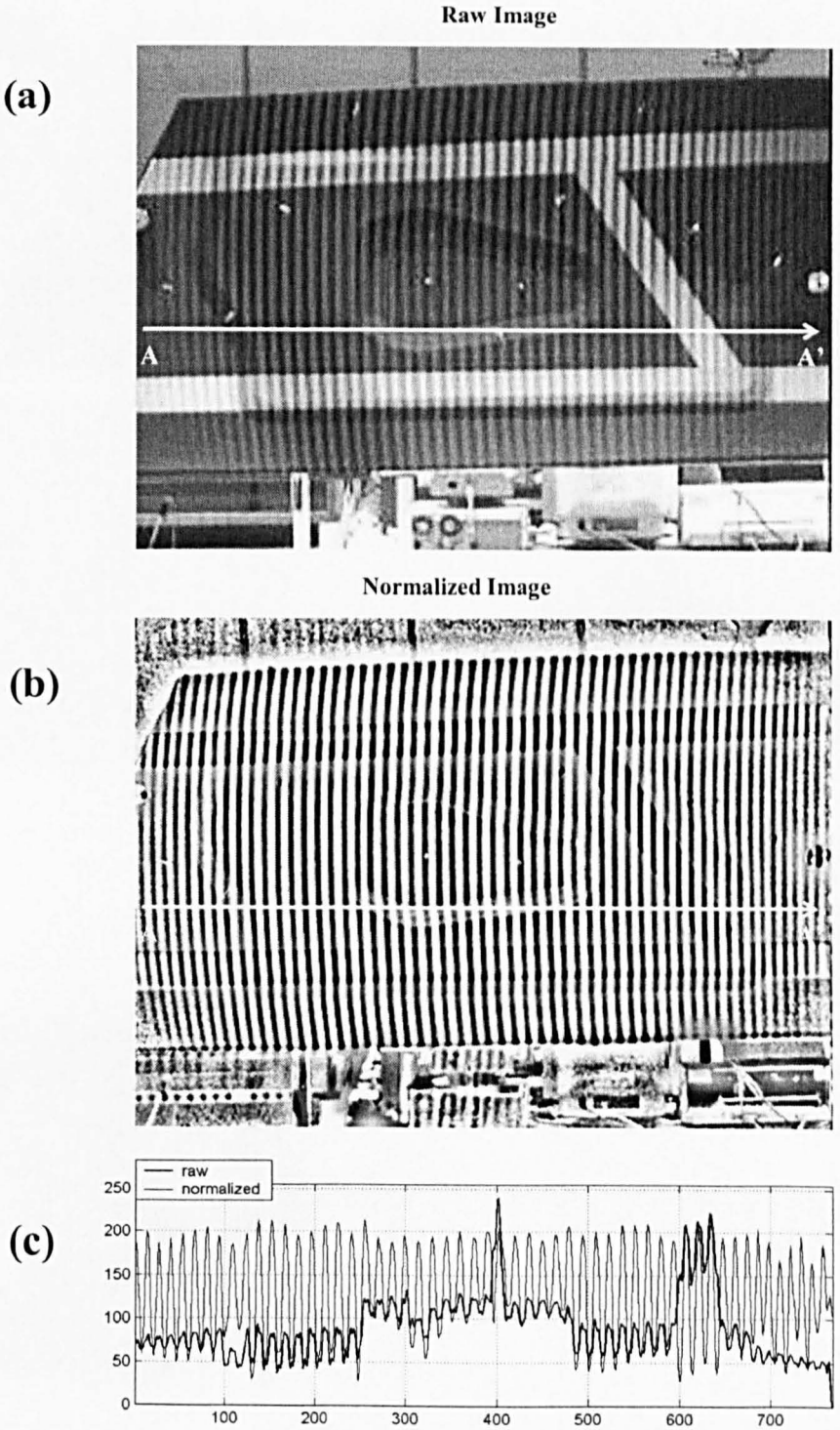

Figure 6.15: Case study 2: (a) Object image of a composite aircraft panel in the ultrasound inspection rig. (b) The normalization applied to the image enhances the fringe pattern so the technique can be used in less than ideal conditions. (c) The graph shows the intensity profile along the line AA' before and after normalization.

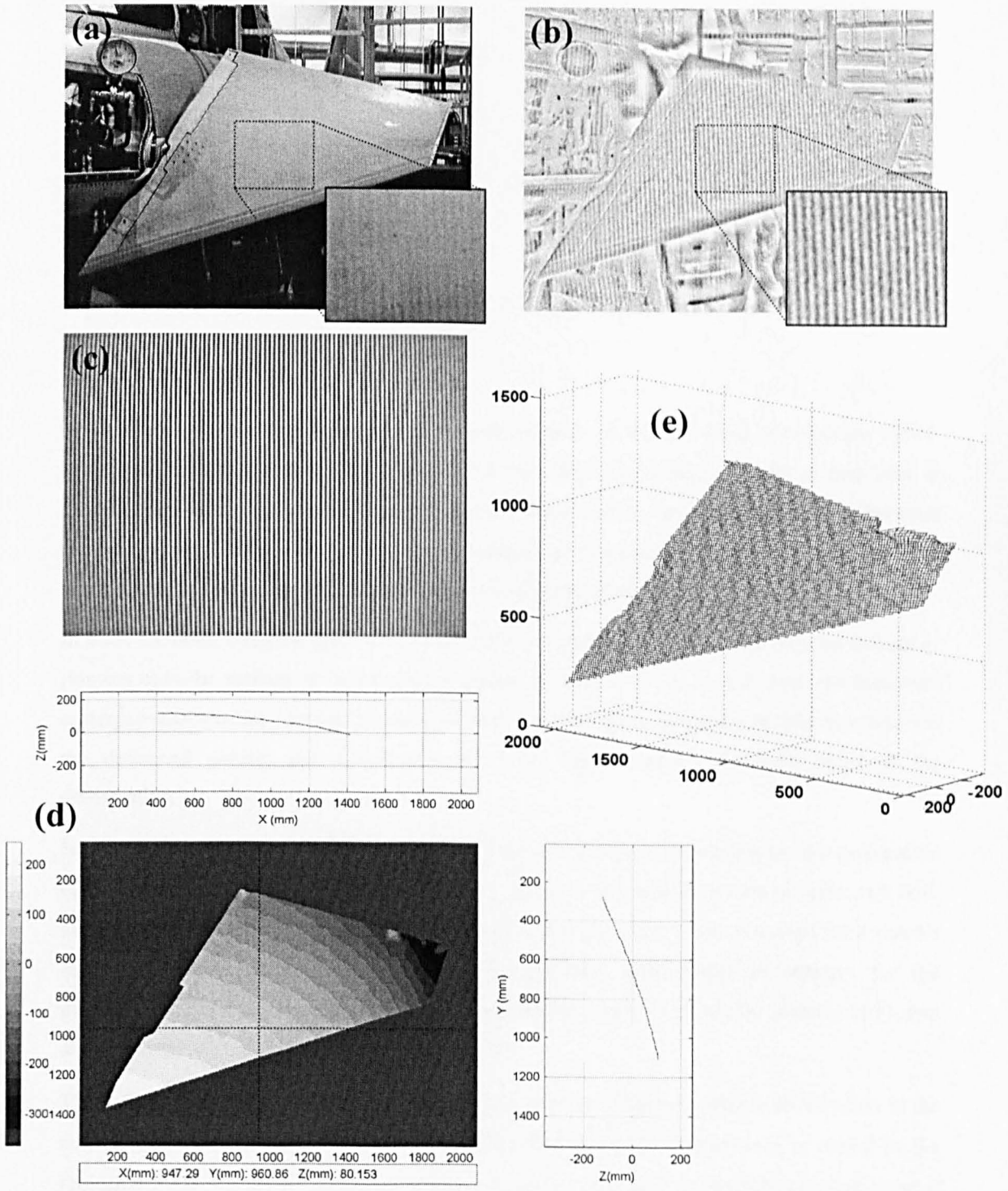

Figure 6.16: Case Study 3: Set of data collected in the hangar during maintenance of an aircraft. (a) Raw input image. The bright illumination caused very poor contrast in the fringes, and glare in the top right area of the canard. (b) Enhanced image using the normalization algorithm. The contrast improves significantly and the effect of the glare is reduced. (c) Reference image, collected in the lab with the same optical configuration. (d) Measured contour map of the surface and profiles along vertical and horizontal lines as indicated in the figure. Units are mm in the axes and on the grey level scale. (e) 3D representation of the surface. Units are millimwetres.

CHAPTER VII
THERMAL MOIRÉ

VII.1 Introduction

The previous chapters of this thesis have concentrated on the so-called out-of-plane moiré. However, conventional moiré techniques have also been extensively used for a long time in experimental stress analysis to evaluate in-plane deformations, as evidenced by the literature review presented in Chapter II. The main variants of in-plane moiré were briefly described there, along with a succinct presentation of the underlying theory.

In these methods, a regular grid or an array of dots is applied to the specimen (*e.g.* by etching or printing onto the surface, or by bonding a grating printed on film), so that when the specimen undergoes deformation, the grating deforms with it. Moiré methods use the interference between the deformed grating and a reference to obtain high-sensitivity full-field maps of the deformation.

Section II.6.1 pointed out two important limitations of existing technologies for the preparation of the specimen gratings in the fact that (i) they require a substantial amount of effort and skill, and (ii) they frequently cause permanent damage to the specimen. There is a need for a simpler and non-invasive method, which would have potential applications in industry for the monitoring of continuous processes (*e.g.* glass, plastics, paper, and textile manufacture), and also in biological sciences to perform *in vivo* tests.

The motivation of this research was to investigate the use of the temperature distribution in the surface of an object as a witness of mechanical deformation. Temperature is bound to the molecular structure of the body and therefore, at least in principle, it should be possible to use it as a marker. However, the actual value of temperature at a given point in the object does not remain constant during deformation because (i) there is a certain amount of heat generation due to the thermoelastic effect, and (ii) conduction heat transfer is continuously acting to reduce the temperature differences between neighbouring particles.

The author suggested overcoming these difficulties by generating a temperature distribution on the surface of the specimen that followed a repetitive pattern or motif, *e.g.* raising the

temperature of either a regular array of spots or a set of parallel bands. Such temperature pattern could then be observed and photographed using an infrared camera, and used as a substitute of the specimen grating of conventional moiré methods. This approach allows traditional fringe pattern analysis methods to be utilised on the thermal images. These methods analyse the frequency content to measure deformation, hence dealing effectively with variations in the absolute temperature, which is modelled by means of the background or modulation terms. To the knowledge of the author, this is the first time this approach has been used, and no previous work on the integrated use of thermographic techniques and moiré methods has been identified in the literature.

This chapter introduces therefore a novel experimental technique for strain measurement, based in a combination of thermography and moiré concepts. The hybrid technique has been named 'thermal moiré', and in essence it involves temporary imprinting a thermal grating onto the surface of an object either by physical contact with a hot stencil, or by patterned radiation from an infrared projector, to form the object grating. This thermal grating can be used as a substitute for conventional gratings, eliminating the need for physically printing, etching or bonding a grating to the specimen. In materials with low diffusivity, the thermal pattern can be observed with an infrared camera for a period of time. The analysis of the distortion that appears in the pattern upon loading of the component allows the measurement of deformation or rigid body motion of the object under study. The technique is sensitive to both in-plane and out-of-plane displacements.

The general method of thermal imprinting can be used to convert many experimental techniques that require surface preparation, such as conventional moiré and image correlation techniques, to a totally non-invasive method. The technique can also be used for flow and motion analysis. The permanence of the thermal pattern depends on the diffusivity of the constitutive material. In most organic materials these thermal patterns last for seconds up to a few minutes, after which there will be no residual evidence that the study was ever performed.

The technique offers significant advantages compared to other methods of experimental stress analysis, provides full-field data of the three components of displacement, and is truly non-invasive, requiring minimal or no surface preparation. This latter feature together with the possibility to operate with service loads provides the potential for non-contacting, non-invasive measurements, for in-service inspections in engineering and for analysis of living tissue in medicine and biology.

Section VII.3 provides a brief background on infrared thermography. Section VII.4 summarises the results of the fundamental studies performed during the initial stage of the research. Section VII.5 describes the laboratory apparatus developed for the generation of thermal patterns and

the experimental procedure. Section VII.6 discusses the processing algorithms that allow obtaining quantitative measurements from the thermal patterns, and which development constituted the third stage of the research project. Some experimental results obtained in the final validation stage are presented in section VII.7 to illustrate the feasibility of the method on a selection of exemplars. Finally, section VII.8 summarises the discussion of the results and presents the conclusions of the research project.

This research was funded by the Engineering and Physical Sciences Research Council (Grant no. GR/R71542/01 'Fundamental study on thermal moiré').

VII.2 Aims

The aim of this research project was to propose and develop a novel experimental technique for strain measurement. The technique relies on generating a thermal fringe pattern on the surface of the sample, which may be observed using infrared imaging equipment. The distortion that appears in the pattern upon loading of the component can be related to the surface deformation using similar principles to those of conventional techniques such as moiré and fringe projection.

This aim was reformulated into four specific objectives:

(i) To develop a theoretical basis for this technique, and hence determine the range of conditions for which the technique is applicable. This involved gaining an understanding of the heat transfer mechanisms and exploring the practical issues related to the application of the proposed technique.

(ii) To implement prototype systems for the laboratory demonstration of the technique, including experimental apparatus and methodology of use.

(iii) To design and implement dedicated algorithms for data processing.

(iv) To validate the technique by comparison with analytical solutions, FE modelling, and experiments in a range of exemplars.

The research programme was structured in four stages to address these four objectives: (i) a fundamental study, (ii) the design and construction of apparatus, (iii) the development of processing algorithms, and (iv) a validation of the technique.

VII.3 Background In Thermal Techniques

Any material body emits electromagnetic radiation with a wavelength distribution characteristic of its absolute temperature and surface emissivity. The Stephan-Boltzmann law states that the emissive power is proportional to T^4 and therefore it constitutes a very sensitive indicator of temperature. For a wide range of body temperatures, between 30 and 1300*(K)*, most of the

radiation emitted falls in the infrared region of the electromagnetic spectrum (1-100μm) (Wright, 1973).

Infrared sensors are devices that measure the amount of radiant energy emitted across some frequency band. Atmospheric absorption of infrared radiation restricts the useful bandwidth to a few discrete windows where its transmittance is high, typically 3-5(μm) and 8-14(μm).

There are two basic types of infrared sensors (i) thermal detectors and (ii) photon detectors (Hudson and Hudson, 1975). Thermal detectors respond to incident radiation by changing their temperature, which in turn produces a change in some electrical characteristic. Resistive bolometers and pyroelectric detectors fall into this category. In contrast, electronic photodetectors are made from a semiconductor material (*e.g.* In/Sb, Hg/Cd/Te) in which carriers may be excited from valence to conduction band by incident radiation. These electronic devices achieve better sensitivity and higher response speed than thermal detectors but, on the other hand, need to be refrigerated to very low temperatures (typically 77K), because the band gap is so small that thermal excitation of carriers may obscure the true signal. Typical sensitivities of modern infrared systems are in the range of 100(mK) for an uncooled microbolometer and 20(mK) for a high quality Ga/As QWIP electronic sensor. Traditionally, thermal cameras used a single scanning detector, but modern systems are more commonly based in focal plane array technology.

Infrared thermography is a quick and versatile technique that allows remote full-field temperature measurements, providing intuitive thermal images that are easy to interpret. Furthermore, infrared radiation is not hazardous and, as a result, the range of applications is very wide. This is a very active field, with a few regular international conferences including the annual SPIE Thermosense conferences in USA (www.thermosense.org), and the QIRT international conferences in Europe (www.gel.ulaval.ca/qirt/). A comprehensive resource on infrared technology and applications is the handbook by Maldague and Moore (2001).

Infrared thermography can be used in medical diagnosis of a number of conditions, such as breast cancer, circulatory disorders or burnt skin (Barnes, 1968). Friction and electricity generate heat, and so thermography can be used in research and development applications to improve the design of mechanical and electrical systems (*e.g.* electronic circuits, bearings). Thermography is also used in preventive maintenance to detect impending failure of mechanical components, overloads and bad connections in power transmission lines, or leaks in pipes and furnaces, to name a few. There are also applications in quality and process control, monitoring equipment or continuous production processes that require remote temperature measurement *e.g.* paper, fabric, metal.

Thermography has also been extensively used in non-destructive testing of components (Maldague, 2001). A temperature gradient is induced in the component, by either heating or cooling using an external source, and the heat diffusion is witnessed using infrared thermal imaging. Propagation of heat depends on the density, heat capacity and thermal conductivity of the material, which allows the detection of material inhomogeneities and defects that disturb the uniformity of heat propagation such as de-bonding, de-lamination, or cracks. A number of techniques have been developed, including: pulse thermography (*e.g.* Cielo, 1984), which uses a pulse of energy; modulated or lock-in thermography (*e.g.* Busse *et al.* 1992), which uses a slowly varying sinusoidal temperature variation; and pulse phase thermography (*e.g.* Maldague and Marinetti, 1996), which combines concepts from the two of them.

It has been recently proposed that inducing an in-plane heat flow improves the detectability of certain types of flaws (Cramer and Winfree, 1992). Forced diffusion thermography (Lesniak and Boyce, 1993) makes use of patterned radiation to force heat flow in-plane for crack detection, and coating tolerant thermography (Lesniak *et al.* 1996) is a variation based on the same principle that allows the separation of the effects of structural defects from variations in surface emissivity.

It is also possible to perform stress pattern analysis by thermal emission using thermoelastic stress analysis (TSA). When a solid body is subjected to a tensile stress, a small decrease in temperature occurs. Conversely, a solid body subjected to compression will slightly increase its temperature. These changes in temperature, which constitute the so-called thermoelastic effect, are typically too small to be of much use. However, when the body is in a cyclic loading regime, for instance during repeated loading or vibration, the input signal of the load can be used to filter the measurements of a sensitive infrared detector and isolate the small cyclic change in surface temperature of the body due to the load. In the elastic regime, this temperature change is directly proportional to the change in the sum of principal stresses on the component surface. A thin layer of matt black paint is typically applied to the surface of the sample to ensure uniform emissivity at the infrared wavelengths used by the detector.

The review paper by Dulieu-Barton (1999) constitutes an easy introduction to the subject of TSA, and the book by Hardwood and Cummings (1991) is a good reference text. Also, the website www.experimentalstress.com contains a comprehensive online literature review on the topic (www.shef.ac.uk/mecheng/mechsol/exptmech/topics/bibthermo.html).

Two important limitations of this technique are (i) the need for cyclic loading of the specimen and (ii) the fact that it only allows the measurement of the sum of principal stresses and not the principal stress vectors.

Some attempts have also been made at correcting for shape effects in pulse thermography, using the *shape from shading* theory from machine vision in thermal images (Pelletier and Maldague, 1997).

No work on the integrated use of thermographic techniques and moiré methods has been identified in the literature. The technology for pattern radiation described by Lesniak and Boyce allows the generation of a thermal fringe pattern on the surface of an object, albeit a very coarse one (typically, three hot stripes several centimetres wide across the whole object). Their work was taken a stage further in this research to create a sufficiently fine thermal pattern and analyse the resulting thermal images by applying concepts from conventional fringe pattern analysis. This represents a novel combined application of thermography and moiré concepts.

VII.4 Fundamental Study

The first part of the work was a fundamental study of the heat transfer mechanisms involved in thermal marking, in order to identify the parameters that control the permanence of the pattern, and the attainable sensitivity. The aim for this study was to determine the range of conditions for which the technique is applicable, and to obtain the key relationships between critical parameters. Typical values for the heat transfer parameters (*e.g.* convection coefficients, contact resistance, and efficiencies) were estimated for a range of configurations with simplified analytical models and validated with basic experiments.

Belgen (1968) derived some analytical models of the permanence of thermal patterns as a function of non-dimensional parameters. His work was carried out in the context of thermoelastic stress analysis, and provided some simple one-dimensional formulae.

In contrast, the approach followed in this research consisted of a combination of simple experimental tests and finite element simulations. The main output of this first stage was the construction and experimental validation of a parametric finite element model of the heat transfer mechanisms involved in the generation of thermal patterns. This tool allowed the prediction of the duration of a thermal pattern on a given specimen as a function of material properties (*e.g.* thermal diffusivity) and geometry of the specimen (*e.g.* thickness), pitch of the thermal grating, energy delivered by the marking device (in terms of the heat flux, irradiation or contact time, efficiency, etc.) and ambient conditions (*e.g.* ambient temperature, convection coefficient, etc.). This section describes the construction of the model and discusses the modelling hypotheses.

Figure 7.1 shows a schematic of the experimental setups used for the two prototype devices for thermal marking, both of which will be described in more detail in section VII.5.

The instrument shown in fig. 7.1(a) is designed to heat up a regular array of spots on the surface of the specimen by contact. A resistive heater controlled by a dimmer switch heats up an array of metal pins. The pins are pressed against the surface of the specimen, so that conductive heat transfer through the contact produces the desired temperature distribution on the surface of the sample.

Figure 7.1(b) shows the experimental setup used for the projector prototype. The energy radiated from a heat source is collected by an ellipsoidal mirror and directed through a grating with a regular array of holes, and towards a set of projecting optics. The resulting pattern contains a regular array of bright spots, which are projected onto the surface of the object of interest. The instrument is designed to let through as much radiation as possible, in a wide range of wavelengths of light from the visible to the infrared spectrum, and project it onto the surface of the object.

The two methods described above enable the generation of a similar temperature profile on the surface of the sample, which can be observed with the help of an infrared thermal imager. The thermal pattern has been enlarged for clarity of display in the figures, but it is typically very fine compared with the dimensions of the test part, which was assumed to be an infinite plate of uniform thickness for modelling purposes. This allows a simplification of the problem, by noting that the geometry and the thermal loads repeat themselves along the horizontal and vertical directions, and it is therefore possible to apply symmetry conditions, reducing the model to the small cube shown in fig. 7.2(a). We can further simplify this model by noting that it presents symmetry also with respect to the diagonal AB, as shown in fig. 7.2(a), and therefore the smallest repeatable section is the prism ABC. Symmetry boundary conditions are imposed in thermal problems by making the boundaries adiabatic (*i.e.* perfectly insulated).

VII.4.1 Loads

In order to evaluate the permanence of the pattern it was necessary to conduct a transient thermal simulation. Transient problems require boundary conditions to be specified in time (*i.e.* initial conditions) as well as in space (*e.g.* symmetry planes) to be completely defined.

The thermal loads in the problem under consideration are:

(i) A thermal load from the external source, be it the contact device or the infrared projector. This load was modelled in both cases as a constant and uniform heat flux $q(W/m^2)$.

(ii) The natural convection acting on the two exposed faces of the specimen.

VII.4.1.1 Initial And Boundary Conditions

The test part was assumed to be in equilibrium with the ambient at the beginning of the test. Hence the air in the room and the sample were initially assumed at a uniform temperature T_0. Symmetry boundary conditions (heat flux q=0) were applied to the sides of the prismatic volume, *i.e.* faces AB, BC and CA in fig. 7.2(a).

VII.4.1.2 External Load By Contact

On a scale of microns, solids are not in perfect contact. Parallel heat flow occurs across contact points and air gaps, and the result is a discontinuity in temperature across the contact. Conductive heat transfer through the contact between the pins and the specimen surface can be modelled with a contact resistance R_c. The heat flux Q through the contact will depend on the temperature difference ΔT between the pins and the sample.

$$\Delta T = QR_c \tag{7.1}$$

The contact resistance R_c is affected by several factors including pressure, material ductility, surface finish and the environment. An increase in the pressure increases the contact area and therefore lowers the thermal resistance of the contact. It is also possible to reduce contact resistance by using thermal greases with high conductivity to fill the air gaps between the contact surfaces.

The heat flux $q(W/m^2)$ across the contact was assumed uniform in space and constant in time. The value was calculated from the effective contact area in the specimen A_s (*i.e.* the section of one pin πr^2 times the number of pins n) the energy consumption of the heater $Q_0(W)$ and an efficiency coefficient e, which takes into account all the losses in the device.

$$q = \frac{eQ_0}{A_s} \tag{7.2}$$

The diagram in fig. 7.1(c) illustrates the heat transfer mechanisms inside the contact device. The electrical analogy was used to find an expression for the efficiency of the device in terms of the thermal resistance of the different elements of the device. The analysis of resulting circuit, shown on the right of the figure, is relatively trivial and yields:

$$Q = \frac{1}{1 + \frac{R_s}{R_{cd1}} + \frac{R_s}{R_2} + \frac{R_s}{R_v}} Q_0 = eQ_0 \tag{7.3}$$

where R_{cd1} is the thermal resistance of the insulating block, R_2=R_{pin}+R_{cd2} models conductive losses, R_v=R_{pin}+R_{conv}, models convective losses, and R_s=R_{pin}+R_c+R_{sample} is the thermal

resistance of the specimen. In practice however, the value of the coefficient e was estimated empirically.

VII.4.1.3 External Load By Radiation

The amount of energy delivered by the infrared projector is virtually independent from the temperature of the specimen because the heat source is at much higher temperature than the specimen. The value of the heat flux q was estimated in eq. (7.2) using the wattage of the halogen-tungsten lamp as the heat source output Q_0, the area irradiated on the specimen A_s, and a coefficient of efficiency of the projection system e.

As shown in fig. 7.1(d), the heat source radiates in all directions, but only a fraction of the energy emitted is actually directed towards the grating after being reflected in the condenser mirror. The efficiency of the condenser e_c can be estimated geometrically, by calculating the ratio of solid angle $\xi(srad)$ covered by the mirror, *i.e.* $e_c=\xi/4\pi$. This estimate assumes a uniform point source and a perfect reflective surface. The analytical calculation of e_c yielded a value of *ca.* 60%.

This value of e_c can be lower in reality due to the finite size of the lamp filament. In addition, the efficiency of the mirror's reflective coating, characterised by the reflectance coefficent r_r, must also be considered.

Regarding the grating, the void ratio v_g is the fraction of the grating surface that actually lets the radiation through (*i.e.* the area of the holes / total area of the grating). The energy delivered to the surface of the specimen was further reduced due to losses in the projection system, such as reflection and absorption in the lenses, the cement of achromatic doublets etc, which were modelled with a coefficient of efficiency in the projection system e_p.

Combining the effects described above allowed obtaining an estimate for the efficiency of the projection device e:

$$Q = e_p v_g r_r e_c Q_0 = e Q_0 \tag{7.4}$$

The irradiated area A_s is proportional to the square of the magnification m of the projection system. The magnification can be conveniently written as the ratio between the pitch of the master p_g and the pitch of the projected grating p.

$$A_s = m^2 v_g A_g = \frac{v_g A_g}{p_g^2} p^2 \tag{7.5}$$

Finally, the incident heat flux q can be written as follows:

$$q = \frac{1}{p^2}\frac{e_p r_r e_c p_g^2}{A_g} Q_0 \tag{7.6}$$

VII.4.1.4 Convection

The average film coefficient was estimated using the following simplified equation for free convection from a vertical plane to air at atmospheric pressure (Holman, 1997).

$$h = 1.42\left(\frac{\Delta T}{L}\right)^{0.25} \tag{7.7}$$

where $\Delta T = T_{surface} - T_{air}$, and L is the length of the vertical plate. A multiple of the projected grating pitch p was considered in this application $L=20p$. The above equation is valid for values of the Rayleigh number Ra between 10^4 and 10^9. The Ra number has the following expression:

$$Ra = \frac{\Delta T g L^3}{\nu \alpha T_{air}} \tag{7.8}$$

in which the properties of air should be evaluated at the film temperature

$$T_f = \frac{T_{air} + T_{surface}}{2} \tag{7.9}$$

Since large temperature variations were not expected in the application under study, Ra was estimated using the following properties of air at $300(K)$ (Holman, 1997): $\nu = 1.569 \cdot 10^{-5} (m^2/s)$, and $\alpha = 2.216 \cdot 10^{-5} (m^2/s)$. Substituting the above values and considering the worst-case situation for ΔT and T_{air} proved that eq. (7.7) was valid in the range $2(mm) < p < 50(mm)$

For a typical $\Delta T = 60(K)$ and $p = 6(mm)$, eq.(7.7) yielded a film coefficient $h = 6.7 (W/m^2 K)$.

It was assumed that the temperature of the surrounding air was unaffected by the projected radiation. In reality, some warming up of the air may occur, although this effect is very difficult to quantify and the results of the simulations indicated that convection does not play a critical role in this application.

VII.4.2 Material Properties

The material properties needed to perform a transient analysis are the density ρ, the thermal conductivity K_{xx}, and the specific heat C. These parameters were assumed isotropic and constant with temperature in the range of interest, and the values were in each case obtained from the literature. For instance, it was assumed $\rho = 1100 (kg\ m^{-3})$, $K_{xx} = 0.13 (W m^{-1} K^{-1})$, and $C = 2010 (J\ kg^{-1} K^{-1})$ for soft rubber, in accordance with Maldague and Moore, (2001).

VII.4.3 Geometry And Meshing

A 3D solid model was defined by drawing the triangle ABC to define the front face and then applying an extrusion in the negative direction of the *z*-axis, to generate a prism of thickness *t(mm)* as shown in fig. 7.2(b). A mapped mesh, shown in fig. 7.2(c), was generated in the volume using 8-node brick elements with a thermal degree of freedom (*SOLID70* in *Ansys*). The maximum element size was specified as 0.4*(mm)*.

In order to apply both convection and heat flux on the irradiated area (A2), a layer of Surface Effect Elements of type *SURF152* was defined. This allowed applying the convection load to the surface elements and the heat flux condition directly to the area A2. Figure 7.2(d) shows the surface elements applied to the exposed faces of the model.

VII.4.4 Steady State Analysis

The use of a finite element model always introduces some mesh discretization errors, causing discontinuities in first order derivative results such as the heat flux. These errors were estimated in a steady state analysis to evaluate the reliability of the simulation results. Figures 7.2 (e) and (f) show respectively plots of the error in thermal dissipation energy (TERR) and the maximum thermal flux deviation (TDSG) for each element of the mesh. The evaluation of the errors in a steady state analysis allowed refining the mesh to ensure that the error remained at an acceptable level in the more complex transient analysis.

The steady-state solution corresponds to the temperature distribution in the specimen when it reaches thermal equilibrium with the external load applied by means of the marking device (*e.g.* the infrared projector or the contact device). A contour plot of temperature in the surface of the object corresponding to the steady-state solution is shown in fig. 7.3(a), and the graph in 7.3(b) represents a temperature profile along the line A-B.

VII.4.5 Transient Analysis

VII.4.5.1 Estimation Of The Time Step

Although in a transient analysis the solution varies continuously with time, the finite element method solves only for a selection of discrete points in time. The integration time step *(ITS)* determines how often the solution is calculated. An adequate selection of the initial *ITS* in each load step helps improve the accuracy of the solution and the convergence behaviour.

The Biot number *Bi* was evaluated for an average element in the mesh to determine whether the problem was dominated by conduction ($Bi<1$) or by convection ($Bi>1$). The *Bi* number is a dimensionless ratio of the convective and conductive thermal resistances:

$$Bi = \frac{h\Delta x}{K_{xx}} \tag{7.10}$$

where Δx is the average element size, h is the film coefficient, and K_{xx} the thermal conductivity. The initial *ITS* can then be estimated using the appropriate expression below:

$$ITS = \beta \frac{\rho C \Delta x}{h} \qquad (Bi>1)$$

$$ITS = \beta \frac{\Delta x^2}{\alpha} \qquad (Bi<1) \tag{7.10}$$

where ρ is the density, C the specific heat, and $\alpha=K_{xx}/\rho C$ the thermal diffusivity of the material. The scaling factor β is related to the Fourier number of the element, a dimensionless parameter that quantifies the relative rates of conduction vs. heat storage in the element, and is arbitrarily chosen in the range $0.1<\beta<0.5$.

In the application under study and for a material such as rubber, the problem was typically conduction-dominated *(Bi<1)*. Therefore the second expression in eq. (7.10) was used, yielding *ITS*=0.1*(s)*.

VII.4.5.2 Load Steps

Figure 7.3(c) shows schematic plots of the evolution in time of the thermal load *Q(W)* applied to the specimen during the thermal marking process, and the maximum temperature difference *ΔT(K)* observed on the surface. Note that this value relates directly to the amplitude of the thermal pattern viewed with an IR camera. The maximum temperature on the surface occurred at point *A*, and the minimum temperature at point *B*, hence $\Delta T=T_A-T_B$.

The following five load steps were defined for the transient analysis:

(i) Switch-on *(LS1)*: Application of the thermal load, which was modelled as a linear ramp of short duration to enhance the numerical stability of the solution and avoid convergence problems. Typical values of the ramp duration t_s were in the range $ITS< t_s <0.5(s)$.

(ii) Activation *(LS2)*: Maintain the thermal load during the activation time $t_{ac}(s)$.

(iii) Switch-off *(LS3)*: Remove the thermal load, ramped $t_s(s)$

(iv) Observation *(LS4)*: Observe the evolution of the temperature distribution on the surface of the object to determine the observation time t_{ob}, defined as the period of time after the removal of the load in which the amplitude of the thermal pattern ΔT remains above the detection threshold of the IR camera ΔT_{th}.

(v) Steady State *(LS5)*: Take to steady state (thermal equilibrium).

Example results of a transient analysis conducted on the numerical model are presented in the graphs of fig. 7.3(d) and (e), which respectively show a plot of temperature vs. time for points A, B and C, and a plot of temperature differences T_A-T_B and T_A-T_C.

These typical results illustrate the thermal response of the specimen predicted by the numerical model. During the activation step t_{ac}, the application of an external thermal load generates and maintains a temperature gradient on the object. After the thermal load is removed, conduction heat transfer in the material tends to even out the temperature gradients, gradually degrading the pattern. Convection in the surface also contributes to this effect because it is more efficient where the sample is warmer (*i.e.* higher temperature difference with respect to the surrounding air). The observation time t_{ob} was arbitrarily defined as the time required by these heat transfer mechanisms to reduce the maximum temperature difference ΔT on the surface of the object below a detection threshold ΔT_{th}, which depends on the sensitivity of the IR camera.

VII.4.6 Experimental Validation

The results of the finite element simulation were validated by comparison with sets of experimental measurements of the observation time t_{ob} (*i.e.* the time that a usable pattern can be observed on the surface of the sample after the removal of the thermal load) obtained varying the value of the activation time t_{ac} (*i.e.* the time that the external thermal load is maintained).

The image in fig. 7.4(a) shows an example thermal pattern generated on a sheet of natural rubber $2(mm)$ thick by means of the prototype infrared projector, corresponding in this case to an activation time t_{ac}=$60(s)$. The device used a $1000(W)$ halogen lamp as a heat source and a CaF_2 lens with $75(mm)$ focal length as the projecting optics. The projector was situated $330(mm)$ away from the specimen, yielding a projected thermal grating with $6.25(mm)$ pitch. The efficiency coefficient of the device was estimated empirically as 0.30, and the dispersion coefficient as 0.63. A measurement of the room temperature yielded T_{air}=$295(K)$.

In a series of experimental tests, the device was switched on for increasing periods of time t_{ac}= 10, 20, 30, 45, $60(s)$ and the thermal response of the specimen was recorded by means of an infrared camera (ThermaCAM PM-675) positioned *ca.* $330(mm)$ away from the specimen and $220(mm)$ away from the projector.

The three pairs of sample points highlighted in fig. 7.4(a) correspond to temperature peaks and troughs of the thermal pattern. The top graph in fig. 7.4(b) shows the plots of temperature versus time for these three pairs of points, and the graph at the bottom of the figure shows plots of temperature difference versus time for each pair. The numerical results obtained from the finite element model are also shown in the figure as a black dotted line superimposed to the

experimental measurements to facilitate the comparison. Note the excellent agreement between experimental and numerical results.

Figure 7.4(c) shows also a graph of observation time t_{ob} versus activation time t_{ac}, where t_{ob} was calculated considering a detection threshold of 1.5(K). Although the experimental data shows some scatter due to non-uniformities in the distribution of the radiation delivered by the infrared projector, the prediction obtained with the numerical model can be considered highly representative of the observed behaviour.

The results show that the experimental observations of the specimen's thermal response confirmed numerical predictions. While the projector was switched on, the heat input produced a steady, quasi-linear increase of the bulk temperature in the specimen. The thermal contrast, defined as the temperature difference between neighbouring peaks and troughs, increased however asymptotically towards a maximum value of *ca.* $\Delta T_{max}=6(K)$. About 90% of the maximum contrast was reached after approximately $35(s)$ of activation.

This asymptotic behaviour can be explained because as the temperature difference increases, conduction heat transfer becomes more effective, until the rate at which heat is transferred from peaks to troughs equals the input heat rate. Beyond that point, the incoming energy can only increase the bulk temperature of the sample, but not the contrast of the pattern.

Therefore there is a maximum contrast attainable in each case which depends on the material properties and the amount of energy delivered per unit time and area (W/m^2). The latter can be modified e.g by acting on the dimmer switch, by changing the wattage of the source or increasing the efficiency of the marking device. The efficiency, in the particular case of the projector device can be improved by increasing the lens aperture or the transmissivity of the projection optics, and in the case of the contact device is favoured by a reduction of the contact resistance. Note that the observation time increases with the contrast of the thermal pattern, as shown in the plots in figures 7.4(b) and (c).

The analysis of experimental data also confirmed that the degradation of the thermal pattern due to natural heat transfer mechanisms produced a decrease of the peak-to-peak amplitude of the pattern but did not modify the carrier frequency. It also showed that the thermal decay occurred first for higher frequency terms (*i.e.* noise) while low frequency terms such as non-uniformities in the background persisted after the thermal pattern had disappeared.

The numerical model provides valuable information needed to determine the suitability of this technique for a given application, including the maximum thermal contrast attainable and therefore the maximum duration of the pattern on the specimen. Also, the simulation predicts the activation time required to generate a pattern with the required contrast onto the sample and the corresponding increase in the specimen's bulk temperature. The effect of environment

parameters such as room temperature, film coefficient, etc. can also be studied in the numerical model.

Graphs of observation time t_{ob} versus activation time t_{ac} such as the one presented in fig. 7.4(c) were found very useful to characterise the thermal marking process for a given set of sample characteristics (material, thickness, etc.) and configuration of the marking device.

Figure 7.5 shows some of these graphs obtained experimentally to validate the conclusions of the numerical study.

The plot in fig. 7.5(a) corresponds to a set of tests conducted to study the effect of increasing the delivery of heat on the sample. The projection device was fitted with an adjustable aperture window, located before the master grating to control the throughput of energy. The results show that increasing the aperture, and therefore the heat throughput, shifts upwards the asymptote of the t_{ob} vs. t_{ac} curve. The system was configured to yield a *9(mm)* projected pitch on the surface of the sample, which was double-layer sheet of corrugated cardboard *ca. 8(mm)* in thickness.

The graph in fig. 7.5(b) shows the result of another set of tests conducted on the same sample, in which the configuration of the optical elements in the projector was modified to yield different values of the projected pitch. The results show that changing the pitch only by optical means in the projector device does not have an effect on the t_{ob} vs. t_{ac} curve. In principle, increasing the pitch of the projected grating should make it possible to achieve higher thermal contrast for the same thermal gradient. However, this potential increase in achievable contrast gets compensated by a decrease in heat flux density *(W/m^2)* inversely proportional to the square of the magnification.

The graph in fig. 7.5(c) corresponds to set of tests conducted on a set of silicone rubber sheets with thicknesses of 1, 1.5 and *2.5(mm)* to study of the effect of sample thickness. The configuration of the system was the same for the three tests, yielding a *16(mm)* projected pitch on the surface of the samples. The results show that there is a negative correlation between the sample thickness and the observation time.

Finally, the graph in fig. 7.5(d) summarises the results of a set of experimental tests on a range of different materials to study the effect of different material properties.

VII.5 Experimental Apparatus

The design and construction of two prototype systems were carried out during the second stage of the project to demonstrate the two variants of the technique.

The first prototype operates by physically placing a hot stencil in contact with the surface of the part. The device is extremely simple and inexpensive, and allows good quality thermal patterns to be created easily on the surface of flat or gently curved objects.

The second prototype is in essence a projector of patterned radiation. The device was designed to maximise the energy throughput and optimise the contrast of the resulting thermal pattern. The projector provides a truly non-contacting technique, which is also appropriate for components with a complex three-dimensional shape.

Both instruments underwent several development iterations to improve their performance and suitability for different applications. Trials of the technique were undertaken in a number of materials including different types of rubber, paper, cardboard, foam, and human skin. The methodologies for use were also developed simultaneously.

The last part of this section is devoted to describing the range of thermal imagers used in the experiments to visualize and record the thermal patterns.

VII.5.1 Contact Prototype

The contact prototype is shown fig. 7.6(a). The left side of the image shows a side view of the device, in which the main elements have been labelled. The right side of the image shows an infrared scan of the device in operation, for a qualitative appraisal of the temperature distribution in the instrument.

The main frame of the instrument consists of three 100×150*(mm)* plates fastened with bolts and spacers. A rectangular array of holes with a pitch of *ca.* 5*(mm)* was drilled in the two lower plates to fit a set of steel pins 0.3*(mm)* in diameter and 50*(mm)* in length. The pins were heated up by means of a 60*(W)* silicone-rubber mat heater (Hedin Chromalox, Loughton, UK). A foam block provided thermal insulation and packing to ensure good contact between the pins and the heater. The infrared scan on the right side of fig. 7.6(a) shows the relatively uniform temperature distribution in the pins due to the high thermal conductivity of steel. This contrasts with the steep temperature gradients in the insulating foam block.

The temperature of the heater was controlled using a 2.5*(kW)* inline dimmer switch (Flashlight Ltd., formerly Lighting Technology, Salford, UK). Dimmer switches are built using solid-state devices known as a thyristors (TRIAC or SCR), which work by chopping the sinusoidal AC power signal. Figure 7.6(b) illustrates the operation of the device. The thyristor is triggered at a given point in the cycle, and keeps conducting until the voltage changes polarity. The power level of the output is proportional to the area shaded in the figure, and can be adjusted by controlling the trigger point of the thyristor. The trigger can be moved to the right in the figure to reduce the power output, or to the left to increase the power. A rotating control on the switch

operates a variable resistor used as the controlling signal. Figure 7.6(c) shows a basic circuit design. These devices reach typical values of efficiency around 99%, which is significantly higher than the 80% efficiency typically achieved with traditional adjustable power resistors (rheostats). Besides the increase in efficiency, electronic dimmer switches have other advantages over rheostats, including their reduced size and weight, lower cost, and the minimal amount of dissipated heat.

Figure 7.6(d) shows the device in operation. The instrument is pressed and held against the surface of the specimen for a few seconds to imprint the thermal pattern. After the instrument is removed, the thermal pattern can be observed with an infrared camera. The contact device is very simple and inexpensive, and allows good quality thermal patterns to be created easily on the surface of flat or gently curved objects.

The performance of this device in generating thermal patterns depends on the temperature of the pins and the contact resistance, the latter being affected by a number of factors as discussed in section VII.4.1.2. These factors include the effective contact area, which in turn depends on the shape and area of the tip of the pins, and also on the applied pressure. Generally speaking, it was found that the quality of the applied thermal patterns increased with the temperature of the pins, the contact pressure, and the duration of the contact.

VII.5.2 Projector Prototype

The construction of an appropriate projector of patterned radiation proved challenging and consumed a large share of the time and resources dedicated to this research project. However, this effort was justified because the projector provided a truly non-contacting technique, which is also potentially appropriate for components with a complex three-dimensional shape.

A diagram of the optical arrangement in the final projection prototype was shown in fig. 7.1(b). A standard configuration of optical elements for a projector in the visible spectrum was employed but the individual elements were selected to maximize the throughput of radiant energy. The radiant energy from a high power heat source was collected using an ellipsoidal mirror and passed through a grating. A set of lenses focused the image of the grating onto the surface of the specimen.

The device was designed to maximize the energy throughput. Since optical properties (reflectivity, transmissivity, etc.) have a spectral dependence, the choice of materials and coatings for the optical elements of the projector (*i.e.* condenser mirror and projection optics) played an important role in the optimisation of its efficiency. A detailed description of the different elements of the system follows.

VII.5.2.1 Heat Source

A 1000*(W)* tungsten-halogen lamp was used as the heat source of the projector. The spectral content of the radiant energy depends on the filament temperature of the source. In this case, the lamp burned at *ca.* 3200*(K)*, hence most of the energy was emitted in the visible and near infrared spectra.

VII.5.2.2 Condenser

The radiation emitted by the source was collected by means of an ellipsoidal condenser mirror purchased from a commercial supplier (Melles Griot, Carlsbad, CA, USA). The mirror was made of a magnesium substrate with an electrolytically deposited rhodium coating. The rhodium coating shows high reflectance in the visible and near infrared range, with values of r_r close to 90% across the visible spectrum (300 – 1000 *nm*) and above 80% in the infrared spectrum (1-18μm), (Source: Melles Griot Product Catalogue 1999).

One of the problems observed in early versions of the device was the presence of strong non-homogeneities in the projected light beam, caused by the large size of the lamp filament. This problem was initially addressed by fitting a diffuser (*i.e.* a frosted glass window) directly before the grating. This solution, however, caused important losses due to (i) de-focusing of the light beam by the diffuser and (ii) absorption in the glass.

In a second attempt to solve the difficulty, the condenser mirror was sand-blasted to achieve the effect of a diffuser, and gold-coated to replace the rhodium coating damaged by the sand-blasting operation. The gold-coating had the added advantage of presenting a very high reflectivity throughout the visible and infrared spectrum.

VII.5.2.3 Grating

Standard glass Ronchi gratings were found not suitable to withstand the high temperatures that occur in the projector. The glass gratings exploded within seconds of exposure to the radiation of the heat source, due to thermal stress caused by differential absorption between the bars and spaces of the grating.

Alternative technologies were investigated to manufacture good quality gratings capable of withstanding the high temperatures in the projector. The grating used in the final prototype was manufactured by a specialist supplier (Tecan Ltd., Dorset, UK) by photo-etching a dot grating with a linear pitch of $p_x=p_y=2$*(dots/mm)* on an 80×80*(mm)* steel plate 0.3*(mm)* in thickness.

Photo-etching allowed accurate replication of the grating on a steel substrate. The choice of plate thickness required balancing three factors. First, (i) the thickness must be sufficient to guarantee the mechanical stability of the grating. However, (ii) reducing the plate thickness

allows more accurate focusing of the projected image of the grating onto the object. Finally, the minimum radius of the profile that can be replicated by photo-etching is determined by the plate thickness. Therefore, (iii) there is a limit in the minimum grating pitch that can be manufactured for a given plate thickness.

The steel substrate was gold-coated using optical quality gold plating 1-2*(μm)* in thickness, to achieve a highly reflective surface. This helped reducing the heating of the grating by sending the radiation back to bounce in the condenser system. In contrast, a black finish with high emissivity on the front face of the grating facilitates the cooling of the part.

The first prototype, essentially a plate with an array of holes, deformed due to thermal stress after a few minutes of exposure to the heat source. This difficulty was overcome by changing the design as shown in fig. 7.7(c), adding cuts to relieve the thermal stresses. The design of the grating was a compromise between (i) providing mechanical relief of the thermal stress induced in the grating by the radiation from the heat source, (ii) optimising the shape of the gaps to reduce the effect of harmonics on the projected gratings, and (iii) maximising the energy throughput to increase thermal contrast on the specimen. The profile of the holes was based on a contour line of the intensity map described by eq. (7.11), see fig. 7.7(a), to reduce the spurious harmonics in the FFT of the resulting images. As shown in the graph of fig. 7.7(b), the 80% contour line provided a good compromise with *ca.* 42% void ratio of the resulting grating (*i.e.* the fraction of the total area of the grating occupied by the holes), and mechanical stability guaranteed by necks of *ca.* 30% the width of the grating pitch.

VII.5.2.4 Lens

Although the source emitted most of the radiation in the visible and near infrared range, high transmissivity of the projection system was also required in the far infrared, because the envelope of the lamp absorbed any radiation emitted by the lamp filament outside quartz's own transmission window of 0.18 -2.5*(μm)*, heating up and turning itself into a long infrared source.

The selection of suitable materials for the projection optics is illustrated in fig. 7.8. The bar diagram in fig. 7.8(a) shows the spectral range of transmission for a range of commercially available materials typically used for visible and infrared optical applications. The bars represent the transmission window for each material, *i.e.* the range of wavelengths to which the material can be considered transparent to radiation. However, some materials present higher transmissivity than others. For instance, Germanium is frequently used for infrared camera optics because its transmissivity remains very homogeneous throughout the infrared spectrum, despite its actual value being *ca.* 42%, which is relatively low. Figure 7.8 (b) shows the average transmissivity for each material in their respective transmission windows. Finally, fig. 7.8(c) shows a comparison of the costs for a typical finished lens, in this case a PCX singlet, 50(mm)

in diameter. The costs are expressed in percentage, with the CaF_2 element representing 100% as a basis for the comparison. The final prototype used a single CaF_2 element with a loss due to reflectance of *ca.* 20% (Source: Janos Product Catalogue, 2000).

VII.5.2.5 Efficiency

The efficiency of the projection device *e* was estimated using eq. (7.4) as *ca.* 20%. However, reverse fitting of the results obtained numerically with the experimental measurements yielded lower values of efficiency than predicted. A detailed study of this effect would require knowledge about (i) the spectral variation of the optical properties for each of the elements, and (ii) the spectral content of the radiation emitted by the source, and was considered outside the scope of this project. However, there are two effects not mentioned so far that can help explain this observation:

(i) the material of the sample has wavelength-dependent coefficients of emissivity, reflectivity and transmissivity, and therefore only part of the incident radiation would be absorbed producing an increase in temperature, and

(ii) due to the spectral dependence of the diffraction properties of the projection optics, all wavelengths of light cannot be focused simultaneously. As a result, some of the de-focused radiation reaches the shadowed areas on the surface of the sample, resulting on lower thermal contrast. This effect was accounted for by introducing a dispersion coefficient in the model.

VII.5.3 Thermal Imagers

A range of commercially available infrared systems was used in this research to visualize and record the thermal patterns. Figure 7.9 shows sample thermal images obtained with each of the devices.

Some preliminary tests were performed using an Insight infrared system on loan from the EPSRC engineering instrument pool. The Insight is a very simple, low cost thermal imager that measures in the far infrared region (8 -14μm), using an array of pyro-electric detectors accessed by an electron beam. This system did not provide a calibrated figure of the temperature but generated colour-coded thermal images as shown in fig. 7.9(a), where the relative temperature changes on the surface of the object can be observed. The device had a composite video output, which was used to register the images. The temperature range can be adjusted between 40*(K)* and 4*(K)*, and the maximum sensitivity was *ca.* ±0.5*(K)*.

A large part of the experimental results collected to validate the finite element models developed during the initial stage of the project were obtained using an Agema 900 infrared

system (FLIR Systems, Portland, OR, USA), also on loan from the EPSRC engineering instrument pool. The Agema 900 is based on a 136×272 array of long wave band (8-12μm) infrared detectors with a sensitivity of 80*(mK)* at 300*(K)*, and a temperature range of 240-1770*(K)*. This instrument required liquid nitrogen for cooling, and the resolution and signal to noise ratio was relatively low when compared with more modern systems. A sample image is shown in fig. 7.9(b).

The Thermkit system (Stress Photonics Inc., Madison, WI, USA) is an uncooled microbolometer, based on a 320×240 array of VO_2 resistive detectors. It operates in the long infrared (8-12μm), and is capable of measurements between 240 and 1570*(K)* with a sensitivity of ±0.2*(K)*. The system was used in experimental tests performed in the facilities of Stress Photonics, Inc. Figure 7.9(c) shows a sample image collected with this device.

Finally, a state-of-the-art system (Thermacam PM-695, made by FLIR Systems, Portland, OR, USA) was also rented from a commercial supplier for short periods on two occasions towards the end of this research. The Thermacam is an uncooled microbolometer based on a 320×240 array of detectors (7.5-13μm), with a temperature range of 230-3270*(K)*. The instrument is handheld and battery-operated, and provided high quality infrared images, as shown in fig. 7.9(d). The signal to noise ratio of this thermal imager was significantly better to that of the Agema 900, despite the fact that both manufacturers quoted the same values of sensitivity (*i.e.* 80*mK* at 300*K*).

VII.6 Analysis Of Thermal Patterns

Stage three of the work was concerned with the design and implementation of processing algorithms to analyse the thermal gratings and measure displacements. A variation of the Fourier transform method (Takeda and Mutoh, 1983) for fringe pattern analysis was implemented.

The intensity of the thermal pattern corresponding to a crossed-grating or array of dots can be mathematically described as follows:

$$I(i,j) = A(i,j) + B(i,j)\{\cos(2\pi f_x j + \Phi_x(i,j)) + \cos(2\pi f_y i + \Phi_y(i,j)) + 2\cos(2\pi f_x j + \Phi_x(i,j))\cos(2\pi f_y i + \Phi_y(i,j))\} \quad (7.11)$$

where A represents the background term, B the amplitude modulation, f_x and f_y are respectively the carrier frequencies in the horizontal and vertical directions, which are related to the pitches P_x and P_y of the dot pattern in the image (measured in pixels), and Φ_x and Φ_y are the modulated phase terms, which encode the information related respectively to the horizontal and vertical components of displacement.

The x and y terms of eq. (7.11) must be disassociated and processed separately in order to extract the two components of displacement. This can be achieved by applying appropriate filters in the frequency domain as indicated in fig. 7.14(d), so as to obtain a pair of fringe patterns associated with each thermal image, namely an image with vertical fringes corresponding to Φ_x, and an image with horizontal fringes related to Φ_y. The two fringe patterns resulting from the object can then be combined in pairs with the ones from the reference by means of a conventional fringe pattern analysis technique to calculate the phase differences. The U and V components of displacement can then be calculated from the phase differences as follows:

$$U = \frac{\Delta\Phi_x}{2\pi} P_x$$
$$V = \frac{\Delta\Phi_y}{2\pi} P_y \tag{7.12}$$

where P_x and P_y are respectively the pitch of the reference cross-grating in the x- and y-direction. Note that in order to calculate the displacements of the specimen from the measurements in the image it is necessary to consider the camera magnification m_p*(mm/pixel)*, *i.e.*

$$u = m_p U$$
$$v = m_p V \tag{7.13}$$

By noting that $p_x = m_p P_x$ and $p_y = m_p P_y$, equations (7.12) and (7.13) can be combined to yield

$$u = \frac{\Delta\Phi_x}{2\pi} p_x$$
$$v = \frac{\Delta\Phi_y}{2\pi} p_y \tag{7.14}$$

An FFT-based processing algorithm was specifically developed for this application. Figure 7.10(a) shows a flowchart describing the main steps of the processing algorithm. The reference and object images were separately processed to extract in each case two different phase maps Φ_x and Φ_y. The carrier frequencies detected in the reference were used as an initial guess to perform the phase extraction in the object image, which was otherwise more complex due to the decay of the thermal pattern. The calculated phase maps were then subtracted in pairs to obtain two maps of phase differences $\Delta\Phi_x$ and $\Delta\Phi_y$. These were finally unwrapped, and the u and v displacement maps calculated in eq. (7.14).

A flowchart describing the phase-extraction procedure in detail is shown in fig. 7.10(b). The input data consists of the thermal image I (reference or object), the corresponding mask Φ (*i.e.* a binary map where 1's represent the region of interest and 0's the background in the input image), and a parameter that indicates the number of loops required for the pre-processing algorithm. The pre-processing consisted of (i) padding the image, (ii) filtering high frequency noise, and low frequency components associated to uneven bulk temperature, and (iii) extrapolating the pattern to the background in order to reduce frequency leakage leading to errors in the calculated phase map (Roddier and Roddier, 1987). A flowchart of the FFT pre-processing loop is shown in fig. 7.11(a).

The next step was analyzing the frequency content of the input image by calculating the fast Fourier transform (FFT) of the pre-processed image I', $I^*=FFT(I')$, and searching for the frequency peaks that correspond to the horizontal and vertical carrier frequencies, respectively f_x and f_y in eq.(7.11). A typical example of frequency content for a dot pattern is shown in fig. 7.12(a). An automatic peak search algorithm specifically developed for this application is described in the flowchart shown in fig. 7.11(a). This algorithm was used to find the horizontal carrier frequency f_x on the FFT map and the vertical carrier frequency f_y in the transposed FFT map. Assisted manual search may also be performed by the operator as an alternative to the automatic procedure.

Hamming window filters centered in the carrier frequencies were applied to remove the high and low frequency components from the FFT maps. This process was carried out separately for the horizontal and vertical components:

$$\begin{aligned} F_x I^* &= filter(I^*, f_x) \\ F_y I^* &= filter(I^*, f_y) \end{aligned} \tag{7.15}$$

The inverse Fourier transform of the two filtered maps was then calculated:

$$\begin{aligned} I_x &= iFFT(F_x I^*) \\ I_y &= iFFT(F_y I^*) \end{aligned} \tag{7.16}$$

And finally the phase maps were obtained as follows:

$$\begin{aligned} \Phi_x &= arctan\left(\frac{real(I_x)}{imag((I_x)}\right) \\ \Phi_y &= arctan\left(\frac{real(I_y)}{imag(I_y)}\right) \end{aligned} \tag{7.17}$$

Artificial datasets such as the ones shown in figures 7.12(c) and (d) will be used in the following to illustrate the processing algorithm described above. A 150×150*(pixels)* reference dot pattern was generated numerically by means of eq. (7.11), considering the pitches of the pattern P_x=P_y=15*(pixels)*, and null terms of modulated phase Φ_x=Φ_y=0*(rad)*. The background and modulation terms in eq. (7.11), A and B were chosen to yield an idealized pattern with optimal contrast in the 8-bit intensity range [0, 256], therefore A=128 and B=64.

The artificial objects were created by applying a simulated displacement field to the reference image, as shown schematically in fig. 7.12(b). First, the new location of each pixel resulting from the application of the displacement maps was calculated. Second, the data was re-sampled by interpolation of the translated points to obtain the new values of intensity corresponding to the locations originally occupied by the pixels in the image.

The dataset in fig. 7.12(c) corresponds to a simulated uniform tensile load applied in the horizontal direction, which results in a 10% elongation of the sample. The Poisson effect was also simulated, introducing a 3% compression in the vertical direction. Figures 7.12(c.1) and (c.2) show respectively the reference and object images generated as described above. The maps of u- and v-components of displacement used for this example are shown respectively in figures 7.12(c.3) and (c.4). The artificial reference and object images were analysed using the processing algorithm described in this section to yield the displacement maps shown in figures 7.12(c.6) and (c.6). Comparison of the displacements applied originally with those calculated using the algorithm allows evaluation of the accuracy of the method. Figures 7.12(c.7) and (c.8) show respectively the error maps corresponding to the u- and v-components of displacement. A second example of artificial data, in which deformation by shear was simulated, is also shown in fig. 7.12(d).

It can be observed that in both cases the algorithm achieved sub-pixel accuracy, with the maximum error remaining below ±0.5*(pixels)* and typical values of the standard deviation of *ca.* 0.1*(pixels)*. However, it must be noted that in real cases the value of the grating pitches P_x and P_y needed to apply eq. (7.12) are unknowns. These values can be estimated from the carrier frequency, although this method yielded in practice inaccurate estimations with typical errors in the order of 10%, leading to scaling errors of the displacement map as large as ±2*(pixels)* in some cases. An alternative that usually gave higher accuracy, was to obtain a direct measurement of the pitch p_x, p_y projected on the surface of the specimen and applying directly eq. (7.14).

Outside scaling errors, typically the largest discrepancies occurred near the edges of the images. These are the so-called frequency-leakage errors (Roddier and Roddier, 1987), which appear because the FFT method assumes that the pattern is periodic, introducing spurious frequency

terms to model the discontinuities in the edges of the pattern. In order to minimize these errors, the images were *padded*, *i.e.* enlarged by adding rows and columns of blank pixels at the boundary (see fig. 7.13(a) for an example). The dot pattern was then extrapolated outside the original limits of the image by means of the pre-processing loop described in the flowchart of fig. 7.11(a). This method applied iteratively a frequency filter consisting of two Hamming windows respectively centred in the horizontal and vertical carrier frequencies, and substituted the areas outside the region of interest in the original image with the corresponding portions from the resulting image to prepare for the following step. Figure 7.13(a) shows an example pattern before pre-processing, and after 2, 4 and 8 iterations of the loop. A rectangular area inside the image was masked to simulate the effect of discontinuities in the pattern. The series of images shows that increasing the number of iterations improved the extrapolation of the pattern. This reduced the distortion of the calculated displacement map, as demonstrated by the graph in fig. 7.13(b), which shows a negative correlation between the error and the number of pre-processing iterations.

A set of reference images with pitches of 5, 10, 15, 20 and 25*(pixels)* is shown in fig. 7.13(c). Corresponding artificial objects were also created using the simulated displacement field shown in fig. 7.12(c). The series of artificial datasets was analysed to study the effect of pitch in the error and the results are summarised in the plot of fig. 7.13(d), which confirms that the accuracy and sensitivity of the new technique are inversely related to the pitch of the master grating. This result was expected because the technique is analogous to conventional in-plane moiré methods.

VII.7 Experimental Results

The final stage of the work explored the applications of the new technique. The technique was applied to simple cases with a known analytical solution of the strain field, and also to more complex examples where the results were validated by comparison with finite element models. Both in-plane and out-of-plane configurations were investigated, although due to time restrictions, validation was performed only in the in-plane case. This can be justified because it is in the in-plane case where the technique offers significant advantages over existing techniques. Some suggestions to achieve the separation of in-plane and out-of-plane components of displacement in the general case are described among the recommendations for future research presented in section VIII.5.

This section presents two examples that demonstrate the measurement of in-plane deformation with new technique. In the first example, the contact prototype was used in a tensile specimen, a simple geometry that allowed the results to be validated with the analytical solution. The second example demonstrates the use of the projection prototype on a specimen with a slightly more complex geometry, which required the use of a numerical model to validate the results.

VII.7.1 Contact Prototype

A set of experiments was performed on a dog-bone tensile specimen made of 3.5*(mm)* thick natural rubber. Figure 7.14(a) shows an overview of the experimental set-up. The specimen was clamped in a set of grips, which was built with a pair of steel plates joined by nuts and bolts. These grips were connected to the loading frame shown in the figure by means of articulated links. The upper link was fitted with a threaded bolt and a nut. Rotating the nut produced a vertical shift of the upper grip, which resulted in a tensile load being applied to the specimen.

The contact array prototype was switched on and allowed to heat up to approximately 340*(K)*. The device was pressed against the surface of the specimen for approximately 8*(s)*. The data collection area is highlighted with a black dotted line in fig. 7.14(b). The configuration of the optical elements yielded a camera magnification of 0.48*(mm/pixel)*

Figure 7.14(d) shows the input data and a schematic of the processing algorithm. The reference image (top left) was collected immediately after removal of the pin array and before the load was applied. The object image (bottom right) shows the same region 5*(s)* later with a vertical tensile load applied. The distortion of thermal pattern in the object image relative to the reference is due to the deformation of the specimen. In addition, conductive heat transfer caused a decay of the thermal pattern in this interval of time, effectively reducing the peak-to-peak amplitude of the temperature profile from about 6*(K)* in the reference image to below 2*(K)* in the object, and washing away higher order harmonics, as shown in the FFT images of the object and reference in fig. 7.14(d).

Figures 7.14(e) and (f) show the maps of u- and v-component of displacement, which were calculated by means of the processing algorithm described in section VII.6. Figure 7.14(e) displays the vector field of displacements on the surface of the specimen after removal of the rigid body translation term. The arrows indicate the magnitude and direction of the displacement. In this map the vertical elongation of the specimen as well as a compression in the horizontal direction due to Poisson's ratio are readily observable.

The range, spatial resolution and accuracy of the technique can be assessed using the same considerations as for conventional moiré techniques. The spatial resolution was given by the inverse of the camera magnification, *i.e. ca.* 2.1*(pixel/mm)*. The pitch of the reference grating, p_x=5.0*(mm)* and p_y=6.0*(mm)* in this example, and a estimate of 0.4*(rad)* for the accuracy of the phase extraction, were substituted in eq. (7.14) to estimate the accuracy of the technique for displacement measurement. This estimate yielded 0.32*(mm)* for u and 0.38*(mm)* for v.

VII.7.2 Projector Prototype

This section presents a case study to demonstrate the use of the prototype projector described in section VII.5.2 for the measurement of deformation using thermal marking.

The specimen was cut out from a *2(mm)* thick sheet of natural rubber to model a curved tie bar with a length L=215*(mm)* and W=55*(mm)* in width. The geometry and dimensions of the specimen are shown schematically in the diagram of fig. 7.15(a).

Figure 7.15(b) shows an overview of the experimental set-up. The specimen was clamped onto the loading frame described in the previous section and viewed using an infrared camera. The configuration of the elements yielded a camera magnification of 0.42*(mm/pixel)*. The projector prototype was positioned to the right of the infrared camera and used to project a dot pattern onto the surface of the sample. The pitch of the projected grating was measured directly on the surface of the specimen yielding $p=p_x=p_y$=5.8*(mm)*. Figure 7.15(c) shows the direction of the applied load, and the field of view of the infrared camera.

Figures 7.15(d) and (f) show two infrared images of the specimen which were respectively used as the reference and the object thermal patterns. These raw infrared images present intensity variations superimposed to the main crossed-grating pattern, such as the brighter spiral-shaped area shown in the figures. They correspond to variations in the bulk temperature on the surface of the specimen, caused by uneven heating due to the formation of ghost images from the lamp filament used as heat source in the projector.

The intensity variations can be modelled in eq. (7.11) by means of modulated background and amplitude terms, respectively $A(i,j)$ and $B(i,j)$. These strong non-uniformities constituted a challenge for the FFT fringe processing algorithm described in section VII.6, because they affected the frequency content of the images to the extent that in some cases they fooled the automatic carrier frequency determination. In order to overcome this difficulty, a variation of the normalization procedure described in section IV.5.3 was applied to the images.

The reference image in fig. 7.15(d) shows the thermal pattern generated on the unloaded specimen after t_{ac}=30*(s)* activation time with the projector prototype. This image was collected immediately after switch-off. A second image was collected after a period of time of *ca.* 13*(s)* to use in the normalization procedure as estimate of the thermal background terms in the image of the dot pattern. This approach is valid because the decay of the thermal pattern occurs faster for temperature differences across small distances, and therefore the bulk temperature variations typically remained long after the dot pattern had disappeared.

The specimen was left to recover thermal equilibrium, and then the projector was switched on again during t_{ac}=30*(s)*. After switch-off, the tensile load was applied to the specimen by rotating

eight complete turns of the nut to produce a relative displacement of the grips of 12.0*(mm)*. The object image in fig. 7.15(f) shows the loaded specimen and was collected 5*(s)* after switch-off. An image of the thermal background was collected 14*(s)* later with the load still applied.

The normalization allowed (i) removing spurious variations in the background of the infrared images, (ii) optimising the contrast, and (iii) enhancing the signal to noise ratio. Figure 7.15(h) demonstrates the steps of the normalization applied to the object image in fig. 7.15(f). The background image (h.2) was subtracted from the raw infrared image (h.1) to yield the difference map in (h.3), which presents enhanced contrast and uniform background, although a significant amount of amplitude modulation remains. A high pass filter was applied to (h.3) so as to eliminate the amplitude modulation, see fig. (h.4). Finally, the latter image was smoothed to eliminate noise and re-scaled to the [0,255] intensity range, as shown in fig. (h.5). Figures 7.15(e) and (g) show respectively the normalized reference and object images resulting from the application of the procedure described above to the raw infrared images in fig. 7.15(d) and (f).

The normalized images were processed using the FFT algorithm described in section VII.6 to yield the experimental results shown in fig. 7.16, namely (a) the map of u-component of displacement, and (b) the map of v-component of displacement. Figure 7.16(c) shows a representation of the direction and magnitude of the displacement vector in the field of view. Note that the arrows have been scaled in the figure to enhance visibility.

These experimental results were validated by comparison with the results of a numerical simulation of the test. A finite element model of the upper half of the specimen was created using 8-node plane elements (PLANE82 in Ansys) with thickness t=2*(mm)*. Boundary conditions in displacements were applied to the horizontal axis of symmetry, v=0*(mm)*, and also to the clamped edge, u=0 and v=6*(mm)*. The analysis assumed plane stress and large deformations hypotheses. Average values for bulk mechanical properties of natural rubber Young's Modulus E=6.9*(MPa)* and Poisson's ratio ν=0.49, were obtained from the literature.

The results of the numerical simulation are shown below the experimental measurements in figures 7.16(d), (e) and (f) for comparison with the corresponding experimental measurements. It can be observed that both sets of results are qualitatively very similar.

The four plots in fig. 7.16 (g) show profiles taken on the maps of experimental measurements (blue solid line) and numerical results (black dashed line) along the lines highlighted in figures 7.16(a) and (b). The superposition of experimental and numerical data allows for quantitative comparison. The profiles plotted in (g.1) and (g.3) correspond respectively to the u- and v-components of displacement along a vertical line through the middle point of the specimen, x=W/2. The graphs in (g.2) and (g.4) correspond to profiles of u and v along the horizontal axis of symmetry of the specimen, y=0.

The resolution of the measurements, given by the inverse of magnification, was 2.36*(pixel/mm)*. The experimental measurements were in remarkably good agreement with the numerical results as shown in Table VII-1, which summarises the standard deviation and maximum deviation of the experimental measurements relative to the numerical results for each of the plots. These values are in good agreement with the predicted value of accuracy of the technique, which was estimated as 0.37*(mm)*, assuming 0.4*(rad)* uncertainty in the phase and substituting in eq.(7.14).

	u_x along $y=0$	u_y along $y=0$	u_x along $x=W/2$	u_y along $x=W/2$
Max. error (mm)	*0.49*	*0.07*	*0.17*	*1.52*
Std. dev. (mm)	*0.21*	*0.04*	*0.09*	*0.38*

Table VII-1: Accuracy of the displacement measurement with thermal marking

The maximum values of the error, which appeared generally near the edges of the images, can be attributed (i) to edge effects closely related to those described in section IV.7.1 for the case of the spatial phase extraction algorithm, combined with (ii) the effect of frequency leakage, which is specific from FFT processing.

The binary mask of the image was extended to exclude from the region of interest a band of width $p/2$ along the perimeter of the specimen, where p is the pitch of the projected grating. The maximum error in the remaining area was typically below ±0.2*(mm)*, with the exception of an artefact in the lower area of the image which produced a larger discrepancy of *ca.* 1.5*(mm)* in the value of the vertical displacement v. The discrepancy in the displacement field appeared systematically upon repetition of the test, suggesting that the effect may correspond to a real feature of the specimen, such as a patch of material with uneven material properties, the presence of an inclusion or a change in thickness.

Current values of attainable accuracy using the thermal marking technique are mainly limited by two factors: (i) the low resolution of commercially available infrared cameras, which is typically well below the current standard for CCD still or even video cameras for applications in the visible range, and (ii) the attainable pitch of the projected grating, which was in the range of 4-8*(mm)* for a typical application with the contact and projector prototypes developed in this research. While it is expected that the first difficulty will soon be overcome at the current rate of technological progress regarding infrared detectors, further research is needed to develop optimised versions of the prototypes capable of producing finer thermal gratings. Some suggestions are included in the last chapter of this thesis.

VII.8 Discussion And Conclusions

A novel experimental technique for strain measurement named thermal moiré has been presented, which consists of temporary imprinting a thermal grating on the surface of the part. This eliminates the need to bond, print or etch a grating or pattern of conventional moiré and image correlation methods. The technique offers significant advantages compared to other methods of experimental stress analysis, provides full-field data of the three components of displacement, and is truly non-invasive, requiring minimal or no surface preparation. This latter feature together with the possibility to operate with service loads provides the potential for non-contacting, non-invasive measurements, with applications for the analysis of living tissue in medicine and biology, and for non-destructive testing in engineering, mainly for materials with low thermal diffusivity such as paper, rubber, or plastics. The general method of thermal imprinting can also be used to convert other experimental techniques that require surface preparation, such as image correlation techniques, to totally non-invasive methods.

Two different methods of thermal imprinting have been explored in this research. The first method relies on a conduction heat transfer mechanism, and essentially consists of placing a hot stencil in physical contact with the object. A hot grid or array of pins is placed onto the surface of the sample to generate a thermal pattern by contact. The second method is based on radiation heat transfer, and works by projecting radiant energy from a heat source through a physical grating and onto the object. Work on the development of laboratory apparatus to imprint thermal gratings by contact and by projection has been described.

The feasibility of this technique has been illustrated with experimental results on a selection of exemplars, with typical values of accuracy and resolution of respectively *ca.* 0.2*(mm)* and 2*(pixel/mm)*. Accuracy and resolution of the technique are analogous to existing in-plane moiré methods. The experimental measurements were in excellent agreement with numerical results. At present, main limiting factors for the accuracy are (i) the resolution of infrared sensors and (ii) the grating pitch attainable by means of the thermal marking devices. In conclusion, all the objectives contemplated in the original program have been successfully achieved.

The generation of thermal fringe patterns can be achieved by other means, which may be suitable for different applications. Two alternative techniques respectively based on the use of lasers and of a spray were also conceived during this research, although they were not pursued due to constraints in the time and resources available. They are included among the recommendations for future research presented in section VIII.5.

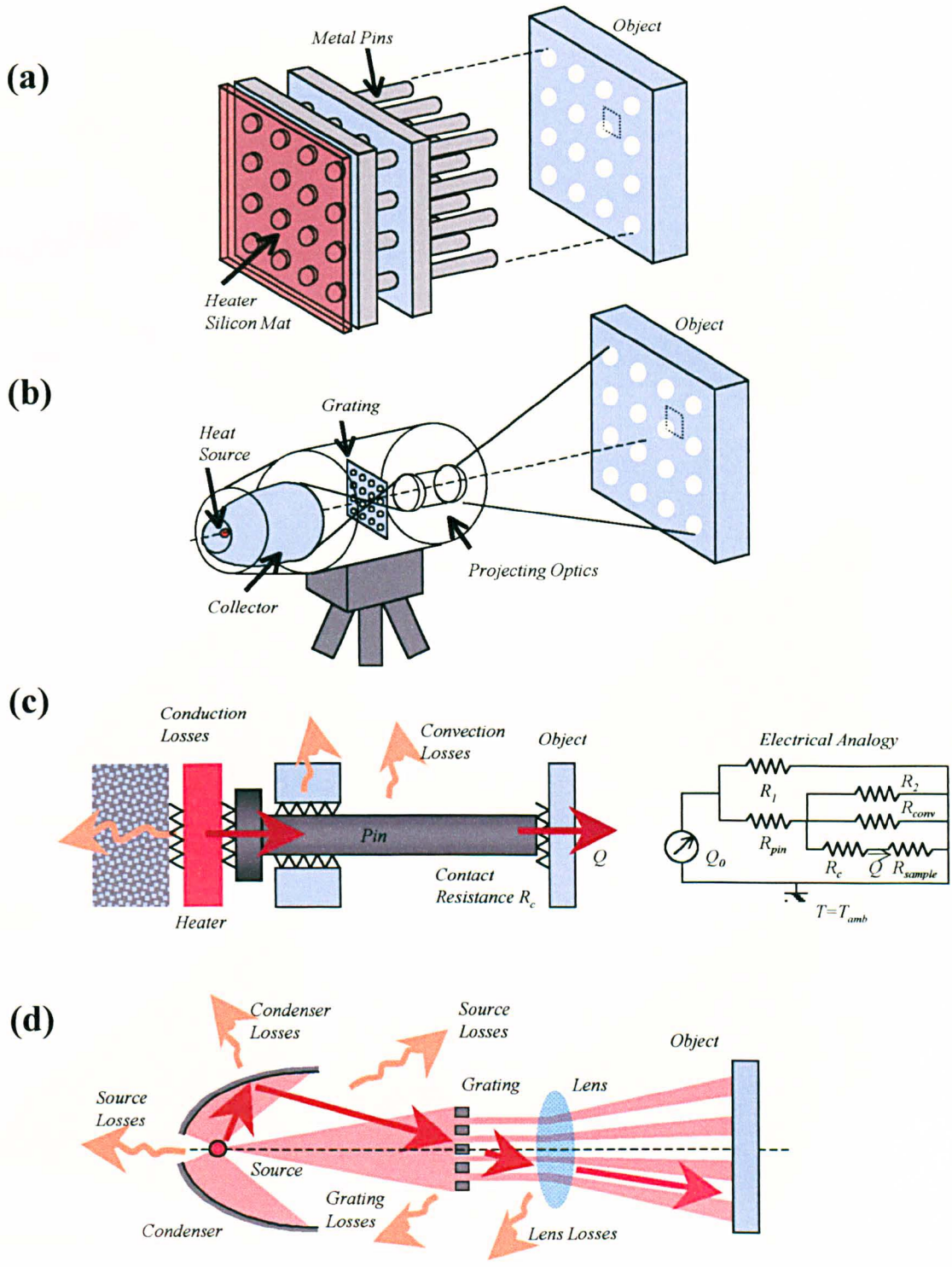

Figure 7.1: Thermal marking concepts (a) Contact with a hot stencil (b) Projection of patterned infrared radiation. Efficiency coefficients (c) Efficiency of the contact device. (d) Efficiency of the projector system.

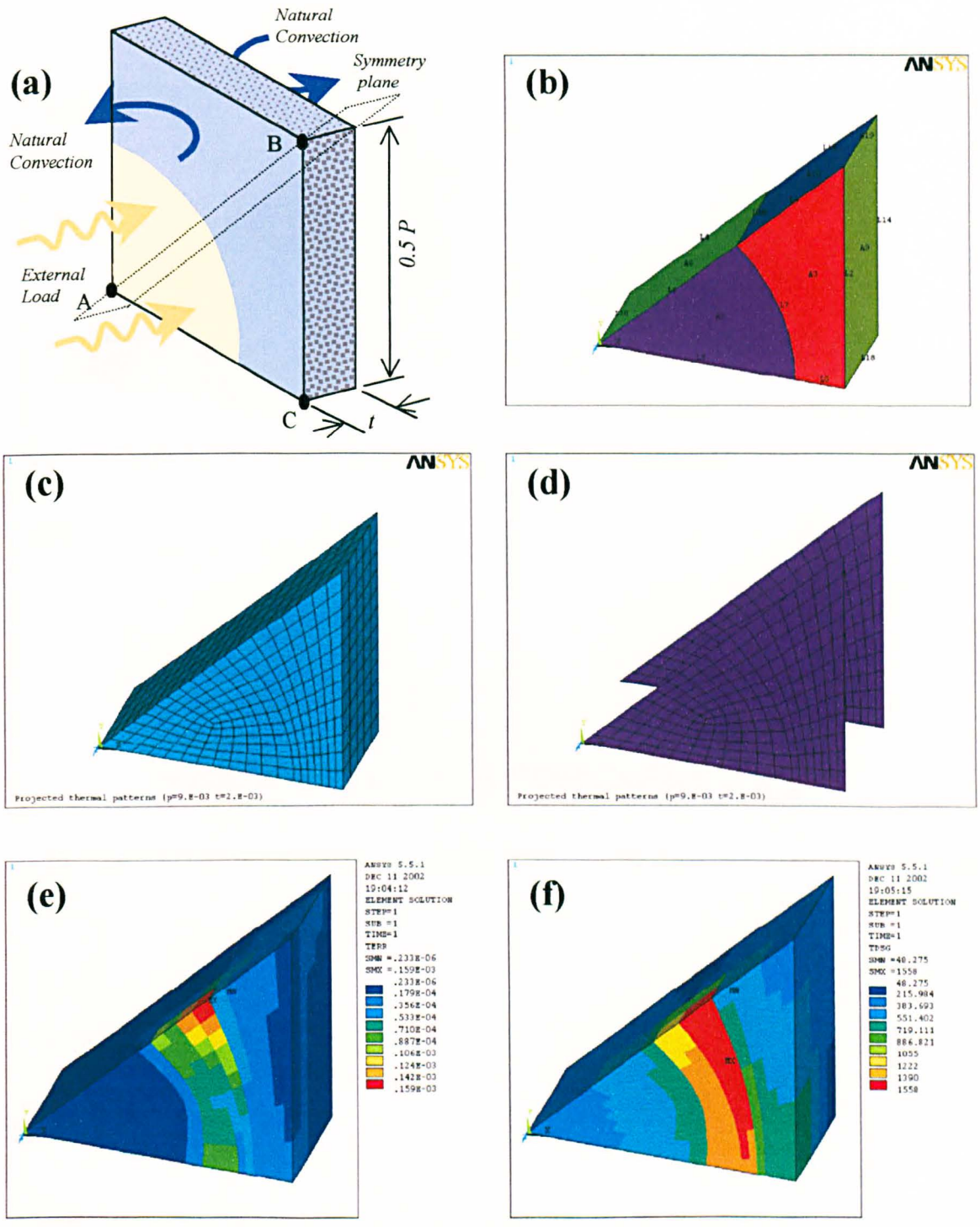

Figure 7.2: Construction of a Finite Element Model (a) Simplified problem (b) 3D Solid Model Geometry (c) 3D mapped mesh made of SOLID70 elements. (ESIZE=0.40) (d) Layer of SURF152 Surface Effect Elements to model convection. Graphs of error estimation to evaluate the reliability of the simulation data. The graphs show (e) the error in the thermal dissipation energy and (f) the maximum thermal flux deviation for each of the elements in the mesh.

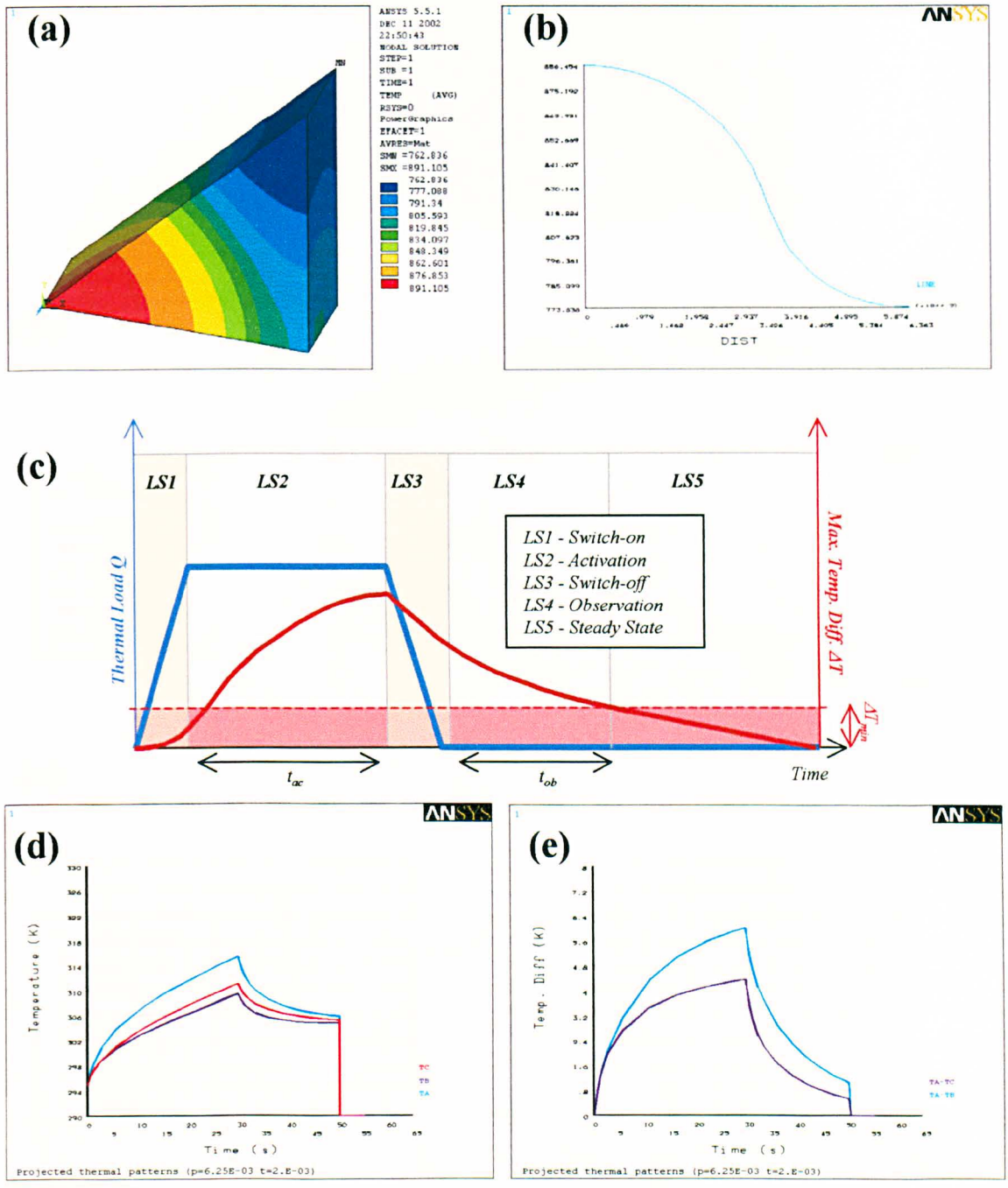

Figure 7.3: Results of the simulation. (a) Contour plot of temperature and (b) Temperature profile along line A-B for the steady-state solution. (c) Diagram of the load steps used for the transient analysis. The graphs in (d) and (e) show example results of the transient simulation, respectively a plot of temperature at points *A*,*B* and *C* versus time, and a plot of temperature differences T_A-T_B and T_A-T_C versus time.

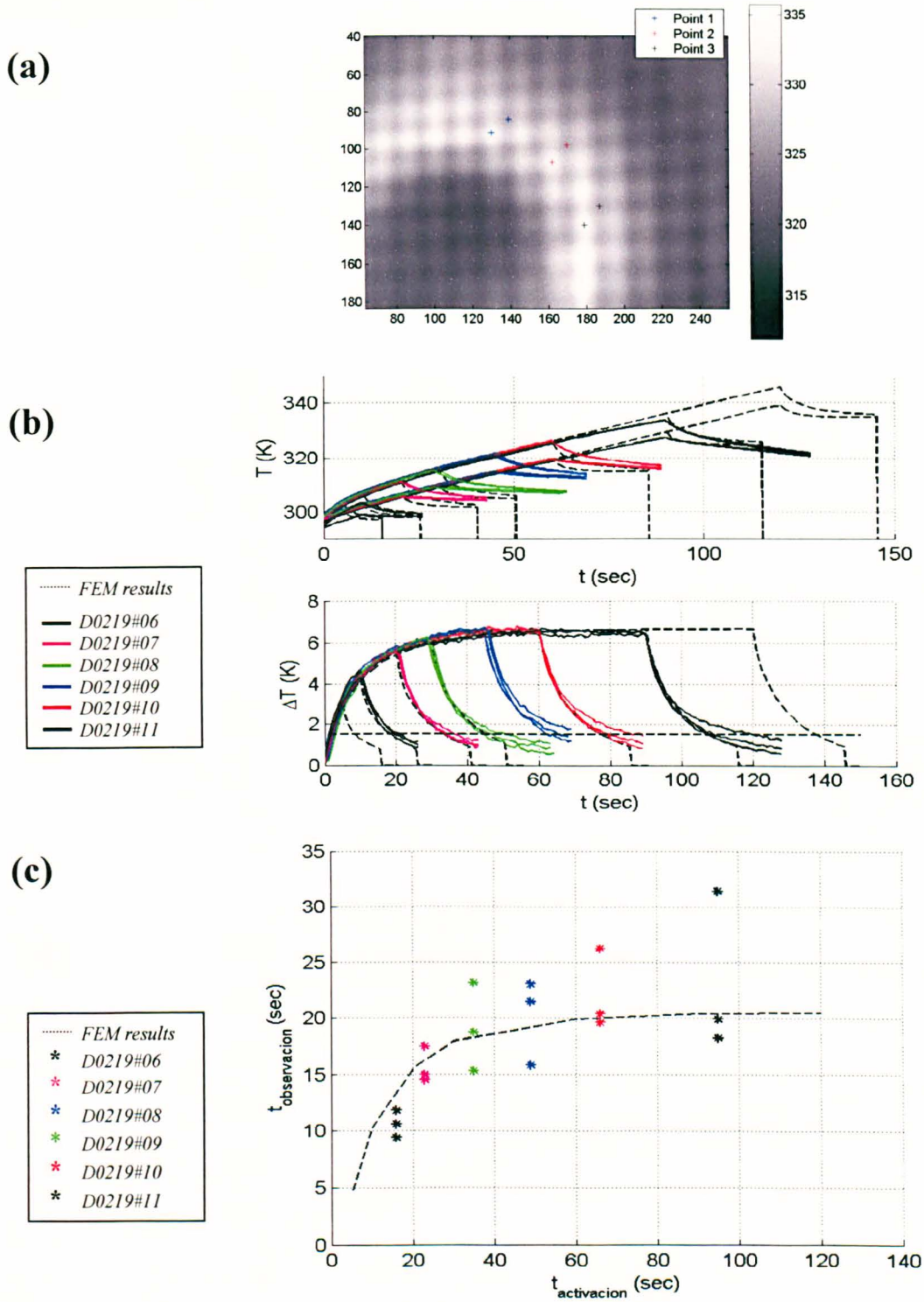

Figure 7.4: Experimental validation of the numerical model. (a) Sample thermal image. (b) Plots of temperature and temperature difference versus time. (c) Plot of observation time versus activation time.

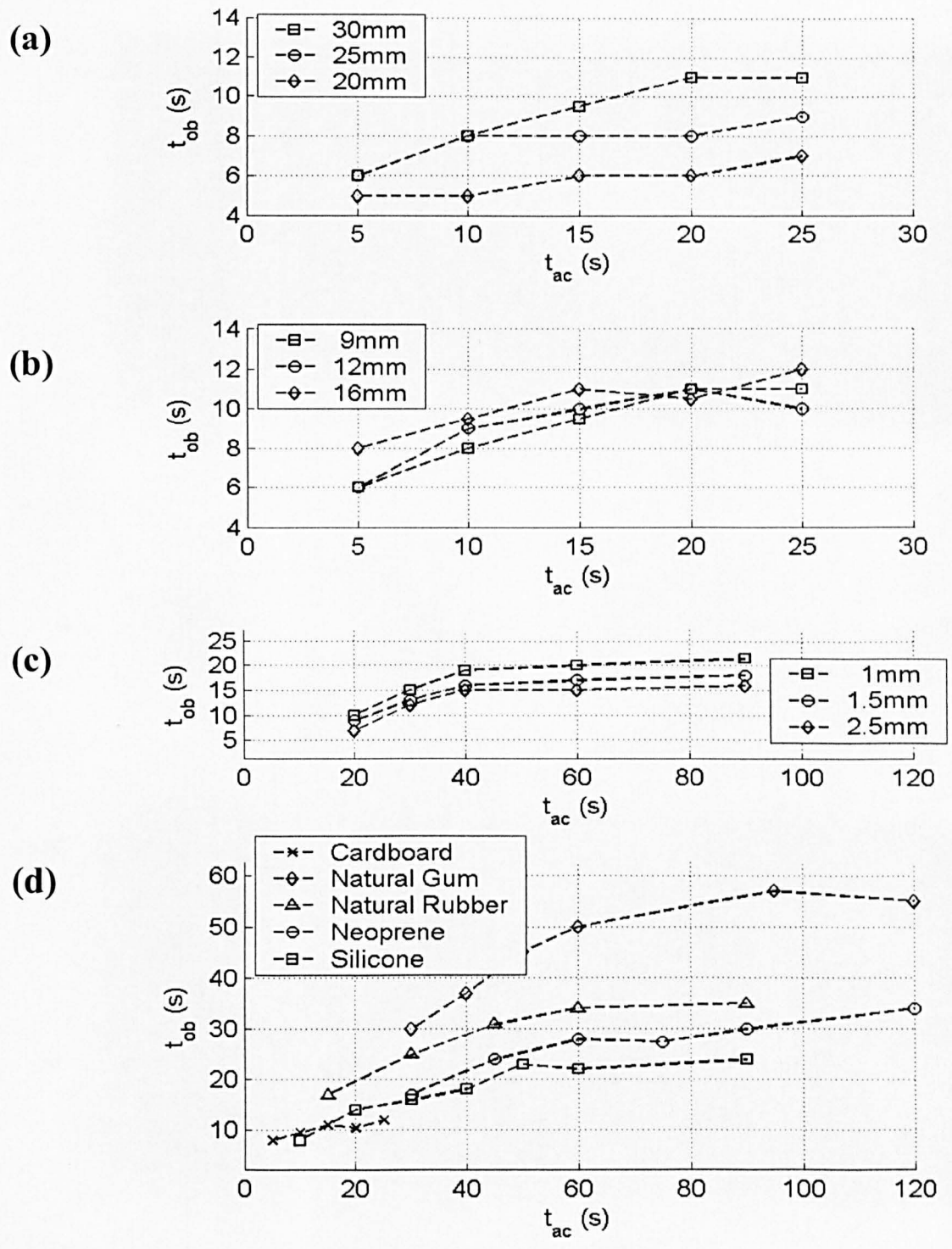

Figure 7.5: Example experimental datasets for the validation of the numerical model. (a) Effect of the aperture diameter (b) Effect of the projected pitch (c) Effect of the sample thickness (a) Effect of the material's properties.

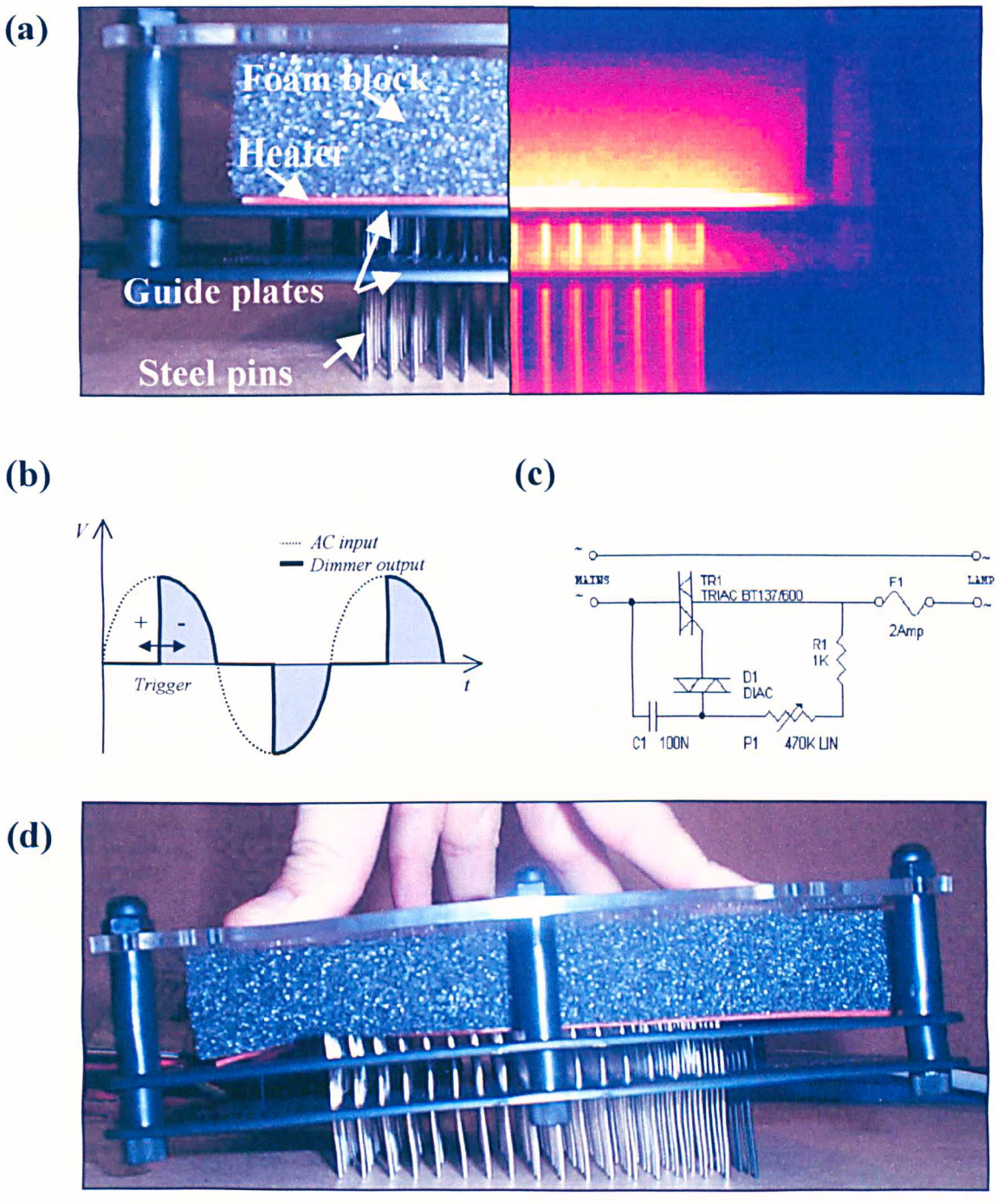

Figure 7.6: Contact pin array prototype. (a) The different parts of the prototype are shown in the image on the left, and the temperature distribution is shown in the infrared scan on the right. (b) Operation of a solid-state dimmer switch (c) Schematic of a basic dimmer switch circuit. (b) The prototype in operation.

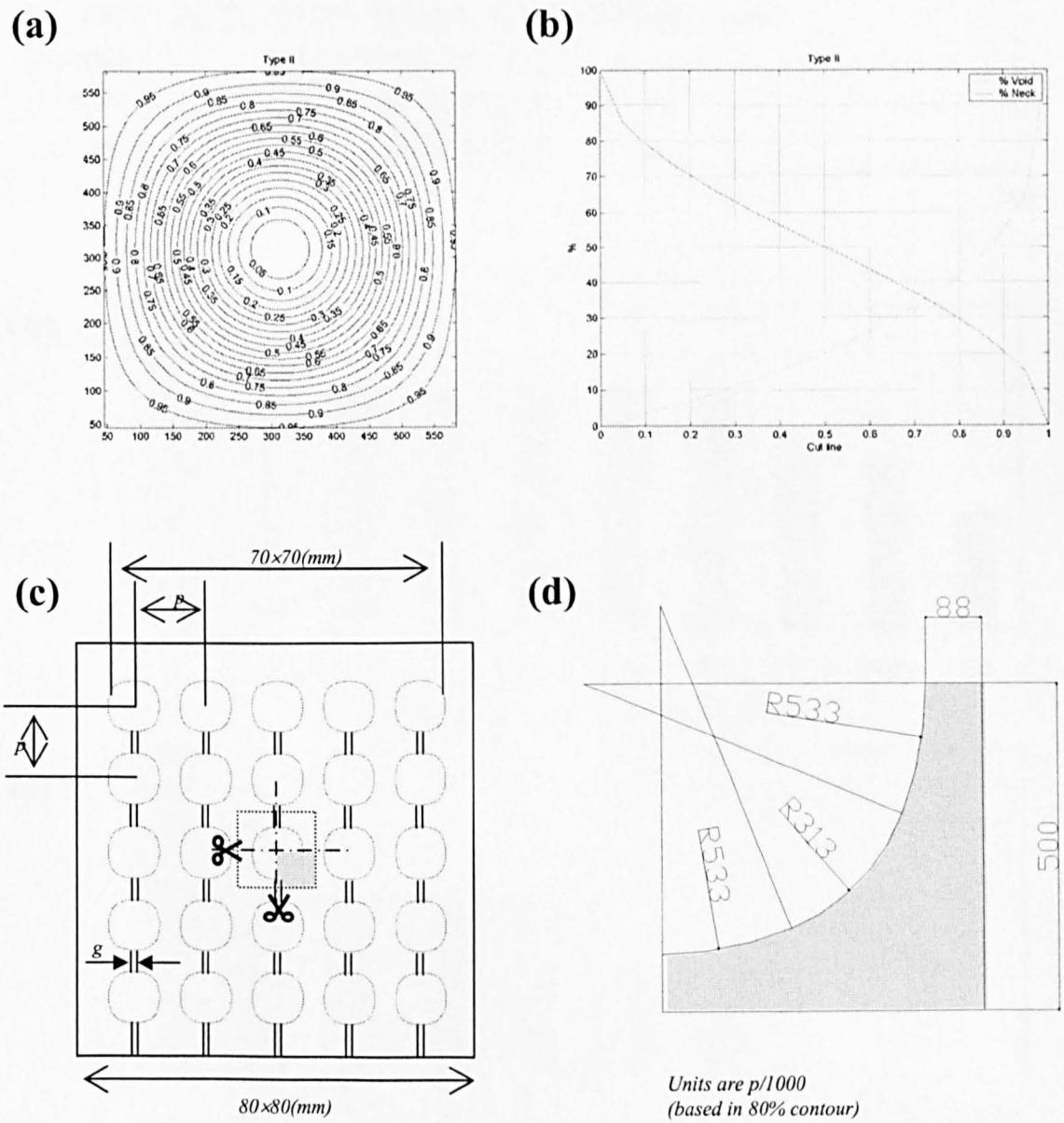

Figure 7.7: Crossed grating design: (a) Intensity contour in one cell (b) Plot of percentage void and neck thickness versus contour line (c) Schematic of the grating design (d) Detail of the grating profile for photo-etching, based on the 40% intensity contour. Dimensions relative to the grating pitch.

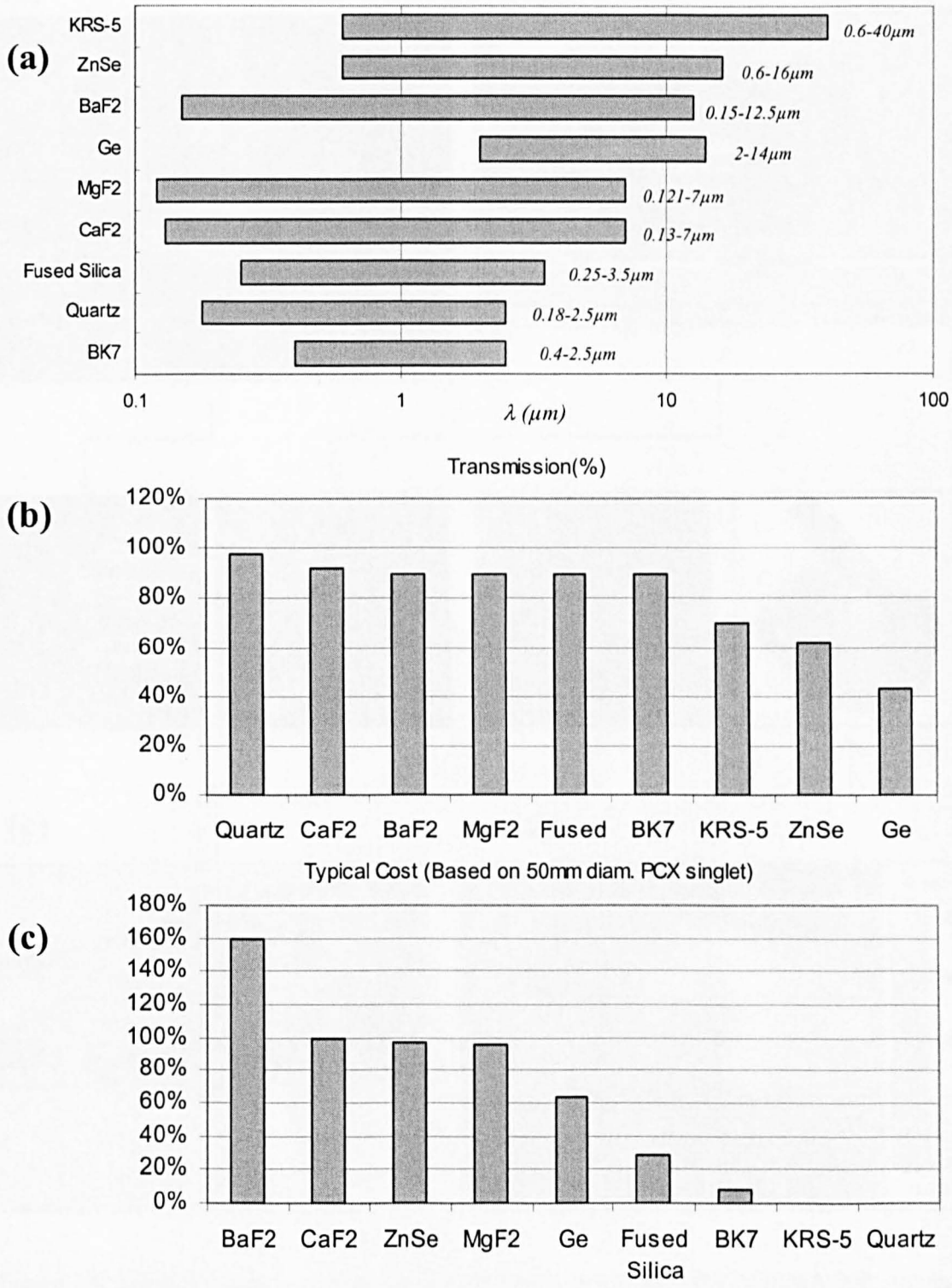

Figure 7.8: Selection of materials for projection optics. (a) Spectral range of transmission (b) Average transmissivity in transmission window (c) Comparison of costs for a typical PCX singlet, 50(mm) in diameter. Costs are expressed as % of the final choice (CaF_2), which was used as a basis.

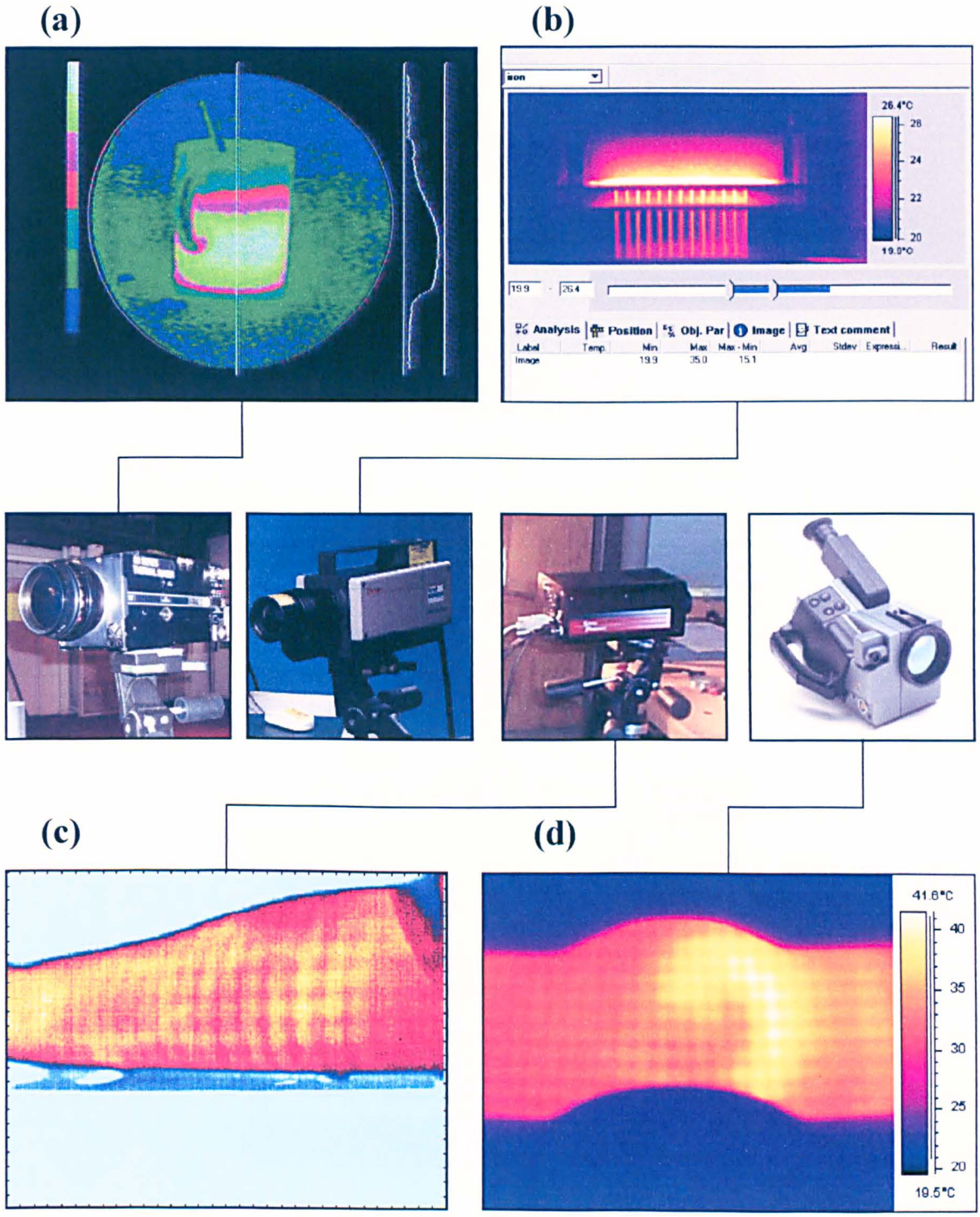

Figure 7.9: Infrared cameras and sample images (a) Insight system (b) AGEMA 900 system (c) StressPhotonics ThermKIT (d) FLIR ThermaCAM PM-695.

(a)

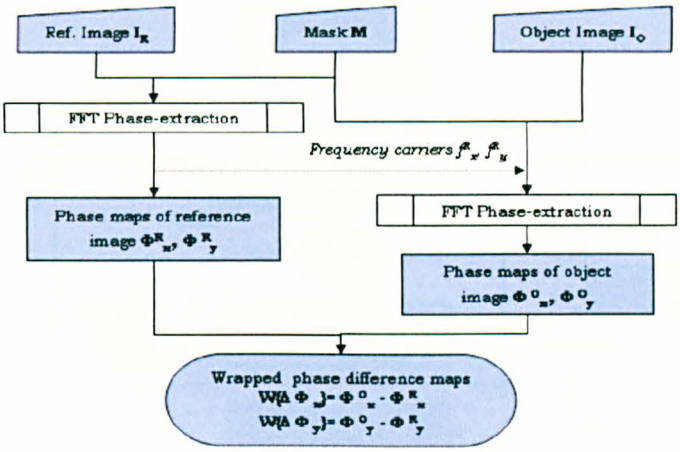

(b)

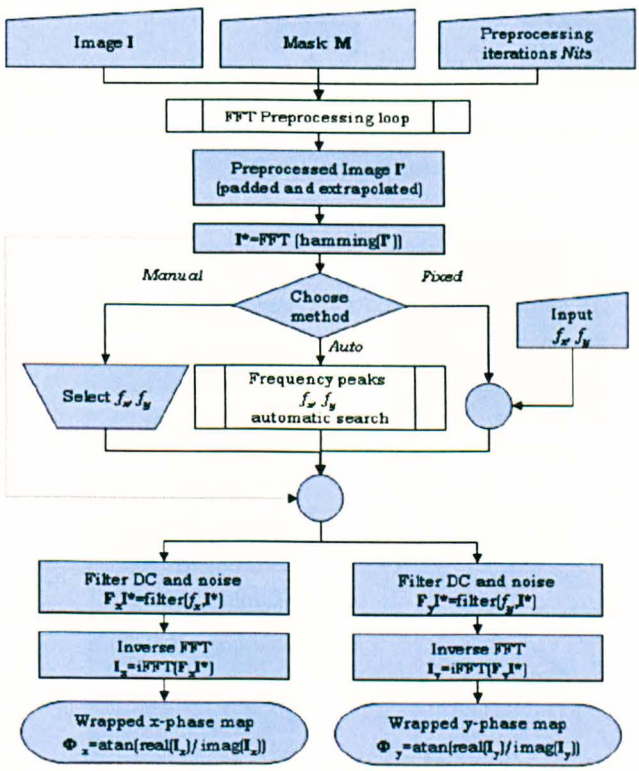

Figure 7.10: FFT processing of dot patterns (a) Flowchart of the main steps of the processing algorithm. (b) Flowchart of the phase extraction.

(a)

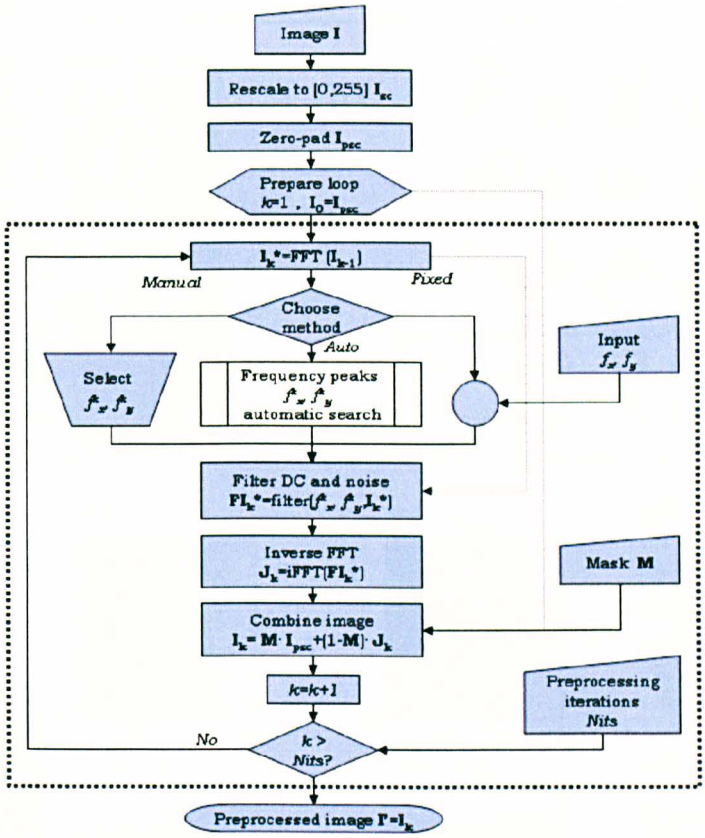

(b)

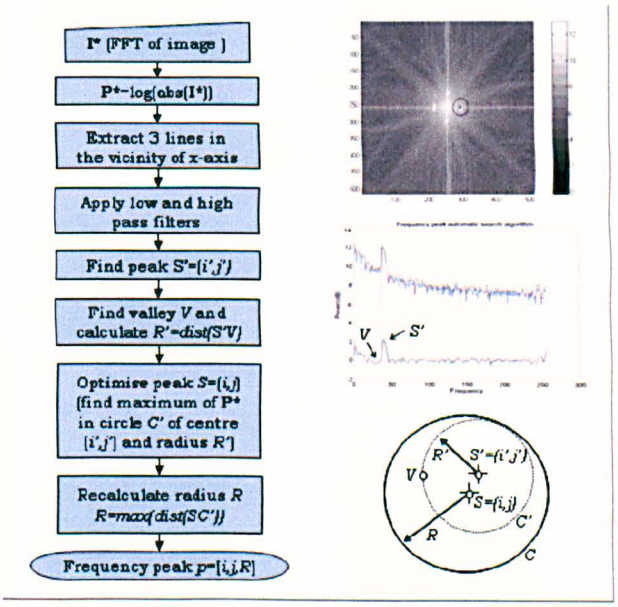

Figure 7. 11: FFT processing of dot patterns (a) Flowchart of the FFT pre-processing loop (b) Detail of the FFT phase-extraction: automatic peak search algorithm.

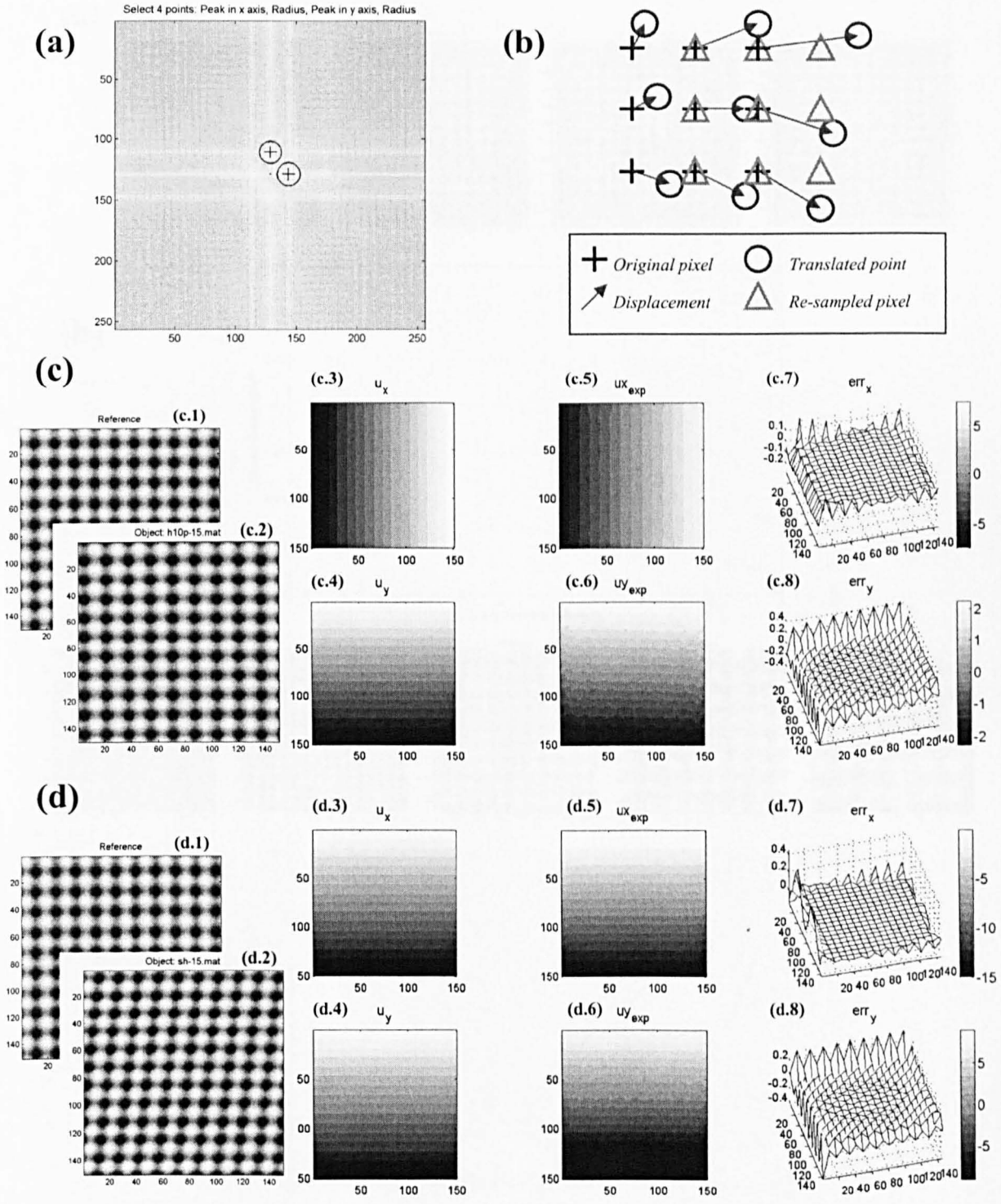

Figure 7.12: Numerical evaluation of the FFT processing algorithm (a) Typical FFT map showing the frequency content of an artificial dot pattern (b) Schematic of the generation of artificial objects (c) Analysis of an artificial dataset with a simulated tensile load (d) Analysis of an artificial dataset with a simulated shear load. The figures show the reference (1), the object (2), the applied displacements u_x (3) and u_y (4), the calculated displacements u_x (5) and u_y, (6) and the error maps in the *x*- (7) and *y*- (8) components.

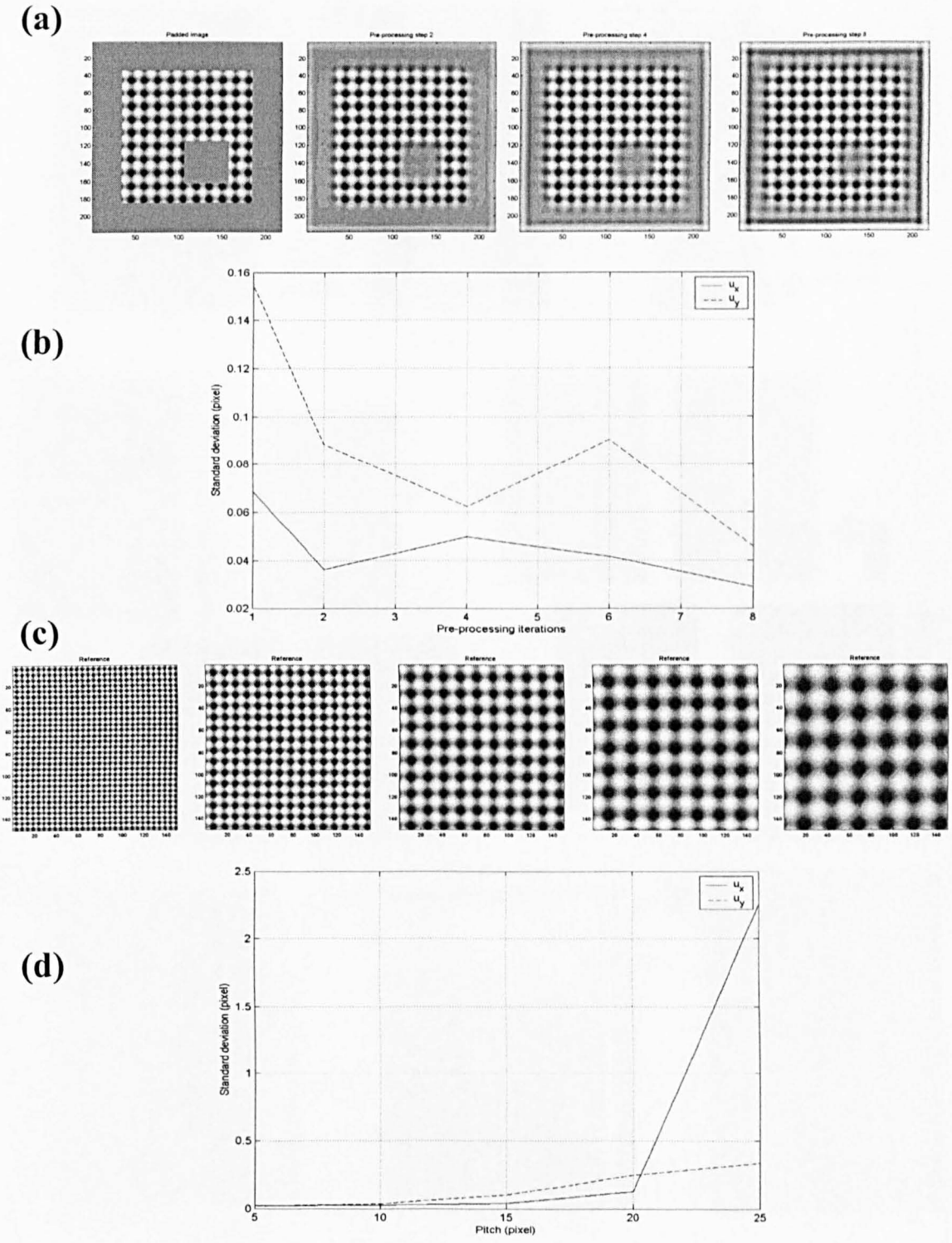

Figure 7.13: Numerical evaluation of the FFT processing algorithm Effect of the pre-processing loop: (a) Example pattern before pre-processing and after 2, 4 and 8 iterations. (b) Plot of error in the calculated displacement versus number of pre-processing iterations. The error was calculated as the standard deviation of the calculated displacement with respect to the applied displacement. Effect of the grating pitch: (c) Example images for pitches of 5, 10, 15,20 and 25*(pixels)*. (d) Plot of error versus pitch.

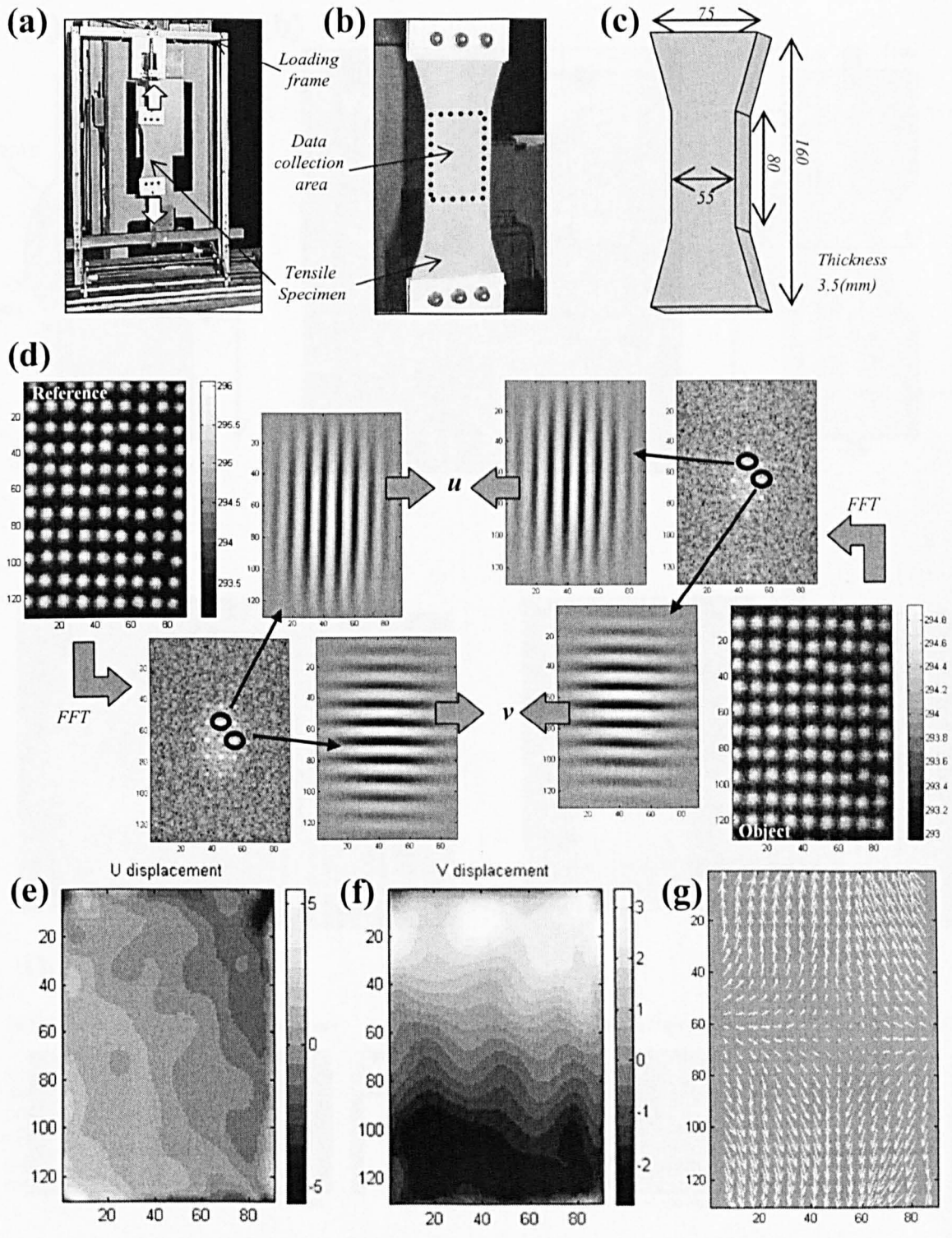

Figure 7.14: Deformation analysis using thermal marking with the contact prototype. (a) Experimental set-up. (b) Detail of the dog-bone tensile specimen and data collection area. (c) Dimensions of the specimen (d) Input data and schematic of the data processing. The reference image (top left) was collected immediately after imprinting the thermal pattern on the unloaded specimen. The load was applied, and the object image (bottom right) was collected after 5*(s)*. Both images were filtered in the frequency domain to obtain two pairs of vertical and horizontal fringe patterns. Analysis of these pairs yielded the maps of u and v components of displacement, respectively shown in (e) and (f). Units are pixels on all axes, and millimetres in the greyscale. (g) Vector field of displacement. The arrows represent the direction and magnitude of the displacement in each point.

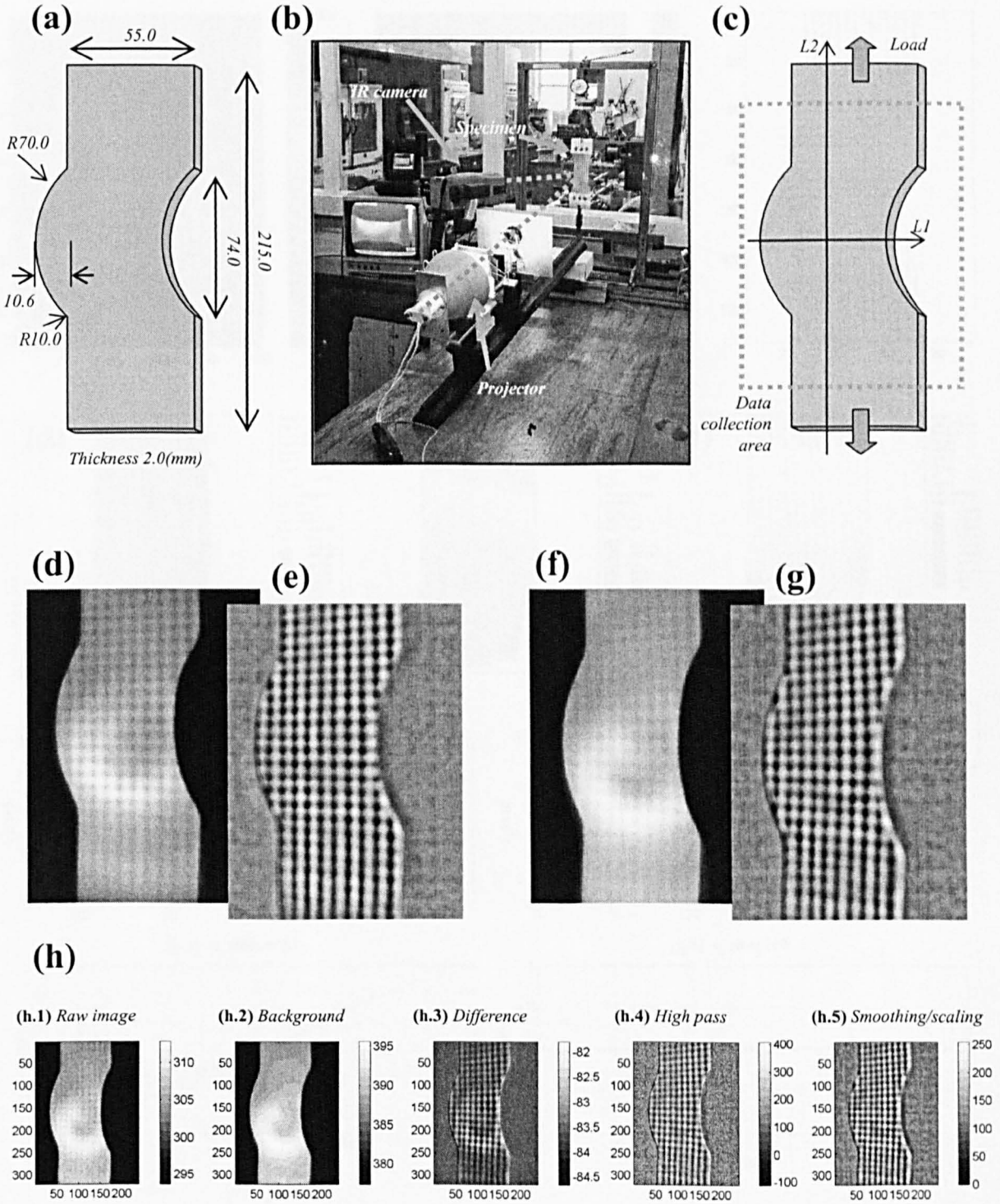

Figure 7.15: Deformation analysis using thermal marking with the projection prototype. (a) Geometry of the curved tie bar specimen. (b) Experimental set-up: the specimen was mounted in a loading frame, and viewed using an infrared camera. The projector prototype was positioned to the right of the IR camera to project patterned radiation. (c) Detail of the direction of the load and the data collection area. (d) Raw reference image. (e) Normalized reference. (f) Raw object image. A vertical tensile load was applied to produce 12.0*(mm)* relative displacement of the grips. (g) Normalized object. (h) Five steps of the normalization of the object image.

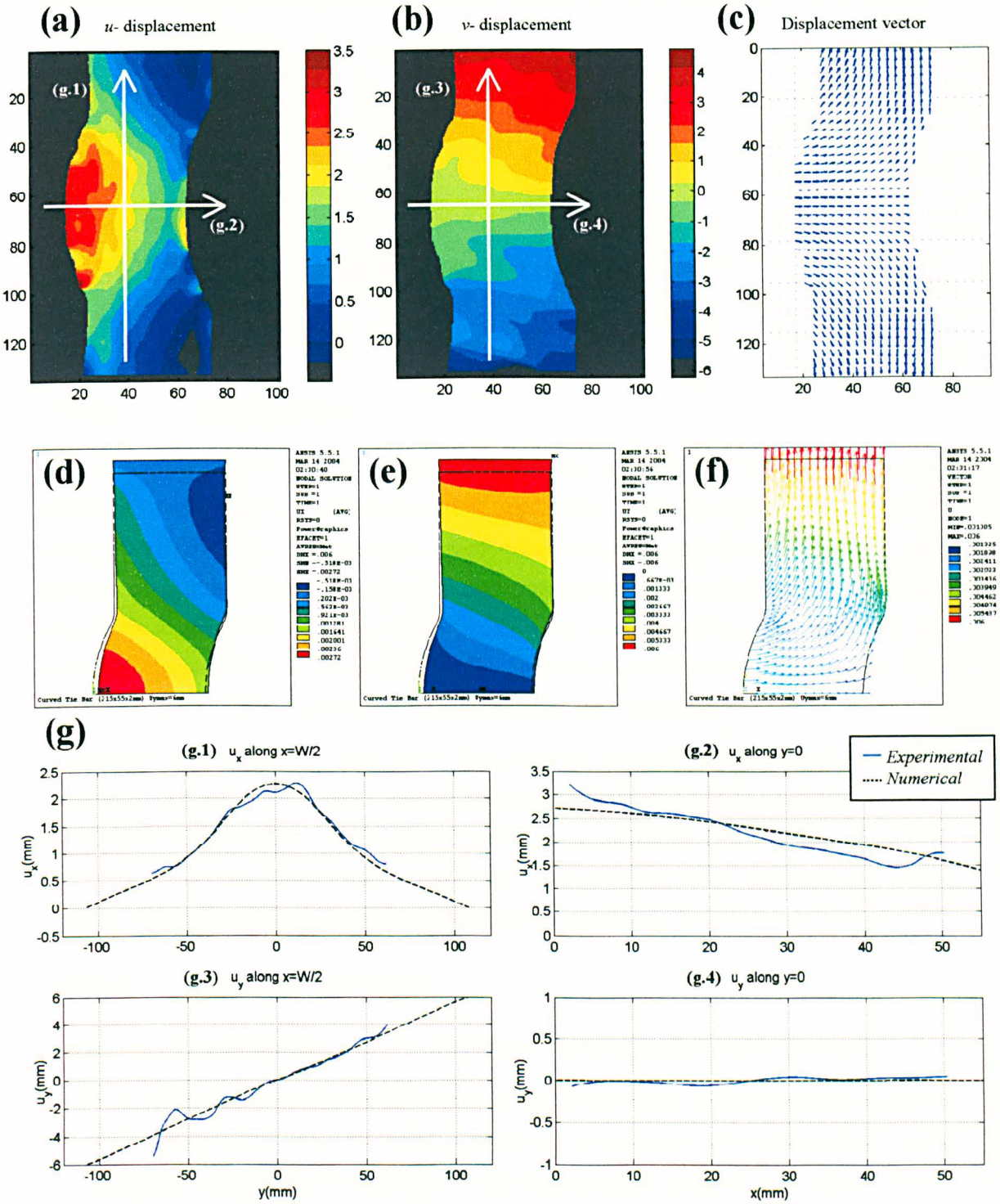

Figure 7.16: Experimental results: (a) Map of *u*-component of displacement, (b) map of *v*-component of displacement, and (c) displacement vector. Numerical results: (d) Map of *u*-component of displacement, (e) map of *v*-component of displacement, and (f) displacement vector. (h) Comparison of experimental results and numerical results.

CHAPTER VIII

DISCUSSION AND CONCLUSIONS

VIII.1 Introduction

The work presented in this thesis emphasizes how the versatility and simplicity of moiré techniques make them well-suited for routine application in industry. However, in order to apply them effectively in an industrial environment, it has been necessary to introduce and develop new tools and methodologies, by exploiting recent technological advances such as digital illumination and recording devices or the ever increasing computing capabilities of computer equipment for image processing. The goal was to build measurement systems that were robust and reliable, simple to use, easy to calibrate, and inexpensive.

The next section rounds up the main conclusions presented in each of the previous chapters. The most important points are brought together in a general discussion, and the degree of success with respect to the original aims is assessed, setting the scene for the conclusions presented in section VIII.3, and the contributions to knowledge listed in section VIII.4. The thesis concludes with the recommendations for future work presented in section VIII.5.

VIII.2 General Discussion

Let us repeat here the general aim of this research, as it was originally stated in section II.7.

- To develop the tools and procedures required for the fabrication of flexible, robust and low cost systems based on moiré techniques for the measurement of location, shape, and deformation of arbitrary objects, in both static and transient situations, and with the focus placed on industrial applications.
- To explore the combination of moiré techniques with other techniques from the fields of stress analysis (*e.g.* photoelasticity), non-destructive evaluation (*e.g.* infrared thermography), or machine vision (*e.g.* laser triangulation).

This general aim was reformulated into the following four measurable objectives:

1. The construction and testing of experimental apparatus more portable, robust, simple to use and flexible to allow the performance of measurements under a wide range of conditions, taking into account the requirements of simplicity, adaptability and robustness discussed in sections II.6.2 and II.6.4.

2. The design and implementation of new computational algorithms for fringe analysis, faster and fully automated so that they can be operated by a non-specialist, and more reliable to deal with adverse conditions such as the issues discussed in sections II.6.3 and II.6.5.

3. The development of a simple and foolproof methodology for the calibration of the system, the data collection and the interpretation of results, capable of addressing the issues regarding flexibility described in section II.6.4.

4. The conception of an innovative experimental technique for deformation measurement, based on a combination of concepts from moiré techniques and thermography, in order to overcome the limitations of the existing technologies for the fabrication of gratings for in-plane applications described in sections II.6.1 and II.6.5.

The work described in chapters III to VII attempted to address these objectives. These attempts have been mostly successful and the aims have been achieved.

Chapter III introduced the subject of adapting moiré techniques for industrial applications, presenting the development of a device for the detection of surface damage during in-service inspections of aircraft. A prototype device based on the shadow moiré technique was designed, built and tested on a range of specimens of different shapes and surface finishes.

The device produces a live moiré pattern that can be observed directly on the surface of the part and provides a clear indication of the location of defects under the visibility threshold, facilitating reliable detection. Defects below $5(mm)$ in diameter and $50(\mu m)$ in depth were successfully detected over an inspection area of $740(cm^2)$.

A quick estimate of defect size can be obtained by manually counting the fringes, and it is also possible to define a pass/no pass criterion by locking the light source arm in the device so as to fix the illumination angle. An automatic data processing technique was developed combining concepts from intensity-based and phase extraction fringe analysis in order to interpret the moiré images recorded with the device and to obtain quantitative measurements of defect size with an estimated accuracy of *ca.* $5(\mu m)$. The results were successfully validated with independent measurements of the defects by means of surface profilometry.

Chapter IV described in detail the apparatus, methodology of use, and data processing algorithms developed in this research to make possible the use of the fringe projection technique for full-field automatic measurement of shape in industrial applications reliably.

A novel five-step spatial algorithm for phase-extraction was introduced, which is computationally very efficient. The method uses a single image and is therefore suitable for the study of transient events. This algorithm was developed independently from similar algorithms existing in the literature (*e.g.* Sough *et al.*, 1990), and brings in unique advantages in terms of flexibility and reliability. A variant of the quality-guided unwrapping algorithm was also described for use in conjunction with the phase-extraction algorithm.

A number of calibration (*i.e.* phase-to-height conversion) expressions suitable for different optical configurations were also presented. An automatic calibration method was presented which had comparable accuracy and higher repeatability than the manual calibration, and was much faster and simpler to implement.

A detailed evaluation of the technique based on numerical and experimental studies was conducted to investigate the conditions of applicability, identify the main sources of error and estimate the accuracy. Random errors typically remained below 0.2*(rad)* in raw images, but could be reduced down to 0.08*(rad)* by normalizing the input images. Systematic errors inherent to the phase extraction algorithm, which vary cyclically with the period, and increase with the slope of the measured surface, were also identified. An expression to quantify these errors was derived analytically and the results confirmed in numerical and experimental tests. This error was typically below 0.3*(rad)* for slopes up to 80% of the maximum measurable range. Finally, other systematic errors related to the choice of calibration expression were studied experimentally. The simple telecentric approximation produced acceptable results in many cases, although the first order approximation with perspective correction was required to provide acceptable accuracy with finite optics. The limits of the technique in terms of minimal resolution of the fringes, the maximum measurable slopes, and errors near edges and surface discontinuities were investigated.

Chapter V dealt with the measurement of shape by means of the fringe projection technique, in objects with complex three-dimensional shape and unfavourable surface finish. Processing algorithms specifically developed for such situations, including the normalization and the automatic generation of masks by thresholding the quality map, were successfully demonstrated. Experimental results were presented with sub-millimetre accuracy.

A combined application of fringe projection and digital reflection photoelasticity was also introduced, in which fringe projection was used to evaluate the orientation of the component surface within the same reference system as the photoelastic data so as to correct oblique incidence and viewing effects. The modifications to the apparatus and experimental procedure required for this application were described, and a case study related to the study of vibration tests on turbine blades was presented to illustrate the technique. However, the conclusion was

that the potential gain in terms of accuracy would not normally justify the effort required to apply the correction, which involved applying stress-separation to the map of stress differences obtained by photoelasticity. This work represents however an advance in knowledge, and further development of the stress-separation methods may lead to an efficient technique that would represent a significant enhancement of existing methods of automated photoelastic analysis.

The measurement of out-of-plane displacements in the context of *in-vivo* tests of human skin was also demonstrated in Chapter V. The fringe projection technique is non-contact and non-invasive, and can deal with transient events, and was therefore uniquely suited for this application. A novel procedure was introduced to perform measurements of displacements non-parallel to the viewing direction. Experimental results were presented with a resolution better than 13*(pixels/mm)* over an observation area of *ca.* 15*(cm^2)*, and with an estimated accuracy of *ca.* 0.2*(mm)*.

Chapter VI described a measurement system that combined the fringe projection and the light spot techniques to obtain measurements of the shape and location in three-dimensional space of arbitrary components, in the context of NDE applications for the aerospace industry. Three real case studies were considered to define the requirements of the system.

The principles of the light spot technique were discussed, and the apparatus and methodology for the combined instrument described. A comprehensive example of location and shape measurement using a full-size complex shape component was presented, including system calibration in non-telecentric conditions, collection of shape and location data, and evaluation of the error. The accuracy of the experimental results was in line with the predictions made in Chapter IV. The integration of the geometrical information contained in the CAD model with the experimental measurements was also demonstrated. This opened the way for many potential applications, some of which were explored, including the automatic generation of scan trajectories for the inspection of complex components, and the use of the CAD model for dimensional control of manufactured parts.

An altogether new experimental technique for strain measurement named thermal moiré was presented in Chapter VII, which essentially consists of temporary imprinting a thermal grating on the surface of the part. Work on the development of laboratory apparatus to imprint thermal gratings by contact and by projection was described, and the feasibility of the two variant of the technique was illustrated with experimental results.

The proposed technique provides a fast, simple and non-invasive method of creating a temporary marking. In contrast to conventional moiré and image correlation methods, the new technique eliminates the need to bond, etch or print a grating or pattern onto the specimen,

which frequently cause permanent damage to the specimen and requires a substantial amount of skill and effort. The technique has potential applications for the analysis of living tissue in medicine and biology, and for non-contacting, non-invasive measurements in engineering, mainly for materials with low thermal diffusivity such as paper, rubber, or plastics.

This innovative technique offers significant advantages compared to other methods of experimental stress analysis, provides full-field data of the three components of displacement, and is truly non-invasive, requiring minimal or no surface preparation. This latter feature together with the possibility to operate with service loads provides the potential for non-contacting, non-invasive measurements, for in-service inspections in engineering and for the analysis of living tissue in medicine and biology.

The technique is uniquely suited to applications where permanent marking is undesirable. Two such examples are monitoring the deformation of paper sheets in the mills during manufacture, or the assessment of the mechanical properties of human skin *in vivo*.

The general method of thermal imprinting can potentially be used as well to convert other experimental techniques that require surface preparation, such as image correlation techniques, to totally non-invasive methods. Some suggestions for further research on this direction will be outlined in section VIII.5.

At the time of the preparation of this thesis, intellectual property disclosure had been made to the University of Sheffield, and the decision on patenting the projector design was pending. License discussions with Stress Photonics, Inc. were also in progress. The technique was also offered as a case study in a business planning module of a Masters course at the University of Sheffield with the aim to explore potential exploitation routes of the technology by the students.

The results of the work reported in this thesis have been presented to specialist international conferences in the UK and abroad. The publication of several articles in international scientific journals ensures worldwide dissemination of the most important findings. A list of the conference papers and publications in journals arisen from this research is included in Appendix AIII. The Appendix refers also to planned future publications, *i.e.* papers currently in review or in preparation.

VIII.3 Conclusions

A summary of the main conclusions of this work follows. A more detailed statement of each of the points can be found in the relevant chapter.

1. Moiré and other related techniques have a significant potential for applicability in a variety of industrial situations.

2. In particular, fringe projection is remarkably well suited for the determination of shape and out-of-plane deformations of arbitrary objects. This technique can be very versatile, robust, simple to use and precise provided the shortcomings described in section II.6 are overcome. Issues related to the experimental apparatus are discussed in Chapter IV. Fast and robust algorithms have been proposed to automatically process the fringe patterns, as described in sections IV.5.1 and IV.5.2. These algorithms are designed to work with a single image, and are therefore suitable for transient applications as demonstrated in section V.4. The flexibility of the system is due in part to the simple calibration procedure presented in section IV.5.3 and has been demonstrated in the wide range of applications described in chapters V and VI.

3. A new experimental technique for the measurement of deformation, born from an innovative combination of moiré and thermography has been proposed in Chapter VII. The details of the method, including elements of the fundamental study in section VII.4, the design of the apparatus in section VII.5, and novel algorithms for fringe processing in section VII.6 have been for the first time made public. The feasibility of the method has been demonstrated in several examples, and the experimental results have been successfully validated against analytical and finite element models.

4. The combination of fringe projection and triangulation using laser beams, allows the determination of the location and orientation of objects, as well as their shape. The principles and implementation of the combined technique have been described in Chapter VI, and a number of real case studies taken from the aerospace industry have been presented to demonstrate its feasibility.

5. The combination of fringe projection with reflection photoelasticity, described in section V.3 allows the determination of the full-field state of stress in the surface of real components of arbitrary complex geometry. The fringe projection technique provides shape information in the same frame of reference of the photoelastic data, which can be used to take into account oblique incidence and viewing effects.

6. The use of flexible gratings presented in Chapter III allowed extending the applicability of the shadow moiré technique to non-flat surfaces.

VIII.4 Contributions To Knowledge

1. Thermal markings have been used for the first time as a witness of deformation. A new technique to measure experimentally in-plane deformations has been proposed in Chapter VII. The technique, based on moiré and infrared thermography, essentially consists of applying a thermal pattern on the surface of the object of interest and observing the

distortion to the pattern upon loading of the component with the help of an infrared camera. This innovative technique is easy to use, fast, clean and non-invasive, opening the way for many exciting new applications in fields such as non-destructive testing and bioengineering.

2. A novel spatial phase stepping algorithm has been developed to interpret the fringe patterns obtained with the fringe projection technique. The algorithm is fast and uses a single image, hence it is appropriate to study transient events. An extensive analysis of the accuracy of the method has been presented in section IV.7.

3. A quick and robust version of the quality-guided algorithm for phase unwrapping has been implemented. The algorithm uses partial sorting in quality bins to reduce the number of computations.

4. A novel procedure for the calibration of the fringe projection system has been developed. The parameters necessary to obtain depth information from the phase map are obtained using calibration targets of known dimensions. This removes the need for accurate measurements of the optical parameters of the system, providing great flexibility to the system. The configuration of the elements can be rapidly changed and calibrated to adapt to a new problem.

5. A simple, robust and portable instrument for the determination of shape, location and out of plane deformation of arbitrary objects, based on the fringe projection technique, has been designed, constructed and demonstrated in a variety of industrial applications.

6. Two different prototypes have been developed for the generation of superficial thermal patterns, one by contact, and another one by radiation.

7. Processing algorithms based on the fast Fourier transform have been developed to interpret the thermal patterns and extract maps of displacement.

8. A prototype based on the shadow moiré technique for the detection of surface defects under the visibility threshold in aeronautical structures has been developed. The device uses a flexible grating to adapt to the inspection surface.

9. A combined instrument to collect fringe projection and photoelastic data within the same frame of reference has been built. The instrument can be used with stroboscopic illumination to collect data in vibrating components.

VIII.5 Recommendations For Future Research

Opportunities for future research have arisen in the form of lines of research that have been considered by the author but could not be fully pursued due to time constraints or limited

resources, and also in the form of advances that occurred during the research which could now be exploited:

1. In the opinion of the author, progress in electronics will tend to reverse the trend away from temporal methods and towards spatial methods for industrial applications, because the latter can be made more robust by moving the complexity away from the mechanical system and towards the electronics. Alternatively, temporal methods can also benefit from electronics-based solutions, which have the potential to simplify the apparatus by using standard off-the-shelf elements. For instance, the use of an LCD projector would provide a flexible, robust and compact solution for the projection of computer-generated gratings.

2. Further development of the pre-processing algorithms used to normalize the input images will increase the robustness and the reliability of the measurement system in unfavourable conditions. Alternative approaches to the extraction of the background and modulation terms from the fringe patterns, such as the technique based in Laplacian pyramids used by Sutton *et al.* (2001), could potentially be used in combination with the algorithm developed in this research to improve the results.

3. Shape measurement with the fringe projection technique is limited to the portion of the object surface visible from the point of view of the camera. The ability to compose depth maps of the same object obtained from different points of view would significantly extend the capabilities of the shape measurement system to analyse complex three-dimensional objects with negatives and sharp edges, and even to obtain the closed volume of an object. This approach has recently been successfully implemented in a range of commercially available measurement systems based on temporal phase-extraction algorithms (ATOS digityzing systems, GOM mbH, Braunschweig, Germany). The author initiated studies using this approach to apply the technique for the shape measurement of human faces, although further work in this direction would be required to develop the method.

4. A combination of fringe projection and digital reflection photoelasticity has been proposed in Chapter V to correct the errors due to oblique viewing and incidence in the photoelastic analysis of complex three-dimensional components. The technique however required a reliable method for stress-separation that could potentially be integrated in the system. Further research is required in this field, potentially leading to a system for automated photoelastic analysis, capable of automatic stress separation and correction for oblique effects. This would represent a significant enhancement of the existing technology.

5. The thermal moiré technique described in Chapter VII has the potential to provide information about both in-plane and out-of-plane components of displacement. However in a general case, data processing is necessary to isolate the out-of-plane component of

displacement contained in the two-dimensional thermal images. The author suggests the following procedure to achieve separation. (i) Imprint a thermal grating on the unloaded specimen, and record a thermal image IM1. (ii) Apply the load, and record a second image IM2 of the distorted grating. Note that the interference of these two images IM1 and IM2 (let's call it IN1) contains the information of both the in- and out-of-plane components of displacement. (iii) Maintain the load, until the thermal pattern degrades and disappears, imprint a fresh grating, and record a third image IM3. Note that the interference of IM1+IM3 contains information only about the out-of-plane component of displacement, because it is identical to what can be achieved with visible moiré. Let's call this interference IN2. Finally, (iv) isolate the in-plane component of displacement by combining the information from IN1 and IN2.

6. The use of image correlation algorithms for the analysis of thermal patterns was only briefly attempted in this research, in an effort to validate the processing algorithm developed for the analysis of thermal cross-gratings, which was described in section VII.6. However, such techniques appear very well suited for the application and should be further investigated.

7. Two methods for thermal imprinting have been proposed in Chapter VII. In addition to work on further optimization of the existing prototypes, at least two alternative approaches were conceived in this research, which are also worth of exploration. The first alternative is a method based on radiation heat transfer that makes use of infrared laser and diffraction optics to generate the gratings. This approach would potentially allow the generation of very fine thermal gratings, although there are health and safety concerns associated with the use of a sufficiently powerful laser.

8. A second interesting alternative for the generation of thermal patterns would be the use of mechanisms based on convection heat transfer, such as depositing or spraying a fluid onto the surface of the specimen, to cool down selected areas of the surface as the fluid evaporates. The thermal pattern thus generated would be random in nature, as opposed to the structured patterns that can be generated with the methods explored in this research (*i.e.* line gratings or dot arrays). The analysis of such random patterns would be best undertaken using image correlation techniques (Rastogi, 2000), rather than fringe pattern analysis techniques.

9. The thermal marking method demonstrated in Chapter VII opens up many potential industrial applications, which should be explored. The paper industry provides many good examples. For instance, the technique could help in the preventive maintenance of the paper rolls. Thermal markings, in the form of arrays of lines or dots, could be applied to the paper

and monitored down the line to measure the deformation of the paper thus detecting potential problems in the installation before the failure occurs.

REFERENCES

Andrews, D.R.; Shadow moiré contouring of impact craters; *Opt. Eng. 21, p650-654, (1982)*

Arai, Y., Yokozeki, S.; Improvement of measurement accuracy in shadow moiré by considering the influence of harmonics in the moiré profile; *Appl. Opt. 38, p3503-3507, (1999)*

Asserin, J., Zahouani, H., Humbert, Ph., Couturaud, V., Mougin, D.; Measurement of the friction coefficient of the human skin in vivo. ; *Quantification of the cutaneous smoothness. Colloids & Surfaces B: Biointerffaces, 19, p1-12, (2000)*

Barnes, R. B.; Diagnostic thermography; *Applied Optics, Vol. 7, p1673-85, (Sept. 1968)*

Bauman, J.U., R.E. Herron, eds.; *Proc. SPIE 1030 Biostereometric 88 – Fifth International Meeting, (1989)*

Becker, A.A., Wang, P., and Jones, I.A.; Application of inverse BE method to stress separation in photoelasticity; *Proc. SEM Annual Conf. On Exp. Mechanics, Milwaukee, USA, paper #26, (2002)*

Belgen, M.H.; Infrared radiometric stress instrumentation application range study; *NASA report cr-1067, Contract no. NAS 1-6082, NASA Langley research center, (1968)*

Benohanian, A.; Antiperspirants & Deodorants.; *Clinics in Dermatology. 19, p.398405, (2001)*

Benoit, P., Mathieu, E., Hormière, J., Thomas, A.; Characterization and control of three-dimensional objects using fringe projection techniques; *Nouv. Rev. Optique, 6(2), p67-86, (1975)*

Boehnlein, A.; US5307152: Moiré inspection system; *April, (1994)*

Bosboom, E.M.H., Hesselink, M.K.C., Oomens, C.W.J., Bouten, C.V.C., Drost, M.A., Baaijens, F.P.T.; Passive transverse mechanical properties of skeletal muscle under in vivo compression. ; *Journal of Biomechanics, 34, p1365-1368, (2001)*

Bradley, W. A.; Laterally loaded thin flat plates; *Trans. American Society of Civil Engineers, paper no. 3194 (1960) (1959)*

Brand, N.E., Gizoni, C.M.; Moiré contourography and infrared thermography - changes resulting from chiropractic adjustments ; *J. Manip. Physiol. Ther., Vol. 5, p113-116, (1982)*

Brooks, R. E. and L. O. Heflinger; Moiré Gauging Using Optical Interference Patterns; *Appl. Opt., 8(5), p935-939, (1969)*

Browne, A.L.; Fluid film thickness measurement with moiré fringes; *Appl. Opt. 11, p2269-2277, (1982)*

Buitrago, J., Durelli, A.J.; On the interpretation of shadow-moire fringes; *Exp. Mechanics, p221-226, (June 1978)*

Burguete, R. L., O'Brien, E.; Personal communication; *Airbus UK, Filton, (2001)*

Burguete, R. L.; Industrial applications of moiré methods for shape and deformation measurement ; *The Rank Prize Funds Symposium on Optical Metrology Techniques for Industrial Applications, Grasmere(UK), (April 2002)*

Busse, G.C., Wu, D.C., Karpen, W.C.; Thermal wave imaging with phase sensitive modulated thermography; *J. Appl. Phys., Vol. 71, p3962-3965, (1992)*

Cabaj, A. Ranninger, G. Windischbauer, G.; Shadowless moiré topography using a single source of light; *Applied Optics Vol.13, No.4, p722-723, (April 1974)*

Cárdenas-García, J. F., Zheng, S., Shen, F. Z.; Implementation and use of an automated projection moiré experimental set-up; *Optics & Lasers in Engineering, Vol. 21, p77-98, (1994)*

Case, S. K., J. A. Jalkio, and R. C. Kim; 3-D Vision System Analysis and Design ; *in Three-Dimensional Machine Vision, Takeo Kanade, Ed., Kluwer Academic Publishers,Norwell, MA, p63-95, (1987)*

Chan, P. H., Bryanston-Cross, P. J.; Spatial phase stepping method of fringe-pattern analysis; *Optics and Lasers in Engineering, 23, p343-354, (1995)*

Chiang, F.P.; A shadow moiré method with two discrete sensitivities; *presented at SESA spring meeting, Chicago, May 11-16 (1975)*

Cielo, P.; ; *J. Appl. Phys. 56, 230 (1984)*

Cline, H.E., Holik, A.S., Lorensen, W.E.; Computer-aided surface reconstruction of interference contours; *Applied Optics Vol. 21, No.24, p4481-4488, (December 1982)*

Cline, H.E., Lorensen, W.E., Holik, A.S. ; Automatic moiré contouring; *Applied Optics Vol.23, No.10, p1454-1459, (May 1984)*

Cloud, G. L.; Optical methods of engineering analysis; *Cambridge University Press, Cambridge, (1998)*

Cramer, K.E., Winfree, W.P.; Thermographic imaging of cracks in thin metal sheets.; *Thermosense XIV Eklund, J.K. Editor Proc. SPIE Vol. 1682, p162-170, (1992)*

Creath,K; A comparison of phase-measurement algorithms; *Proc. SPIE, 680, 19 (1986)*

Dally J. W. Riley, W. F.; Experimental stress analysis; *Mc Graw Hill, (1991)*

Dantu, P.; Recherches diverses d'extensometrie et de determination des contraintes; *Anal. Contraintes, Mem. GAMAC, tome 2, no.2, p3-14, (1954)*

Den Hartog, J.P.; Advanced strength of materials; *Dover Publications, Inc., New York, (1952)*

Der Hovanesian, J., Hung, Y.Y.; Moiré contour-sum, contour-difference, and vibration analysis of arbitrary objects.; *Appl. Opt., 10(12), p2734-2738 (1971).*

Der Hovanesian, J., Hung, Y.Y.; Moiré contour-sum, contour-difference, and vibration analysis of arbitrary objects; *Appl. Optics, Vol. 10, No.12, p2734-2738, (Dec. 1971)*

Dessus, B., LeBlanc, M.; The fringe method and its application to the measurement of deformations, vibrations, contour lines and difference of objects; *Opt. Electron. 5, p369-390, (1975)*

Dirck J.J, Decraemer, W.F.; Human tympanic membrane deformation under static pressure; *Hear. Res. 51, p93-105, (1991)*

Doty, J.L.; Projection moiré for remote contour analysis; *J. Opt. Soc. Am., Vol. 73, No.3, p366-372, (March 1983)*

Dulieu-Barton, J.M.; Introduction to thermoelastic stress analysis; *Strain, 35, 2, p35-39, (May 1999)*

Durelli, A.J., Parks, V.J.; Moiré Analysis of Strain; *Prentice-Hall, Englewood Cliffs, NJ, (1970)*

Dykes, B.C.; Analysis of displacements in large plates by the grid-shadow moiré techniques; *Proc. 4h Int. Symp. Moiré fringe topography and spinal deformity, Munster, W. Germany, (1971)*

Faugeras, O.; Three-Dimensional Computer Vision, a geometric viewpoint; *MIT Press, (November 19, 1993)*

Forno, C.; Deformation measurement using high resolution moiré photography; *Optics and Lasers in Engineering 8, p189-212, (1988)*

Gao B.Z., Schulz O., Pandya S., Hwang, N.H.C.; A Structured Light Technique for Monitoring Bioprosthetic Heart Valve Leaflet Surface Contours; *Cardiovascular Engineering: An International Journal, vol. 1, no. 1, p3-13, (March 2001)*

Gasvik, K. J.; Optical Metrology; *Wiley, Chichester, (1987)*

Ghiglia, D. C., Pritt, M. D.; Two-dimensional phase unwrapping; *Wiley-Interscience, New York, (1998)*

Greene, R.J,. Patterson, E.A.; Industrial applications of combined thermo-photo-elasticity; *Proc. SEM Annual Conf. On Exp. Mechanics, Milwaukee, USA, paper #101, (2002)*

Guild, J.; Diffraction Gratings as Measuring Scales; *Oxford University Press, London (1960)*

Guild, J.; The Interference Systems of Crossed Diffraction Gratings; *Clarendon Press, Oxford, (1956)*

Halioua, M., Krishnamurthy, R. S., Liu, H. Chiang, F. P.; Projection moiré with moving gratings for automated 3-D topography; *Applied Optics Vol. 22, No. 6, p850-855, (March 1983)*

Halioua, M., Liu, H.C.; Optical Three-Dimensional Sensing by Phase Measuring Profilometry; *Opt. Lasers Eng., 11(3), p185-215 (1989)*

Harding K.G., M. Michniewiccz A. Boehnlein; Small angle moiré contouring; *Proc. SPIE 850, p166-173, (1988)*

Harding, K.G., R. Tait; Moiré techniques applied to automated inspection of machined parts; *Proc. SME Vision'86 Conf, (1986)*

Hariharan,P., Oreb,B.F., Eiju, C.H.; Digital phase-shifting interferometry: a simple error-compensating phase calculation algorithm; *Appl. Opt., 26, 2504 (1987)*

Harwood, N., Cummings, W.M.; Thermoelastic Stress Analysis; *IOP Publishing Ltd, Bristol, (1991)*

Heida, J.H., Bruinsma, A.J.A.; D-Sight technique for rapid impact damage detection on composite aircraft structures; *7th European Conference on Non-Destructive Testing, Copenhagen, Denmark, 26-29 May (1998)*

Heredia Ortiz, M., Patterson, E. A.; Moiré and fringe projection testing methods for aerospace applications; *Proc. SEM Annual Conf. On Exp. Mechanics, Milwaukee, USA, paper #96, (2002)*

Heredia Ortiz, M., Patterson, E. A.; Fringe projection for optical path length correction in reflection photoelasticity; *Proc. BSSM Conf. on Strain measurement in the 21st Century, Lancaster, UK, (2001)*

Holman, J.P.; Heat Transfer; *8th Ed. Mc Graw Hill, New York, (1997)*

Holzaphel, G.; Biomechanics of soft tissue; *In Handbook of Material Behaviour Models. Academia Press, (2001)*

Hovanesian, J. Der, Haskell, R.E., and Powell, R.L.; Use of a projected-ruling moiré method for vibration and deflection measurement of three-dimensional structures; *Proc. Eng. Applications of holography (Symposium), Los Angeles, USA, Feb. 16-17, (1972)*

Hudson, R.D., Hudson, J.W., eds; Infrared detectors; *Dowden, Hutchinson & Ross, (1975)*

Huntley, J.M.; Automated fringe pattern analysis in experimental mechanics: a review; *J. Strain Anal. Eng. Design, Vol. 33, p105-125, (1998)*

Idesawa, M., Yatagai, T., Soma, T.; Scanning moiré method and automatic measurement of 3-d shapes; *Applied Optics Vol.16, No.8, p2152-2162, (August 1977)*

Ikeda, T. H. Terada; Development of the moiré method with special reference to its application to biostereometrics; *Opt. Laser Technol. 13, p302-306, (1981)*

Indebetouw, G.; Profile Measurement Using Projection of Running Fringes; *Appl. Opt., 17(18), 2930-2933 (1978)*

INDUCE Confidential report: Alvaro, M., Cortes, V.; Requirements' Definition for 3D-Moiré; *CR-2210-CASA-02, (March 2000)*

INDUCE Confidential report: Heredia, M., Patterson, E.A.; Operational requirements; *TR-4211-UofS-02, (July 2000)*

Judge, T. R., Bryanston-Cross, P.J.; A review of phase-unwrapping techniques for fringe analysis; *Optics & Lasers in Engineering, Vol. 21 p199-239, (1994)*

Kähler, K., Haber, J., Seidel, H.-P.; Reanimating the dead: reconstruction of expressive faces from skull data; *ACM Transactions on Graphics (SIGGRAPH 2003 Conference Proceedings), 22(3), (2003)*

Kao, T. Y., and Chiang, F. P.; Family of grating techniques of slope and curvature measurements for static and dynamic flexure of plates.; *Optical Engineering, 21, 4: 721-42. (1982)*

Kenny, B.; The casting of a low exotherm epoxy resin; *J. Sci. Instruments, V. 42, p719-720, (Sept. 1965)*

Khetan, R. P.; Applications of projection moiré methods; *Doctoral dissertation, Stony Brook, NY, State University of New York (1975)*

Kim, S. W., Y. B. Choi J. T. Oh; Reverse engineering: high-speed digitisation of free-form surfaces by phase shifting grating projection moiré topography; *Int. J. Machine Tools & Manuf. 39, p389-401, (1999)*

Klette, R., Koschan, A., Schluns, K. ; Computer vision: three-dimensional data from images; *Springer-Verlag New York; London (1998)*

Kobayashi, A. S. (Ed.); Handbook on experimental mechanics; *Prentice-Hall, Englewood Cliffs, NJ, (1987)*

Kokidko D., Gee L., Chou S.C., Chiang F.-P.; Method for measuring transient out-of-plane deformation during impact; *Int. J. Impact Engng. 19, (2), p127-133, (1997)*

Lesniak, J.R., Bazile, D.J., Zickel, M.J.; Theory and application of coating tolerant thermography.; *Thermosense XX SPIE AeroSense Symposium, (1998)*

Lesniak, J.R., Bazile, D.J., Zickel, M.J.; Structural integrity assessment via coating tolerant thermography; *SPIE Aging Infrastructure Conference in Phoenix, A, (1996)*

Lesniak, J.R., Boyce, B.R.; Forced diffusion thermography; *Non-destructive inspection of aging aircraft, San Diego, Valley, M., del Grande, N., Kobayashi, A., Proc. SPIE Vol. 2001, p92-102, (1993)*

Ligtenberg, F. K.; The Moiré Method; *Proc. Soc. Exp. Stress Anal. (SESA), 12(2), 83-98 (1955)*

Ligtenberg, F.K.; The moiré method: a new experimental method for the determination of moments in small slab models; *Proc. SESA, 12, no. 2, p83-98 (1954)*

Malacara, D.; Optical shop testing; *Wiley-Interscience, 2nd. ed. (1992)*

Maldague, X.A.; Theory and practice of infrared technology for nondestructive testing; *John Wiley and Sons Ltd, New York, (2001)*

Maldague, X.A., Marinetti, S.A.; Pulse phase infrared thermography; *J. Appl. Phys., Vol. 79, p2694-2698, (1996)*

Maldague, X.A., Moore, P.O.; Infrared and thermal testing; *3rd ed. Nondestructive testing handbook Vol. 3, American Society for Nondestructive Testing, Columbus (2001)*

Marasco, J.; Use of curved grating in shadow moiré; *Exp. Mech. 15, p464-470, (1975)*

McKelvie, K.; Moiré strain analysis: an introduction, review and critique, including related techniques and future potential; *Journal of strain analysis Vol. 33, No. 2, p137-151, (1998)*

Meadows, D.M., Johnson, W.O., and Allen, J.B.; Generation of surface contours by moiré patterns; *Appl. Opt., 9(4), 942-947 (1970)*

Moore, D.T., Truax, B.E.; Phase-locked moiré fringe analysis for automated contouring of diffuse surfaces; *Applied Optics Vol.18, No.1, p91-96, (1979)*

Morse, S., Durelli, A.J., Sciammarella, C.A.; Geometry of moiré fringes in strain analysis; *J. Eng. Mech. Div., ASCE, vol. 86, no. EM4, p105-126, (1960)*

Oppel, G.; Polarisationsoptische untersuchung raumlicher spannungs- und dehnungszustande; *Forsch. Geb. Ingenieurw., vol. 7, p240-248, (1936)*

Oreb, B.F., Larkin, K.G., Fairman, P.S., Ghaffar, M. ; Moiré based optical surface profiler for the minting industry. ; *SPIE Conference on Interferometry: Surface Characterisation and Testing, 1776, (1992)*

Pacey, M.N., Haake, S.J., Patterson, E.A.; A Novel Instrument for Automated Principal Strain Separation in Reflection Photoelasticity; *Journal of Testing and Evaluation, 28(4): 229-235 (2000)*

Parks, V. J., and Durelli, A. J.; Moiré patterns of partial derivatives of displacement components.; *Journal Applied Mechanics, E33, 4: 901-6. (1966)*

Patorski, K.; The Handbook of the Moiré Fringe Technique; *Elsevier, Oxford; (1993)*

Patterson, E.A.; Digital photoelasticity: principles, practice and potential; *Strain, Vol. 38, No.1, p27-39, (2002a)*

Patterson, E.A.; Personal communication; *Dept. Mech. Eng., U. of Sheffield, (2002b)*

Patterson, E.A., Wang, Z. F.; Towards full field automated analysis of complex components; *Strain, Vol. 27, No. 2, p49-56, (May 1991)*

Pekelsky, J.R.; Automated contour ordering moiré topograms for biostereometrics; *Biostereometrics 85 (ed. A.M. Coeblentz and R.E. Herron), Proc. SPIE, 620, p6-17, (1986)*

Pelletier, J.F., Maldague, X.F.; Shape from heating: a two-dimensional approach for shape extraction in infrared images; *Opt. Eng., Vol. 36, p370-375, (1997)*

Perrin, J.C., Thomas, A.; Electronic Processing of Moiré Fringes: Application to Moiré Topography and Comparison with Photogrammetry; *Appl. Opt., 18(4),563-574 (1979)*

Pirodda, L.; Shadow and projection moiré techniques for absolute or relative mapping of surface shapes ; *Opt. Eng., Vol. 21, No.4, p640-649, (July 1982)*

Pirodda. L.; Principie applicazioni du un metodo fotogrametrico basato sull'impiego del moiré; *Rivista di Ingegneria, Vol.12, (Dec. 1969)*

Polsky, Y.C., Ume, I.C.; Thermoelastic modeling of a PWB with simulated circuit traces subjected to infrared reflow soldering with experimental validation ; *J. Electron. Packag., Vol. 121, p263-270, (1999)*

Post, D.; Developments in Moiré Interferometry.; *Opt. Eng., 21(3), 458-467 (1982)*

Post, D.; Moiré interferometry in white light; *Appl. Optics, 18, 24, p4163-4167, (1979)*

Post, D.; The moiré grid-analyser method for strain analysis; *Exp. Mech., vol. 5, no. 11, p368-377, (1965)*

Post, D.; The Moiré Grid-Analyzer Method For Strain Analysis; *Exp. Mech., vol. 5, no. 11, p368-377, (1965)*

Post, D., Han, B. Ifju, P.; High sensitivity moiré; *Springer-Verlag, (1994)*

Rastogi, P.K. (Ed.); Photomechanics ; *Berlin, London, Springer (2000)*

Rayleigh, Lord; On the Manufacture and Theory of Diffraction-Gratings; *Phil. Mag. SA, 47(310) p81-93 and p193-205 (1874)*

Reid, G.T.; Moiré fringes in metrology; *Opt. Lasers Eng., 5(2), p63-93 (1984)*

Reid, G.T., Rixon, R.C., Messer, H.I. ; Absolute and comparative measurements of three-dimensional shape by phase measuring moiré topography. ; *Opt. & Laser Technology, 16, p315-319, (1984)*

Righi, A.; Sui Fenomeni Che si Producono colla Sovrapposizione dei Due Reticoli e sopra Alcune Lora Applicazioni: I; *Nuovo Cim., 21, 203-227 (1887)*

Robinson, D.W., Reid, G.T.; Interferogram analysis - digital fringe pattern measurement techniques, ; *Institute of Physics Publishing, (1993)*

Roddier, C., Roddier, F. ; Interferogram analysis using Fourier transform techniques; *Applied Optics Vol. 26, No. 9, p1668-1673, (May 1987)*

Rowe, S. H. and W. T. Welford; Surface Topography of Non-Optical Surfaces by Projected Interference Fringes; *Nature, 216(5117), p786-787 (1967)*

Sciammarella, C.A., Durelli, A.J.; Moiré fringes as a means of analysing strains; *J. Eng. Mech. Div., ASCE, vol.87, no. EM1, p55-74, (1961)*

Sciammarella, C.A., Lamberti, L., Sciammarella, F.M.; High accuracy contouring using grating projection; *in Proc. XXX Convegno Nazionale AIAS, Alghero, p811-820, (Sept. 2001)*

Scotese, A.D., Huang, S.L.; Low velocity impact damage detector for composite laminated structures; *USAF Structural Integrity Program Conference, San Antonio, TX, (1988)*

Shagam, R.; Heterodyne Interferometric Method for Profiling Recorded Moiré Interferograms; *Opt. Eng., 19(6), p806-809 (1980)*

Shough, D.M., Kwon, O.Y., Leary, D.F.; High-speed interferometric measurement of aerodynamic phenomena; *SPIE Vol. 1221, Propagation of High Energy Laser Beams through the Earth's Atmosphere, p394-403, (1990)*

Soares, O.D., Fernández, J.C., Grosmann, M.; Asymmetries in podomoirégraphy; *Proc. SPIE 370, p138-142, (1982)*

Starck, J., Hilton, A., Illingworth, I.; Reconstruction of animated models from images using constrained deformable surfaces; *10th Conf. on Discrete Geom. for Comp. Imag., Lecture Notes in Computer Science, Springer-Verlag, Vol. 2301, pp 382-391, (2002)*

Stiteler, M.R., Ume, I.C.; System for real-time measurement of thermally induced PWB/PWA warpage ; *J. Electron. Packag., Vol. 119, p1-7, (1997)*

Sutton, M.A., Zhao, W., McNeill, S.R., Schreier, H.W., Chao, Y.J.; Development and assessment of a single-image fringe projection method for dynamic applications; *Exp. Mechanics, 41(3), p205-217, (Sept. 2001)*

Takasaki, H. ; Moiré topography from its birth to practical application; *Opt. Lasers Eng. 3, p3-14, (1982)*

Takasaki, H.; Moiré topography; *Applied Optics Vol. 12, No. 4, p845-850, (April 1973)*

Takasaki, H.; Moiré topography; *Applied Optics Vol. 9, No. 6, p1467-1472, (June 1970)*

Takeda, M., H. Ina, and S. Kobayashi; Fourier-Transform Method of Fringe-Pattern Analysis for Computer-Based Topography and Interferometry; *J. Opt. Soc. Am., 72(1), 156-160 (1982)*

Takeda, M., Mutoh, K.; Fourier transform profilometry for the automatic measurement of 3-d object shapes; *Applied Optics 22, 24, p3977-3982 (1983)*

Theocaris, P.S.; Moiré fringes in strain analysis; *Pergamon Press, New York (1969)*

Theocaris, P.S.; Moiré fringes: a powerful measuring device; *Appl. Mech. Rev., 15(5), p333-339 (1962)*

Theocaris, P.S.; Moiré patterns of isopachics; *J. Sci. Instrum., 41, no. 3, p133-138, (1964a)*

Theocaris, P.S.; Isopachic patterns by the moiré method; *Exp. Mech., 4, 6, p153-159, (1964b)*

Tollenaar, D.; Moire: Interferentieversschijnselen bij Rasterdruk; *Amsterdam Instituut voor Grafische Techniek, Amsterdam, (1945)*

Trucco, E., Verri, A.; Introductory techniques for 3-D computer vision; *Prentice Hall 1st edition (March 6, 1998)*

Ume I.C.; US patent no 5835223: System for measuring surface flatness using shadow moiré technology; *Nov. 10, (1998)*

Wang Z., Tan, Y., Zhao, H., Chen, W.; Frequency-shifting shadow moiré technique; *Proc. SPIE 3479, p130-137, (1998)*

Wang, Z.F. Patterson, E.A.; Use of phase-stepping with demodulation and fuzzy sets for birefringence measurement.; *Optics and Lasers in Engineering, 22, p91-104, (1995)*

Wasowski, J.; Moiré topographic maps; *Opt. Commun., 2(7), p321-323 (1970)*

Weissman, E.M.; Experimental tyre mechanics by moiré; *Opt. Lasers Eng. 13, p117-126, (1990)*

Welford, W. T.; Some applications of projected interference fringes; *Opt. Acta, 16(3), p371-376 (1969)*

Weller, R., Shepard, B.M.; Displacement measurement by mechanical interferometry; *Proc. SESA, vol 6, no. 1, p35-38, (1948)*

Wright, H.C.; Infrared techniques; *Oxford University Press, (1973)*

Wu, J.Z., Dong, R.G., Rakheja, S., Schopper, A.W.; Simulation of mechanical responses of fingertip to dynamic loading. ; *Medical Engineering & Physics, 24, p253-264, (2002)*

Wykes, C. Morshedizadeh, R.; Surface topography measurement using digital moiré contouring - errors and limitations; *Proc Instn Mech Engrs Vol 209, p317 (1995)*

Yagatai, T., Idesawa, M.; Automatic fringe analysis for moiré topography; *Optics & Lasers in Engineering 3(1), p73-83, (1982)*

Zandman, F. Wood, M.R.; Photostress; *Product Engineering, 27, p167-178, (1956)*

APPENDICES

AI Five-Step Spatial Phase Measurement Algorithm

AI.1 Generalized Five-Step Algorithm

Temporal and spatial phase measurement methods for fringe pattern analysis are conceptually very similar. In both cases, the starting point is a phase-modulated signal I that can be described as follows

$$I = A + B\cos(\Phi + \lambda) \tag{A1.1}$$

where A, B, and Φ are unknown constant terms, I is the measurable signal and λ is a phase carrier term. It is assumed that the value of the signal I can be measured, and the value of the phase carrier λ can be controlled by some means.

The goal of these methods is to obtain the modulated phase Φ from measurements of the signal I. This can be accomplished by measuring the signal I for at least three different known values of the phase carrier λ and solving the resulting system of equations for the three unknowns A, B, and Φ. Some methods use more than three measurements of I to produce an over-deterministic system, which is more stable in the presence of experimental error.

The five-step algorithm, originally developed by Hariharan for temporal phase shifting, is presented in the following in a generalised form. The method uses five measurements $I_1,\ldots,I_5$ of the signal, performed at equispaced phase-shifts of the carrier of value α.

$$\begin{aligned} I_1 &= A + B\cos(\Phi - 2\alpha) \\ I_2 &= A + B\cos(\Phi - \alpha) \\ I_3 &= A + B\cos(\Phi) \\ I_4 &= A + B\cos(\Phi + \alpha) \\ I_5 &= A + B\cos(\Phi + 2\alpha) \end{aligned} \tag{A1.2}$$

The method combines these measurements in the following expression to estimate the phase:

$$\Phi^* = \arctan\frac{2(I_2 - I_4)}{2I_3 - I_5 - I_1} \tag{A1.3}$$

The expression of the estimate can be obtained by substitution,

$$\Phi^* = \arctan\frac{2(A + B\cos(\Phi - \alpha) - A - B\cos(\Phi + \alpha))}{2A + 2B\cos\Phi - A - B\cos(\Phi + 2\alpha) - A - B\cos(\Phi - 2\alpha)} \tag{A1.4}$$

Cancelling terms and operating yields

$$\Phi^* = \arctan\frac{2\cos(\Phi - \alpha) - 2\cos(\Phi + \alpha)}{2\cos\Phi - \cos(\Phi + 2\alpha) - \cos(\Phi - 2\alpha)} \tag{A1.5}$$

Which upon further processing can be reduced to

$$\Phi^* = \arctan\left(\frac{\tan\Phi}{\sin\alpha}\right) \tag{A1.6}$$

For the case $\alpha=\pi/2$ the above expression reduces to

$$\Phi^* = \arctan(\tan\Phi) = W\{\Phi\} \tag{A1.7}$$

where $W\{\}$ represents the wrapping operator (*i.e.* $W\{\Phi\}=\Phi+K\pi$, K being the integer that makes $W\{\Phi\}\in[-\pi,\pi]$).

AI.2 Application To The Analysis Of Projected Fringes

The intensity distribution I of an image of projected fringes of pitch p can be described by the following equation

$$I(x,y) = A + B\cos\left(\frac{2\pi}{p}x + \Phi\right) \tag{A1.8}$$

Here the modulated phase Φ contains the information relative to the surface shape, and the terms that account for non-planar contours in non-telecentric configurations, as discussed in section II.3.2.4.

Comparison of the previous expression with eq. (A1.1) reveals some parallelisms. In this case the measurable signal corresponds to the intensity distribution I of the image. Also, one can define a spatial carrier term by making $\lambda=\lambda(x)=2\pi x/p$, where p is the pitch of the projected fringes, so that horizontal translation steps in the image of value $x=p/4$ provide the desired $\pi/2$ phase shifts, *e.g.*

$$
\begin{aligned}
&I(x+p/4,y)= \\
&=A+B\cos\left(\frac{2\pi}{p}(x+p/4)+\Phi\right) \\
&=A+B\cos\left((\frac{2\pi}{p}x+\Phi)+\frac{\pi}{2}\right)
\end{aligned}
\tag{A1.9}
$$

Similar expressions can be derived for the five phase-shifted measurements required for the method and defined in eq. (A1.2), resulting in

$$
\begin{aligned}
&I_1(x,y)=I(x-p/2,y) \\
&I_2(x,y)=I(x-p/4,y) \\
&I_3(x,y)=I(x,y) \\
&I_4(x,y)=I(x+p/4,y) \\
&I_5(x,y)=I(x+p/2,y)
\end{aligned}
\tag{A1.10}
$$

AI.3 First Order Approximation Analysis Of The Error

In the previous derivation we assumed that A, B and Φ were constant. In our application, A and B are the background intensity and the amplitude modulation of the fringe pattern, which may vary across the field of view of the image.

More significantly, the modulated phase term Φ encodes the information about the surface shape, and will be a function of position in any other than the trivial case of a flat plate perpendicular to the viewing axis. We consider here a first order approximation to illustrate the errors of the phase measurement associated to this hypothesis. The following expression assumes that the modulated phase is locally a linear function of x

$$
I(x)=A+B\cos\left(\frac{2\pi}{p}x+mx+n\right)
\tag{A1.10}
$$

One can calculate the effect associated to a translation $x=p/4$

$$
\begin{aligned}
&I(x+p/4)= \\
&=A+B\cos\left(\frac{2\pi}{p}(x+p/4)+m(x+p/4)+n\right) \\
&=A+B\cos\left((\frac{2\pi}{p}x+mx+n)+\frac{\pi}{2}+m\frac{p}{4}\right)
\end{aligned}
\tag{A1.11}
$$

Therefore the phase shift can be written as

$$\alpha = \frac{\pi}{2} + \xi \tag{A1.12}$$

where $\xi = mp/4$ is the error incurred by the method in the phase shift, which is proportional to the slope of the modulated phase and the pitch of the carrier.

We can substitute this in eq. (A1.6) to obtain an expression for the phase estimator provided by the method in this case

$$\Phi^* = \arctan\left(\frac{\tan\Phi}{\sin\left(\frac{\pi}{2} + \xi\right)}\right) \tag{A1.13}$$

An alternative interpretation of the error can be obtained by inspecting eq. (A1.10) and noting that the linear change in phase produces a change in the pitch of the observed fringes. One can define the pitch p' of the resulting fringe pattern

$$\begin{aligned} I(x) &= \\ &= A + B\cos\left(\left(\frac{2\pi}{p} + m\right)x + n\right) \\ &= A + B\cos\left(\frac{2\pi}{p'}x + n\right) \end{aligned} \tag{A1.14}$$

and comparing the two expressions one can write m in terms of p and p'

$$\begin{aligned} \frac{2\pi}{p} + m &= \frac{2\pi}{p'} \\ m &= 2\pi\frac{p - p'}{pp'} \end{aligned} \tag{A1.15}$$

Substituting m in ξ yields an expression of the error as a function of the change in pitch between the reference and the object images

$$\xi = \frac{mp}{4} = \frac{\pi}{2}\frac{p - p'}{p'} \tag{A1.16}$$

Substituting this in eq. (A1.13) yields an expression of the phase estimator as a function of the relative change in pitch between the reference and the object images

$$\Phi^* = \arctan\left(\frac{\tan\Phi}{\sin\left(\frac{p}{p'}\frac{\pi}{2}\right)}\right) \qquad \text{(A1.17)}$$

Figure A1.1 shows graphical representations of equations A1.13 and A1.17. The error function is periodic with twice the frequency of the object image, it has zero amplitude at $m=0$ or $p/p'=1$, and increases as one moves away from that point. Note that the error function presents singularities for $m=\pm 2\pi/p$ in eq. (A1.13), which correspond respectively to $p'=p/2$ and $p'=\infty$ in eq. (A1.17). Near these limits, the lower term in the fraction tends towards zero, and the error function reaches a maximum of $\pm\pi/2$ (rad). Beyond that, the argument of the arctan changes sign, and as a result the sign of the phase estimator appears inverted with respect to the true value of the phase.

AI.4 Conclusions

It can be concluded that the proposed phase measurement algorithm can provide an estimate of the true value of the phase at each point in the image by sampling the intensity at five points distributed at $p/4$ intervals along a horizontal line of the image with centre in the point of interest.

The algorithm provides principal values of phase, *i.e.* values in the interval $[-\pi,\pi]$, which need to be unwrapped to obtain a continuous phase map.

The estimate of the phase will only be exact if the background intensity and the amplitude modulation of the fringe pattern terms A and B, and also the modulated phase term Φ are constant for the five points sampled by the algorithm.

Non-uniformities of the terms A, B, and Φ will result in errors in the measurement of the phase value.

An expression of the estimated phase has been derived in first order approximation (*i.e.* considering linear variation) for the case of non-uniform Φ to evaluate the error. The effect of a linear variation in the phase is equivalent to introducing an error in the phase shift proportional to the slope of the phase and the pitch p of the projected fringes. An alternative expression of the estimated phase in terms of the relative change in pitch between the reference and the object images has also been produced.

AII JOSHUA Software For Fringe Pattern Analysis

JOSHUA is a software application written in MATLAB language and compiled into a stand-alone software package that runs under Window based operating system. The installation creates two different shortcuts in the Program launcher. The *JOSHUA X.X.X* shortcut allows running the software directly under Windows. The *Console* shortcut opens a MS-DOS windor and allows running the program with command line arguments. Calling the program with the *–h* modifier displays help describing the options available.

AII.1 Welcome Screen And Main Menu

Launching the program opens the *Welcome* screen shown in fig. AII.1(a) and the *Main Menu* window in fig. AII.1(b). The four menu options available are *File*, *Action*, *View* and *Help*.

AII.2 File Menu

The *File* menu, fig. AII.1 (b.1), has three options: Batch processing, Preferences and Exit.

AI.1.1 Batch Processing

The *Batch processing* option launches the *Open File* dialog to select a text file containing the processing parameters required to carry out automatic batch processing of groups of files without the need for user interaction.

AI.1.2 Preferences

The *Preferences* option launches the *joshua.ini* configuration file in a text editor, as shown in fig. A2.1 (d). This allows setting the processing preferences, including calibration parameters, standard folder, and algorithms for phase extraction, quality map calculation etc.

AI.1.3 Exit

Close all windows and exit the application.

AII.3 Action Menu

AI.1.4 Normalize

This option launches the *Open File* dialog to select an input image and apply the normalization algorithm. The application offers the possibility of opening as well a background image of the object without the projected fringes, and use it to improve the quality of the normalization.

AI.1.5 Run

This option launches the *Open File* dialog, shown in fig. AII.2(e), to select the input data. The software accepts native MOI files (*.moi) which contain the reference and object images, and optionally also a binary mask. Joshua results files, in MAT Matlab proprietary format (*.mat) containing array variables *ref*, *obj* and *mask* are also supported. The input data can also be read as separate images in several standard image formats such as JPEG, BMP or TIFF.

The *Mask Creation* screen shown in fig. AII.2 (f) opens after the input data is read into memory. The screen shows the object image and a set of tools that allow creating a mask to cover background areas in the image that do not contain fringe pattern information. These tools include: pixel selection based on thresholding the reference image, the object image, or the quality map, mouse selection of rectangular, circular and polygonal shapes, logical erosion and dilation of the mask, as well as general *Invert*, *Clear* and *Undo Last* tools. *Export* and *Import* of masks is also possible in native BKG format, or in the BNG format used by the photoelastic software package VISION.

After the mask is created, a window opens offering three options for the calibration of the dataset: performing a *New* calibration, using the *Last* calibration values stored in the *joshua.ini* file, or applying *None*. The *New* calibration option opens the *Calibration* screen shown in fig. AII.2(a), and should only be selected when the input dataset contains a calibration cone. The software determines automatically the location of the apex and edge of the cone, which can be manually fine-tuned by the operator if necessary. The *Change geometry* tool reverses the sign of the phase map depending on the location of the projector to the right or to the left of the camera. The physical dimensions of the calibration cone needed for the calibration can be selected from the pull-down menu.

The *Results* screen shown in AII.2(b) allows the display and analysis of the input images and intermediate and final results such as the calibrated depth map, the wrapped phase, and the quality map. The map to be displayed can be selected in the pull-down menu shown in the detail AII.2 (b.4). Clicking on the image displays vertical and horizontal profiles of the active map. The coordinates and the value of the current point are also displayed below the image.

The *Copy* menu in the detail (b.1) allows creating a copy of the *Results* screen to the clipboard or saving it as a bitmap image. The *Colormap* menu in (b.2) provides tools to control the color scale of the data. Finally, the *Modify* menu in (b.3) contains two tools that allow modifying the depth map. *Tilt* implements the processing algorithm described in section V.4.5 to calculate displacements oblique to the viewing direction and *Piston* provides piston term adjustment either by manually selecting a point in the image with a known value of depth or by means of the automatic distance measurement algorithm described in section VI.4.3, which

makes use of an additional input image of a laser spot. The second pull-down menu, see detail (b.5), gives access to the range of post-processing options described in the next section, including the piston correction routines under the *Piston term* option.

A results file containing intermediate and final results together with the input images and information relative to the processing are stored in MAT format. These results files con be later opened with JOSHUA in one of two ways: (i) with the *Run* option, if only the input data *ref*, *obj* and *mask* are required in order to re-calculate the results, or (ii) with the *Postprocessing* option in order to review the stored results.

AI.1.6 Postprocessing

The *Postprocessing* option in the *Action* menu launches the *Open file* dialog to select a results file to display it in the *Results screen.* A number of post-processing routines can then be accessed via the second pull-down menu in fig. AII.1 (b.5).

The *3D Display* option opens a window with a three-dimensional plot of the active map, as shown in fig. AII.3(a). The associated control panel allows modifying display options. *Obliquity* is related to the generation of the correction maps described in section V.3.3. This option launches the screen shown in fig. AII.3(b), which includes filtering tools to smooth out noisy depth maps previous to the calculation of the derivatives. The *Export* option opens the dialog shown in fig. AII.3(c) to export the data as ASCII text files or bitmap images. The *Profile* option allows selecting an arbitrary line in the image and plotting a profile of the active map as shown in fig. AII.3(d). *Info* opens the screen in fig. AII.3(e), which shows information such as processing parameters, times and algorithms, input and output files and calibration parameters. *Piston term* launches the piston correction routines, see fig. AII.3(f).

AII.4 View Menu

The *View Menu*, see fig. AII.1(b.3), contains only the *View Image* option. This option opens a viewer application that handles a range of formats including standard JPEG, BMP, and TIF image files, BKG and BNG binary masks, FAC photoelastic datasets created with VISION, native MOI files and results files in MAT format.

AII.5 Help Menu

The *Help Menu* in fig. AII.1(b.4) gives access to the *About JOSHUA* option, which launches the *Welcome screen* in fig. AII.1(a), and the *Help* option, which opens the HTML help files.

AIII List Of Publications

AIII.1 Published Conference Papers

Heredia, M., Patterson, E.A.; Projection moiré for optical path length correction in reflection photoelasticity; *Proceedings of the 2001 International Conference of the British Society for Strain Measurement. pp68-71, (2001) Lancaster, (UK), 5-6 Sep 2001.* This paper was awarded the 1st Prize in the Young Stress Analyst Competition 2001.

Heredia, M., Patterson, E.A.; Design and development of moiré systems for industrial applications; *Rank Prize Funds Mini-Symposium on Optical Metrology Techniques for Industrial Applications, Grasmere. (UK), 8-11 April 2002*

Heredia, M., Patterson, E.A.; Moiré and fringe projection testing methods for aerospace applications; *Proceedings of the 2002 SEM Annual Conference & Exposition on Experimental and Applied Mechanics, paper #96, Milwaukee, Wisconsin, (USA), 10-12 June 2002*

Heredia, M., Patterson, E.A., Lesniak, J.R.; Deformation data from thermal marking; *Proceedings of the BSSM International Conference on advances in experimental mechanics (2002). pp41-45, Stratford-Upon-Avon, (UK), 27-29 Aug. 2002.* This paper was awarded the 2nd Prize in the Young Stress Analyst Competition 2002.

Heredia, M., Patterson, E.A., Lesniak, J.R.; On the use of thermal marking to measure deformation; *Proceedings of the 2003 SEM Annual Conference on Experimental and Applied Mechanics, paper #13. Charlotte, North Carolina (USA), Aug. 2003*

Patterson, E.A., Greene, R.J., Heredia, M., Lesniak J.R.; Hybrid thermal methods in experimental stress analysis; *ATEM'03 JSME-MMD, Nagoya (Japan), 10-12 Sep. 2003*

AIII.2 Published Papers In International Journals

Heredia, M., Patterson, E.A.; On the industrial applications of moiré and fringe projection techniques; *Strain, Vol. 39, pp95-100, Aug. 2003*

Heredia, M., Patterson, E.A., Lesniak, J.R.; Deformation data from thermal marking; *Strain, Vol. 39, pp149-152, Dec. 2003*

AIII.3 Papers In Preparation

Heredia, M., Patterson, E.A.; Location, shape and deformation measurement using a portable fringe projection system; *submitted to Experimental Mechanics.*

Heredia, M., Patterson, E.A., Lesniak, J.R.; A novel technique of strain analysis using thermal gratings; *in preparation for submission to Experimental Mechanics.*

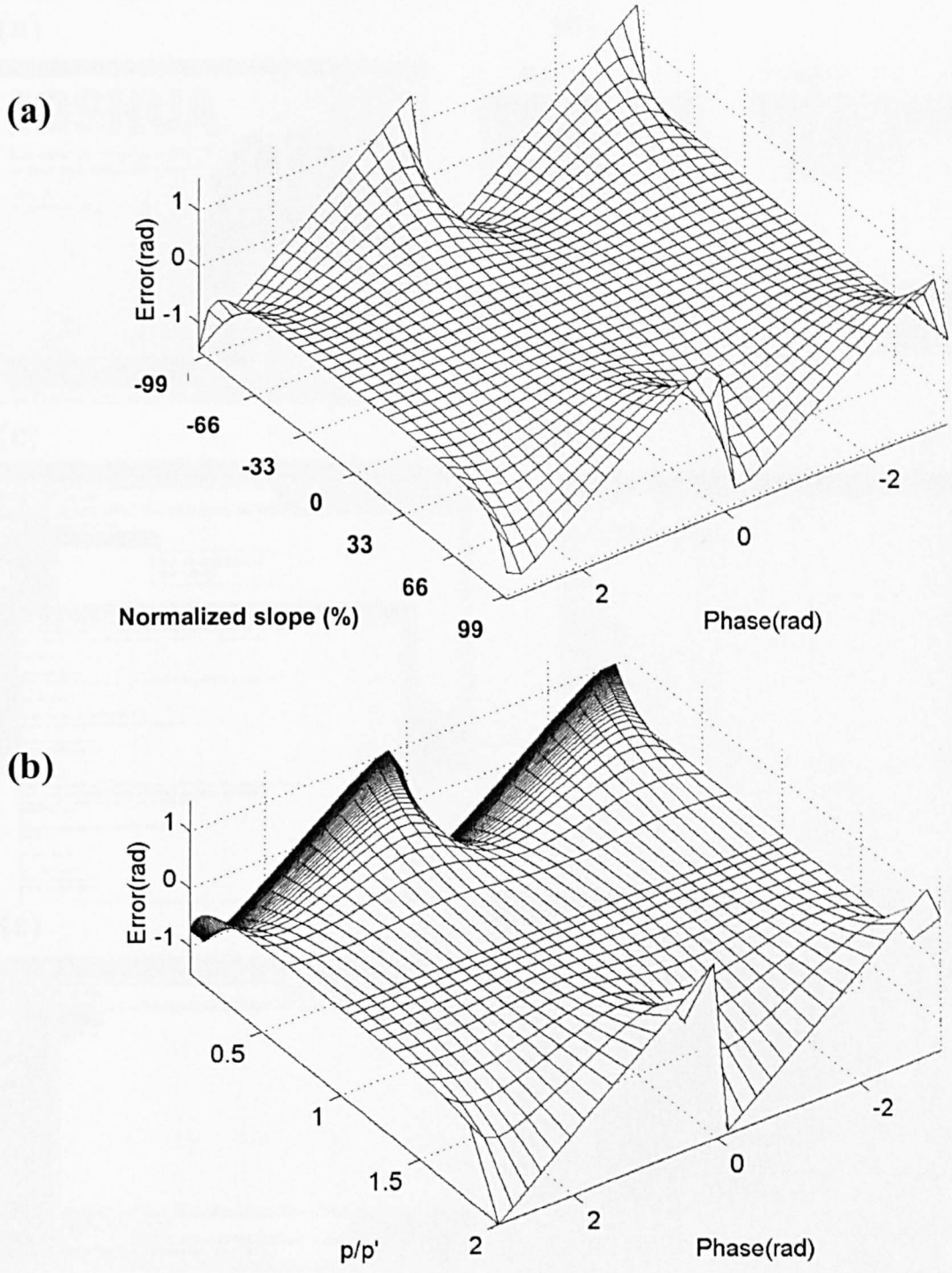

Figure AI.1 Graphical representation of the error in the estimation of phase with the novel five-step spatial algorithm shown (a) as a function of the slope of the modulated phase and (b) as a function of the ratio between the pitch of the reference and the object images p/p'. The error function is periodic, therefore only the principal phase values $[-\pi,\pi]$ have been graphed. Beyond the region plotted, i.e. for $m<-2\pi/p$ or $m>2\pi/p$ in (a) and for $p/p'<0$ or $p/p'>2$ in (b), the sign of the error function is reversed abruptly.

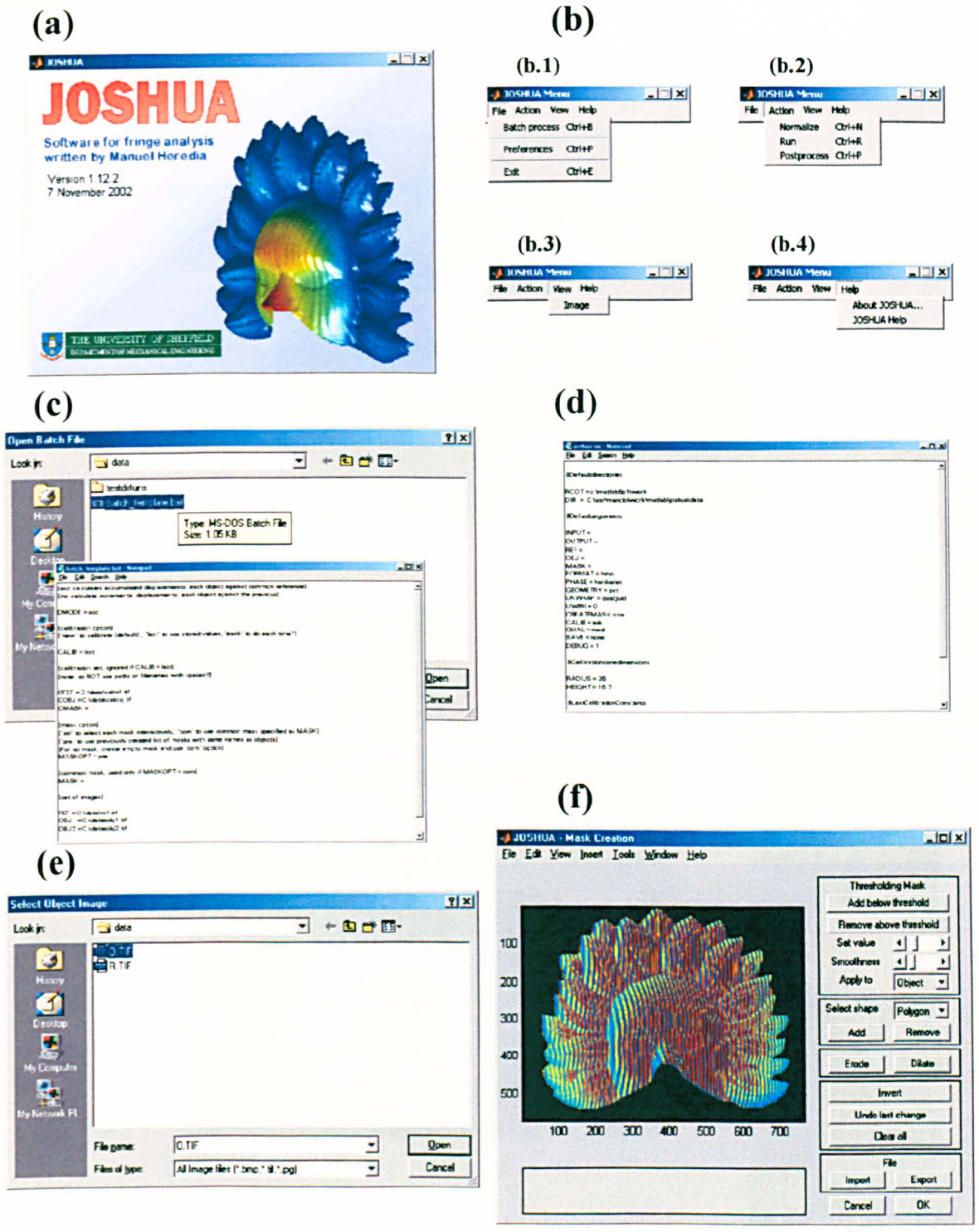

Figure AII.1: Joshua software (a) Welcome screen (b) The main menu has four options: (b.1) File menu, (b.2) Action menu, (b.3) View menu and (b.4) Help menu. File menu: (c) Batch processing reads the processing parameters from a text file allowing automatic batch processing without user interaction (d) Setting preferences in the *joshua.ini* file. Action menu: (e) Open input files needed to Run the processing (f) Mask generation.

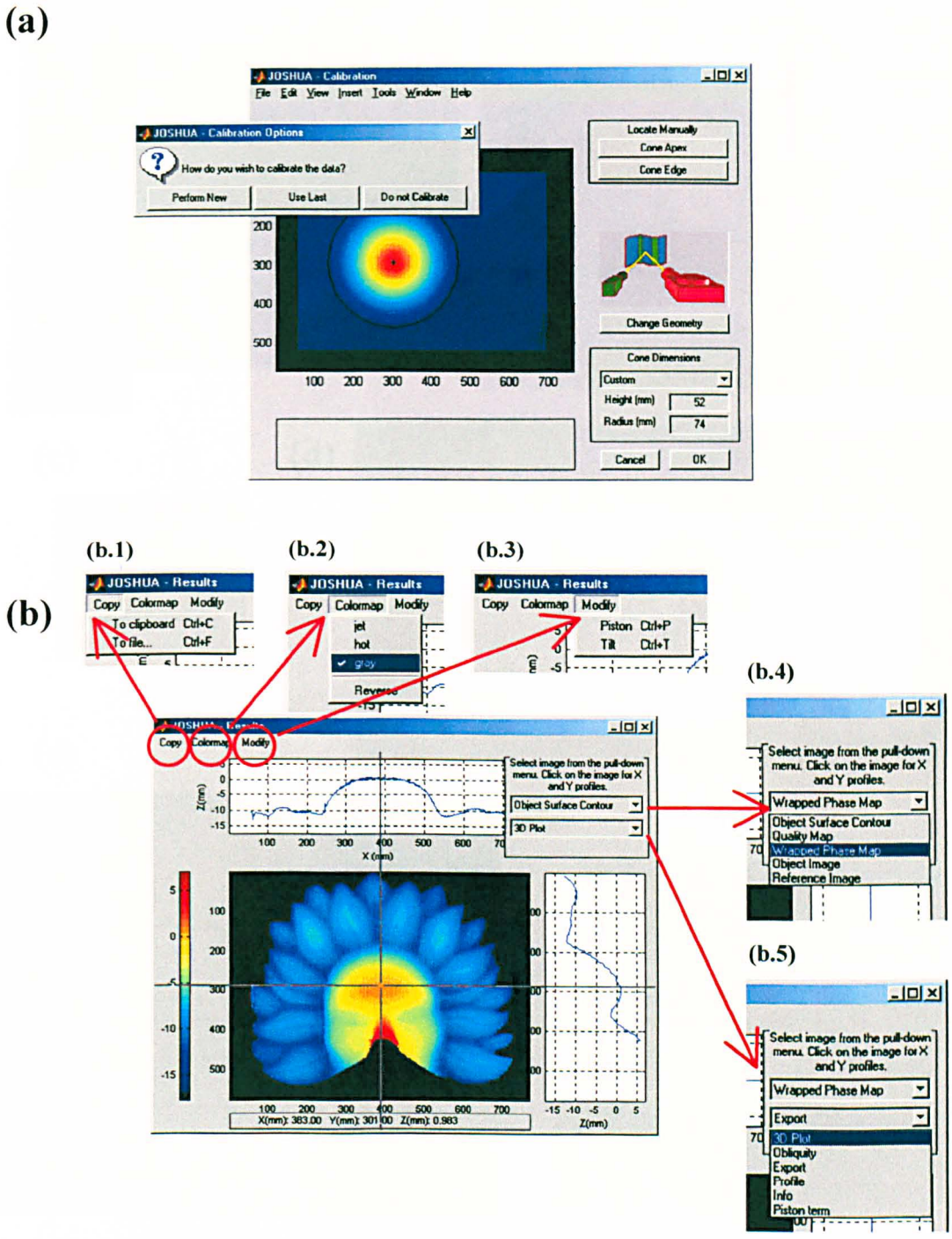

Figure AII.2: Joshua software: (a) Calibration screen (b) Results screen (b.1) Copy screen to clipboard or bitmap file, (b.2) Colour scale options, (b.3) Modify the depth map: Tilt and Piston term adjustment. (b.4) Selecting an image to display in the pull-down menu (b.5) Post-processing options.

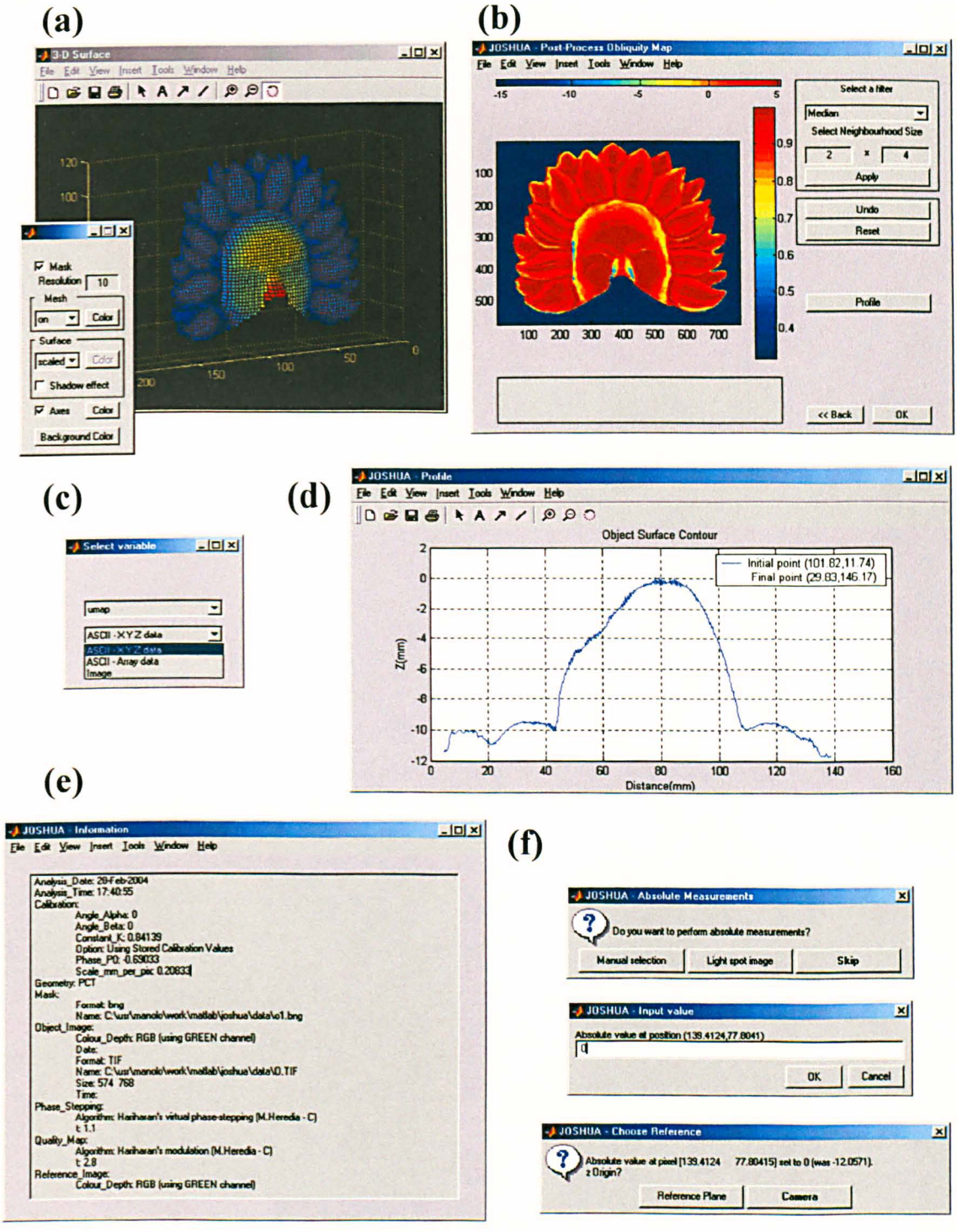

Figure AII.3: Post-processing options implemented in Joshua Software: (a) 3D display (b) Obliquity maps (c) Data export as ASCII files or bitmap image (d) Plotting profiles (e) Information screen (f) Piston term correction can be applied manually or with help of an additional laser spot dataset.